NIM: The Neutral Gas and Ion Mass Spectrometer to Explore the Galilean Ice Worlds

Inauguraldissertation
der Philosophisch-naturwissenschaftlichen Fakultät
der Universität Bern

vorgelegt von

Martina Föhn

von Muotathal

Leiter der Arbeit:
Prof. Dr. Peter Wurz
Physikalisches Institut, Universität Bern

NIM: The Neutral Gas and Ion Mass Spectrometer to Explore the Galilean Ice Worlds

Inauguraldissertation
der Philosophisch-naturwissenschaftlichen Fakultät
der Universität Bern

vorgelegt von

Martina Föhn

von Muotathal

Leiter der Arbeit:
Prof. Dr. Peter Wurz
Physikalisches Institut, Universität Bern

Von der Philosophisch-naturwissenschaftlichen Fakultät angenommen.

Bern, 17.12.2021

Der Dekan
Prof. Dr. Zoltán Balogh

Abstract

The JUpiter ICy moons Explorer (JUICE) of the European Space Agency (ESA) has the purpose to investigate Jupiter and its icy moons Europa, Ganymede and Callisto in great detail. Among other scientific goals, JUICE will investigate the Jupiter system as a potential habitable system because the three icy moons have subsurface oceans where life might be possible. On board of JUICE is the Particle Environment Package (PEP), which consists of six individual instruments measuring electrons, ions and neutral particles in an energy range from meV up to MeV. One of these six instruments is the Neutral gas and Ion Mass spectrometer (NIM) from the University of Bern. The NIM instrument is designed to measure the chemical and isotope composition of the icy moons' exospheres during the flybys of JUICE of the icy moons and also during JUICE final destination in Ganymede's orbit. Knowing the chemical and isotope composition allows to investigate the origin and evolution processes involved in the formation processes of the icy moons, Jupiter and our solar system.

NIM is a time-of-flight mass spectrometer able to measure thermal neutral molecules and ionospheric ions. This thesis shows the journey from finalising the flight design of the NIM instrument to the actual testing, qualification, and calibration until delivery of the NIM Proto-Flight (PFM) instrument in December 2020 to the JUICE spacecraft. On this journey, different flight components were tested and analysed as they became available during the development and finalisation of the PFM and Flight-Spare (FS) instrument. From the foreseen scientific scope for the NIM instrument, a list of measurement requirements was delivered. This work shows that NIM PFM and NIM FS meet all these requirements.

Contents

List of Acronyms

ADC	Analogue-to-Digital Converter	**NIM**	Neutral Gas and Ion Mass Spectrometer
CASYMIR	CAlibration SYstem for the Mass spectrometer Instrument ROSINA	**NIMS**	Near Infrared Mapping Spectrometer
CReMA	Consolidated Report on Mission Analysis	**NGMS**	Neutral Gas Mass Spectrometer
ESA	European Space Agency	**P-BACE**	Polar Balloon Atmospheric Composition Experiment
Fil	Filament electrode	**PCB**	Printed Circuit Board
FoV	Field-of-View	**PEP**	Particle Environment Package
FS	Flight-Spare Model	**PFM**	Proto-Flight Model
FWHM	Full Width at Half Maximum	**R**	Reflectron (ion-mirror)
HV	High-Voltage	**ROSINA**	Rosetta Orbiter Spectrometer for Ion and Neutral Analysis
i	ion	**RTG**	Radioisotope Thermoelectric Generators
IS	Ion-Source	**RTOF**	Reflectron Time-Of-Flight mass spectrometer
JDC	Jovian plasma Dynamics and Composition analyser	**S/C**	Spacecraft
JEI	Jovian Electrons and Ions	**SATANS**	Supersonic cATion and ANion Source
JENI	Jovian Energetic Neutrals and Ions	**SN**	Serial Number
JNA	Jovian Neutrals Analyser	**SNR**	Signal-to-Noise Ratio
JoEE	Jovian Energetic Electrons	**TF**	Time Focus
JUICE	JUpiter ICy moon Explorer	**th**	thermal
LV	Low-Voltage	**TOF**	Time-Of-Flight
MCP	Multi-Channel-Plate		
MEAP	Mars Environment Analogue Platform		
n	neutral		

1. Introduction

1.1. Mission Introduction

Investigation of the stars and the night sky started a long time ago. Back then, the movement of the Sun, the Moon and the stars was used to derive time, for navigation and for religious rituals. First records of systematic observations of the night sky date back to the Assyro-Babylonians around 1000 BCE. In the third century BCE Greek astronomers tried to estimate the distances between the different cosmic objects with geometrical tools [3]. The invention of telescopes in the early 17th century allowed then a closer look at the objects in the night sky and lead to the discovery of the Galilean moons' Io, Europa, Callisto and Ganymede by Galileo Galilei in 1610. Galileo discovered that these objects were orbiting around another object than the Sun, namely Jupiter. The invention of the first modern rockets during the cold war, opened the opportunity of on site exploration of solar system bodies. The data acquired through those in situ measurements gave further insight into the formation processes and history of our solar system. The missions Pioneer 10 & 11 and Voyager 1 & 2 were the first space missions, which took close images of Jupiter and its icy moons. They discovered Jupiter's ring system and detected more small moons of Jupiter than only the four big Galilean moons. The missions Galileo (1995-2003) and JUNO (2016-2025) were two missions specifically with the objective to further investigate Jupiter itself (JUNO) and its icy moons (Galileo) with the main outcome of giving strong evidence for salty subsurface oceans on the moons Europa, Ganymede and Callisto by measuring the induced magnetic fields. These oceans could be environments where life might be possible. In addition, the Galileo mission provided data that Ganymede has an intrinsic magnetic field interacting with the strong magnetic field of Jupiter [42].

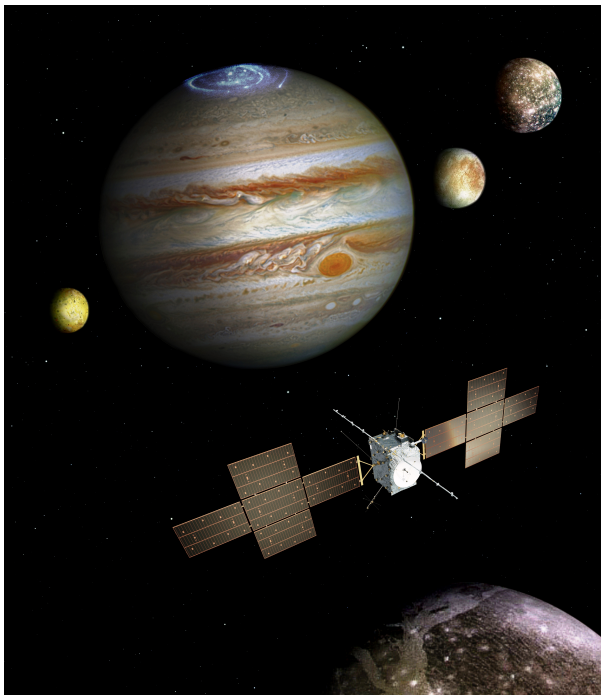

Figure 1: Artist impression of the Juice mission exploring the Jupiter system [14].

The JUpiter ICy moons Explorer (JUICE) built by the European Space Agency ESA has the objective to further investigate Jupiter, its environment and its icy moons with regards to their potential of harbouring life. JUICE will characterise Jupiter as a planet, Jupiter's plasma environment and it will characterise Jupiter's icy moons Europa, Ganymede and Callisto. JUICE will characterise Jupiter's atmospheric dynamics, composition and chemistry and the atmosphere's vertical structure. It will charac-

terise Jupiter's magnetosphere to understand the role of the moons as sources and sinks for the magnetospheric plasma. JUICE will study Jupiter's ring system, its small satellites and it will study Io's activity and surface composition with its remote sensing instruments.
With regards to the icy moons, the main objectives are to characterise their potential subsurface oceans and their non-icy material. Europa consists mainly of silicates with a water layer and an ice crust on top of that. Europa's surface is fairly young showing almost no impact craters, which implies that the icy crust frequently resurfaced similar to plate tectonics. Ganymede is until now the only satellite in our solar system known having an intrinsic magnetic field generated by a magnetic dipole field. Therefore, JUICE will investigate the interaction processes of that magnetic field with Jupiter's magnetic field because it is strong enough to successfully shield the moon against most of the plasma flow from Jupiter's magnetosphere. Callisto is the outer most of the Galilean moons and by far the most cratered. It lacks small craters indicating some minor erosion processes. Compared to the other three Galilean moons, Callisto lacks any larger tectonic activity [24].

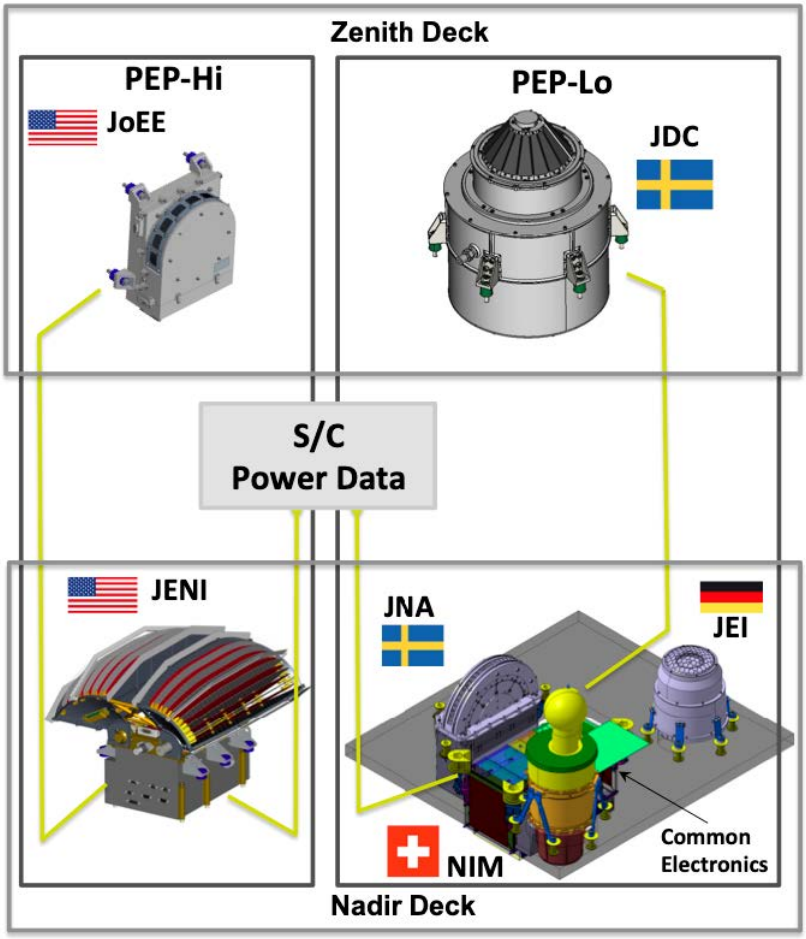

Figure 2: Sketch of the six PEP instruments and their organisation on the spacecraft [8].

To fulfil the scientific goals, JUICE has an instrument suit consisting of 11 instruments on board ranging from cameras, spectrometers, magnetometers, to particle instruments, and gravity measurements. One of these instruments is the Particle and Environment Package System (PEP) (Fig. 2). The main focus of PEP is to characterise Jupiter's plasma environment and the composition of the icy moons' exospheres. Therefore, PEP has six instruments to measure neutral particles, ions and electrons with energies from thermal (< 5 eV) up to 5 MeV (ions) [8]. One of these six instruments is the Neutral Gas and Ion Mass Spectrometer NIM. The focus of NIM lays on the characterisation of the icy moons' exospheres and the detection of ions with an energy less than 10 eV to complete the plasma measurements for slow ions of the other PEP instruments. With the capability of measuring slow ions, NIM is able to detect a potential ionosphere of the icy moons [31]. NIM will be the first mass spectrometer taking in situ measurements of the icy moons exosphere. The exosphere is formed by particles released from the moons' surface by ion bombardment, sublimation and photon interaction processes. By sampling the exosphere, we get a deeper insight in the surface composition and the formation processes involved of the icy moons themself. For example, there are two major theories about when the icy moons were formed. One suggests that the icy moons' were formed in the protostar nebula of our solar system implying that the moons have a similar age as Jupiter. Another hypothesis suggests that the icy moons' were formed in the subnebula of Jupiter, implying that they are younger than Jupiter. By determining the particle density and isotope ratios of the detected species, we can distinguish between these two formation processes giving us a deeper insight in how our solar system was formed and which processes in the formation of the icy moons' are the most relevant [41, and references therein].

The instruments sent to space missions are highly customised to fulfil the specific requirements. For space missions, the instruments have to be small, light and low power consumptive. Especially for missions having targets in the outer solar system, such as JUICE with target Jupiter, power is a very limited resource. At Jupiter, the solar flux density is by a factor 25 lower than at Earth because Jupiter is five times farther away from the Sun than Earth. Therefore, missions flying to the outer solar system often use radioisotope thermoelectric generators (RTGs) as power sources instead of solar panels because they are longer lasting and provide more power. The biggest drawback is that they are very inefficient and produce a lot of heat, which cannot be used [25]. Another main challenge is the harsh radiation environment of Jupiter. The penetrating particles lead to upset in the electronics and damage components. Therefore, a proper radiation shielding concept was necessary.

NIM is a time-of-flight mass spectrometer with heritage from previous TOF instruments developed at the University of Bern. These are the RTOF/ROSINA/Rosetta [7, 37], P-BACE/ MEAP [2] and NGMS/Luna-Resurs [47, 16]. Mass spectrometers are single ion counting instruments. Therefore, they can estimate the density distributions of the measured species much more precisely than remote sensing instruments. The biggest advantages of time-of-flight mass spectrometers compared to other mass spectrometer types is that they are extremely robust from the mechanical point of view and have a better sensitivity than scanning instruments. Magnetic sectors are heavy and require high accuracy mechanics. Quadrupole mass

spectrometers fulfil the requirements regarding size, weight and power but have a lower sensitivity than TOF instruments because to increase the mass resolution they loose sensitivity [18]. In addition, scanning instruments have a relatively long cadence [6] leading to a bad spacial resolution during the flybys of the spacecraft on the icy moons. Therefore, TOF instruments are often used in space missions.
NIM is designed to measure complex molecules up to 1000 u with a mass resolution up to m/Δm 1000 with a signal-to-noise ratio (SNR) of 6 decades. Based on present knowledge we expect in the icy moons exosphere only species with masses up to 100 u but with the ability to measure also species with higher masses, NIM is able to detect also potential organic compounds if they are present [4]. To separate species with such high masses, it requires a mass resolution of m/Δm 1000 to be able to distinguish between the different unit masses. With a SNR of 6 decades, NIM is able to measure down to partial pressures of 10^{-16} mbar corresponding to a particle density of 1 cm^{-3}. During the flybys at the icy moons, the spacecraft velocity is 1–8 km/s. Depending on the mass of the particles, the highest energy they have is up to 100 eV which is the highest energy NIM has to deal with. NIM is designed to measure neutral particles with thermal energy up to energies of 100 eV. NIM has an open and a closed source entrance for neutral particles and ions. Through the open source entrance slit, neutral particles and ions enter the ionisation region directly without interacting with the instrument structure. The closed source consists of an antechamber that thermalises incoming neutrals. Neutrals with higher speeds are therefore easier to detect than with the open source channel where particles enter the ionisation region with spacecraft velocity. As mentioned above, mass and power are for these missions very limited resources. The NIM ion-optical system has a mass of 3.13 kg from which 48 % is shielding mass to shield the detector locally to reduce noise induced by high energetic particles originating from Jupiter's plasma environment. The primarily power allocated for the NIM instrument from the spacecraft is 18.5 W, including margin.

1.2. Thesis Outline

This thesis follows up the PhD thesis of Stefan Meyer [31]. At the end of his thesis, the NIM prototype was built and the flight design the NIM was almost completed.
The objective of this thesis was to finalise the design of the NIM flight model, to build and test the NIM Proto-Flight-Model (PFM) to deliver it to the JUICE spacecraft and to build and test the NIM Flight-Spare (FS) model, which stays on Earth as a ground reference. This required environmental tests of various flight subcomponents as they became available with finally testing the ion-optical system of the NIM PFM and FS model. Ion-optical simulations were performed to set constrains on the design of the flight power supplies as they were still under development during the early phases of this thesis.
The thesis consists of three main parts: Chap. 2 shows theoretical analyses of key components of the NIM instrument such as the performance of the antechamber of the closed source. In addition, it completely presents the theoretical aspects needed to understand the performance results of the different subsystems presented in Chap. 4. Chap. 3 compares the design of the NIM prototype with the final flight design and shows the main differences between the two

models. A special focus lays there in the improvements done on the design of the detector. Chap. 4 sums up the performance tests of different subsystems partially tested stand alone (detector) or as part of the NIM Prototype (antechamber, ion-mirror). The chapter ends with performance tests of the two NIM flight models (PFM and FS).

2. Theory

NIM is a time-of-flight mass spectrometer consisting of an ion-source, a mass analyser and a detector. Fig. 3 shows a schema of the NIM ion-optical system. Gaseous particles enter the ion-source either through a closed source antechamber where they get thermalised or directly through an entrance slit. The measuring mode where the thermalised particles entering through the antechamber are analysed is called thermal mode (th-mode). The measuring mode where neutral particles are analysed, which enter the ionisation region directly is called neutral mode (n-mode) and the mode where ions are analysed is called ion mode (i-mode). The neutral particles are ionised by electron impact ionisation. A filament is heated to a temperature where it emits electrons. The electrons are accelerated up to an energy of about 70 eV. In the ionisation region, the electrons knock out electrons from the neutral gas generating positive ions. The ions are then accelerated to an energy of about 250 eV by applying a high voltage pulse on the extraction grid. NIM has a two-field ion source meaning that with the ion-optical lenses the ions are additionally accelerated and focused to compensate when the ions have different initial energies. Light species fly faster through the time-of-flight mass spectrometer

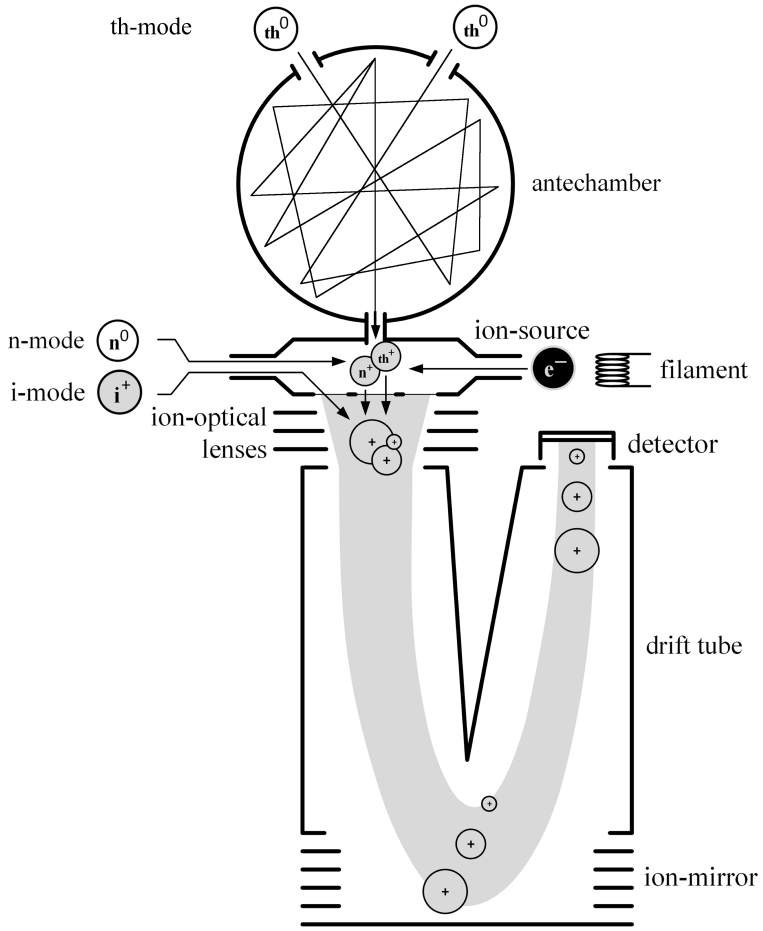

Figure 3: Schematics of the NIM mass spectrometer. Adapted from [31].

than heavier ones resulting in a separation of the species by their mass. An ion-mirror is used to increase the flight distance and to refocus ions of the same species with different energies. The ions are detected with a Microchannel-Plate (MCP) detector.
This chapter gives an overview from the theoretical perspective over the different subunits of the NIM ion-optical system. Chap. 4 shows test results of the different subunits and performance tests of the NIM Prototype, the NIM Proto Flight Model (PFM) and the Flight Spare (FS) models.

2.1. Mass Resolution

The generated ions in the ion-source are trapped in the centre by the potentials of the electrodes and the electron beam. The ions are extracted into the analysis section by a high voltage pulse applied onto the extraction grid. All ions are accelerated to the same energy W:

$$W = \int_0^{s_0} qE_s ds = \frac{qU_0}{2} \tag{1}$$

With s_0 the distance from the centre of the ion-source to the extraction grid corresponding to half the height of the ion-source. q is the particle charge, E_s is the applied electric extraction field strength induced by the voltage U_0 applied on the extraction grid. The nominal starting position of the ions is in the centre of the ion-source. Therefore, they have the kinetic energy $qU_0/2$ when reaching the extraction grid:

$$\frac{qU_0}{2} = \frac{1}{2}mv^2 \tag{2}$$

With m and v the mass and velocity of the ion. Rearranging this formula results in:

$$\frac{m}{q} = U_0 \frac{t^2}{D^2} \tag{3}$$

With t the time of flight and D the flight distance from the extraction grid to the detector. U_0 and D^2 are merged into one constant C resulting in:

$$\frac{m}{q} = C(t - t_0)^2 \tag{4}$$

t_0 corresponds to a time offset between the start of the mass axis and the time axis. The two calibration constants C and t_0 are determined by at least knowing two species in the mass spectrum. The correctness of the mass scale can be verified by checking the other mass peaks in the mass spectrum, which all have to be on integer masses, ignoring the small deviations for now. The mass is therefore proportional to t^2:

$$m = c \cdot t^2 \tag{5}$$

The derivative is:

$$\frac{dm}{dt} = 2\ ct \tag{6}$$

$$dm = 2\ ct \cdot dt \tag{7}$$

Dividing Eq. (5) by Eq. (7) results in:

$$\frac{m}{dm} = \frac{ct^2}{2\,ct \cdot dt} \tag{8}$$

$$\frac{m}{dm} = \frac{t}{2\,dt} \tag{9}$$

With:

$$dt \rightarrow \Delta t_i = FWHM \tag{10}$$

$$t \rightarrow t_i \tag{11}$$

Results in:

$$\frac{m}{dm} = \frac{t_i}{2FWHM} \tag{12}$$

With t_i the centre of the mass peak in the time domain and $FWHM$ is the full width at half maximum of the mass peak [46].

In the following section, the different contributions affecting the mass resolution are analysed. The focus is on the contributions originating from the ion source because they have the biggest impact on the mass resolution of the instrument.
The total time spread dt_i of the signal of a particle species i at the detector is:

$$dt_i = \sqrt{\sum_k dt_k^2} = \sqrt{dt_D^2 + dt_{ADC}^2 + dt_{th}^2 + dt_s^2 + dt_{tfall}^2} \tag{13}$$

With the different contributions dt_k assumed to be independent from each other. When an ion hits the detector, it generates a charge pulse with pulse width dt_D. For the NIM detector, the pulse width is $\sim$ 0.7 ns. The generated pulse is converted into a digital signal with an analogue-to-digital converter (ADC). The ADC used in the laboratory has a sampling rate of 4 GHz resulting in a time resolution dt_{ADC} of 0.25 ns. The flight ADC has a maximal sampling rate of 2 GHz corresponding to a time resolution of 0.5 ns. The contribution to the time spread by the ion-mirror is small compared to the other effects and can therefore be neglected.

The time spreads resulting from the thermal energy of the ions dt_{th}, from the different start positions of the ions within the ionisation region dt_s and from the fall time of the high voltage pulse dt_{tfall} are coupled because they all affect the energy deviation from the nominal energy (Eq. (1)) of the ions. Initially, the ions in the ion-source have thermal energy W_{th}:

$$W_{th} = \frac{3}{2} \cdot k_B \cdot T \tag{14}$$

With k_B the Boltzmann constant and T the temperature. The thermal energy leads to an initial velocity distribution of the ions with a mean velocity of v_{init} (Fig. 4 top panel). Ions number 1 and 3 have the same thermal energy but one is directed towards the extraction grid where the other one is directed towards the backplane.

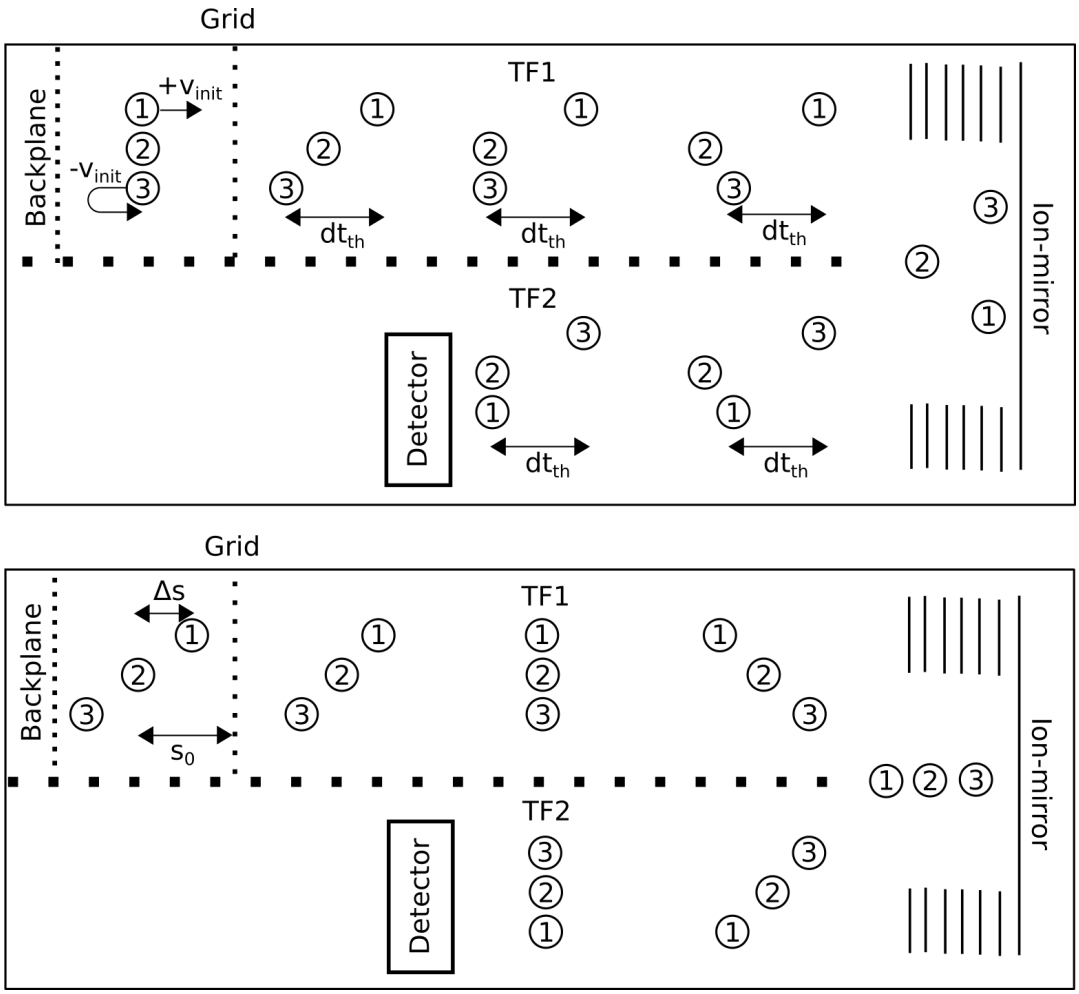

Figure 4: Flight path of ions with different thermal energy (top panel) and start positions (lower panel). v_{init} is the initial velocity of the ions and dt_{th} the turn-around time. TF1 and TF2 are the locations of the first and second time focus respectively.

When a high voltage pulse is applied on the extraction grid, ion number 3 has to be turned around. The time difference between ions 1 and 3 is called turn-around time. At a certain point in time, ion 3 will overtake ions with less energy (ion 2). The turn-around time cannot be corrected with the ion optics. The only option to reduce the turn-around time would be to cool the ions, which is not possible for a space instrument.
The total energy W the ions get in the ionisation region is:

$$W = \int_{s_{init}}^{s_0} q \cdot E(t) \cdot ds \tag{15}$$

With s_{init} the initial position of the ions, s_0 the distance from the centre of the ionisation region to the acceleration grid, q the particle charge and $E(t)$ the electric field strength depending on the time t. When the ions start at different positions in the ionisation region s_{init}, they receive a different amount of energy because their flight distance in the acceleration field is different

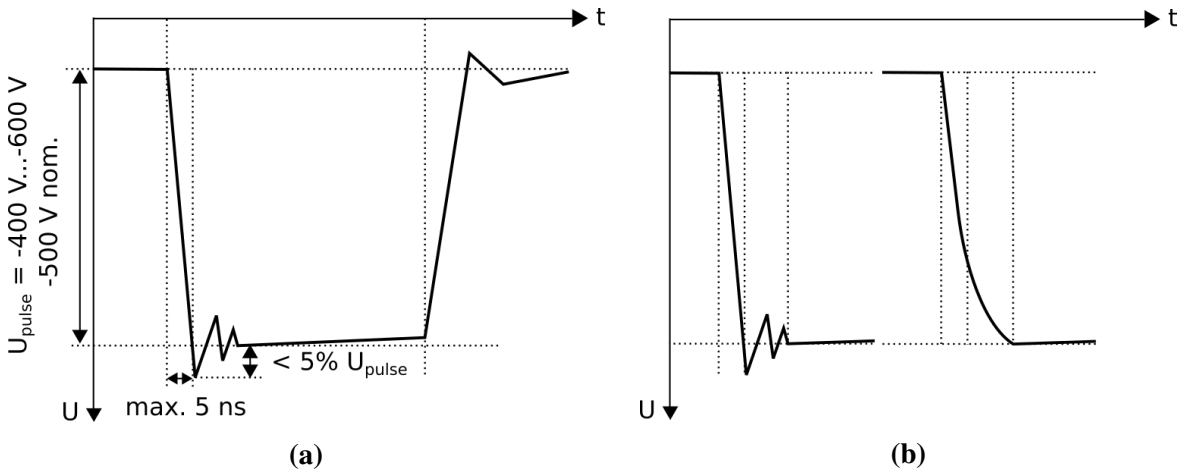

Figure 5: a) Shape of a realistic high voltage pulse applied on the extraction grid. b) Two different possible shapes of the falling edge of the high voltage pulse.

(Fig. 4 lower panel).At a certain distance on the flight path, ions with higher energy will overtake ions with lower energy. The time spread induced by the different start positions of the ions is dt_s. With a two-field ion source, like NIM, dt_s can be minimised at the first time focusing point TF1. With an ion-mirror ions with an energy spread up to 10 % are refocused. Ions with higher energy penetrate deeper into the ion-mirror resulting in a longer flight path of the higher energetic ions. The best position for the detector is when all ions with different energies are at the same position, which is at the time focus of the ion mirror TF2.

Ideally, the shape of the extraction pulse is a rectangle. Fig. 5a) shows the shape of a realistic extraction pulse. The pulse needs the time t_{fall} to build up the extraction potential on the extraction grid. Fig. 6 top panel shows the changing electric field as a function of the position for atomic hydrogen (H_1) and oxygen (O_1) in case when these two species start at the same position. The total energy W of the ions at the exit of the extraction region corresponds to the area under the curves. The energy as a function of the flight distance s in the ionisation region is plotted on the bottom panel of Fig. 6. Hydrogen is lighter than oxygen and therefore, it leaves the ionisation region earlier. This results in a smaller amount of energy for hydrogen than for oxygen. The shorter the fall time of the high voltage pulse is, the smaller is the energy difference because it shifts the position of the ions at the fall time $s_i(t_{fall})$ towards zero. When looking at the shape of the falling edge of the pulse (Fig. 5b), it is more important to have a small fall time with an overshoot than a pulse slowly converging to the maximum because the resulting energy deviation in the first case is much smaller than in the second.

In the following section the influence of the fall time of the high voltage pulse t_{fall} in combination with the longitudinal spacial spread Δs of the ions in the ionisation region and the thermal energy of the ions on the mass resolution is analysed. To investigate the impact of these effects, this model does not include any focusing lenses and has no ion-mirror.
The derivation of the equation of motion is based on [1]. The electric field $E(t)$ in the ionisa-

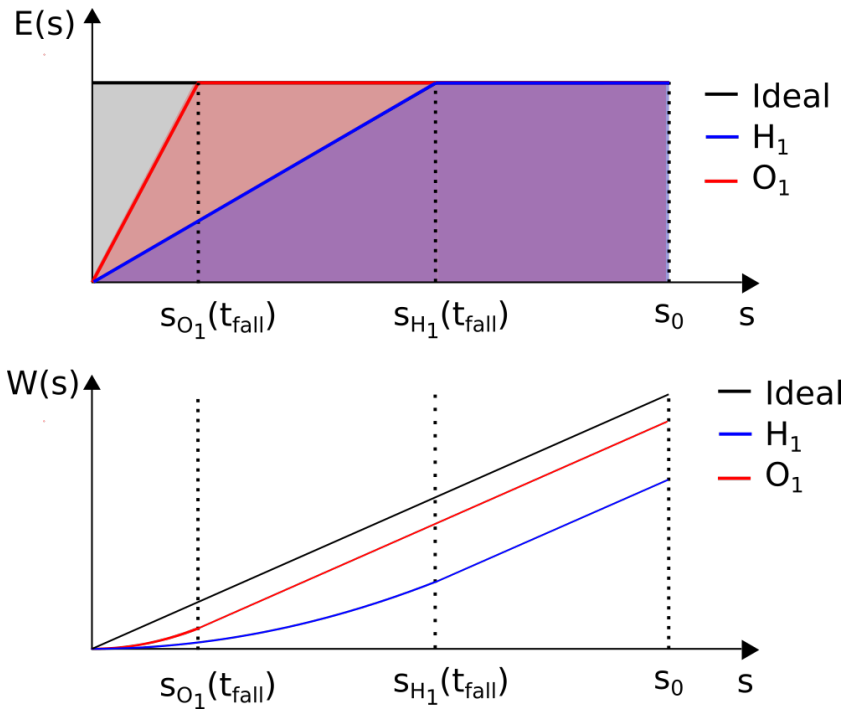

Figure 6: Top panel: Electric field $E(s)$ an ion experiences, as a function of the distance between the centre of the ionisation region and the extraction grid s_0 for two hydrogen (H_1) and oxygen (O_1). $s_i(t_{fall})$ is the position of the corresponding species at the fall time t_{fall}. Lower panel: Energy $W(s)$ of the ions as a function of their position.

tion region is approximated with a linear function during the fall time t_{fall} and as a constant during the rest of the time:

$$E(t) = \begin{cases} E_1 \cdot \frac{t}{t_{fall}}, & (0 \leq t \leq t_{fall}) \\ E_1, & t_{fall} < t \end{cases} \tag{16}$$

E_1 is the electric field strength when the high voltage pulse is fully applied:

$$E_1 = \frac{U_0}{2 \cdot s_0} \tag{17}$$

With U_0 the voltage on the extraction grid. The equation of motion for the ions during the fall time is:

$$a_{fall}(t \leq t_{fall}) = \frac{q \cdot E_1}{m \cdot t_{fall}} \cdot t \tag{18}$$

With a_{fall} the acceleration of the ions and m the ion mass. The velocity of the ions v_{fall} is:

$$v_{fall}(t \leq t_{fall}) = \frac{q \cdot E_1}{2 \cdot m \cdot t_{fall}} \cdot t^2 + v_{init} \tag{19}$$

With v_{init} the initial velocity of the ions before applying the extraction pulse. v_{init} originates from the ion's thermal energy. The position of the ions s_{fall} at the time t is:

$$s_{fall}(t \leq t_{fall}) = \frac{q \cdot E_1}{6 \cdot m \cdot t_{fall}} \cdot t^3 + v_{init} \cdot t + s_{init} \tag{20}$$

With s_{init} the initial position of the ions. When the high voltage pulse is fully applied and the ions did not reach the extraction grid until that time, the acceleration of the ions a_p is:

$$a_p(t > t_{fall}) = \frac{q \cdot E_1}{m} \tag{21}$$

The velocity v_p is:

$$v_p(t > t_{fall}) = \frac{q \cdot E_1}{m}(t - t_{fall}) + v_{fall}(t_{fall}) \tag{22}$$

With $v_{fall}(t_{fall})$ the velocity of the ions at the time t_{fall}. The position s_p is:

$$s_p(t > t_{fall}) = \frac{q \cdot E_1}{2 \cdot m}(t - t_{fall})^2 + v_{fall}(t_{fall})(t - t_{fall}) + s_{fall}(t_{fall}) \tag{23}$$

With $s_{fall}(t_{fall})$ the position of the ions at the time t_{fall}. When the ions leave the ionisation region before full high voltage is applied on the extraction grid, the time they spend in the ionisation region t_{IS} is calculated by setting $s_{fall} = s_0$ and solving the cubic Eq. (20) for t. The velocity v_{Grid} of the ions at the extraction grid is determined by inserting t_{IS} in Eq. (19). When the ions leave the ionisation region after the high voltage is fully applied, the time they spend in the ionisation region t_{IS} is calculated by setting $s_p = s_0$ and solving Eq. (23) for t. The velocity v_{Grid} of the ions at the extraction grid is determined by inserting t_{IS} in Eq. (22). The total flight time of the ions in this model is:

$$t_{TOF} = t_{IS} + t_D \tag{24}$$

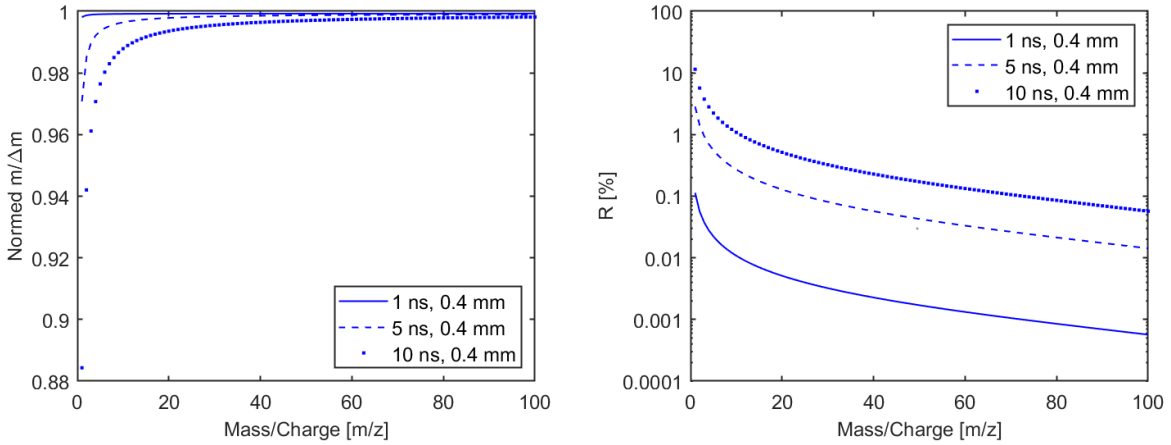

Figure 7: Left: Calculated mass resolution as a function of the mass/charge ratio of the ions for three different fall times of the extraction pulse. Right: relative deviation of the mass resolution from the mass resolution plateau as a function of the mass/charge ratio.

With t_D the time of flight the ions need for the distance between the extraction grid and the detector. The mass resolution is calculated according to Eq. (9). To have a measure for the impact of the fall time on the different masses, the deviation R of the mass resolution of ions with a mass/charge ratio i relative to the mass resolution of ions with a mass/charge ratio of 200 is calculated:

$$R = 1 - \frac{m_i/\Delta m_i}{m_{200}/\Delta m_{200}} \tag{25}$$

The mass resolution reaches a plateau for high mass ions because the term dt_s gets dominant over the other error contributions from Eq. (13). dt_s increases linearly with the time t and therefore the mass resolution reaches a plateau for high mass ions (see Fig. 7 left). The deviation R is a measure by what fraction the mass resolution of the low mass ions deviates from that plateau. The mass resolution of mass/charge ratio 200 was taken as a reference. The calculations revealed that for low mass ions the impact of the ion temperature is negligible compared to the impact of the spatial spread Δs and the pulse fall time t_{fall}. The impact of t_{fall} is shown in Fig. 7 left. The initial range of starting positions is $\pm$ 0.4 mm which corresponds to the diameter of the electron beam in the ionisation region. With decreasing fall time, the deviation in mass resolution decreases. This is also visible in the right figure. An improvement in the fall time by one decade results in an improvement of 1 decade of the relative error. With a fall time of 1 ns, the maximum relative deviation is only 10^{-3}. The impact of the fall time is also visible in measurements. Fig. 8 shows measurements with two different pulse generators with fall times of 1.5 ns and 3.5 ns.
Fig. 9 left shows the mass resolution as a function of the position deviation Δs for mass 1 u. The ionisation region has a diameter of 2 mm. Therefore the maximal deviation of the ions

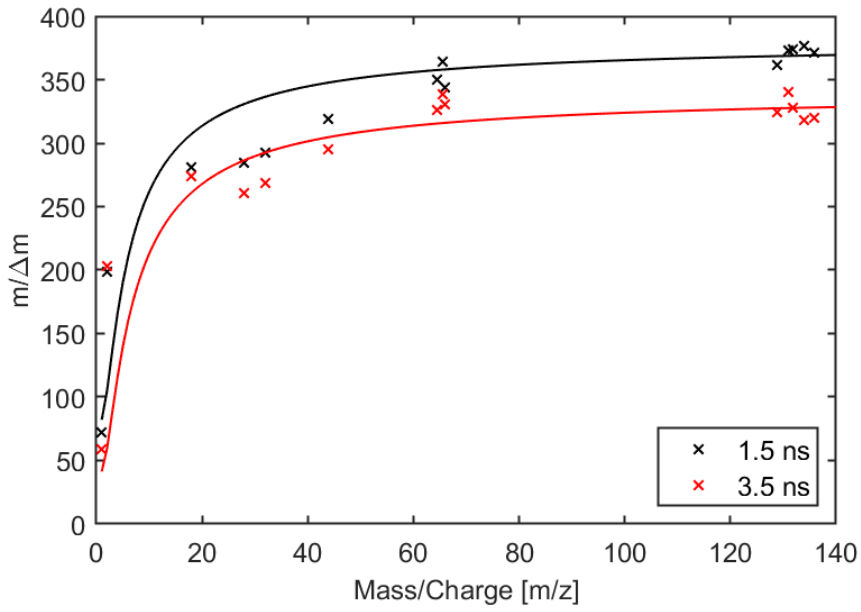

Figure 8: Measurement results of two different pulser generators with 1.5 ns and 3.5 ns fall time. Crosses are measurement points and solid lines are trend lines.

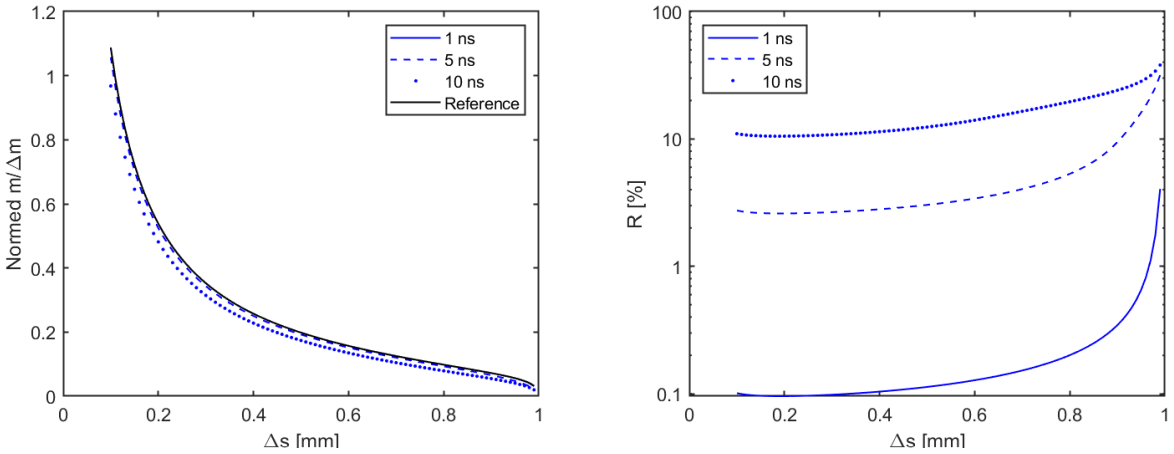

Figure 9: Left: Calculated mass resolution as a function of the spatial spread Δs for three different pulser fall times. Right: relative deviation of the mass resolution from the plateau as a function of the mass/charge ratio.

is 1 mm. With increasing Δs the mass resolution drops very rapidly. Therefore it is very important to focus the ions in the centre of the ionisation region. The better the ions are focused, the better is the mass resolution. The relative deviation increases significantly for position deviations close to 1 mm because there, some ions already leave the source when the high voltage pulse is not fully applied.

2.2. Signal-to-Noise Ratio

The Signal-to-Noise Ratio (SNR) is defined as the ratio of the background corrected mass peak amplitude I_p and the standard deviation of the base line σ_{Base} [20, 30]:

$$SNR = \frac{I_p}{\sigma_{Base}} \tag{26}$$

The number of detected ions is proportional to the area under the detected mass peak. Therefore, a better focusing of the ions in the time domain leads to a higher and narrower signal peak resulting in a better mass resolution and signal-to-noise ratio. This is a special feature of time-of-flight mass spectrometers: higher mass resolution results in a higher SNR. For magnetic sector instruments, the mass resolution is improved by limiting the phase space leading to a loss in signal intensity and therefore a worse signal-to-noise ratio. The noise in the spectrum originates from different sources such as from the electronics operating the instrument. Noise with a fixed frequency can be subtracted later from the signal eg. by Fourier filtering. The random noise induced by high energetic particles from Jupiter's harsh radiation field is attenuated by shielding the detector with a tungsten copper shield [17]. In addition, NIM has a special designed ion-storage source to store the produced ions during the time when no extraction pulse is applied at the ion extraction grid (Chap. 3). Ions which are produced and not

stored in the ionisation region are lost and also contribute to the random noise of the measured signal [1].

2.3. Filament

NIM uses specially designed Y_2O_3 filaments provided by *Kimball Physics, Wilton, USA* to ionise neutral particles entering the ionisation region. These filaments have an improved coating Y_2O_3 to enhance the filament lifetime to 10'000 h of operation time. In addition, they have longer filament wires to reduce the power loss to the filament base by thermal conductivity (Fig. 10). The longer wires make the filament more delicate in terms of mechanical stress. Therefore, a vibration and shock test were done, which showed no anomalies in terms of performance between the normal Y_2O_3 and the specially designed Y_2O_3e filaments [15]. In the following sections a power estimation of these filaments is done and also a characterisation of the NIM PFM and FS filament controller boards, which provide the power for the filaments in the NIM PFM and FS instruments.

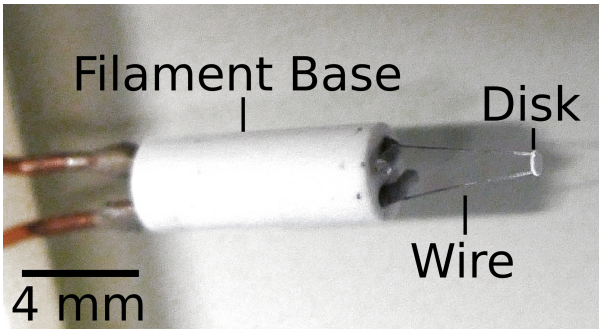

Figure 10: Y_2O_3e filament.

2.3.1. Power Calculation

In this chapter, the power of the Y_2O_3e filaments (Fig. 10) used in the NIM instrument is estimated and compared with the power consumption of the standard filaments Y_2O_3 filaments. The Y_2O_3 is heated up by the heater current I_{heat} until it emits electrons. The required temperature depends on the desired emission current I_{em}. The Richardson law for thermionic electron emission gives the emission current density j for a material as a function of the temperature T_D:

$$j = A_G T_D^2 e^{-\frac{W}{k_B T_D}} \tag{27}$$

With A_G the Richardson constant, which for Y_2O_3 is 10^4 $\mathrm{A\,m^{-2}\,K^{-2}}$ [11], W is the work function of Y_2O_3 which is 2.4 eV [11] and k_B the Boltzmann constant. The emission current I_{em} is the current density multiplied by the area A_D of the filament disk:

$$I_{em} = j \cdot A_D \tag{28}$$

The total power required to reach the temperature at the disk to emit electrons is the power lost through thermal conductivity P_{cond} through the thin wires connecting the filament disk with the filament base and the power lost through thermal emissivity P_{rad} of the wire and the disk. This power corresponds to the power dissipated by the resistive losses P_R of the wire:

$$P_R = P_{cond} + P_{rad} \tag{29}$$

The power lost through thermal conductivity to the filament base is estimated:

$$P_{cond} = 2 \cdot A_w k \frac{\Delta T}{l_w} \tag{30}$$

$$= 2 \cdot A_w k \frac{T_D - T_B}{l_w} \tag{31}$$

With A_w the wire cross section, k the thermal conductivity (150 W/(K m) for W3Re [28] and 150 W/(K m) for Ir [22]). ΔT is the temperature difference between the disk T_D and the filament base T_B and l_w the wire length. The factor 2 is because there are two legs connecting the disk with the base. The power lost through thermal radiation P_{rad} is the sum of the power lost by the wire P_{wire} and by the disk P_{disk}:

$$P_{rad} = P_{wire} + P_{disk} \tag{32}$$

$$= 2\sigma \cdot \epsilon_w \cdot A_w T_w^4 + \sigma \cdot \epsilon_{df} \cdot A_D T_D^4 + \sigma \cdot \epsilon_{db} \cdot A_D T_D^4 \tag{33}$$

With σ the Stefan-Boltzmann constant, ϵ_w the emissivity of the wire material (0.2 for W3Re [28] and 0.3 for Ir [10]), ϵ_{df} the emissivity of the coating (0.5 for Y_2O_3 [29]), ϵ_{db} the emissivity of the disk material (0.325 for Ta [34] and 0.3 for Ir [10]) and T_w the temperature of the wire. The thermal emission depends strongly on the temperature. To estimate the radiated power of the wire, the temperature profile was assumed to be linear resulting in:

$$P_{wire} = 2\sigma\epsilon_w 2r\pi \int_0^{l_w} \left(\frac{\Delta T}{l_w} l + T_B \right)^4 \cdot dl \tag{34}$$

$$= 2\sigma\epsilon_w 2r\pi \int_0^{l_w} \left(\frac{(T_D - T_B)}{l_w} l + T_B \right)^4 \cdot dl \tag{35}$$

$$= 2\sigma\epsilon_w 2r\pi \int_0^{l_w} \left(\frac{(T_D - T_B)^4}{l_w^4} l^4 + 4\frac{(T_D - T_B)^3}{l_w^3} l^3 T_B \dots \right.$$
$$\left. + 6\frac{(T_D - T_B)^2}{l_w^2} l^2 T_B^2 + 4\frac{(T_D - T_B)}{l_w} l T_B^3 + T_B^4 \right) \cdot dl \tag{36}$$

Solving the integral results in:

$$P_{wire} = 2\sigma\epsilon_w 2r\pi \cdot l_w \left(\frac{1}{5}(T_D - T_B)^4 + (T_D - T_B)^3 T_B + 2(T_D - T_B)^2 T_B^2 \dots \right.$$
$$\left. + 2(T_D - T_B) T_B^3 + T_B^4 \right) \tag{37}$$

$$= 2\sigma\epsilon_w 2r\pi \cdot \frac{1}{5} l_w \left(T_D^4 + T_D^3 T_B + T_D^2 T_B^2 + T_D T_B^3 + T_B^4 \right) \tag{38}$$

With r the wire radius and T_B the temperature of the filament base. The power generated by ohmic losses P_R is:

$$P_R = RI_{heat}^2 \tag{39}$$

$$= \rho \frac{l_w}{A_w} \cdot I_{heat}^2 \tag{40}$$

With ρ the electric resistivity of the wire (0.45 µΩm for W3Re [13] and 0.45 µΩm for Ir [5]). The resulting total power matches the values measured in the laboratory within about 10 %, which is good enough for this rough estimation. The Y_2O_3e filaments consume about 40 % less power than the standard Y_2O_3 filaments. The biggest loss of power is through thermal conductivity to the base, which could be reduced by 45 %. The radiative losses of the wire increased because the wires are longer and therefore the surface area of the wire increased, leading to a bigger area to radiate.

2.3.2. Flight Filament Controller Boards Characterisation

In this chapter the electrical characteristics of the NIM PFM and FS controller boards used to power the electron emitting filaments in the NIM instrument are discussed.
Fig. 11 shows the electrical characteristics of the load line of a sample filament controller board (black) and a theoretical filament (blue). Note that the resistance of the tungsten heater wire increases substantially with temperature, which explains the curvature of the blue line [43]. The intersection of the load line with the x-axis corresponds to the maximal current the filament controller board can provide and the intersection with the y-axis corresponds to the maximal voltage. Every point below the load line can be reached by the controller board.

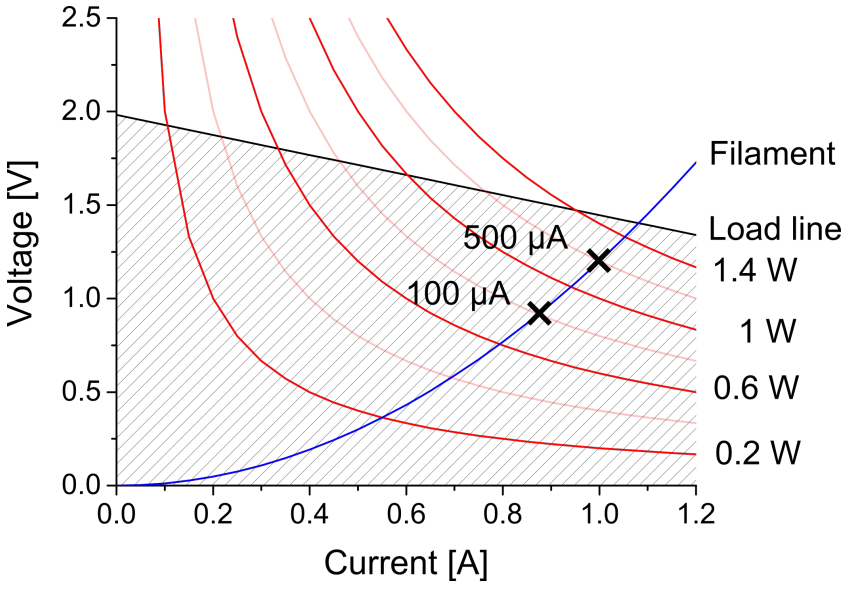

Figure 11: Electrical characteristics of a sample filament (blue) and the load line of an electronic board (black). The red lines show different power levels.

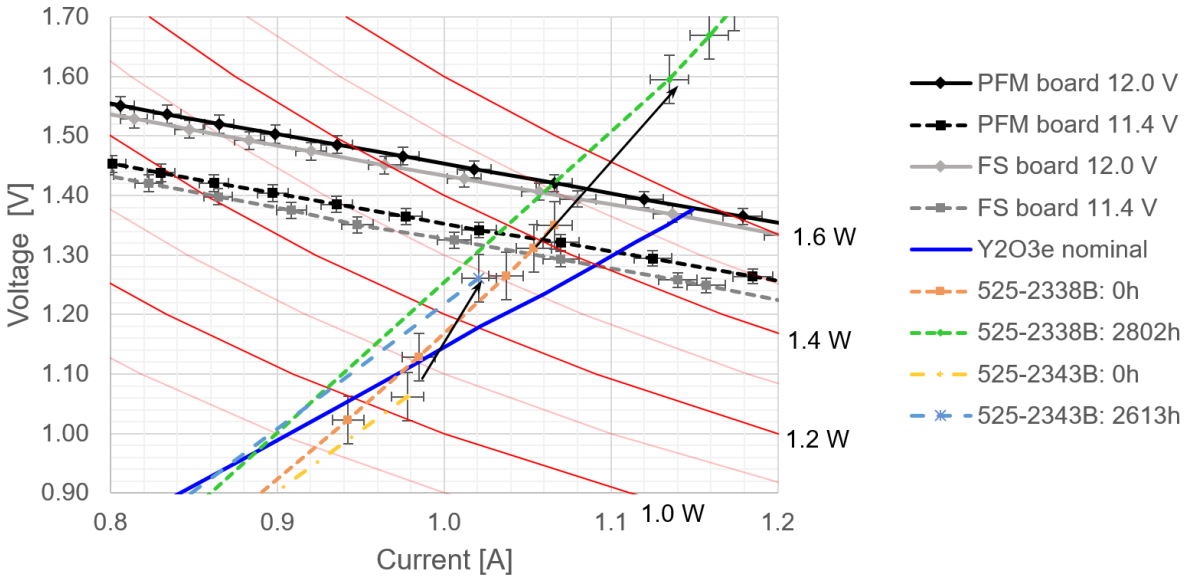

Figure 12: Electrical characteristics of selected Y_2O_3e filaments and the NIM PFM and FS controller boards showing the maximal I-V capabilities of the two power supplies at nominal supply voltage of 12.0 V and reduced supply voltage of 11.4 V. The red hyperbolas in the background show the power levels (adapted from [15]).

The red curves show the lines of constant power. Depending on the desired emission current, the filament disk has to be heated to a certain temperature (Eq. (27)). The higher the temperature is, the higher is the power consumption of the filament due to power losses through thermal conductivity and thermal radiation. Therefore, a higher emission current requires higher power. The current and voltage settings for a given emission current are the intersection of the filament line with the corresponding power line. For two emission currents, these points are marked as black crosses as an example.
Fig. 12 shows the electrical characteristics of the NIM PFM (black) and FS (grey) controller boards once for nominal supply voltage of 12.0 V and once for the minimal supply voltage of 11.4 V from the DC power supply of the PEP experiment. The blue line shows the nominal behaviour of a Y_2O_3e filament. At the current state, long term tests with filaments at different emission currents are running to verify their operation time of 10'000 h. The filaments displayed in this graphic are the one with the worst electrical characteristics from each batch. Filament 525-2343B has a target emission current of 50 µA and filament 525-2338B has a target emission current of 300 µA. For a bad filament such as 525-2338B the flight controller boards could not provide the required power. If the target emission is 50 µA the two boards can provide the power even after 2300 h of operation time. The difference in performance between the nominal filament and the filaments used in our tests originates from the different test setups in which the filaments were tested. The extraction fields in the test setup of the nominal filament were set to optimise electron emission to minimise power consumption. This is not a realistic case for a flight instrument where the extraction fields also have to focus the electron beam in the ionisation region. Therefore, the test setup for the long term tests was

built as a replicate of NIM's electron extraction region. The applied extraction voltages are set to nominal values used during filament operation. Therefore, the filaments are more stressed than in a setup which is optimised to extract the electrons from the filament disk [15].

2.4. Ion Storage

Ion storage of positive ions in the ionisation region is mainly achieved by the negative space charge potential of the electron beam. Together with the other focusing electrodes in the ionisation region, a 3D electrostatic trapping field is generated to store the ions produced during the time when no high-voltage pulse is applied on the extraction grid (IS 5 in Fig. 13). NIM has a nominal duty cycle of 10 kHz and the pulse duration of the extraction pulse is 1–2 μs. In the remaining 98 μs per cycle ions are produced, which have to be stored in the source between two extraction pulses because lost ions add to the random noise level reducing the signal-to-noise ratio. In the following section, the potential in the centre of the electron beam is calculated. The electron emission current I_e is:

$$I_e = n_e q_0 v \pi R_e^2 \tag{41}$$

With n_e the electron number density, q_0 the elementary charge, v the velocity of the electrons and R_e the radius of the electron beam (Fig. 14). The electrons get accelerated by the negative potential applied at the filament base. This potential is –70 V resulting in a kinetic energy U of 70 eV. The velocity of the electrons is:

$$v = \sqrt{\frac{2U}{m_e}} \tag{42}$$

With m_e the mass of the electron. Solving Eq. (41) for the volume density n_e and inserting Eq. (42) for the velocity results in:

$$n_e = \frac{I_e}{q_0 \pi R_e^2} \sqrt{\frac{m_e}{2U}} \tag{43}$$

The electric field $E(r)$ from the space charge of the electron beam in the ionisation region is calculated for $R_e < r < h_{Is}/2$ with r the distance from the centre of the beam and h_{Is} the height of the ion source. The electric flux is defined as the surface integral of the electric field through the surface of an enclosed volume, which is in this case a cylinder volume. Using Gauss's law the electric flux through the beam surface A_{beam} is equal to the total charge Q inside the cylinder volume. In this calculation, the base and deck area are neglected:

$$A_{beam} E(r) = \frac{Q}{\epsilon_0} \tag{44}$$

$$2\pi r l E(r) = \pi R_e^2 l n_e q_0 \frac{1}{\epsilon_0} \tag{45}$$

With l the cylinder length, q_0 the elementary charge and ϵ_0 the vacuum permittivity. Replacing the number density n_e with Eq. (43) and solving the equation for the electric field $E(r)$ results in:

$$E(r) = \frac{I_e}{2\pi\epsilon_0}\sqrt{\frac{m_e}{2U}}\frac{1}{r} \tag{46}$$

The potential $\Phi_o(r)$ at a position r outside of the electron beam is:

$$\Phi_o(r) = -\int_{h_{Is}/2}^{r} E(r')dr' = -\frac{I_e}{2\pi\epsilon_0}\sqrt{\frac{m_e}{2U}}\ln\left(\frac{r}{h_{Is}/2}\right) \tag{47}$$

The electric field inside the electron beam at position $0 < r < R_e$ is calculated by using again Gauss's law:

$$2\pi r l E(r) = \pi r^2 l n_e q_0 \frac{1}{\epsilon_0} \tag{48}$$

Replacing the number density n_e with Eq. (43) and solving the equation for the electric field $E(r)$ results in:

$$E(r) = \frac{I_e}{2\pi\epsilon_0}\sqrt{\frac{m_e}{2U}}\frac{r}{R_e^2} \tag{49}$$

The electric potential $\Phi_i(r)$ is:

$$\Phi_i(r) = -\int_{R_e}^{r} E(r')dr' = -\frac{I_e}{4\pi\epsilon_0}\sqrt{\frac{m_e}{2U}}\left(\frac{r^2}{R_e^2} - 1\right) \tag{50}$$

And relative to the border of the ion source:

$$\Phi_i(r) = -\frac{I_e}{4\pi\epsilon_0}\sqrt{\frac{m_e}{2U}}\left(2\ln\left(\frac{R_e}{h_{Is}/2}\right) + \frac{r^2}{R_e^2} - 1\right) \tag{51}$$

For an electron emission current of 100 µA the electric potential in the centre of the electron beam is 0.5 V. This potential well is deep enough to trap ion species at thermal energies. For faster species, NIM has a special designed ionisation region (Fig. 13). The electrodes IS 1, IS 5 and IS 6 trap the ions in x-direction where the two ring electrodes IS 2 and IS 4 trap the ions in the other two directions.

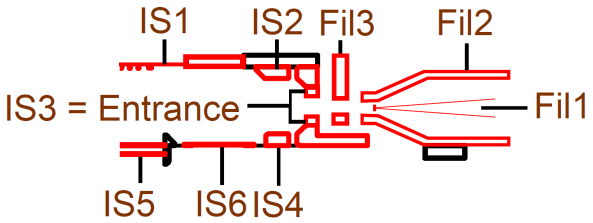

Figure 13: Detail of NIM's ionisation region.

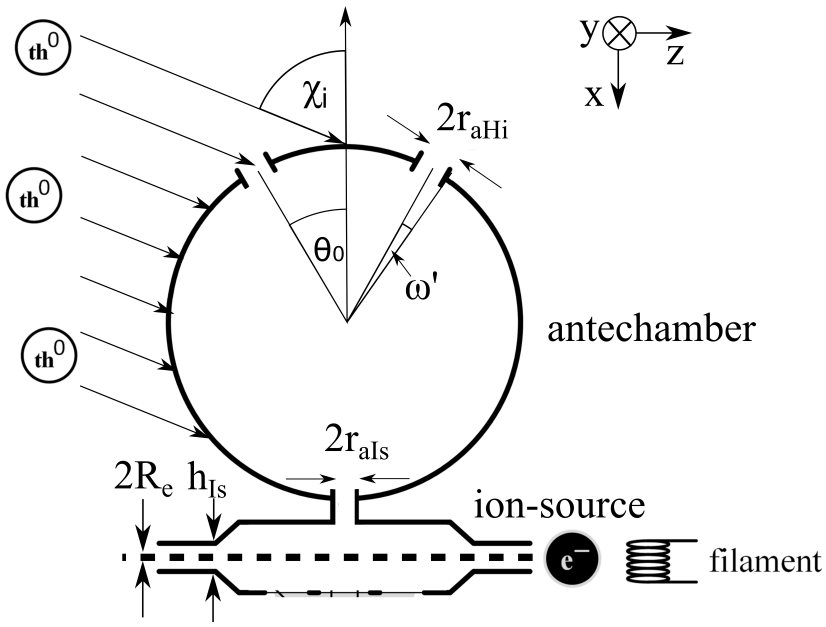

Figure 14: Schematics of the antechamber and the ionisation region.

2.5. Density enhancement of a Closed Source

NIM has an open source entrance where neutral particles and ions enter the ionisation region directly and a closed source entrance where particles enter the ionisation region after being thermalised in an antechamber. In this chapter the density enhancement of the closed source entrance is determined. The density enhancement model described in [45] is used and adapted for the geometry of NIM's antechamber. The particle density n_{cs} in the ionisation region is:

$$\frac{n_{cs}}{n_a} = \sqrt{\frac{T_a}{T_s}} \cdot \frac{k \cdot \sin^2\left(\frac{\omega}{2}\right) \cdot \cos^2\left(\frac{\omega}{2}\right)}{1 - k \cdot \cos^2\left(\frac{\omega}{2}\right)} \cdot \frac{\Big(F(S_1) + F(S_2)\Big)}{2} \cdot \frac{r_{aIs}^2 \cdot a}{2 \cdot r_{aHi}^2 + r_{aIs}^2 \cdot a} \tag{52}$$

With:

$$F(S_i) = e^{-S_i^2} + \pi^{1/2} \cdot S_i \cdot \Big(1 + \mathrm{erf}(S_i)\Big) \tag{53}$$

With n_a the ambient particle density of the gas outside the instrument. For the tests in the laboratory n_a is the particle density of the neutral gas beam. In flight, the ambient particle density is the particle density of the moons atmosphere. T_a is the temperature of the ambient gas. In the laboratory it is the temperature of the neutral particle beam. T_s is the temperature of the antechamber. k is the probability of a particle being re-emitted after colliding with the antechambers inner surface during thermalisation and is close to 1 because otherwise the particle would be absorbed. Ω is the total solid angle of all openings leading into the antechamber. NIM has two entrance holes with the same hole diameter and therefore the total solid angle Ω is the sum of the two solid angles of the entrance holes Ω':

$$\Omega = 2 \cdot \Omega' \tag{54}$$

All openings into the antechamber have a circular shape therefore, the solid angle Ω is replaced by an angle ω in the x-z-plane to simplify the equation Eq. (52) [21]:

$$2\pi(1-\cos(\omega)) = 2 \cdot 2\pi(1-\cos(\omega')) \tag{55}$$

$$\cos(\omega) = 2\cos(\omega') - 1 \tag{56}$$

$$\omega = \cos^{-1}(2\cos(\omega') - 1) \tag{57}$$

ω' is the half angle of one entrance hole (Fig. 14). S_i in Eq. (53) is the speed ratio along the normal axis of the entrance holes:

$$S_i = \begin{cases} 0, & \cos(\chi \pm \theta_0) < 0 \\ v_{sc} \cdot \cos(\chi + \theta_0) \cdot \sqrt{\frac{m}{2k_B T_a}}, & i = 1 \\ v_{sc} \cdot \cos(\chi - \theta_0) \cdot \sqrt{\frac{m}{2k_B T_a}}, & i = 2 \end{cases} \tag{58}$$

with v_{sc} the velocity of the neutral gas beam relative to the antechamber corresponding to the spacecraft velocity, m the average particle mass of the gas and k_B the Boltzmann constant. χ is the angle of the test gas relative to the x-axis of the instrument and θ_0 is the angle between the x-axis and the axis normal of the entrance hole. $\chi \pm \theta_0$ is the angle between the normal axis of the entrance hole and the gas inflow direction. $\chi \pm \theta_0$ has to be between $\pm 90°$ to enter the antechamber which implies that $\cos(\chi \pm \theta_0)$ cannot have negative values. $i = 1$ is the index of one of the two entrance holes and $i = 2$ is the index of the other entrance hole. The antechamber has three openings for the gas to flow out of the antechamber. The last term in Eq. (52) gives the ratio of how many particles leave the antechamber through the hole connecting the antechamber with the ionisation region compared to the amount of particles leaving the antechamber through the two entrance holes. The radius of the entrance holes is r_{aHi} and the radius of the hole connecting the antechamber with the ionisation region is r_{aIs}. This term takes the molecular flow conductance of the different holes into account. The molecular flow conductance of a thermalised gas is:

$$C_0 = A\bar{v}/4 \tag{59}$$

with A the cross-section of the opening and $\bar{v}$ the average velocity of the thermalised gas flowing through that opening. This formula is only valid in case the length of the tube is close to zero. Otherwise, the transmission probability a has to be added resulting in:

$$C = C_0 \cdot a \tag{60}$$

The transmission probability depends on the length-to-radius ratio L/R of the opening. van Essen and Heerens [39] compared different models to determine the transmission probability and calculated the values for specific length-to-radius ratios. The model that comes closest to reality is the one by Nawyn and Meyer (published by [39]). To calculate the transmission probability for any length-to-radius ratio, the data resulting from Nawyn and Meyer's model were fitted with the following function:

$$a = y_0 + y_1\left(1 - e^{-\frac{L/R}{t_1}}\right) + y_2\left(1 - e^{-\frac{L/R}{t_2}}\right) \tag{61}$$

y_0	0.998 ± 0.001	t_1	7.4 ± 0.3
y_1	-0.48 ± 0.01	t_2	1.13 ± 0.04
y_2	-0.45 ± 0.01		

Table 2: Fit parameters of Eq. (61).

The fit parameters are listed in Table 2. For the two gas entrance openings of the antechamber a is 1 because they have a sharp edge and therefore the length of the opening is close to zero. The opening between the antechamber and the entrance has a length-to-diameter ratio of 8 resulting in a $a = 0.23$. The amount of gas flowing through this opening relative to the total outflow is:

$$G_{open} = \frac{C_{aIs}}{C_{aIs} + 2 \cdot C_{aHi}} \tag{62}$$

$$G_{open} = \frac{\frac{r_{aIs}^2 \cdot a \cdot \bar{v}}{4}}{\frac{r_{aIs}^2 \cdot a \cdot \bar{v}}{4} + 2\frac{r_{aHi}^2 \cdot \bar{v}}{4}} \tag{63}$$

$$G_{open} = \frac{r_{aIs}^2 \cdot a}{r_{aIs}^2 \cdot a + 2 \cdot r_{aHi}^2} \tag{64}$$

With $r_{aIs} = 2$ mm and $r_{aHi} = 2.5$ mm resulting in $G_{open} = 0.067$ meaning that about 6.7% of all particles entering the antechamber actually reach the ionisation region due to losses of the geometry.

T_a	295 K	r_{aHi}	2.5 mm	χ	0°
T_s	320 K	r_{aIs}	2 mm	θ_0	30°
k	1	v_{sc}	2.5 km/s	m	18 u
a	0.23				

Table 3: Values used for the variation of the different variables of the amplification factor of the antechamber (Eq. (52)).

In the following section the different parameters of the density enhancement equation Eq. (52) were varied to determine their impact. For this analysis the particle density in the ionisation region n_{cs} was divided by the particle density of the test gas n_a outside of the antechamber and n_a was set 1 to get the amplification of the antechamber. For this analysis the parameters were set according to Table 3 unless otherwise mentioned. The temperatures are the ones used in the laboratory. The used particle velocity was 2.5 km/s because it is the velocity of the spacecraft in Ganymede orbit and therefore the velocity at which most of the measurements will be

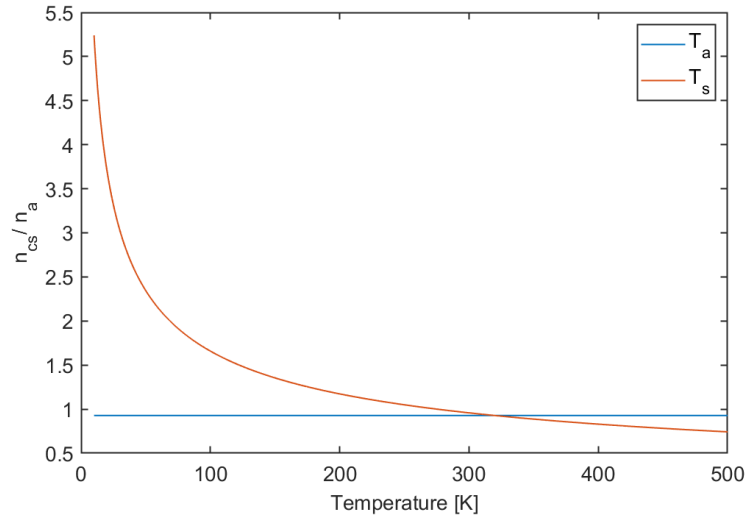

Figure 15: Density enhancement n_{cs}/n_a of the antechamber as a function of the ambient gas temperature T_a and the temperature of the antechamber wall T_s according to Eq. (52).

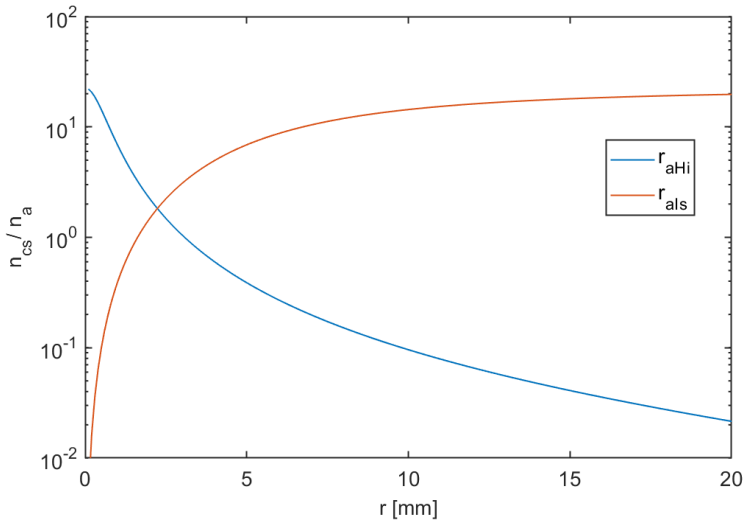

Figure 16: Density enhancement n_{cs}/n_a of the antechamber as a function of the entrance hole radius r_{aHi} and the radius connecting the antechamber with the ionisation region r_{aIs}.

done. The particle reflection coefficient k of the inner coating of the antechamber was set 1 assuming an ideal coating reflecting all particles. The transmission probability a of the hole connecting the antechamber with the ionisation region, the radius of the antechamber entrance holes r_{aHi}, the radius of the hole connecting the antechamber with the ionisation region r_{aIs} and the angular position of the entrance holes θ_0 are defined by the geometry of the antechamber. χ was set to 0°. The main gas inflow direction lies then between the two entrance holes.

The used test gas was water with a unit mass of 18 u.
The first parameter that was varied was the gas temperature T_a. This temperature can be varied between 0 and 1000 K without significantly influencing the density enhancement of the antechamber (Fig. 15). When looking closer, a slight increase in density enhancement is observed with increasing temperature.
The temperature of the antechamber T_s has a bigger impact on the density enhancement. Ideally this temperature should be as low as possible to slow down the particles when they hit the chamber inner walls (see also Eq. (52)). When the temperature of the antechamber is too low, the gas condenses at the antechamber walls. Therefore, the particle reflection coefficient of k will decrease with decreasing temperature depending on the particle species. For this calculation, this effect was ot taken into account. In flight, the antechamber is kept at temperatures higher than –17 °C during measurements to avoid condensation on the antechamber walls.
The radius r_{aIs} of the hole connecting the antechamber with the ionisation region has to be as big as possible. A bigger radius leads to a smaller length-to-diameter ratio resulting in a bigger transition probability a. This is consistent with Eq. (61). When L/R is larger, the exponential terms are smaller. Since they are subtracted, that leads to a larger transition probability. The amount of gas flowing into the ionisation region increases (Fig. 16). The radius of the entrance holes r_{Hi} should be as small as possible to increase the number of collisions of the neutral particles with the antechamber walls to thermalise them. In addition, when the entrance holes are big, a big amount of gas flows out through them. From that perspective, the biggest gain is achieved when the radius of the entrance hole is close to zero. Eq. (52) does not take into account that at a certain opening radius is needed to allow particles to enter the antechamber for being amplified. The equation is only valid for small openings to guaranty enough collisions of the gas with the chamber walls. Therefore, the requirement was that

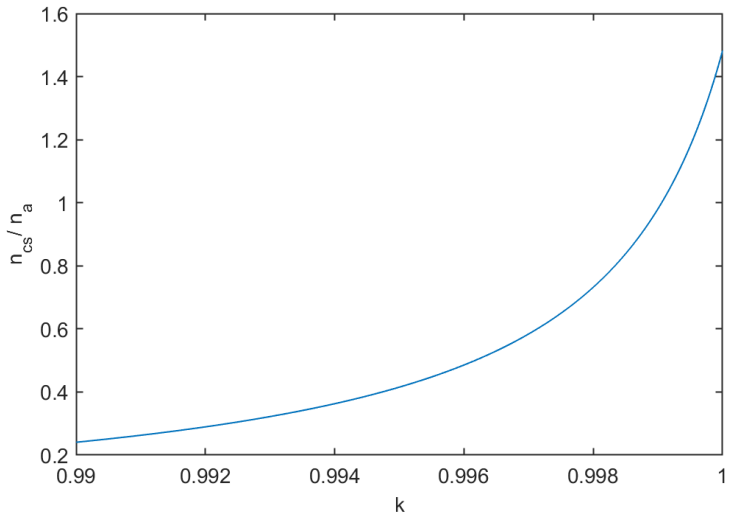

Figure 17: Density enhancement n_{cs}/n_a of the antechamber as a function of the particle reflection coefficient k.

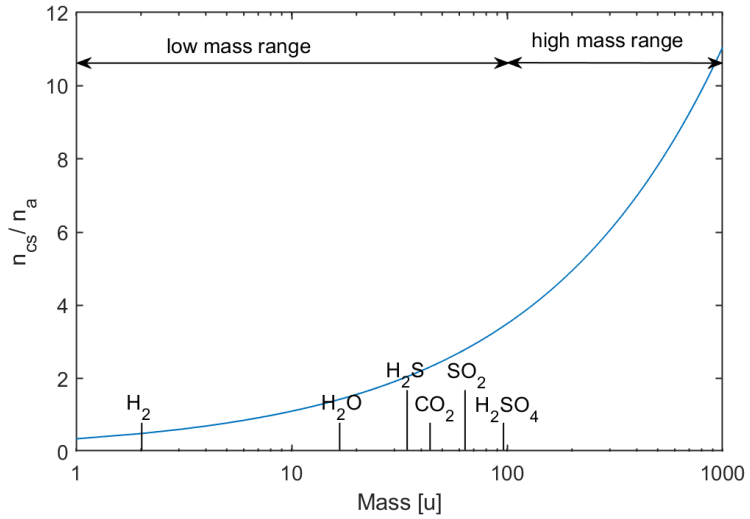

Figure 18: Density enhancement n_{cs}/n_a of the antechamber as a function of the particle mass m.

the area of all openings of the antechamber has to be 10% of the total sphere surface.
It is very important to take materials with a high particle reflection coefficient k for the coating of the antechamber's inner surface. The particle reflection coefficient gives the probability of a particle being re-emitted when hitting the surface thus this value has to be close to 1. NIM has a gold coated antechamber because gold is electrically conductive preventing the surface from charging in the strong radiation field of Jupiter. In addition, gold is chemically inert and therefore, there is a low probability of building chemical bonds with the gas induced into the antechamber. Fig. 17 shows the density enhancement of the antechamber as a function of k. Already a change of 1‰ has a huge impact. The impact of k also depends on ω. A small ω implies a big surface area with which the particles interact before being detected. The bigger the number of interactions is, the bigger is the influence of k. The ω of NIM's antechamber is about 5.06°, which is very small and therefore a small change in k has a big impact on the density enhancement.
Fig. 18 shows the density enhancement of the antechamber as a function of the particles unit mass [u]. The figure shows that higher mass species have a higher density enhancement factor than low mass species. Since the higher mass species are usually of low abundance in the icy moons exospheres [41, 40], this mass dependence of the density enhancement factor is very helpful.
Fig. 19 shows the density enhancement of the antechamber as a function of the spacecraft velocity for different species. We expect H_2O and different radiolysis products such as H_2, O_2 or HO in the icy moons' exosphere. Absorption lines in the near infrared recorded by the Near Infrared Mapping Spectrometer (NIMS) on board of the Galileo spacecraft indicate CO_2 bond to other solid materials in the soil. Sulphur is ejected by the Galilean moon Io and is therefore part of the Jupiter's plasma torus. The sulphur compounds are a result of the ion bombardment on the icy moons' surface. Sulphur reacts with water resulting in various

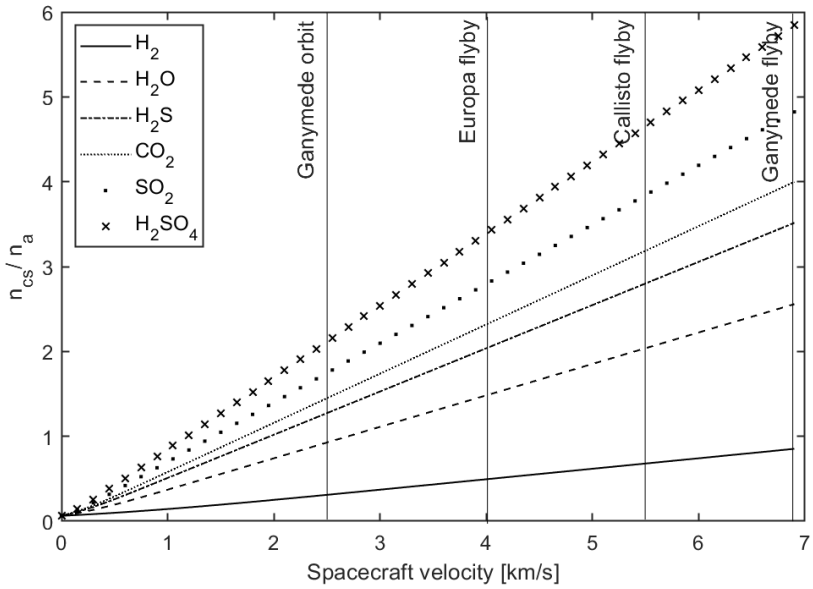

Figure 19: Density enhancement n_{cs}/n_a of the antechamber as a function of the spacecraft velocity v_{sc} for different species expected in the icy moons exospheres.

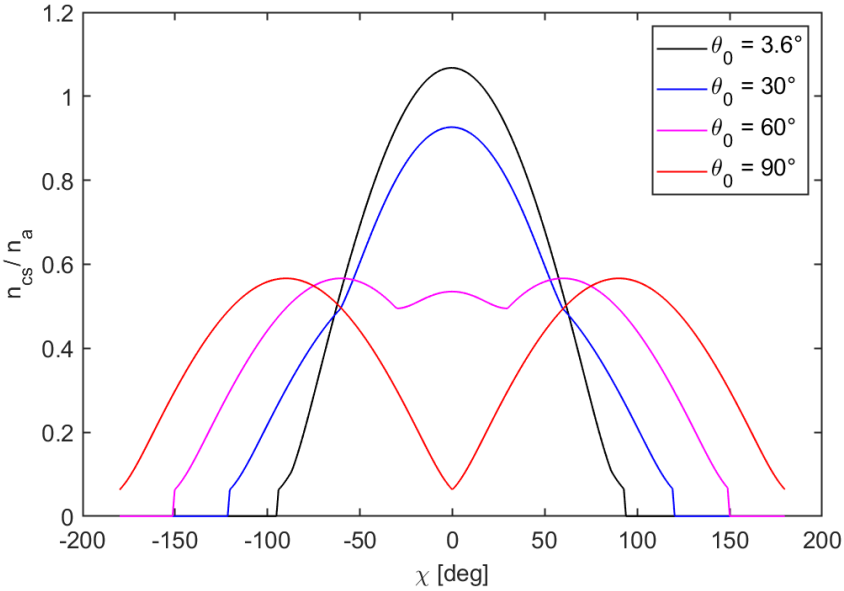

Figure 20: Density enhancement n_{cs}/n_a of the antechamber as a function of the angle χ between the gas inflow direction and the x-axis of the instrument for different positions of the two entrance holes θ_0. $\theta_0 = 30°$ is the position of the holes in flight configuration.

different compounds such as sulphur dioxide (SO_2) or sulphuric acid (H_2SO_4) [12]. Fig. 19 shows that with increasing flyby velocity, the particles get more amplified. Heavier species

are stronger amplified than light ones as it was already shown in Fig. 18.
Fig. 20 shows the density enhancement of the antechamber as a function of different particle influx angles χ. χ is measured in the x-/y- plane of NIM's coordinate system (see Fig. 14). The function was evaluated for different positions of the entrance holes. The minimal angle the two entrance holes can be apart from each other without overlapping is 3.6°. The holes of the PFM antechamber are at $\theta_0 = \pm 30\,^\circ$. With that configuration the biggest signal intensity is measured with a spacecraft ramp direction of 0°. When the two holes are at ±60° the intensity distribution has a plateau between $\pm 60\,^\circ$ and also a wider angular range. This is an interesting feature under certain circumstance. For NIM it is unnecessary because the spacecraft blocs the field of view (FoV) for angles bigger than 100° (see also Chap. 2.6).

2.6. Field-of-View Analysis

In the following section, the fourth Callisto flyby of JUICE according to the Consolidated Report on Mission Analysis (CReMA) version 3.2 trajectory 141a [9] is analysed as an example of the expected particle flux directions during a flyby. Fig. 22 – Fig. 27 show the changing FoV orientation of the NIM instrument at different times. The reference coordinate system is *ECLIPJ2000*, which is an ecliptic geocentric coordinate system with the x-axis pointing from earths spring point to the Sun. During the flyby, the spacecraft changes its orientation leading to a different appearance of the objects in the figures. The centres of the entrance holes of the antechamber are marked as blue circles, the FoVs of the entrance holes of the antechamber are marked as dashed blue lines (actually, the 30° radius line of the FoV), the entrance slit at the open source entrance is the blue, striped band with the sinusoidal shape. The solar panels and the rim antenna of the spacecraft are marked in red. The gas inflow direction is marked as an orange asterisk. Fig. 22 shows the FoV orientation 1 h before closest approach 15'600 km above Callisto's surface. The gas inflow direction is in between the two entrance holes of the antechamber thus both holes collect gas from Callisto's exosphere. As the spacecraft moves closer to the moon, the gas inflow direction moves towards the entrance slit. 5 min. before closest approach, NIM changes from thermal to neutral mode because of the narrow FoV of

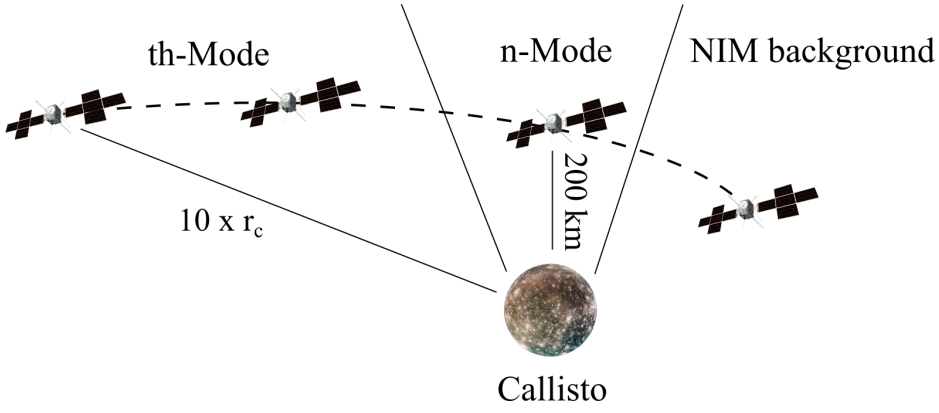

Figure 21: Schematics of the operation during a flyby at Jupiter's moon Callisto.

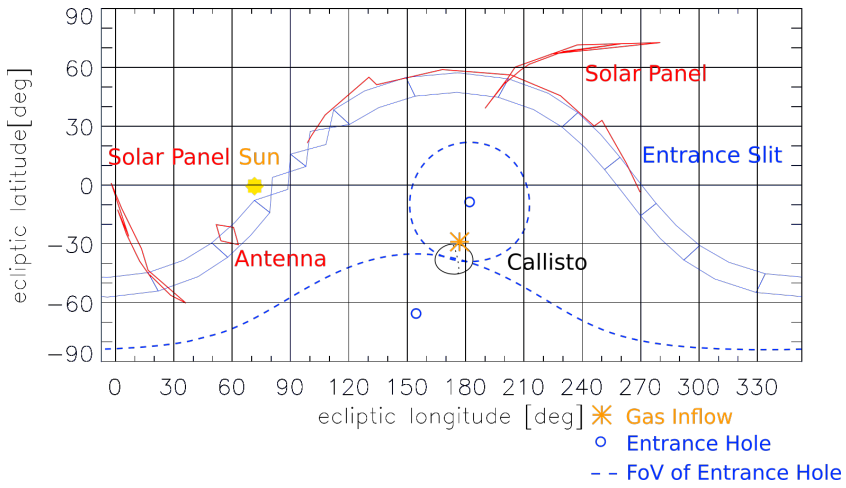

Figure 22: Full-sky map as viewed from NIM during the fourth Callisto flyby based on calculation of CReMA 3.2 trajectory 141a [9] 1 h before closest approach 15'600 km above Callisto's surface.

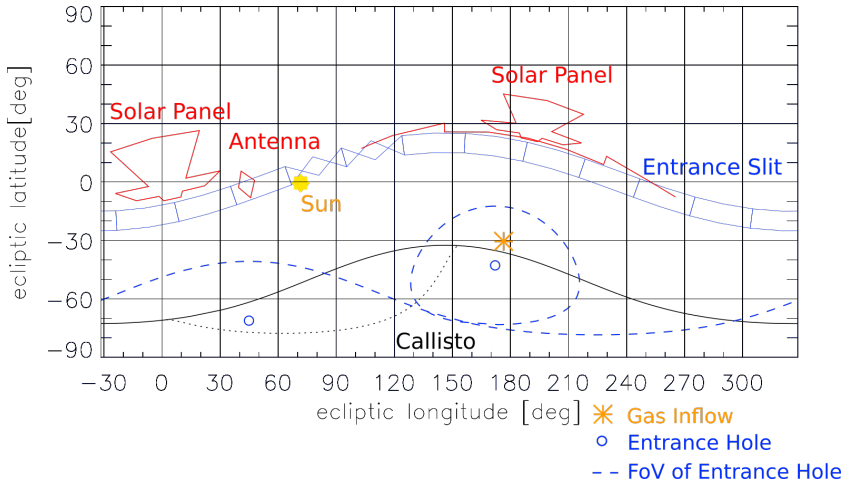

Figure 23: Full-sky map as viewed from NIM during the fourth Callisto flyby based on calculation of CReMA 3.2 trajectory 141a [9] 10 min. before closest approach 1'560 km above Callisto's surface.

10° width of the entrance slit and the short time window during which the gas inflow direction is within the FoV of the entrance slit (Fig. 24). At this time, the gas inflow direction is still in the FoV of the antechamber. The design goal for the switch over between the two modes is 1 s to minimise the number of lost measurements due to this mode change. These measurements are very crucial because the closer the spacecraft gets to the moon's surface, the higher is the exospheric density and therefore the signal intensity (see Fig. 30). 5 min. after closest approach, the gas inflow direction is below the FoV of the neutral gas channel and NIM takes background measurements (Fig. 27). In addition, the spacecraft structure obstructs angles higher than 105° either by the platform on which NIM is mounted or by the solar panels

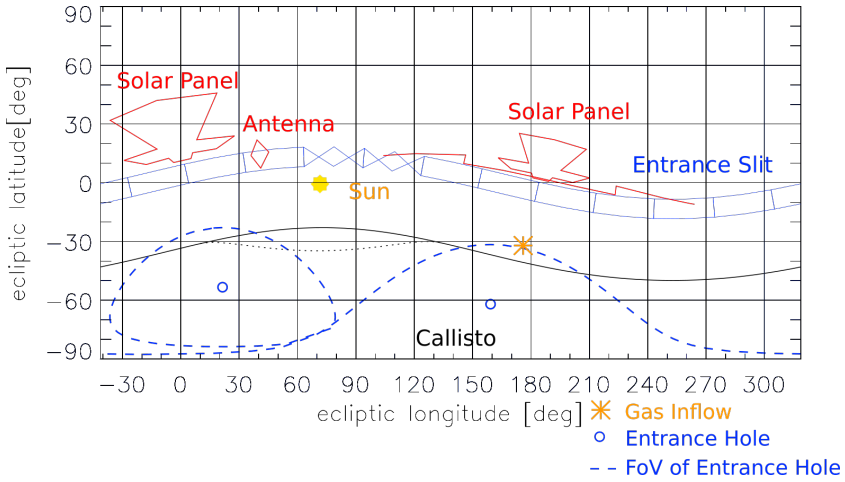

Figure 24: Full-sky map as viewed from NIM during the fourth Callisto flyby based on calculation of CReMA 3.2 trajectory 141a [9] 5 min. before closest approach 580 km above Callisto's surface.

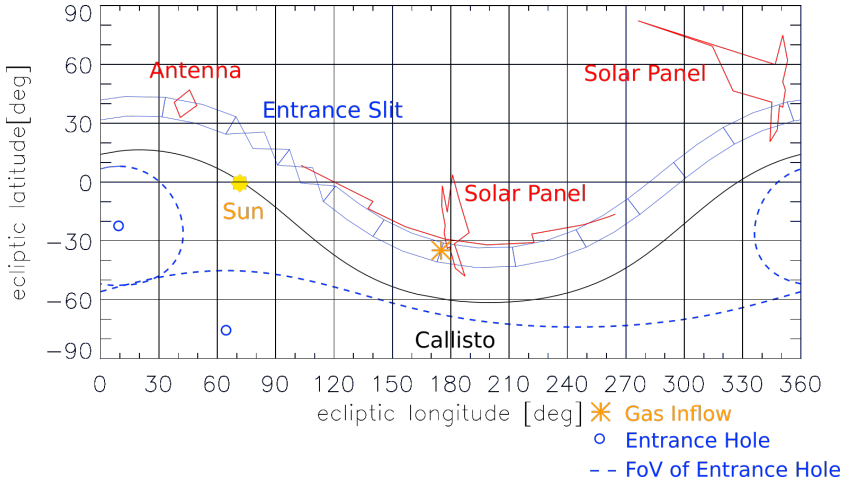

Figure 25: Full-sky map as viewed from NIM during the fourth Callisto flyby based on calculation of CReMA 3.2 trajectory 141a [9] closest approach 200 km above Callisto's surface with the spacecraft solar panels oriented toward the Sun to maximises power generation.

[38]. Fig. 28) shows the JUICE spacecraft with the solar panels in straight up position where they limit NIM's FoV to 75° in the direction along the solar panels. When the solar panels are tilted by 90°, they obstruct NIM's FoV for angles bigger than 100° which is configuration of the closest approach when NIM is measuring with the neutral gas channel. When gas strikes the spacecraft is sputters particles from the spacecraft's surface. NIM is not able to determine if these particles are part of the moons exosphere or if they originate from the spacecraft. In general, the solar panels are adjusted perpendicular to the Sun where possible to maximise power generation. 10 min. before closest approach, the solar panels are tilted to leave the FoV of NIM unobstructed to measure with the neutral gas mode. In case the solar panels would

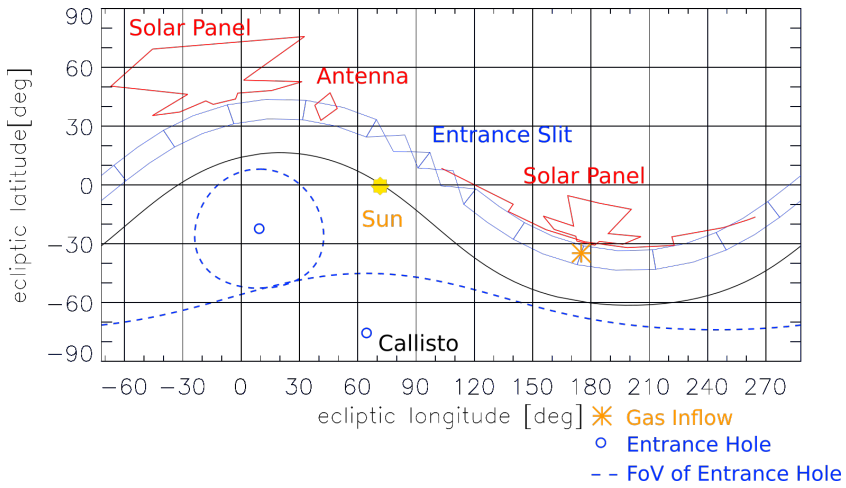

Figure 26: Full-sky map as viewed from NIM during the fourth Callisto flyby based on calculation of CReMA 3.2 trajectory 141a [9] closest approach 200 km above Callisto's surface with solar panels tilted to leave unobstructed NIM's field-of-view of the n-Mode.

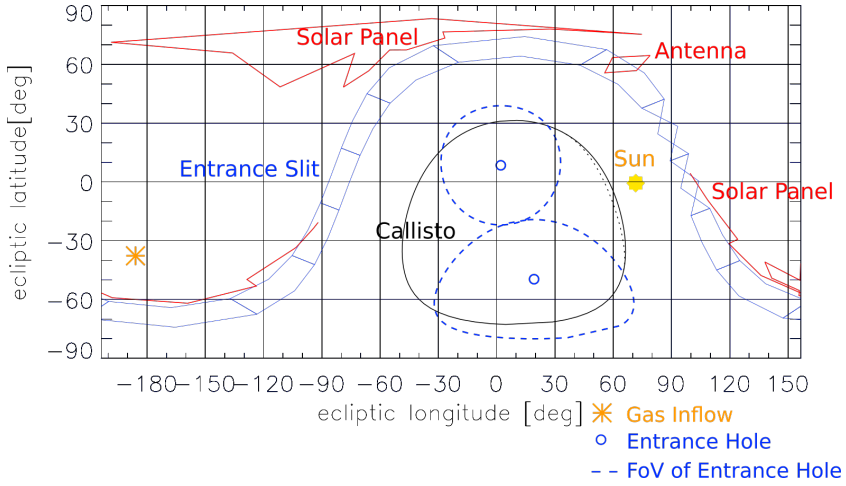

Figure 27: Full-sky map as viewed from NIM during the fourth Callisto flyby based on calculation of CReMA 3.2 trajectory 141a [9] 5 min. after closest approach 640 km above Callisto's surface.

stay perpendicular to the Sun, the gas would graze the surface of the solar panel as it is shown in Fig. 25. Fig. 26 shows the same scenario but with the solar panels tilted to leave NIM's FoV unobstructed for the neutral gas channel.
Fig. 29 shows the density enhancement of the antechamber with the total FoV of the two entrance holes marked as red area $\pm 30°$around the position of the two entrance holes. The orange asterisks mark the gas inflow direction for the various scenarios mentioned above. Depending on the flyby, the main gas inflow direction is from the $+\chi$ or $-\chi$ side. Therefore, it was decided to make two entrance holes in the antechamber to allow measurements with

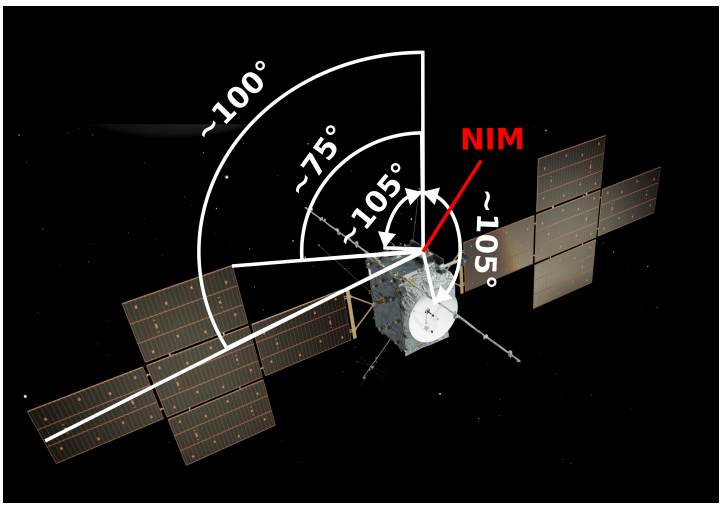

Figure 28: NIM field-of-View on the JUICE spacecraft.

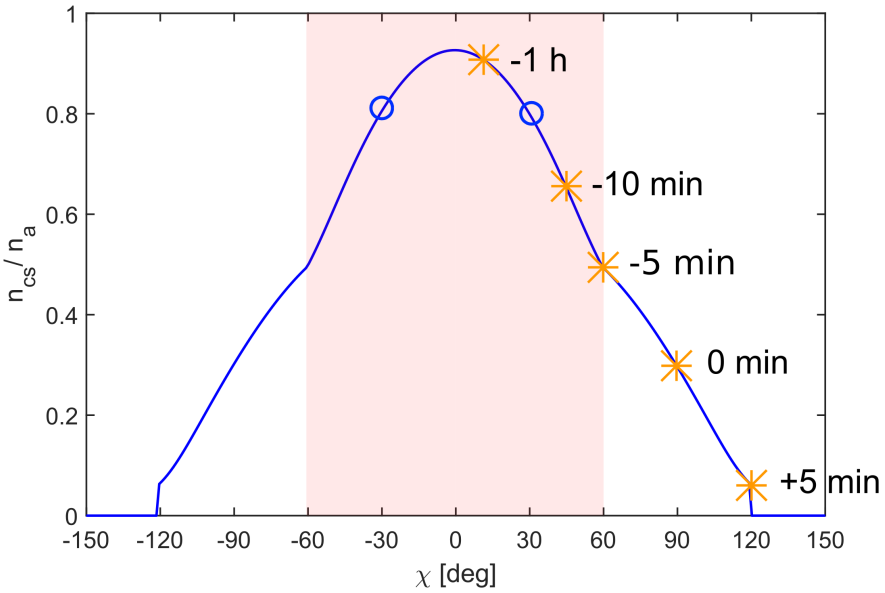

Figure 29: Density enhancement n_{cs}/n_a of the antechamber as a function of the angle χ between the gas inflow direction and the x-axis of the instrument for different positions of the two entrance holes θ_0. The blue circles mark the entrance hole positions and the red area marks the FoV. The asterisks mark the gas influx direction from 1 h before until 5 min. after closest approach of CReMA 3.2 trajectory 141a [9].

angles different to the main direction to enlarge the FoV of the antechamber. The holes should also not be too close at the entrance because structures of the spacecraft bloc angles bigger than 105° and the density enhancement at such big angles would be useless.
Fig. 30 shows simulated density profiles of Callisto's exosphere. In this model, the particles

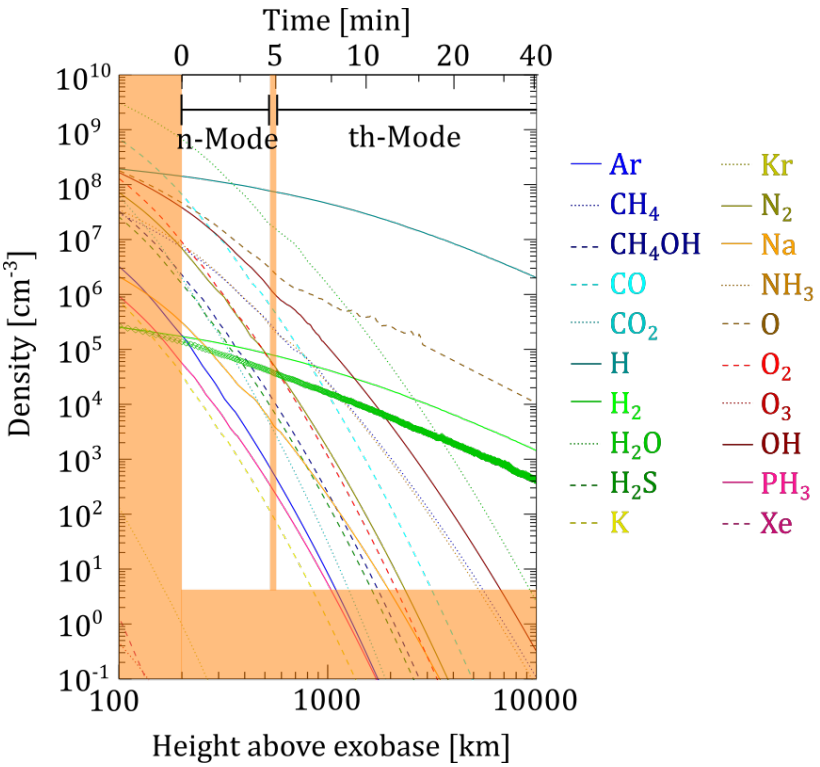

Figure 30: Gas density profiles of Callisto's exosphere simulated by Vorburger et al. [41]. Orange areas mark regions NIM is not able to detect any species either because the JUICE spacecraft does not fly closer to the moon's surface or due to the detection limit of the NIM instrument.

have been sublimated from Callisto's ice surface at the sub-solar point [41]. The x-axis at the bottom shows the height above the exobase and the x-axis at the top shows the time before closest approach of the spacecraft. The orange areas are density distributions NIM is not able to detect. For the flyby discussed above, the closest approach of the spacecraft is at 200 km above Callisto's surface. The detection limit of NIM in Jupiter's strong radiation environment is 4 cm^{-3} for an integration time of 5 sec [26]. 5 min before closest approach, NIM changes from thermal to neutral mode indicated with the small orange bar at position 5 min. During the mode change, NIM cannot record any spectra. The longer the switch over takes, the bigger is therefore this area where precious spectra get lost.
NIM has different measuring modes with regards to the recording configuration of the spectra. One of these configuration parameters is the integration time. The integration time is the time during which the instrument sums up all recorded single spectra. With a pulse frequency of 10 kHz, a spectrum with an integration time of 5 sec consists of 50'000 summed up single spectra. The SNR increases with the square root of the integration time because the random noise only grows with the square root of the integration time and the gas peaks grow proportionally because they appear always at the same position in the spectrum. Therefore, a longer integration time improves the SNR and the amount of acquired data per time is smaller, which is an advantage because JUICE can only transmit a certain amount of data per day back to

Earth. A longer integration time also implies a worse spacial resolution of the density profile along the flight path of the spacecraft because the sampling rate is lower.
For a flyby, 12 h before closest approach at the moons, NIM will start with a bake out and warm up of the system to get the system in a stable thermal state. The bake out is necessary to get rid of condensed particles at the instrument. Otherwise, these particles are released during operation of the instrument and are then visible in the recorded mass spectra. These particles cannot be distinguished from particles originating from the moons' exospheres. To get an estimate of the background originating from the spacecraft, NIM will take measurements during the cruse phase of the spacecraft to Jupiter. The main contribution is expected to be water.
The integration time can be set to 1, 5, 10, 100 or 300 seconds. When the spacecraft is far away from the moon (11 h before closest approach), the integration time is set to 300 sec because at these far distances the neutral particle density is very low and therefore a longer integration time is favourable because it corresponds to a higher SNR. In addition, spacial resolution is of minor importance at these distances. When JUICE gets closer to the moon, the integration time is decreased because the neutral particle number density increases and to get a better picture from the spacial distribution of gas composition in the icy moons' exosphere. At closest approach for the flybys at Ganymede and Callisto, the integration time is about 5 sec. To reduce the amount of produced data, NIM records most of the time spectra with a reduced mass range which records masses between 0–300 u. For the two Europa flybys, the recorded mass range will be 0–1000 u because there the main focus lies on the detection of potential organic compounds. As a trade-off the minimal integration time will be set to 10 sec. instead of 5 sec. as for the flybys at Ganymede and Callisto. This on one hand results in an increased sensitivity but on the other hand, the spacial resolution is then worse for these flyby. The Galileo spacecraft recorded plumes of water vapour on Europa. JUICE would like to fly through one these plumes and therefore, NIM has a special plume mode where the integration time is only 1 sec to get a good spacial resolution of the plume. since the signal is expected to be high in the plume SNR should be good.

2.7. Shutter Performance

With the open-source entrance, NIM is able to measure neutral particles and ions directly without any interaction with the structure. Since the n-mode and the th-mode use the same ion-source, NIM has a shutter to close the passage between to the antechamber and the ionisation region. This shutter is mounted between the ionisation region and the antechamber (Fig. 31 left). When the shutter is open, the gas flows from the antechamber right through the hole into the ionisation region. When the shutter is closed, the hole in the shutter moves to the side as it is indicated in Fig. 31 right panel. The shutter does not close the hole perfectly and therefore a small amount of gas flows through the gap around the shutter into the ionisation region. In the following section, the molecular flow conductance of the closed shutter is determined. The molecular flow conductance C is:

$$C = \frac{A \cdot \bar{v} \cdot a}{4} \tag{65}$$

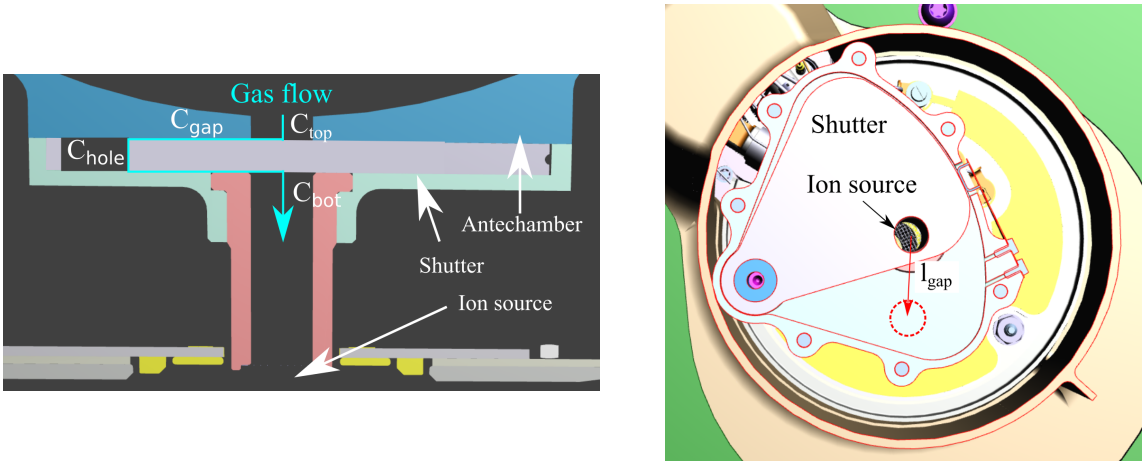

Figure 31: Left: side view when shutter is closed. Right: Top view with open shutter. When the shutter is closing, the central hole of the shutter blade moves to the red position.

With A the cross-section of the tube connecting the antechamber and the ionisation region, $\bar{v}$ the average velocity of the thermalised gas flowing through the opening and the transmission probability a depending on the length-to-diameter ratio of the tube (Eq. (61)). When the shutter is closed, the conductance of the tube C_{tot} is divided into four terms: The conductance of the upper part of the tube C_{top}, the conductance of the gap between the shutter blade and the pocket C_{gap}, the conductance of the hole in the shutter C_{hole} and the conductance of the lower part of the tube connecting the antechamber with the ionisation region C_{bot} (Fig. 31 left):

$$C_{top} = \frac{r_{aIs}^2 \cdot \pi \cdot \bar{v} \cdot a_{top}}{4} \tag{66}$$

$$C_{gap} = \frac{2 \cdot r_{aIs} \cdot \pi \cdot h_{gap} \cdot \bar{v} \cdot a_{gap}}{4} \tag{67}$$

$$C_{hole} = \frac{r_{aIs}^2 \cdot \pi \cdot \bar{v} \cdot a_{hole}}{4} \tag{68}$$

$$C_{bot} = \frac{r_{aIs}^2 \cdot \pi \cdot \bar{v} \cdot a_{bot}}{4} \tag{69}$$

With a_{top}, a_{gap}, a_{hole} and a_{bot} the transmission probabilities of the different sections (Eq. (61)) and h_{top}, h_{gap}, h_{hole} and h_{bot} the height of the different sections. r_{aIs} is the radius of the tube connecting the antechamber with the ionisation region and l_{gap} is the minimal distance between the hole in the shutter and the tube connecting the antechamber with the ionisation region. The nominal values for these parameters are listed in Table 4. The average velocity $\bar{v}$ cancels out during the derivation of the geometry factor. The molecular flow conductance of the tube when the shutter is closed C_{tot} is:

$$\frac{1}{C_{tot}} = \frac{1}{C_{top}} + \frac{2}{C_{gap}} + \frac{1}{C_{hole}} + \frac{1}{C_{bot}} \tag{70}$$

a_{top}	0.73	h_{top}	1.5 mm
a_{gap}	0.07	h_{gap}	0.01 mm
a_{hole}	0.67	h_{hole}	2 mm
a_{bot}	0.28	h_{bot}	12 mm
r_{aIs}	2 mm	l_{gap}	7 mm

Table 4: Nominal transmission probabilities a, tube heights h, tube radius r_{aIs} and minimal gap length l_{gap} when the shutter between the antechamber and the ionisation region is closed.

The conductance of one of the entrance holes of the antechamber is:

$$C_{aHi} = \frac{r_{aHi}^2 \cdot \pi \cdot \bar{v}}{4} \tag{71}$$

The geometry factor of the tube when the shutter is closed G_{close} is:

$$G_{close} = \frac{C_{tot}}{C_{tot} + 2 \cdot C_{aHi}} \tag{72}$$

The geometry factor for the tube when the shutter is open was calculated with Eq. (64). Fig. 32 shows the attenuation factor G_{open}/G_{close} as a function of the gap size h_{gap} of the gap between

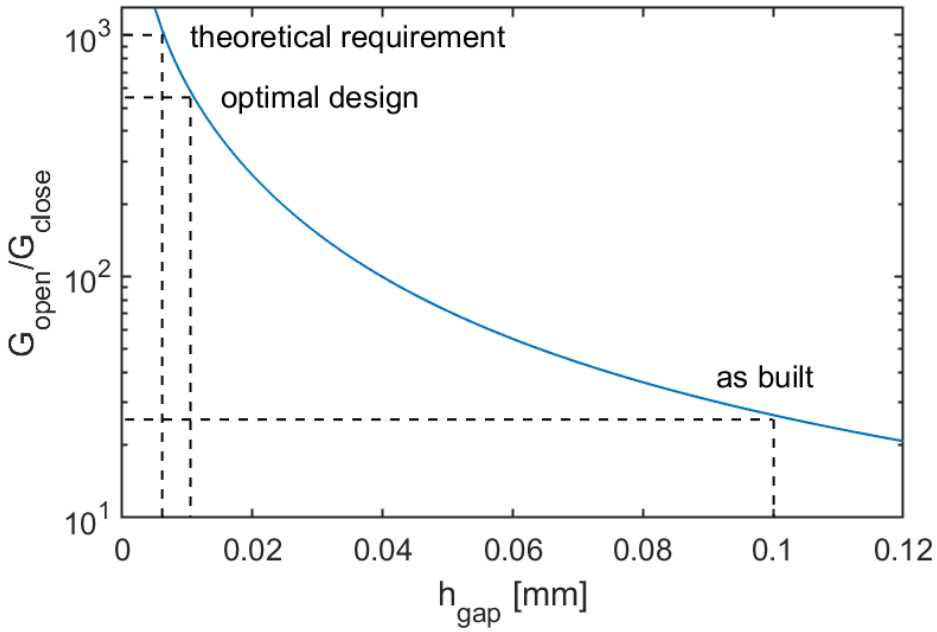

Figure 32: Damping factor G_{open}/G_{close} of the shutter as a function of the gap size h_{gap} of the gap between the shutter and antechamber.

the shutter and antechamber. With increasing gap size, the attenuation factor reduces significantly. The theoretical requirement was to attenuate the signal from the antechamber by a factor 1000 when the shutter is closed. A realistic gap size from the mechanical point of view is 0.01 mm resulting in an attenuation factor of 600 (optimal design), which is close enough to the requirement.
When measuring with the open source channel, a small amount of gas will enter the ionisation region through from the closed source antechamber. The open source slit is in the y-/z- plane and therefore the gas inflow angle χ is 90° (Fig. 14) leading to an attenuation by a factor 5 of the antechamber itself compared when the gas inflow direction is 0° because the antechamber is not designed to measure gas penetrating with such high gas inflow angles into the antechamber. When the shutter is closed, about 0.05 % of the signal originates from the antechamber, assuming an attenuation factor of the shutter of 600. Unfortunately, the actual realisation of the shutter gives a attenuation factor of only 25 (see Chap. 4.5) implying a gap size of 0.1 mm. This can happen when the shutter is not properly fabricated and the tolerances are therefore bigger than originally designed. With an attenuation factor of only 25, 1.1 % of the measured signal originates from the antechamber.

2.8. Multichannel Plates

To register even single ions, NIM uses Microchannel Plates (MCPs) in its detector to amplify the signal. MCPs are thin glass plates consisting of many small channels. When an ion hits a channel, an electron is ejected and accelerated along the channel axis until it hits the opposite wall of the channel wall. There it ejects more electrons, and with ensuing the repetition of the process generating an electron avalanche resulting in an impulse of electrons at the exit of the MCPs. One single MCP is able to amplify the signal of an ion by a factor of up to 10^4 [44]. NIM has two MCPs in Chevron configuration (Fig. 33) to reach a gain of about 10^6 for regular operation (Chap. 4.7).

2.8.1. MCP Gain

In this section, the gain of a single MCP is derived as a function of the voltage U_{MCP} applied over the MCP. The derivation is based on the lecture notes of [46]. When an incoming particle hits the MCP channel wall there is a certain probability that it ejects an electron. By applying an electric field E over the MCP plate, this electron gets accelerated along the channel axis until it hits the opposite wall, where it ejects more electrons (Fig. 33):

$$E = \frac{U_{MCP}}{l} = \frac{F}{q_0} = \frac{am_e}{q_0} \tag{73}$$

With U_{MCP} the voltage applied over the MCP, l the channel length, F the force applied on the electron, q_0 the elementary charge and m_e the mass of the electron. The acceleration a of the

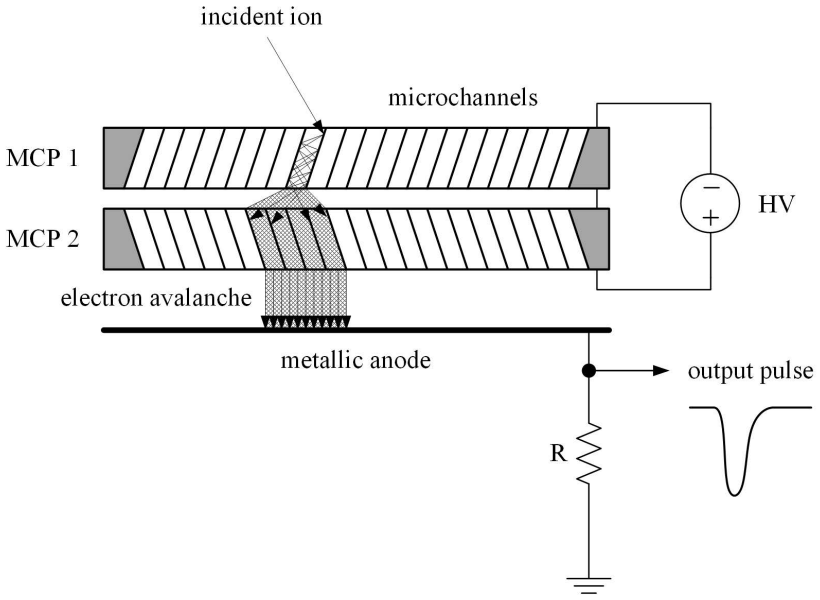

Figure 33: Working principle of a Multichannel Plates (MCPs) detector [44, 31].

electron along the channel is:

$$a = \frac{U_{MCP} \cdot q_0}{l \cdot m_e} \tag{74}$$

The distance s the electron travels along the channel until it reaches the opposite channel wall is:

$$s = \frac{1}{2}at^2 = \frac{U_{MCP} \cdot q_0 \cdot t^2}{l \cdot m_e \cdot 2} \tag{75}$$

With t the flight time of the electron until it hits the wall again. Assuming the initial velocity v_{init} of the initial secondary electron is perpendicular to the channel wall, the flight distance until it hits the opposite channel wall is the channel diameter d. The flight time t can be written as:

$$t = \frac{d}{v_{init}} \tag{76}$$

v_{init} is derived from the electron's initial kinetic energy U_{init}:

$$U_{init} = \frac{1}{2}m_e v_{init}^2 \rightarrow v_{init} = \sqrt{\frac{2U_{init}}{m_e}} \tag{77}$$

where U_{init} is the mean energy of a released electron (secondary electron) upon electron impact on the surface. By inserting Eq. (76) and Eq. (77) in Eq. (75) leads to:

$$s = \frac{q_0 \cdot U_{MCP} \cdot d^2}{l \cdot 4U_{init}} \tag{78}$$

The energy U_c the electron gains during the flight time t is:

$$U_c = q_0 E s = q_0 \cdot \frac{U_{MCP}}{l} \cdot \frac{q_0 \cdot U_{MCP} \cdot d^2}{l \cdot 4U_{init}} \tag{79}$$

$$= q_0^2 \frac{U_{MCP}^2 \cdot d^2}{l^2 \cdot 4U_{init}} \tag{80}$$

The secondary electron emission coefficient δ is proportional to the square root of the energy U_c:

$$\delta = A \cdot \sqrt{U_c} = A \cdot \frac{q_0 U_{MCP} \cdot d}{2\sqrt{U_{init}} \cdot l} \tag{81}$$

With A a constant containing the details of the interaction of the impinging electron with the electrons of the surface. After n collisions with the channel walls, the gain G_{ch} of one channel is:

$$G_{ch} = \gamma \cdot \delta^n = \gamma \cdot \delta^{l/s} \tag{82}$$

With γ containing the probability to emit the first electron upon ion impact. The number of collisions is the channel length l divided by the distance s an electron flies within the channel before it hits the channel wall and ejects more electrons. Inserting now Eq. (81) and Eq. (78) in Eq. (82) leads to:

$$G_{ch} = \gamma \left(A \cdot \frac{q_0 U_{MCP}}{2\sqrt{U_{init}}} \cdot \frac{d}{l} \right)^{\frac{4U_{init}}{q_0 U_{MCP}} \left(\frac{l}{d}\right)^2} \tag{83}$$

By writing the channel length to diameter ratio $\frac{l}{d}$ as α and expressing the electrons initial energy U_{init} in [eV], the equation turns into:

$$G_{ch} = \gamma \left(A \frac{U_{MCP}}{2\alpha\sqrt{U_{init}}} \right)^{\frac{4 \cdot U_{init} \cdot \alpha^2}{U_{MCP}}} \tag{84}$$

With γ in the range of 0.1–10, A approximately 0.2 $\left(\frac{1}{eV}\right)^{1/2}$ [44], U_{MCP} in [eV], α is a dimensionless number, and U_{init} in the range of a few [eV].

2.8.2. Dead time

In this chapter, the dead time τ of the MCPs used in the NIM detector is derived. The dead time is the time one single channel of the MCP needs to replenish 63% of its charge. After 5τ the channel is fully recharged. When the ion count rate is too high, an ion will hit the channel during the time the channel is recharging. The corresponding channel discharges and the triggered signal will be lower because the channel was not fully charged when the signal was triggered. Therefore, it is important to know the dead time to get an estimation of the upper limit of the count rate of the detector.

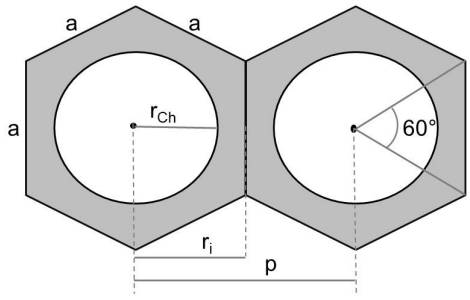

Figure 34: MCP honeycomb structure [35].

The number of channels N of a MCP is its active area A_{act} divided by the area of one channel A_{hex}. The MCP has a honeycomb like structure (Fig. 34). Thus, the area of one channel is the area of a hexagon:

$$N = \frac{A_{act}}{A_{hex}} = \frac{2 \cdot \pi r_{act}^2}{\sqrt{3} p^2} \tag{85}$$

r_{act} is the radius of the active area of the MCP, which is for the NIM MCPs 8 mm and p is the distance between the centres of two channels which is 6 µm. This results in $1.6 \cdot 10^6$ channels of a NIM MCP. The resistance of a single channel is the resistance of the whole MCP plate R_{MCP} times the number of channels N. The single channels act as separate resistors connected in parallel to one MCP:

$$R_{ch} = R_{MCP} \cdot N \tag{86}$$

The channel resistance depends on the voltage applied over the plate. For a nominal voltage of 1000 V R_{MCP} is ∼70 MΩ resulting in a channel resistance of about 10^{14} Ω. The MCPs consist of two different materials: the structure (grey), which consists of a type of lead glass, and the hole, which is approximated with vacuum (white) (Fig. 34). The area of the structure is equal to the area of the hexagon A_{ch}^{hex} minus the area of the channel hole A_{ch}^{hole}. The capacitance of one channel C_{ch} is:

$$C_{ch} = \frac{\epsilon_0(\epsilon_r \cdot (A_{ch}^{hex} - A_{ch}^{hole}) + A_{ch}^{hole})}{l_{ch}} \tag{87}$$

With ϵ_0 the vacuum permittivity, ϵ_r the relative permittivity of lead glass and l_{ch} the MCP thickness which is 0.3 mm. The manufacturer does not give details about the material characteristics as it is a company secret. In [35] is an analysis of different values for ϵ_r found in literature. These values are between 6 and 20. With these values, the resulting capacity is 5 aF per channel. The dead time of a single MCP channel is the channel resistance R_{ch} times the channel capacitance C_{ch}:

$$\tau = R_{ch} \cdot C_{ch} \tag{88}$$

This results in a dead time of $\tau = 500$ µs. With a duration of about 100 µs for the recording time of one waveform, this channel would be blind for the time when the next five waveforms are recorded. With $1.6 \cdot 10^6$ channels and assuming a uniform distribution of ions on the MCP surface, saturation is assumed at particle rates I_p higher than 10^9 particles/s. The current drawn

by the MCPs due to that high count rate is the particle count rate I_p times the MCP gain G and the elementary charge q_0

$$I_{MCP} = I_p \cdot G \cdot q_0 \tag{89}$$

resulting in a current of $\sim$100 µA. The MCPs have a leakage current between 6–30 µA. The additional current drawn by the NIM detector due to the amplification of the ions is lower than a few µA resulting in two decades of margin before the detector reaches saturation.

3. Instrument

This chapter compares the NIM prototype (Fig. 35) with the NIM ProtoFlight Model (PFM) (Fig. 36) from the mechanical point of view. The NIM prototype was developed in the thesis of Stefan Meyer [31], and is a complete ion-optical realisation of the system. However, the mechanical design is just for laboratory use, and is not suitable for flight.
The NIM PFM instrument is the flight realisation of this ion-optical system, with some simplifications and optimisations. In Fig. 36, left panel, the ion-optical system of the PFM is shown, and in the right panel the entire NIM PFM is shown, with the ion-optical system inside the housing and the operating electronics in their separate radiation shielded box. Comparing Fig. 35 and Fig. 36 shows the key differences between the two models. Special focus lay hereby on the design of the detector because there were made some major design improvements.
Fig. 37 left shows the prototype antechamber and right the PFM antechamber. To improve the performance of the antechamber, the flight antechamber was made twice as big as the old one of the prototype. In addition, it has two entrance holes at $\pm 30°$ relative to the x-axis of

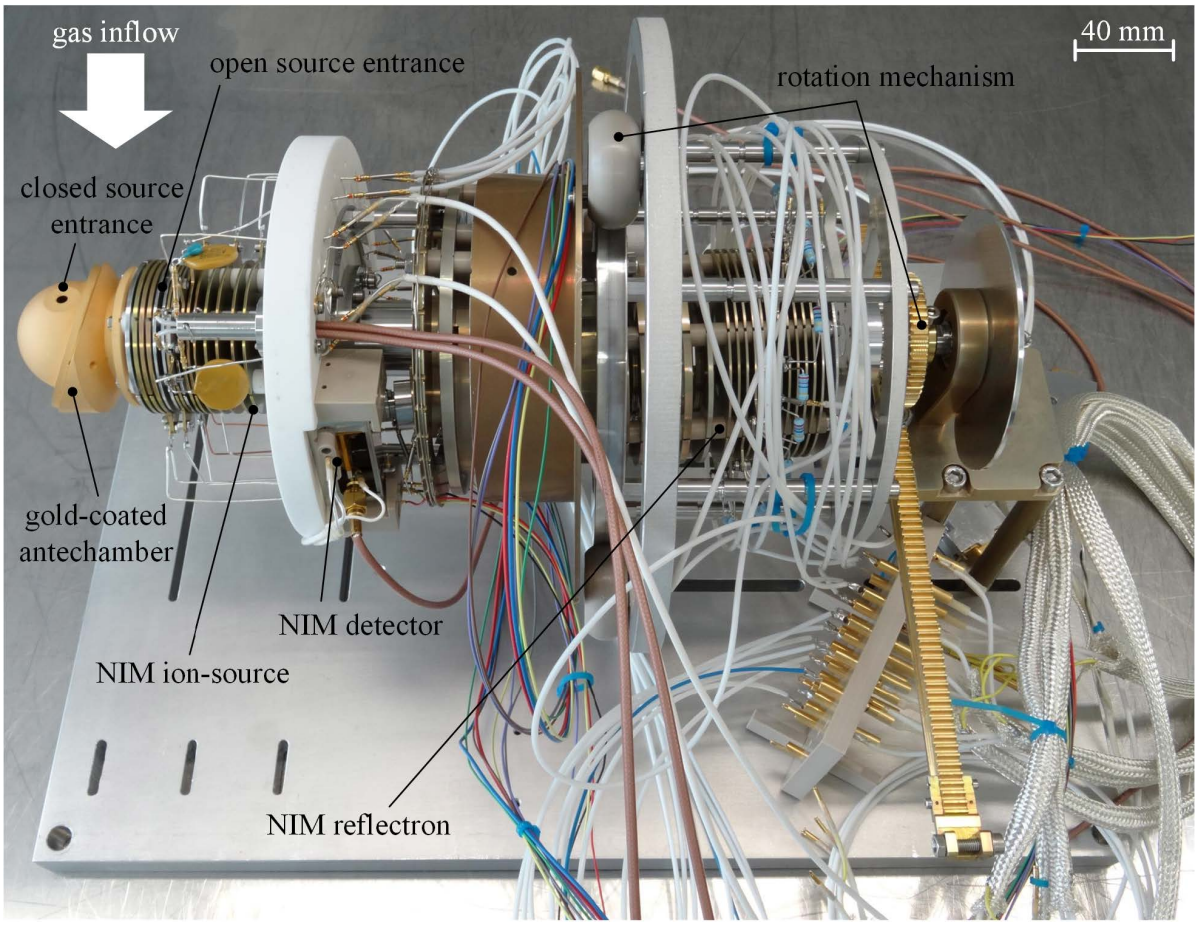

Figure 35: The NIM Prototype [31].

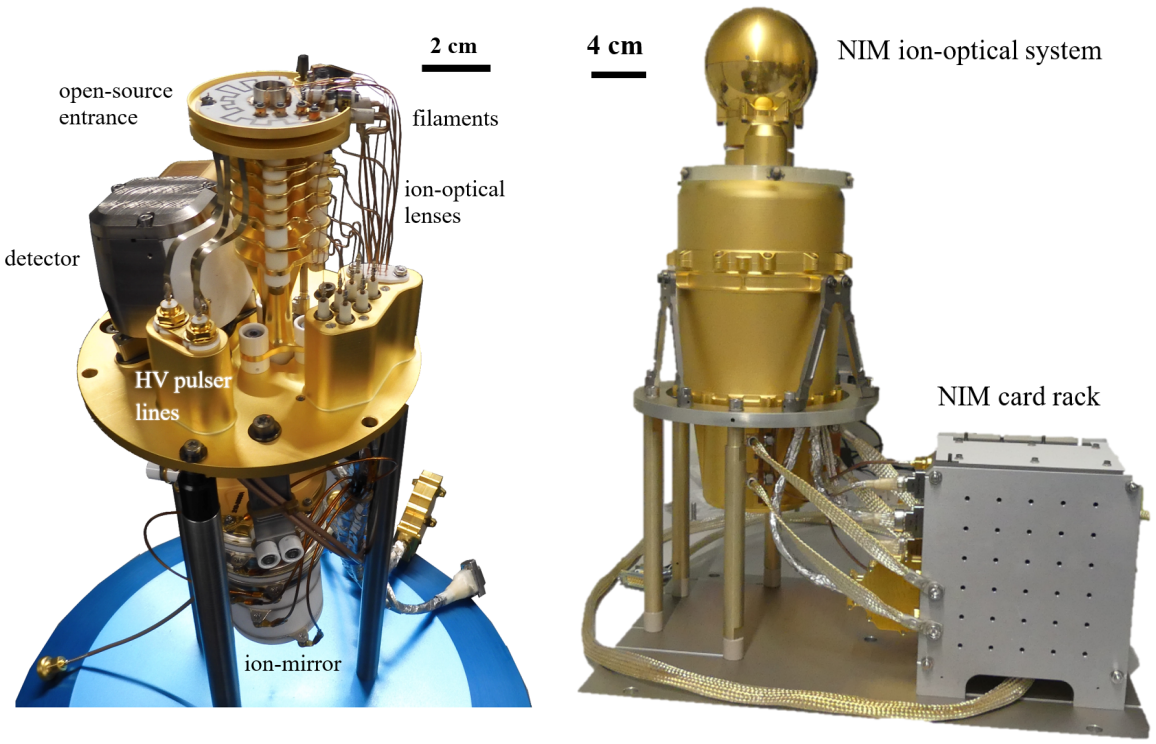

Figure 36: Left: NIM PFM ion-optical system without the antechamber and the housing. Right: The complete NIM PFM ion-optical system with electronic box (card rack) attached [17].

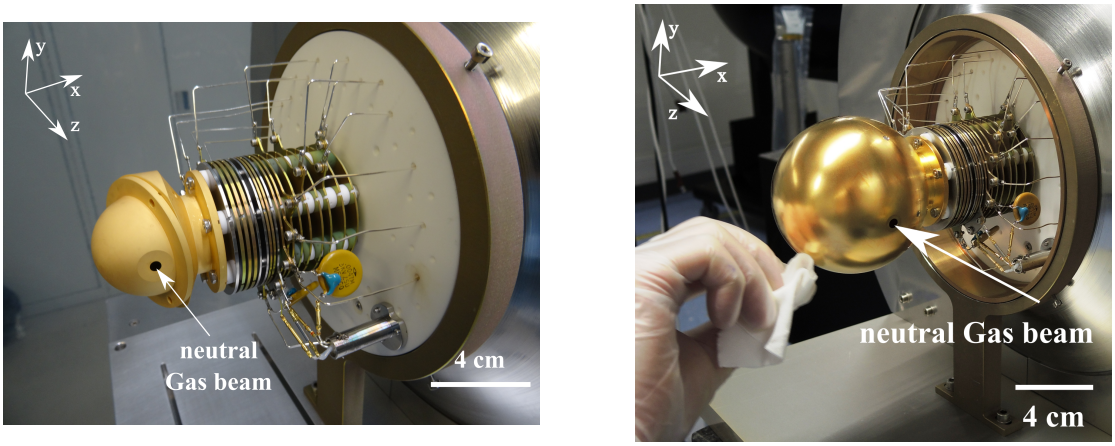

Figure 37: Left: Prototype antechamber [31]. Right: Flight-like antechamber. Both installed on the NIM prototype ion-optical system.

the instrument to be able to measure gas coming from both directions of the instrument (see Chap 2.6). Since the flight version has two entrance holes and the interface to the ion-source contains a shutter, a larger surface area of the antechamber was needed to compensate for the openings. The main inflow direction of the neutral particle beam generated by the CASYMIR

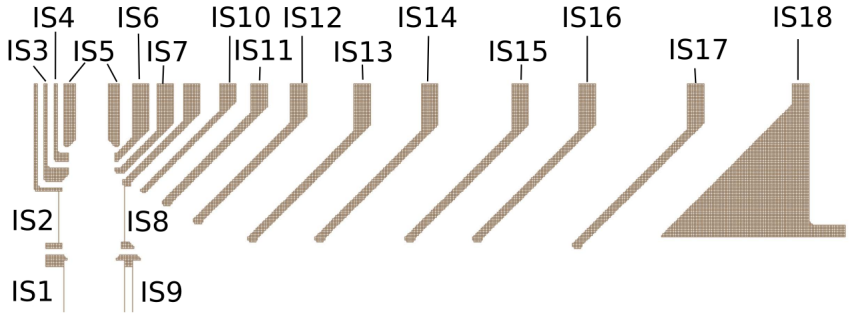

Figure 38: SIMION Model of the Ion-Source of the NIM Prototype [31].

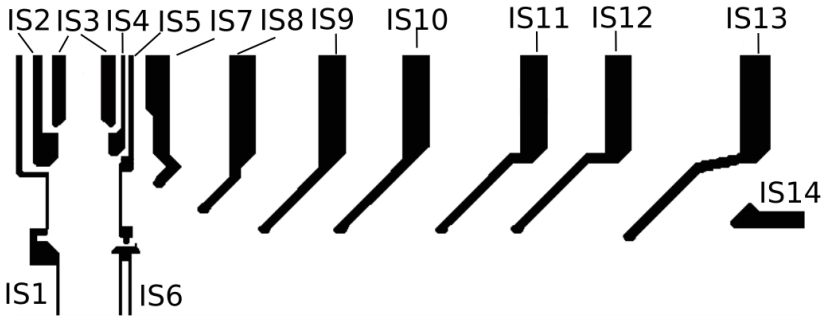

Figure 39: SIMION Model of the Ion-Source of the NIM ProtoFlight Model.

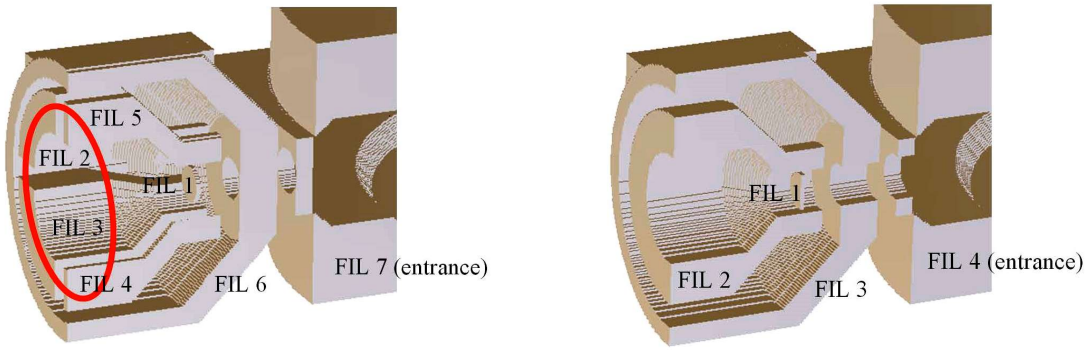

Figure 40: Left: Prototype filament housing [31]. Right: PFM filament housing [31].

test facility is 90° [19]. Therefore, a second flight-like test antechamber was made which has the second entrance hole at position 90° to be able to test the flight antechamber.
The antechambers consists of two parts which are hold together with screws. Tests of the prototype antechamber revealed that two of the mounting screws generate signal artefacts [32]. Therefore, the outer surface of the antechamber was redesigned (see also Chap. 4.2).
Fig. 38 shows the SIMION model of the Prototype ion-source, Fig. 39 shows the ion-source of the PFM and Fig. 40 shows the filament housing of the Prototype (left) and of the PFM (right). The PFM ion-source has seven electrodes less then the prototype to simplify the source and

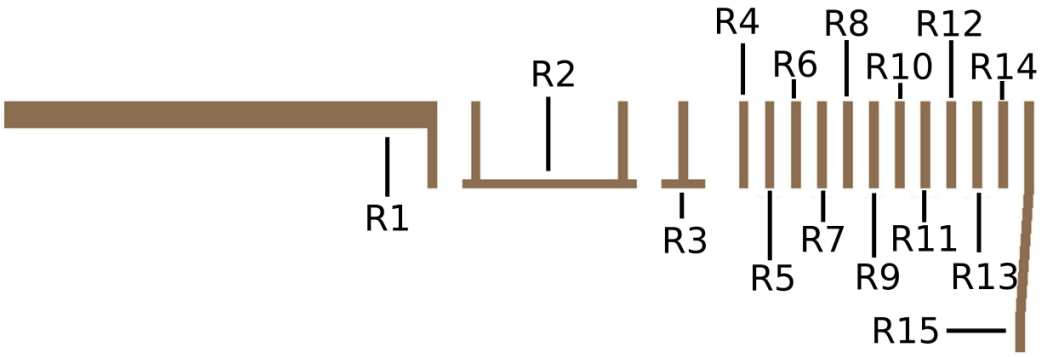

Figure 41: SIMION Model of the ion-mirror of the NIM Prototype [31].

the flight electronics, in particular to reduce the number of high voltages needed. Several low-voltage electrodes were taken together such as IS 1 and IS 2, IS 3 and IS 4 and IS 6 and IS 7. IS 10 was removed and IS 11 was shifted towards the ionisation region.
In the filament housing the electron repelling electrodes Fil 2 – Fil 5, which served to stear the electron beam through the ionisation region, were taken together to one single electrode Fil 2. The electron repelling electrode in the prototype was split into four parts to compensate with the electric fields for a bad alignment of the filament. For the PFM, the mounting of the filament holder was improved and therefore these four electrodes could be taken together to one single electrode.
Fig. 41 shows a schematics of the ion-mirror. The prototype ion-mirror consists of 14 ring-electrodes (R 2 – R 15) to establish a potential gradient. Electrode R 1 is the drift tube. R 2 is the ion-mirror lens electrode, R 3 is on drift potential. The set R 1-R 2-R 3 establishes a thick lens (similar to geometric optics). Electrodes R 4 –R 25 establish the actual ion-mirror. Between the electrodes R 4 – R 15 are resistors to connect the electrodes with each other to generate a linear voltage gradient when a voltage is applied at electrodes R 4 and R 15. In addition, a voltage can be applied on electrode R 8 allowing additional focusing of the ions within ion-mirror. The flight version of the ion-mirror consists of a ceramic tube with two resistance spirals on its inner walls replacing electrodes R 5 – R 7 and R 9 – R 14 respectively. From the electrical and ion-optical point of view, the two ion-mirrors behave the same.

The NIM Prototype detector has a rigid Printed Circuit Board (PCB) on which the electrical components and the drift tube adapter with the MCP stack are mounted (Fig. 42 left panel and Fig. 43). Due to Jupiter's strong radiation field, the detector has to be shielded to reduce the noise level induced by the strong radiation and to increase the detector's lifetime. To minimise the required shielding mass, the flight detector has to be very compact. This was achieved by using a flex PCB to fold the detector into a PEEK housing (Fig. 42, right panel).
Fig. 44, left panel shows the mechanical design of a preliminary design of the PEEK housing containing the MCPs. The MCPs lay on a ledge 1 mm above the anode. A Zener diode generates a voltage between the MCP backside and the anode to accelerate the electrons from the MCP backside towards the anode (see electrical scheme Fig. 45). There are two contact lugs on top and at the bottom of the MCP stack to apply a voltage over the MCPs. The MCPs are fixed with a PEEK screw within the housing. In the old design, the screw threads were

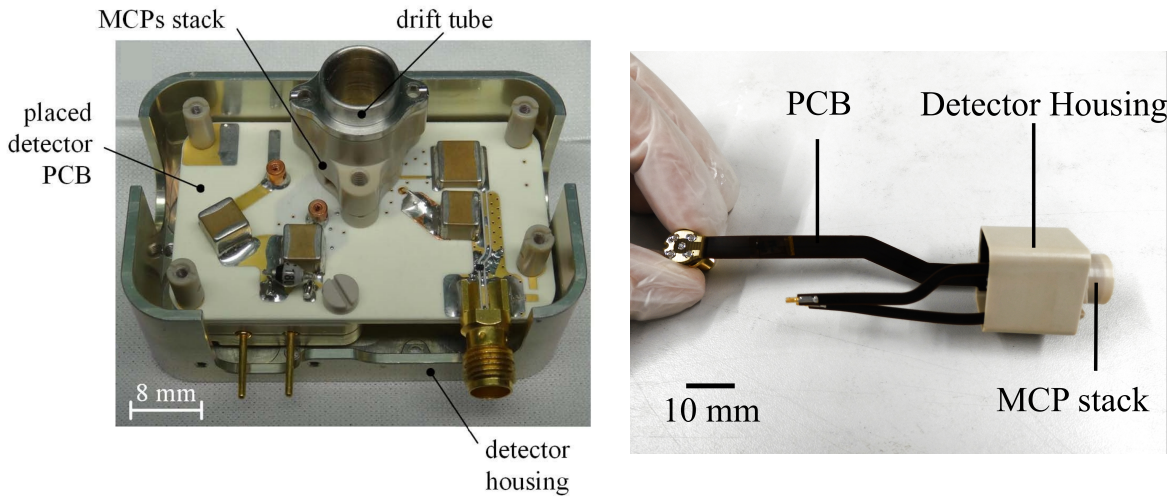

Figure 42: Left: NIM Prototype detector [31]. Right: NIM Flight detector without its radiation shield.

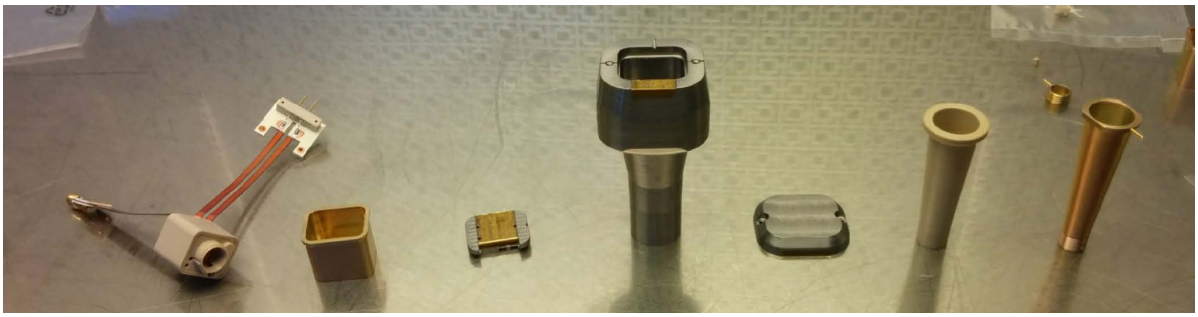

Figure 43: Components of the NIM flight detector. From left to right: Detector folded in PEEK housing, Al cover, Ta shielding, PEEK drift tube to electrically isolate the Al drift tube from the shielding [26].

milled down to the ledge. When the MCPs were mounted, they often canted in the threads. In addition, it was not possible to determine, how much the screw had to be tightened. When the screw was tighten too much, the MCPs broke as they consist of lead glass and are therefore very fragile. When the screw was too loose, the two contact lugs had no reliable electrical contact to the MCPs. When applying a high voltage over the whole MCP stack, the gaps between the contact lugs and the MCPs act as an additional resistors over which the voltage builds up resulting in a discharge between the electrodes and the MCPs. The discharge can propagate through the whole MCP stack and damages the readout electronics. As a consequence, the screw thread was milled less far and an additional mechanical stop was made to tighten the screw only down to that stop (Fig. 44, right panel). This prevented the MCPs from canting in the screw thread thus it was not milled down to the bottom of the lower ledge and with the mechanical stop, the screw could not be tightened too much to break the MCPs. In addition, a PEEK spacer was added between the screw and the MCPs to push down the MCPs uniformly. Due to the mechanical tolerances in the manufacturing process of the different parts of the

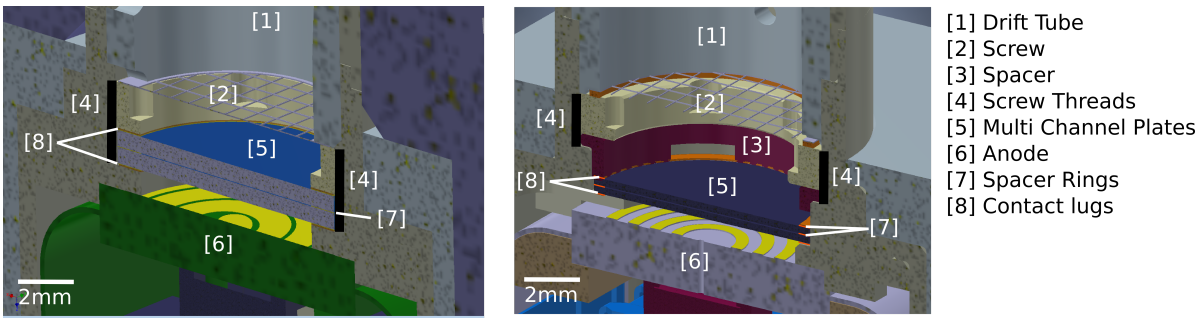

Figure 44: Schematics of the PFM detector housings. Left: preliminary design. Right: final flight design.

housing, metallic spacer rings are added between the PEEK spacer and the contact lug of the top MCP to close the resulting gap. The number of added rings varies between each detector because the gap resulting from the varying mechanical tolerances is different for each manufactured housing. With this design, the electrical contact between the MCPs and the contact lugs could be improved but from the electrical point of view its still not a reliable electrical contact.

To make the system more robust against discharges the Zener diode was exchanged through a resistor (R_D in Fig. 45). The flight electronics sets the voltage U_{stack} between the top MCP and the anode. The MCPs and the Zener diode act as voltage dividers, which are connected in series. Therefore, the potential drop over the MCPs depends on the potential drop over the Zener diode. The voltage drop over the Zener diode is 180 V independent of U_{stack}. Therefore, the voltage over the MCPs U_{MCP} is 180 V lower than U_{stack}. When having a resistor R_D instead of a Zener diode, the voltage over the MCPs cannot be calculated by just having U_{stack} because the resistance of the MCPs R_{MCP} depends on the voltage U_{MCP} applied over them. The resistance also changes with time due to ageing because the conductive material inside the MCP channels degrades over time. Therefore, the current I_{MCP} flowing through the system has to be known to be able to calculate U_{MCP}. The NIM flight electronics is not designed to measure this current because it was designed for a detector with a Zener diode where a current measurement would be unnecessary. A calibration with the laboratory electronics was done to determine the relationship between U_{stack} and U_{MCP} (Chap. 4.7).

In the following section, U_{MCP} is derived as a function of the different voltages known when measuring with laboratory electronics. Fig. 45 shows the circuit diagram of the detector when operated with laboratory electronics and Table 5 summarizes the used variables. The current flowing through the MCPs I_{MCP} is measured with the resistor R_M:

$$I_{MCP} = \frac{U_{RM}}{R_M} \tag{90}$$

With U_{RM} the voltage over the resistor R_M which is:

$$U_{RM} = U_{PSA} - U_A \tag{91}$$

$$= U_{PSMCP} + U_{PSD} - U_A \tag{92}$$

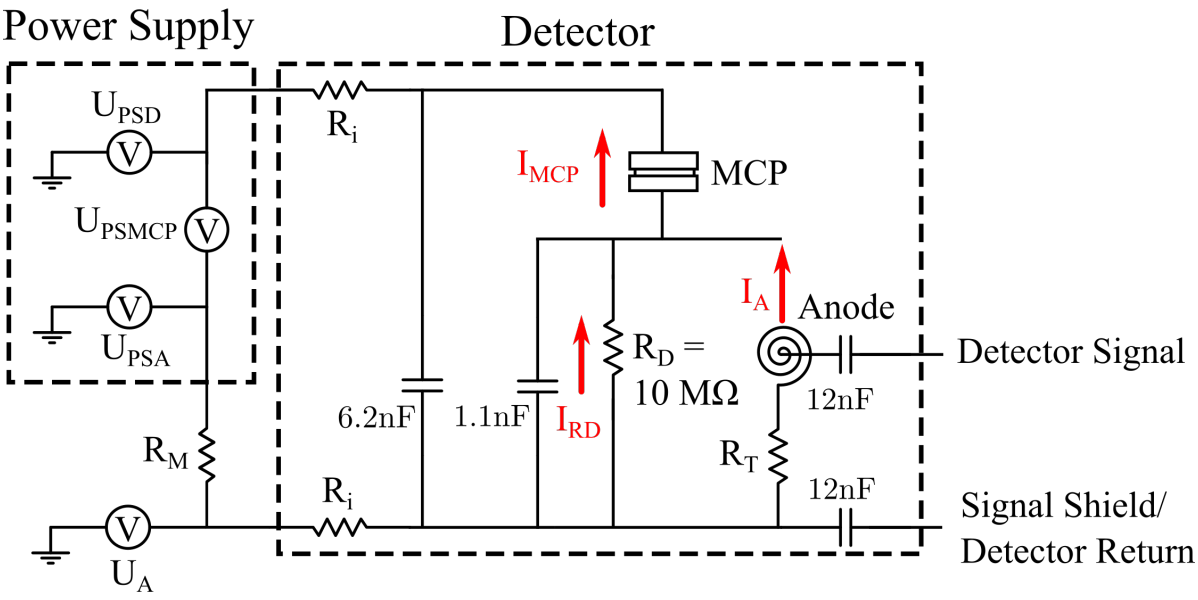

Figure 45: Electrical schematics of the NIM flight detector with laboratory electronics attached.

With U_{PSA} the power supply output voltage for the anode, U_A the voltage applied on the detector anode, U_{PSD} the power supply output voltage applied at the top contact lug of the MCP stack and U_{PSMCP} the voltage difference between the two power supply outputs. U_{PSMCP} is:

$$U_{PSMCP} = U_{RM} + 2 \cdot U_{Ri} + U_{RD} + U_{MCP} \tag{93}$$

With U_{Ri} the voltage over the input resistors R_i, which are there to damp noise coupled into the detector circuit from the power supply:

$$U_{Ri} = I_{MCP} \cdot R_i \tag{94}$$

U_{RD} is the voltage over the resistor R_D replacing the former diode. The current I_A induced when an ion generates an electron avalanche, is very low compared to the current I_{RD}. Therefore, $I_{MCP} = I_{RD}$ and:

$$U_{RD} = I_{MCP} \cdot R_D \tag{95}$$

Solving Eq. (93) for U_{MCP} and inserting the different voltages results in:

$$\begin{aligned} U_{MCP} =& U_{PSMCP} - U_{RM} - 2 \cdot U_{Ri} - U_{RD} && (96)\\ =& U_{PSMCP} - U_{PSMCP} + U_{PSD} - U_A - 2 \cdot I_{MCP} R_i - I_{MCP} R_D && (97)\\ =& (U_A - U_{PSD}) \cdot \left(1 + \frac{2R_i + R_D}{R_M}\right) - U_{PSMCP} \frac{2R_i + R_D}{R_M} && (98) \end{aligned}$$

The measurements with this setup (Fig. 45) of the MCP voltage and resistance are presented below, in Chap. 4.7.

R_D	Resistor replacing the former diode	U_A	Voltage on the detector anode
R_i	Detector input resistor	U_{MCP}	Voltage over the MCPs
R_M	Resistor used to determine I_{MCP}	U_{PSA}	Anode voltage output of power supply
R_{MCP}	MCP resistance	U_{PSD}	Drift voltage output of power supply
R_T	50 Ω termination	U_{PSMCP}	Voltage difference between U_{PSA} and U_{PSD}
I_A	Current induced in the MCPs when an ion hits the MCPs	U_{RD}	Voltage over R_D
I_{ion}	Ion current hitting the MCPs	U_{Ri}	Voltage over R_i
I_{MCP}	Current flowing through the MCPs	U_{RM}	Voltage over test resistor R_M
I_{RD}	Current flowing through R_D		

Table 5: List of the variables used in the schematics of the flight detector Fig. 45 when the detector is operated with laboratory electronics.

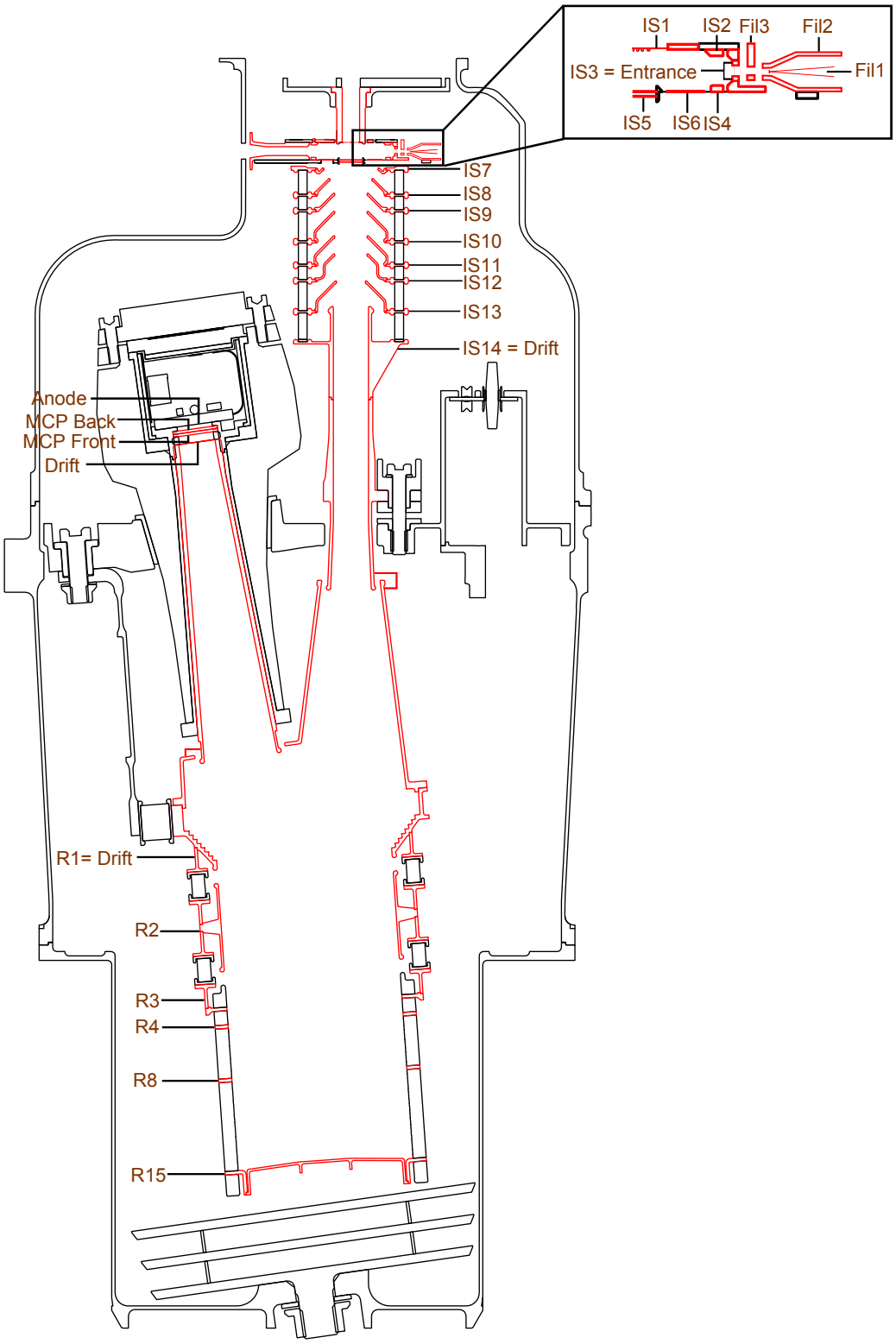

Figure 46: Schematics of the NIM flight design with all electrodes of the ion-optical system marked in red.

4. Experiments

This section includes tests of flight components and also system tests of the NIM Proto Flight Model (PFM) and the Flight Spare (FS) model. The tests of the flight ion-mirror and the flight antechamber were performed with the NIM Prototype whereas the other tests were performed with the NIM PFM model unless otherwise mentioned.

4.1. Flight Ion-Mirror

In this section the performance of two ion-mirrors is compared. As described in Chapter 3, the prototype ion-mirror consists of several ring-electrodes connected with each other with resistors to generate a linear voltage gradient. The flight ion-mirror consists of a ceramic tube with two resistance spirals replacing some of the ring-electrodes. Fig. 47 left shows the prototype ion-mirror and Fig. 47 right shows the flight ion-mirror mounted to the NIM prototype in the test setup. An ion-mirror of the same type as the flight ion-mirror was also used in the RTOF mass spectrometer, which flew in the ROSINA [36] and in the NGMS instrument [23]. From the electrical point of view, the two ion-mirror types behave the same.
The measurements were performed in a vacuum chamber. The residual gas pressure for the measurements with the prototype ion-mirror was $5 \cdot 10^{-10}$ mbar and for the measurements with the flight ion-mirror $1.4 \cdot 10^{-9}$ mbar. The test gases were injected directly through a leak valve to increase the chamber pressure up to $1 \cdot 10^{-8}$ mbar. The used test gases were: Ne, Ar, Kr and Xe. 3 Mio. single spectra were histogramed for each of the measurements. All voltages of the instrument were manually optimised for the measurements with the two ion-mirrors. Table 6 shows the signal-to-noise ratios and the mass resolution of the different test gases measured with the two instrument configurations.
The SNR of the measurements with the flight ion-mirror is for all gases lower than the SNR of the measurements with the prototype ion-mirror, the mass resolution of the flight ion-mirror is slightly better than with the prototype ion-mirror. The better SNR performance of the prototype ion-mirror is due the much longer calibration time, and thus better optimisation of

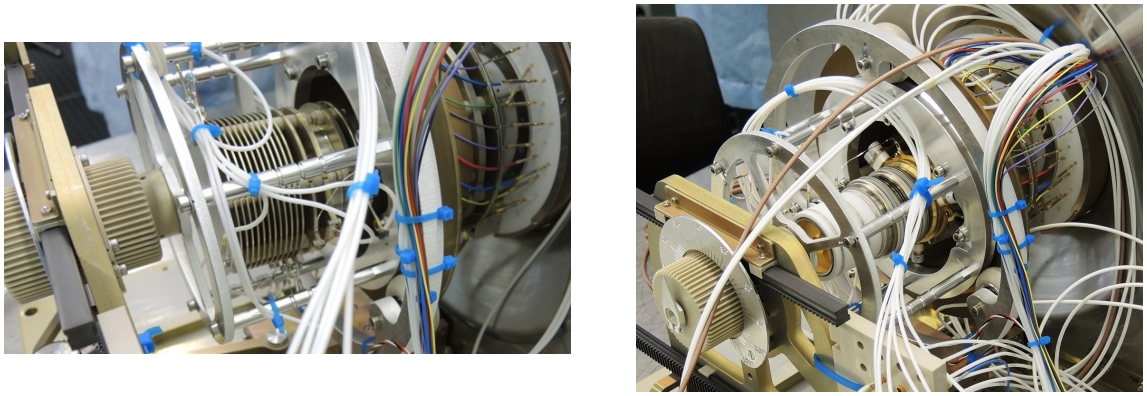

Figure 47: Prototype ion-optical system with prototype ion-mirror with ring-electrodes (left panel) and flight ion-mirror attached (right panel).

Gas	SNR ProtoR	SNR PFMR	m/Δm ProtoR	m/Δm PFMR
^{20}Ne	2022.9	562.4	200 ± 12	236 ± 16
^{40}Ar	4732.6	1808.4	212 ± 9	267 ± 15
^{86}Kr	746.1	414.3	224 ± 7	292 ± 12
^{136}Xe	185.5	97.1	265 ± 8	332 ± 13

Table 6: Table listing the signal-to-noise ratios (SNR) and the mass resolution (m/Δm) of the prototype ion-mirror (ProtoR) and the flight ion-mirror (PFMR).

the ion-optical system, of the Prototype with the prototype ion-mirror. To set constrains for the different subsystems of the NIM ion-optical system, a whole calibration campaign was performed with the prototype ion-mirror attached [31]. Therefore, this configuration is much better optimised than the configuration where the flight ion-mirror is attached to the Prototype ion-optical system. Nevertheless, the flight ion-mirror showed good performance considering the short optimisation time available to verify its performance.

4.2. Flight Antechamber

After successfully testing the flight ion-mirror, the flight antechamber was tested. A picture of the prototype and the flight antechamber is shown in Fig. 48. The antechambers consist of two parts. In the old design the two parts of the antechamber had a rim on which the screws were mounted to put the two parts together. These screws were at position $\pm 45°$. Tests with this antechamber revealed that neutral particles hit these screws and scatter into chamber (Fig. 49 a) [32]). Therefore, an antechamber with a flat outer surface was required. In the new design the screws are recessed into the 1 mm thin surface of the antechamber to get rid of the needed rim in the old design. In addition, the new antechamber is by a factor two bigger than the prototype antechamber with the aim to get more signal. Simulations of the flight trajectory revealed that two holes were required at positions $\pm 60°$ to get optimal signal [9]. The CASYMIR test facility is not able to direct the neutral particle beam under an angle of 60° onto the instrument. To test the new design, an slightly different antechamber was used with the second entrance hole at position $\theta_0 = -90°$ instead of –60°. With a rotation mechanism, the instrument can be rotated around the x-axes by $\pm 90°$.

These measurements were conducted at the CASYMIR test facility at the University of Bern. CASYMIR is able to generate a neutral particle beam with velocities up to 5.5 km/s [19]. For these measurements the particle velocity was about 2.5 km/s because this is the velocity of the spacecraft in Ganymede orbit, which will be 90% of the measuring time of NIM.

Fig. 49 a) shows measurements conducted with the thermal mode when the old antechamber was attached [32]. For these measurements, the instrument was rotated around the x-axis by keeping the beam at the same position. When rotating the antechamber, the hole moves out

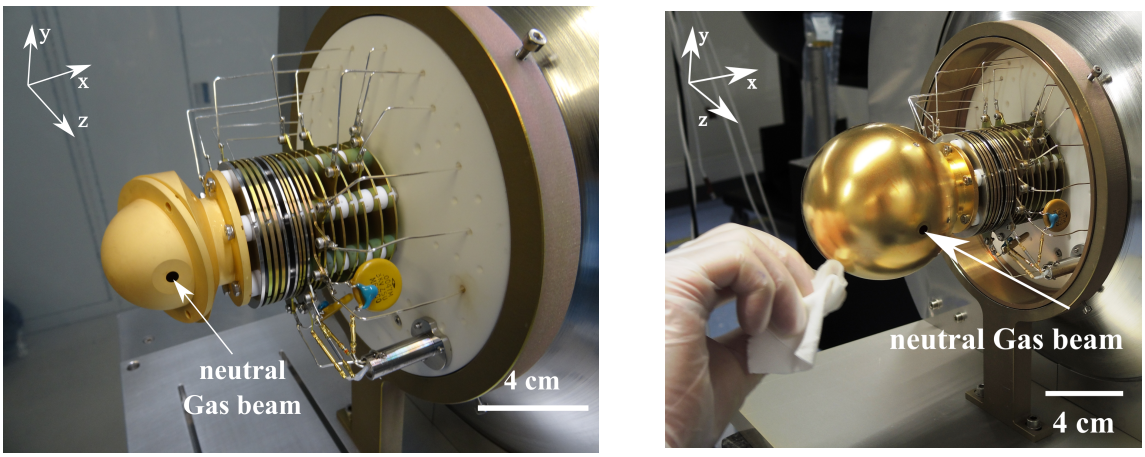

Figure 48: Left: Prototype antechamber. Right: flight-like antechamber with two entrance holes at positions +60° and –90°.

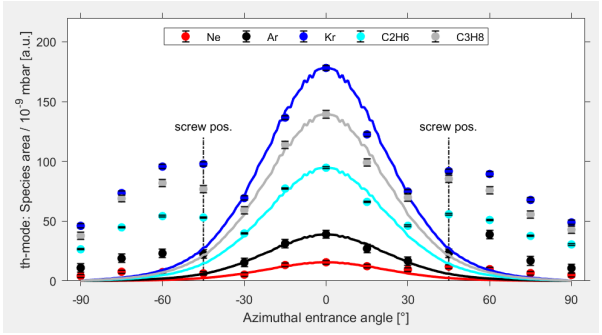

(a) Prototype antechamber, thermal mode.

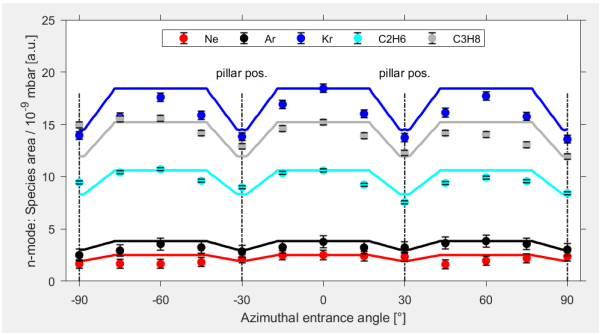

(b) Prototype antechamber, neutral mode.

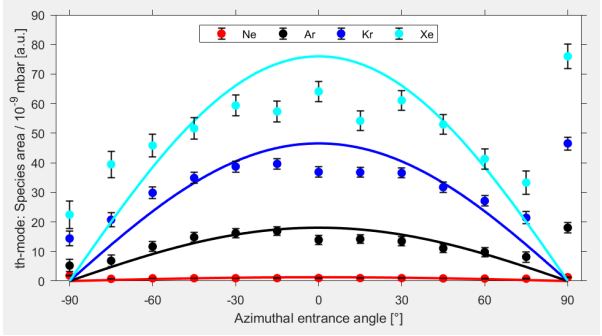

(c) Flight-like antechamber, thermal mode.

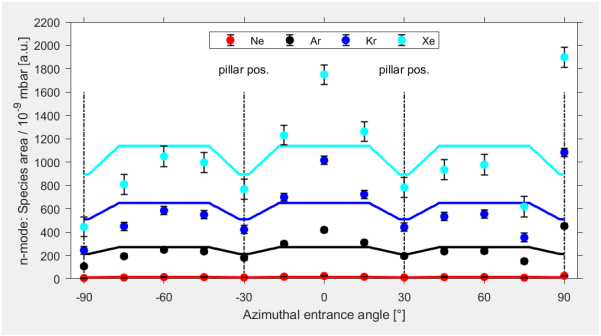

(d) Flight-like antechamber, neutral mode.

Figure 49: Panel a) an b) show measurements done with the NIM Prototype ion-optical system with the old antechamber attached. a) shows measurement conducted with the thermal gas mode and panel b) shows measurements of the neutral mode respectively [32]. c) and d) are the corresponding measurements performed with the new antechamber attached to the NIM Prototype.

of the neutral particle beam because the beam is smaller than the antechamber. The expected intensity distribution I_{ant} is a combination of the function of the moving hole through the beam with a normal distribution:

$$I_{ant} = \frac{A}{\sigma\sqrt{2\pi}} \int_{x_{min}}^{x_{max}} \exp^{\frac{(x-\mu)^2}{2\sigma^2}} dx \tag{99}$$

With A a constant taking the beam intensity into account, σ the standard deviation of the beam and μ the position of the beam centre relative to the centre of the antechamber, which is zero in this coordinate system. The borders of the integral (Eq. (99)) determine the section of the beam entering the antechamber:

$$x_{max} = r_{ant} \sin\alpha - r_{aHi} \cos\alpha \tag{100}$$

$$x_{min} = r_{ant} \sin\alpha + r_{aHi} \cos\alpha \tag{101}$$

With r_{ant} the radius of the antechamber and r_{aHi} the radius of the antechamber entrance hole. The sine contribution considers the shift of the hole in y-direction when the hole is rotated. The cosine contribution originates from the projection of the beam on the entrance hole. For the measurements with the new antechamber, the shift in y-direction when rotating the instrument was compensated by shifting the whole instrument. Therefore the sine contribution in Eq. (100) and Eq. (101) cancels leading to a cosine-like function.
When comparing Fig. 49 a) and c), the artefacts successfully vanished after the redesign. The higher intensity at angle +90° is an outlier because it appears in both the thermal (Fig. 49 b)) and the neutral mode figure (Fig. 49 d)) of the measurements with the new antechamber. The lower measured signal intensity for the measurements with the new antechamber is a result of having an additional entrance hole which was necessary because of the flyby trajectories (see Chap. 2.5).
Fig. 49 b) shows measurements conducted with the neutral gas mode with the old antechamber attached and Fig. 49 d) shows measurements conducted with the neutral gas mode when the new antechamber was attached. At position ±30° and ±90° are pillars holding the stack of the ion-optical lenses together. When the beam hits these pillars, the particles scatter in all directions leading to a reduction of the signal. For the neutral gas channel, no difference in the signal distribution and intensity is expected because a change in the antechamber design does not influence the signal measured with the neutral gas channel. The observed signal of the neutral gas mode when the new antechamber is attached, is significantly higher than with the old antechamber. This is due to a better voltage set. A different voltage set for the voltages in the ionisation region changes the distribution of the electron beam thus leading to a different ion distribution in the ionisation region. This leads to a different angular distribution of the signal for the neutral gas channel when comparing the results of the two measurement series.

4.3. Density Enhancement

For the first tests with the NIM PFM, the front side of the NIM instrument was scanned with the neutral particle beam to find the position of the entrance slit and the antechamber entrance

hole to align the beam properly with the instrument. Fig. 50, left panel shows the scan of the front side and Fig. 50, right panel shows the corresponding structural part. The antechamber entrance hole is clearly visible as a small dot. Fig. 51 shows a zoom with a better resolution of the antechamber entrance hole which shows a nice Gaussian distribution. When looking at the entrance slit, there are two positions with increased intensities. The zoom on Fig. 52 reveals that the positions of biggest intensity is were the beam hits the structure covering the two electron emitting filaments. The other intensity maximum is where the beam hits the supporting structure opposite of the filament bloc. When the gas hits these structures, the gas slows down leading to a local increase of the gas density. Therefore, the structure partially thermalises the gas similar as the closed source antechamber. This was not intended because with the neutral gas channel the aim is to measure incoming neutral particles and ions directly without any interaction with the structure. In the design of the PFM, the filament bloc and the supporting structure act like a funnel directing the scattered gas to the central grid. The thermalisation of the incoming gas when it hits the filament bloc is unavoidable. For the supporting structure opposite of the filament, a pillar instead of the plate like structure would have been the better option. When the gas hits the pillar, the pillar scatters the gas in all directions instead of scattering only in the direction of the central grid. This phenomenon was observed when doing a similar measurement with the NIM prototype (Fig. 53).

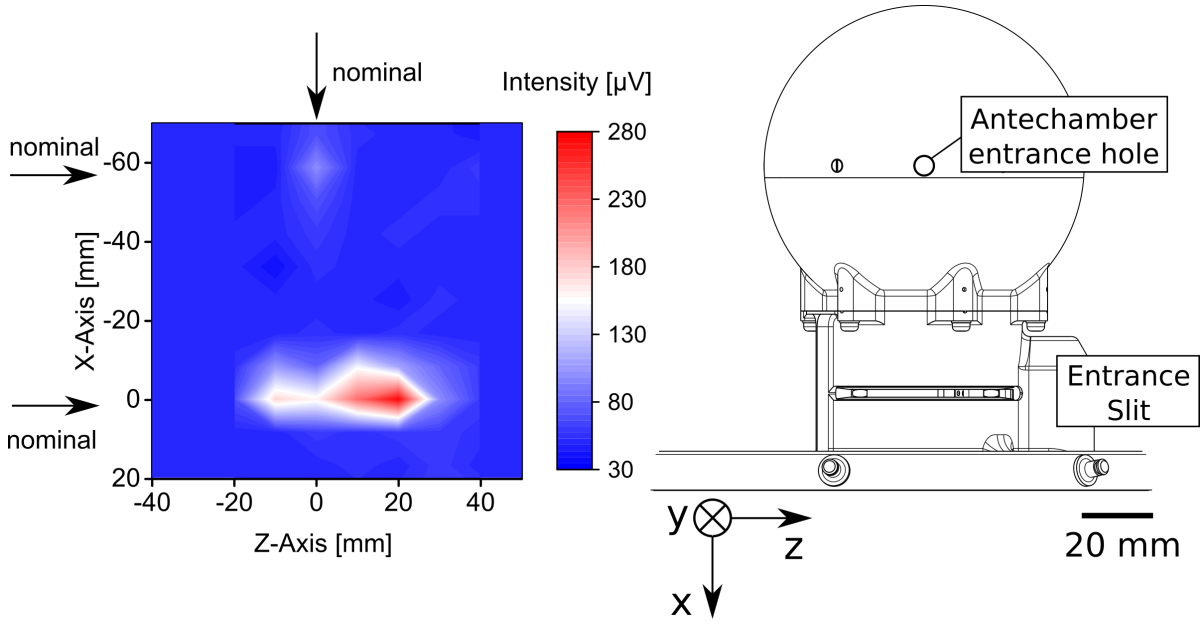

Figure 50: Left: Intensity profile when directing the neutral particle beam at the structure of the NIM PFM instrument. Right: Front view as seen by the neutral particle beam.

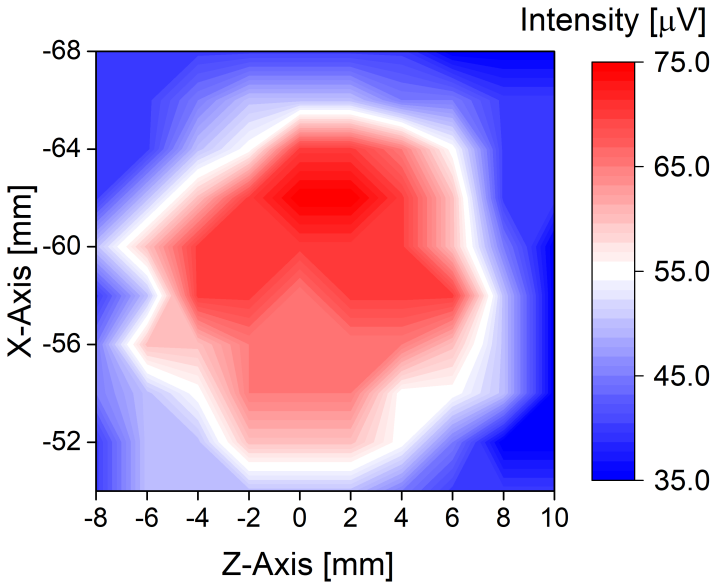

Figure 51: Detail on the antechamber hole when directing the neutral particle beam at the structure of the NIM PFM instrument. Note that the intensity scale is different to Fig. 50

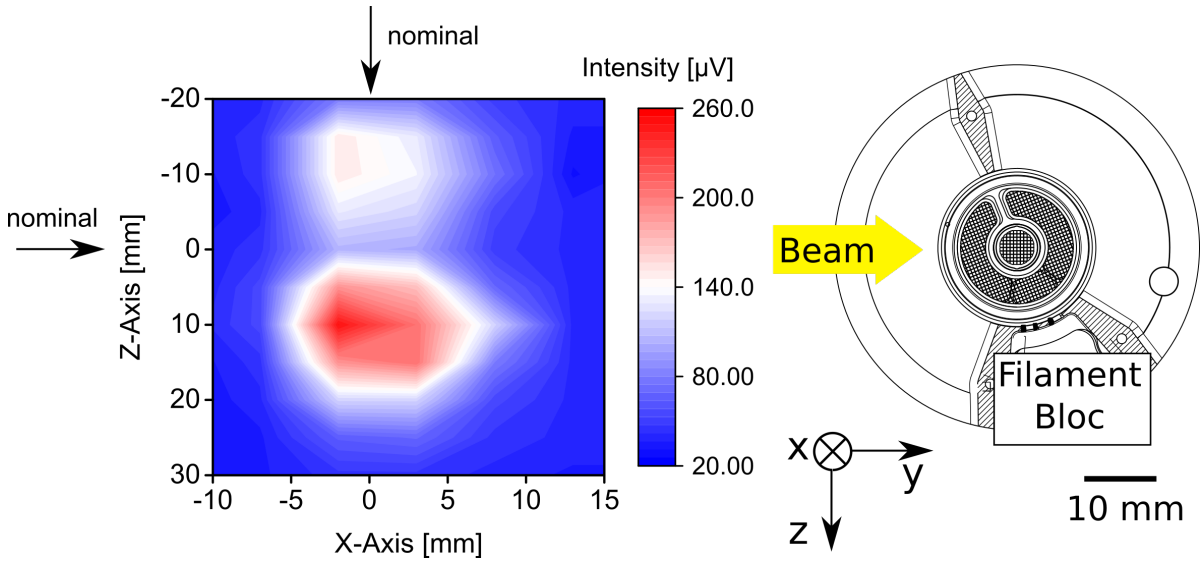

Figure 52: Left: Detail of the scan of the front side of NIM with the neutral particle beam (Fig. 50 right). Right: Top view on the ionisation region.

The ion-source of the prototype had six pillars holding the different focusing lenses together. In Fig. 53 the pillars are marked as red circles. The electron emitting filament was opposite of the main gas inflow direction. For these measurements, the ionisation region was scanned with the neutral particle beam at angles 0° and ±60° to direct the beam in between the pillars over the extraction grid. When scanning from the front side, the signal intensity has a nice Gaussian

shape. When scanning the ionisation region at angles of ±60° the Gaussian distribution is visible when the neutral particle beam is aligned over the centre grid with an asymmetry toward the side of the filament bloc. The gas hitting the filament bloc gets thermalised leading to a higher signal than on the other side of the were the gas only scatters on the pillars. Here the signal increase due to thermalisation is less dominant than in the design of the PFM because the part of the filament structure seen by the beam is tilted outward. At distances bigger than ±25 mm from the centre, the signal drops again. This is where the beam is completely outside of the ionisation region.

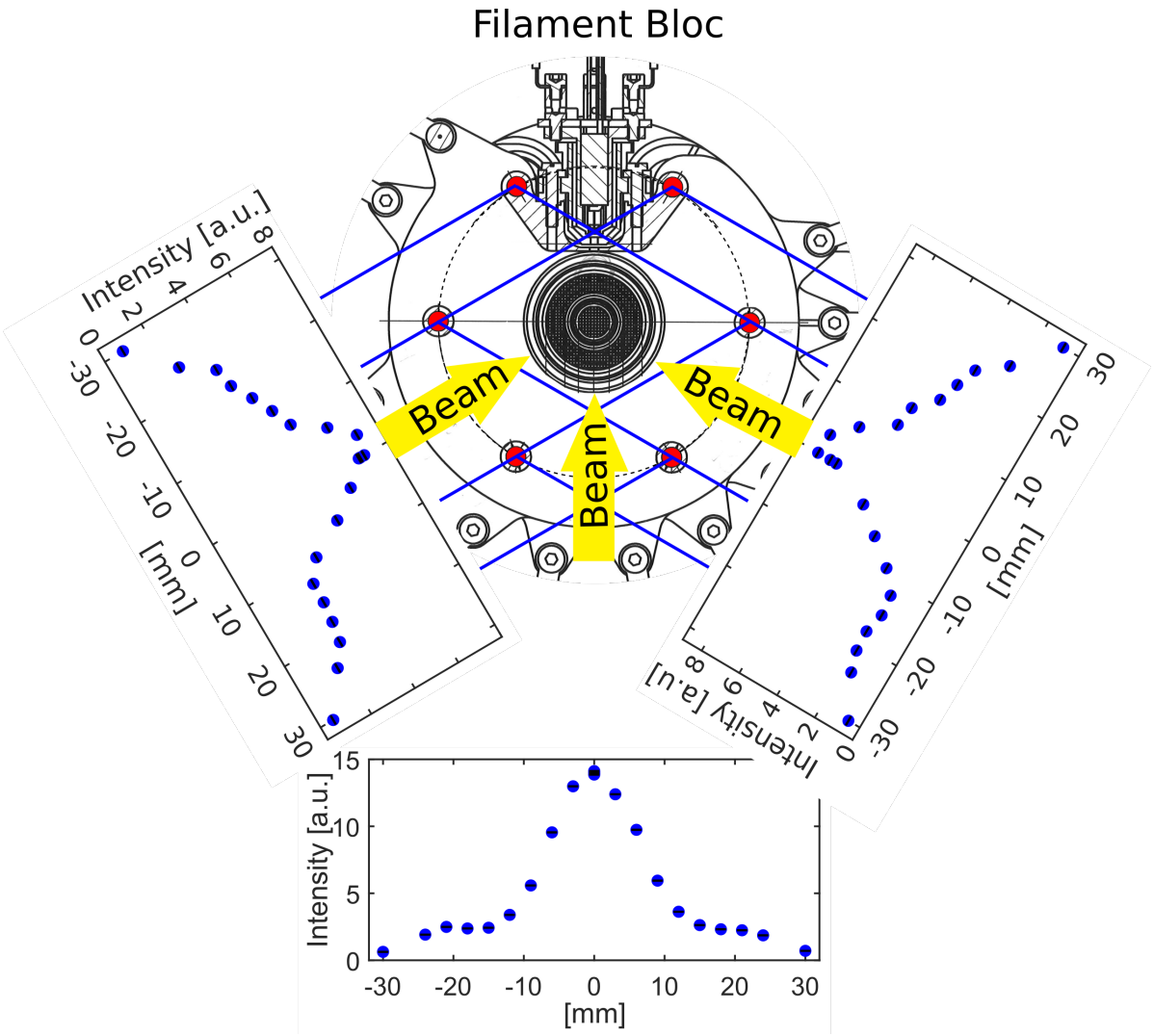

Figure 53: Detail on the entrance seen from above the entrance plane when directing the neutral particle beam at the structure of the NIM Prototype. The red circles mark the positions of the pillars holding the ion source together.

4.4. Entrance Ion and Electron Position Simulations

This chapter shows at which start positions the ions in the ionisation region have to be to successfully reach the detector when the extraction pulse is applied on the extraction grid. In addition, this chapter includes simulations of the flight path of the electron beam which is used to ionise the neutral particles.
Fig. 54, top panel shows the ionisation region from the side. The pink tube opposite of IS 5 is the tube connecting the antechamber with the ionisation region. Neutral particles are ionised with an electron beam (blue arrow) and pulled into the analyser section with the inner extraction grid IS 5 (th-Mode and n-Mode). Ions penetrating the ionisation region are pulled with the outer extraction grid IS 6 into the analyser section (i-Mode). Fig. 54 bottom shows the top view of the ionisation region when looking from the antechamber. On the right side are the two filaments used to generate the ionising electron beam and on the left side is a supporting structure to support the antechamber from the other side. In n-Mode and i-Mode, the gas

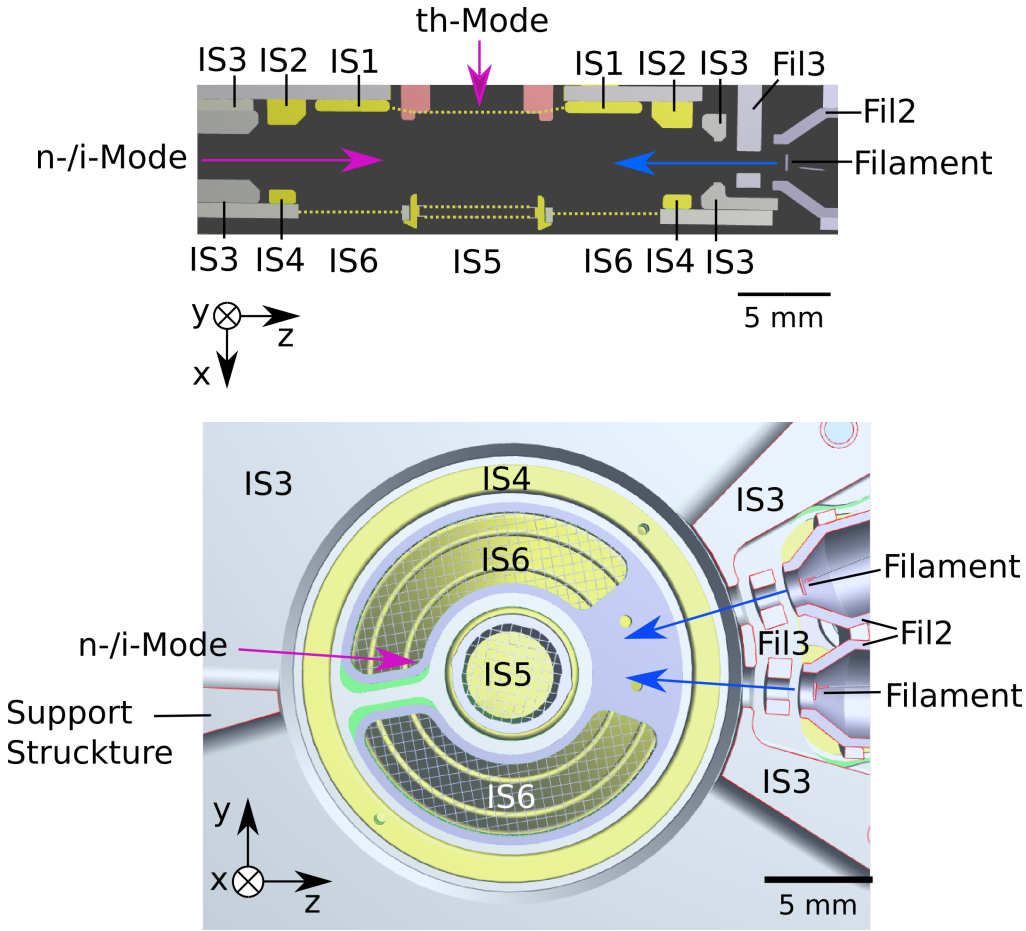

Figure 54: Side (top) and top view (bottom) of the ionisation region. The violet arrows mark the gas inflow direction and the blue arrows mark the direction of the electron beam.

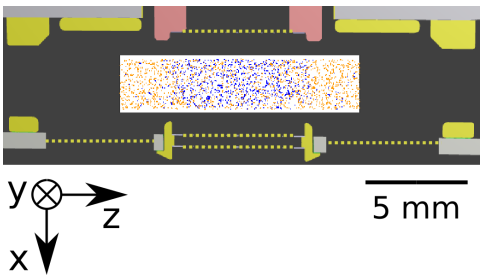

(a) Side view, thermal mode.

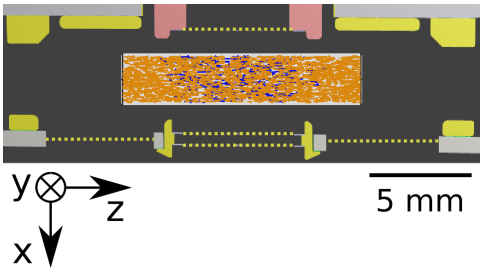

(b) Side view, neutral mode.

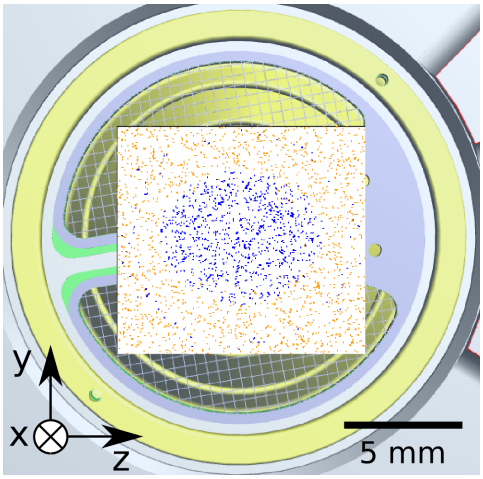

(c) Top view, thermal mode.

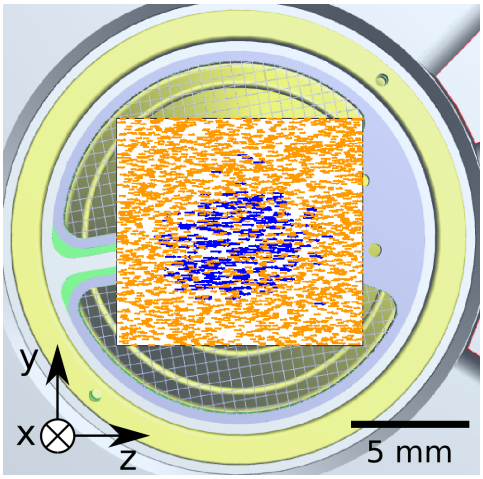

(d) Top view, neutral mode.

Figure 55: Simulated ions marked as small arrows starting at different positions in the ionisation region. The simulated ions in n-Mode have a velocity of 4 km/s whereas the simulated ions in th-Mode have thermal velocity. The blue ions reach the detector whereas the orange ions hit the structure during their flight to the detector.

can enter the ionisation region from every direction in the yz-plane except from where the filaments and the supporting structure are, resulting in a field-of-view of 300°. For the laboratory measurements, the gas inflow direction is from the bottom in the +y-direction as it is also shown in Fig. 52. For the simulations, a gas inflow direction parallel to the electron beam was chosen as it is marked in Fig. 54, bottom panel. The generated ions of the th-Mode and n-Mode were generated in a cuboid volume with a height of 2 mm and a square base area of 8x8 mm. For the simulations of the i-Mode, the base area was 20x20 mm because the ions are pulled with the outer extraction grid into the spectrometer.
Fig. 55 a) and c) show the simulated data for thermal mode where the incoming particles have thermal velocity. Fig. 55 b) and d) show the simulated data for the neutral mode and Fig. 56 shows the simulated data for ion mode where the incoming neutrals and ions respectively have a velocity of 4 km/s. The particles are displayed as velocity vectors. The ions marked in blue are the ones reaching the detector and the orange ones hit the structure somewhen during their flight to the detector. The simulated particles have unit masses from 1 up to 1000 m/z. Fig. 55 shows that only ions reach the detector that are generated directly above the inner extraction

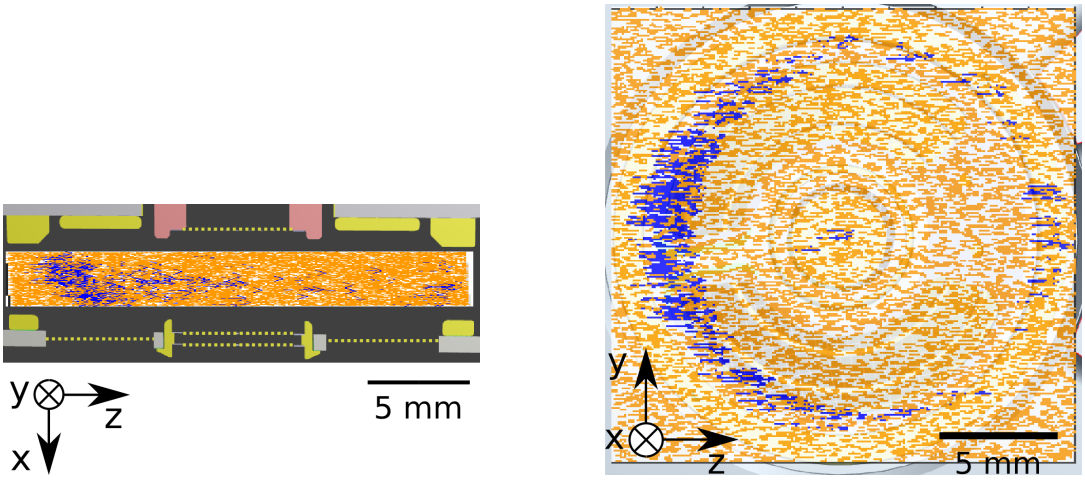

(a) Side view, ion mode.

(b) Top view, ion mode.

Figure 56: Simulated ions marked as small arrows starting at different positions in the entrance slit with a velocity of 4 km/s. The blue ions reach the detector whereas the orange ions hit the structure during their flight to the detector.

grid IS 5, which is also the one extracting the ions in thermal and neutral mode. In thermal mode, also some ions generated in the volume above the outer grid IS 6 reach the detector. They are visible as a small blue ring close to the structure separating the inner and the outer grid in Fig. 55c) c). In thermal mode the neutral particle flow comes through the pink structure and is directed over the inner pull grid. Therefore, only a small amount of gas reaches the outer grid. In neutral mode, only ions generated over the inner grid reach the detector due to their velocity perpendicular to the x-axis of the instrument. In ion mode, the ion optics are optimised for ions penetrating the ionisation region from the side as it is shown in Fig. 57. Due to their charge, ions react to the electric field as soon as they are close to the ion-optical lenses of the ionisation region. Their main starting position is therefore at the edge of the ionisation region and not in the centre as it is for the neutral particles. The ionisation of the neutral particles is optimised above the central extraction grid and therefore, most of the ions are generated above the inner extraction grid IS 5. When measuring with the ion mode, the ion-optical system is optimised for ions starting close the focusing lenses in the ionisation region as it is shown in the simulations in Fig. 57 and Fig. 56. The inner extraction grid is close to 0 V to additionally deflect the ions.
Fig. 58 and Fig. 59 show the flight path of the electrons, which are used to ionise the neutral gas. During vibration tests of the ion-optical system, a weakness in the structure of the ion source was identified. This lead to a small redesign where the opening for the electron beam in the entrance electrode IS 3 had to be enlarged (Fig. 58). Simulations were done to see how big the impact of that design adaption was. Fig. 58 bottom panel shows the old design with an additional ring to reduce the diameter of that hole and the top panel shows the new design without the ring in the entrance electrode. Dark blue lines are the flight paths of the electrons and light blue lines show the electric potential lines. The adaption of IS 3 had not impact on the flight path of the electrons. As previously discussed, the aim is to ionise the neutral particles

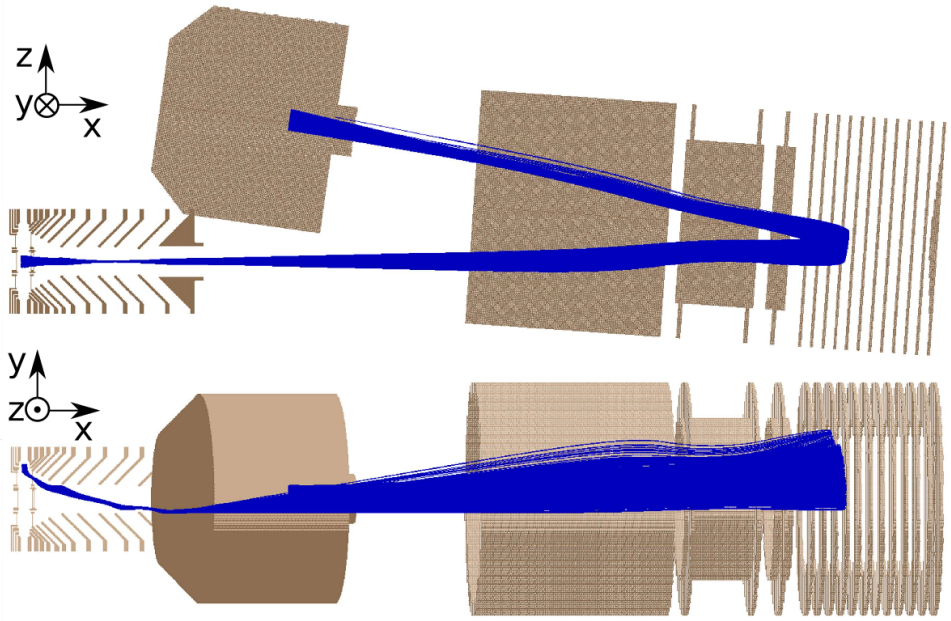

Figure 57: SIMION ion-optical model of the NIM prototype with ion trajectories in optimised i-Mode, arriving from the -y direction [31].

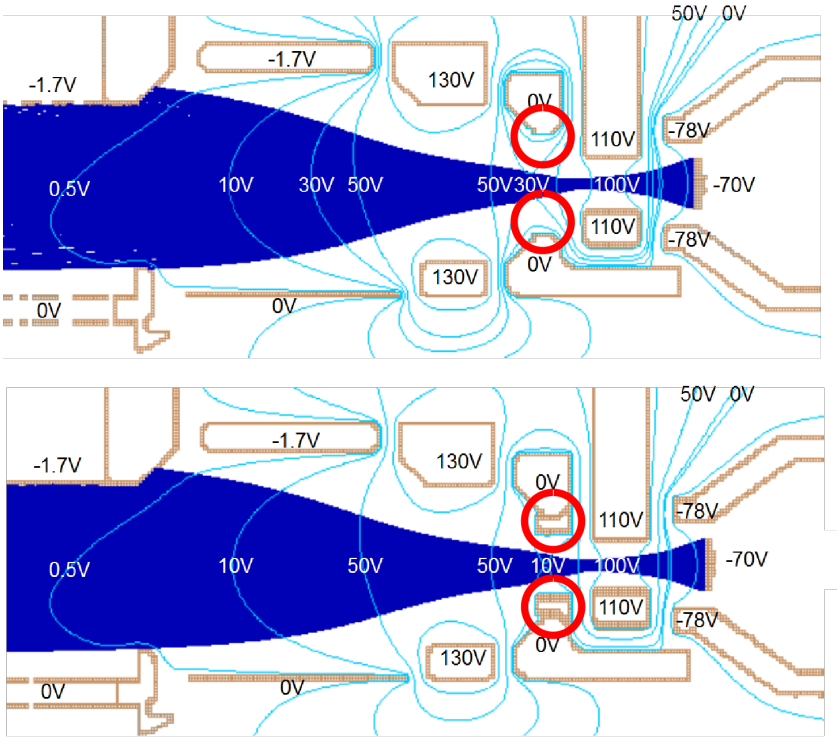

Figure 58: Top: New entrance with enlarged hole for the electron beam. Bottom: Old entrance with additional ring to reduce the diameter of hole.

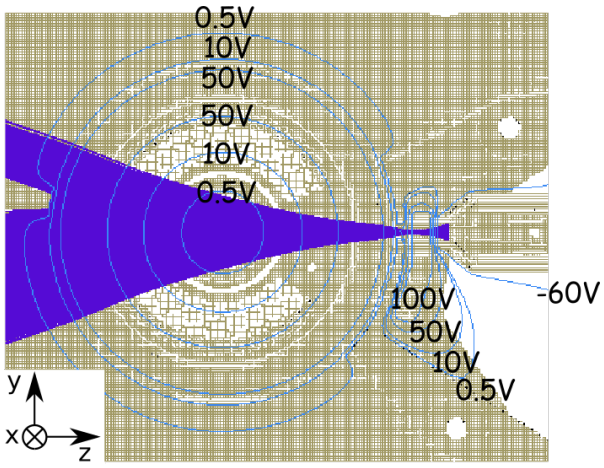

Figure 59: Top view onto the ionisation region of NIM with simulated electron beam trajectories (dark blue) and potential lines (light blue).

in the cylinder volume above the inner pull grid efficiently because only ions generated in this volume will reach the detector. Therefore, the electron beam should cover the whole cylinder volume. Fig. 59 shows the top view from the ionisation region. The porous ring structure is the outer extraction grid IS 6. The inner grid is not visible because it is covered by the electron beam. In this model, only one filament is displayed. Between the two potentials lines which mark the 50 V ring is electrode IS 4 which is on 130 V. Fig. 58 top and Fig. 59 show, that with the applied voltages the electron beam covers the whole volume over the inner extraction grid.

4.5. Shutter Performance Test

When measuring with the neutral gas channel, the aim is that the particles are measured directly without any interaction with the structure of the instrument. Therefore, a shutter between the antechamber and the ionisation region was required to close the particle entrance from the antechamber. In this section the performance of the shutter was tested. According to the model stated in Chap. 2.7 the closed shutter should attenuate the signal in the ionisation region generated by particles from the antechamber by a factor 600.
These tests were performed with the NIM PFM. The PFM was operated with laboratory electronics. The tests were performed at the CASYMIR test facility. The used particle beam consisted of hydrogen and xenon with a velocity of 2 km/s. Three different measurements were performed: One with the beam directed onto the antechamber with the shutter open, one with the shutter closed and a background measurement, where the particle beam was pointed onto the outer structure of NIM to estimate how much of the signal arises from the test gas scattering into the ionisation region when the beam is directed in an arbitrary direction. This background was subtracted from both signals before they were divided through each other to determine the attenuation factor G_{close} of the shutter.
The resulting attenuation factor of the shutter is 12 instead of the required 600 with a proper fabricated shutter. The biggest impact has the actual thickness of the gap between the shutter

and the antechamber when the shutter is closed. The reduction becomes significantly lower when the gap is bigger than actually designed. This is shown in Fig. 32 in Chap. 2.7. With a gap size of about 0.1 mm instead of 0.01 mm the attenuation factor is only about a factor 25. Other reasons are that the portion of the beam that scatters on the antechamber outer walls gets thermalised in the vacuum chamber and adds to the signal intensity in the neutral channel, which is estimated to contribute equally to the measured signal. In the outer space, the gas scatters on the antechamber but does not reach the ionisation region because it will flow around the instrument.

4.6. Pulser

The high-voltage pulse generator (pulser) is used to accelerate the generated ions in the ionisation region to a certain energy. During the time when no high voltage pulse is applied, the potential has to be stable at the bias voltage to allow ion storage as previously discussed in Chapter 2.4.
Fig. 60 shows a schema of a realistic high voltage pulse and Table 7 shows the characteristics of the flight pulser compared to the requirements. The fall time is the time to build up the negative high voltage on the extraction grid. This time has to be very short to give all ions the same amount of energy. When the fall time is long, low mass ions receive less energy resulting in a lower mass resolution for these species. A fall time of 1 ns leads to a 0.1 % lower mass resolution of hydrogen compared to an ion with mass 200 u. A fall time of 5 ns results in a reduction by 10 % (see Chap. 2.1). The fall time of the flight pulser is a bit longer than according to the specifications.

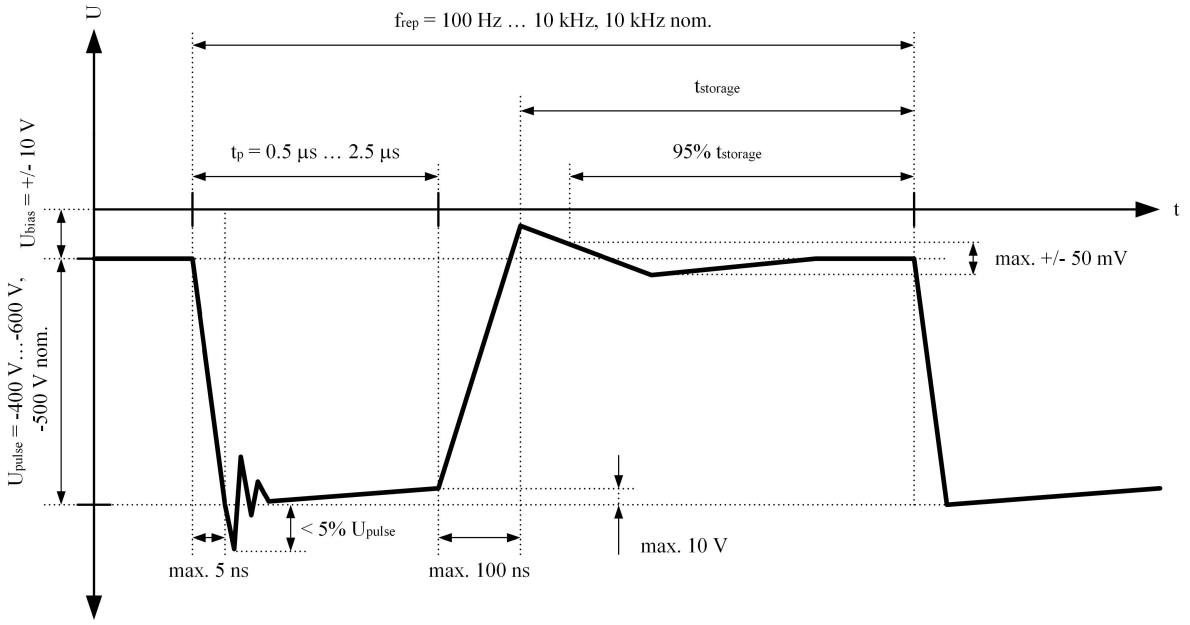

Figure 60: Specifications for the pulse shape generated by a realistic pulser [31].

	Ringing of HV Pulse	Pulse drop at full HV	Baseline Ripple	Fall Time	Rise Time
Requirement	$< 5\%$	< 10 V	± 50 mV	< 5 ns	< 100 ns
Flight Pulser	2.5%	1.9 V	300 mV	5.76 ns	19.7 ns

Table 7: Characteristics of the flight pulser compared with the requirements.

When applying a high voltage, the pulse overshoots its set value and drops slightly. The overshoot and the voltage drop result in a variation of the ion energy for the different species. The ringing of the high voltage, and the pulse drop of the flight pulser are within the specifications. The pulse duration has to be longer than 2 µs because that is the minimum time ions with masses of 1000 u need to leave the ionisation region. With some margin, the specifications were set to 5 µs. The rise time to bias voltage should be smaller than 100 ns to leave enough time for ion storage. This is well achieved with the flight pulser. The ripple of the bias voltage should be smaller than ± 50 mV to generate a stable electric field during the time when no high-voltage is applied on the extraction grid. A variation by ± 100 mV of the voltage of the electrode opposite of the pulser grid results in a visible variation of the signal intensity during manual optimisation with laboratory electronics. However, the baseline ripple of the flight pulser exceeds this value.

4.7. Detector Tests

This chapter describes the testing procedure of the flight detectors and shows the calibration results. The flight detectors consist of a flexible PCB (Printed Circuit Board) for the proximity electronics, accommodated within a PEEK housing for the MCPs (Chap. 3). Due to Jupiter's harsh radiation environment, the NIM detector has to be shielded with a tungsten copper shielding of about 1.1 kg. To minimise the shielding mass, a flex PCB was used to fold the detector with its proximity electronics into the small PEEK structure to minimise the detector volume. The detectors are tested in flat configuration with test MCPs and in folded configuration with flight MCPs (Fig. 61). The detectors were put in a vacuum chamber and baked out for 2 days. The conditioning was started one day after bake out when a residual gas pressure in the chamber lower than $5 \cdot 10^{-8}$ mbar was reached. Since the detector has lots of enclosed volumes, sufficient time for their evacuation has to be foreseen. The conditioning procedure is attached in the Appendix Chap. A.2. Depending on the outgasing behaviour of the detector, the conditioning took 2.5 to 4.5 h. After the conditioning, the measurements of the detector gain were performed.
Fig. 62, left panel shows the gain curves of two FS detectors in flat and folded configuration (see Fig. 61). The conditioning and the measurements in the folded configuration were done only up to lower voltages to minimise the usage of the potential flight MCPs. The gain of the MCPs depends on different factors. As described in Chapter 2.8 the MCP gain is a strong

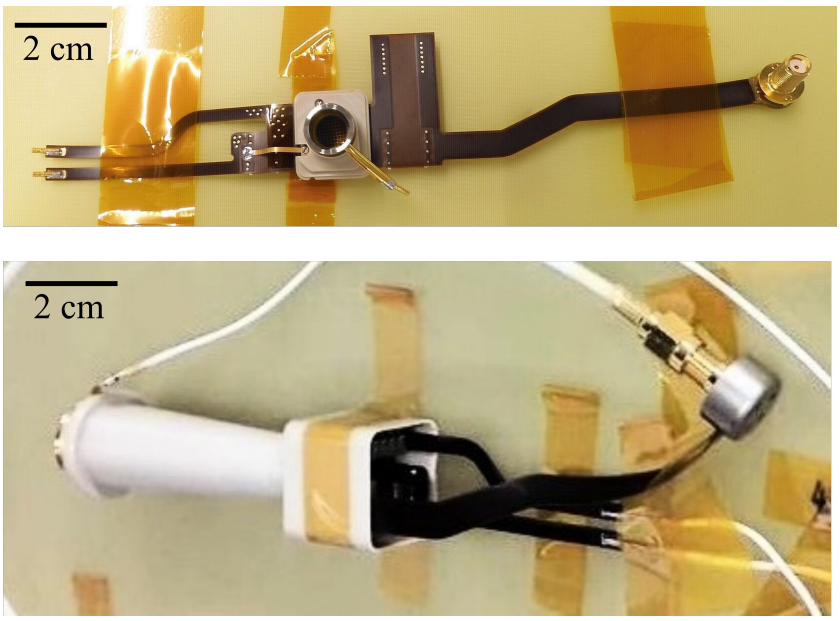

Figure 61: NIM flight detectors ready for tests. Top: flat configuration. Bottom: folded configuration.

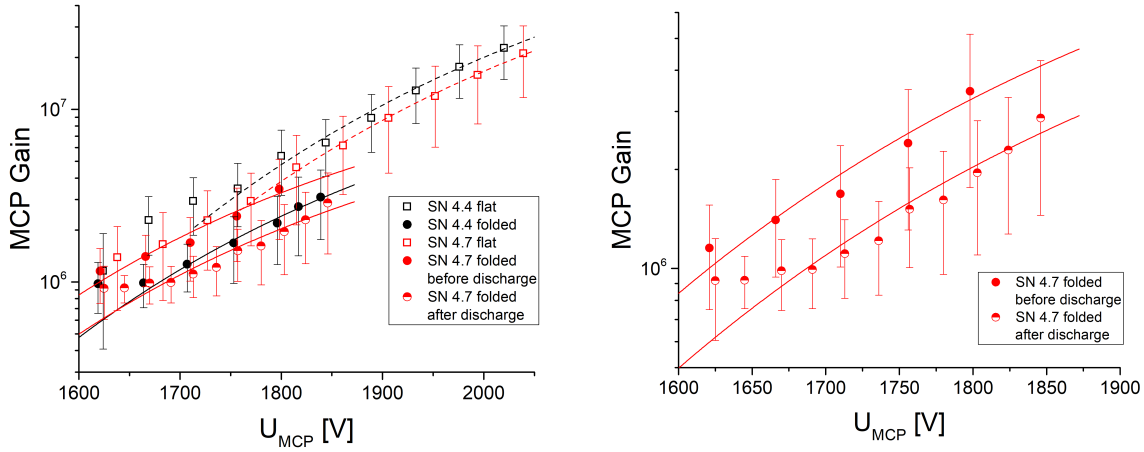

Figure 62: Left: Gain curves of two NIM FS detectors, in flat and in folded configuration (see Fig. 61). The difference in gain is because for each measurement curve, a different set of MCPs was used. Right: Gain curves of a folded NIM FS detector. The lower gain curve was recorded after a discharge at an MCP voltage of 1.8 kV.

function of the voltage applied over the MCPs as it is shown in Fig. 62. With usage given by the amount of the extracted charge from the MCPs, the MCPs degrade over time. This process depends on the residual gas pressure at which the MCPs are operated and the residual gas composition. The rapid decline in gain during the first few operation hours is a result of cleaning the channels mostly from water through operation (Fig. 63). When the MCPs were exposed to air, water and other substances deposit in the MCP channels. During operation, these deposits are sputtered from the channel surfaces, and thus the surface of the channels

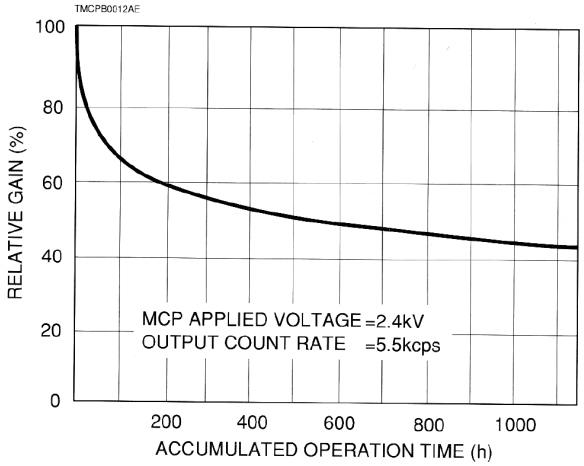

Figure 63: Relative gain of an MCP as a function of operation time [46].

.

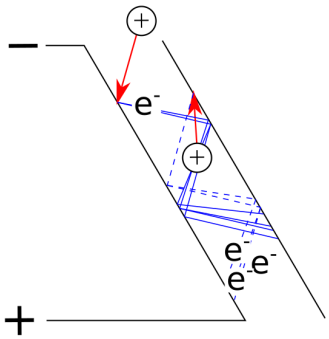

Figure 64: One single MCP channel when an ion triggers and electron avalanche. The ion in the channel centre is generated by the electrons when the gas pressure in the channel is too high.

are cleaned. After a few hours of operation, the gain reaches a plateau. In flat configuration detector SN 4.7 has a lower gain than SN 4.4 because its conditioning took longer than the conditioning of detector SN 4.4. Therefore it was cleaned better. In the folded state, SN 4.4 was 3 days longer in vacuum than SN 4.7 and had therefore more time to outgas. Fig. 62 right shows a zoom on the two measurement series of SN 4.7 both recorded in folded configuration. During the first measurement series, a discharge happened when the MCP voltage was at 1.8 kV. To amplify a signal, a minimal voltage has to be applied over the MCPs. When they are barely used, this voltage is in the range of 1.6 kV. During ageing, the decrease in gain can be compensated by increasing the MCP voltage. When an ion induces an electron avalanche, the electrons are freed in the channel and their main moving direction is towards the channel output because of the electric field applied over the MCPs (Fig. 64). If the local pressure in the MCPs is too high, the electrons ionise the gas in the channels and generate positive ions. These ions are accelerated back towards the MCP front and eject other electrons from the

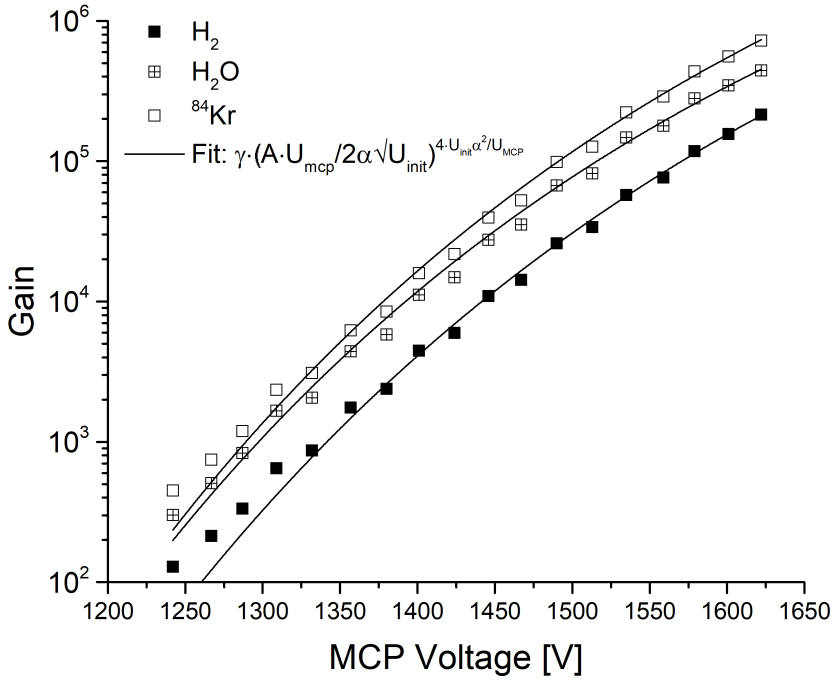

Figure 65: Gain curves of the detector SN 4.7 measured with the NIM FS ion-optical system.

channel walls triggering another electron avalanche. This process generates a plasma in the MCP channels destroying the channel coating. The process is stopped when the power supply is unable to provide the current and voltage to sustain the plasma. The triggered discharge leads to a signal reduction of about 30 % depending on at which voltage it appeared. The higher the MCP voltage was at the time of the discharge, the higher is the signal loss.
Fig. 65 shows the gain curve of detector SN 4.7 recorded when it was integrated into the NIM FS instrument. H_2 and H_2O are part of the residual gas and ^{84}Kr is the used test gas. The curves follow nicely the theoretical curve (see Chap. 2.8.1 Eq. (84)) by fitting U_{init} and A, where the initial energy of the released electrons U_{init} is about 4 eV, which is a typical value for secondary electron emission, and the prefactor A containing information about the interaction of the impinging electron with the electrons from the surface is 0.2 eV$^{-1/2}$. γ contains information about the probability to emit the first electron for the three species and is in the range of 0.1–10.
The NIM flight detector has a resistor built in between the MCPs and the anode to establish a potential difference to accelerate the electrons from the MCP exit towards the anode. The flight power supply sets the voltage between the MCP front and the anode U_{stack}. To determine the relation between the voltage over the MCPs U_{MCP} and the stack voltage U_{stack} a calibration was done with the laboratory power supplies.
The resistance of the MCPs is a weak function of the applied voltage, thus a fit to the MCP voltage of the form

$$U_{MCP} = a \cdot U_{stack}^2 + b \cdot U_{stack} \tag{102}$$

was necessary. Moreover, this fit allows for the extrapolation to higher U_{stack} values that have

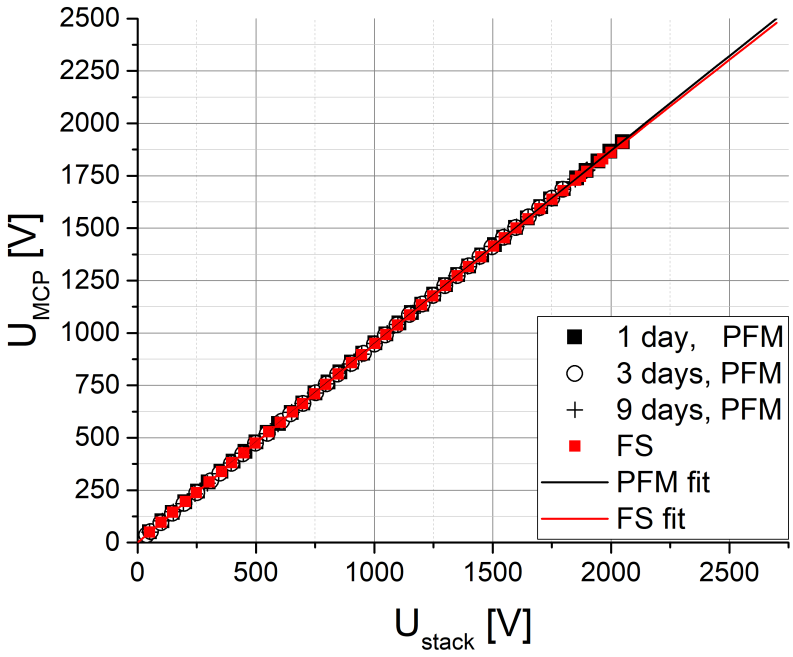

Figure 66: MCP voltage (U_{MCP}) as a function of the voltage applied between the MCP front and the anode (U_{stack}) for different measurement series with the PFM (black symbols) and the FS instrument (red squares) with the quadratic extrapolation.

	PFM	FS
a	$(-1.25 \pm 0.05) \cdot 10^{-5}$	$(-1.54 \pm 0.05) \cdot 10^{-5}$
b	0.96 ± 0.001	0.96 ± 0.001

Table 8: Fit parameters of the quadratic interpolation (Eq. (102)) for the calibration of the MCP voltage of the PFM and the FS detector.

not been tested. Fig. 66 shows the results of that calibration for the PFM and the FS detector with an extrapolation up to 2.4 kV for the MCP voltage. 2.4 kV is the upper voltage limit of the MCPs according to the manufacturer. The fit parameters for Eq. (102) are given in Table 8. The MCPs in the two detectors have similar resistances, which is the reason why the measurement data of the two detectors overlap. For the PFM detector, a longer measurement campaign was done to characterise the PFM instrument (Chap. 4.8.1). During that campaign, this curve was recorded frequently every time the instrument was turned on. The resistance did not change significantly during the short time of the measurement campaign.

4.8. Instrument performance tests

This chapter shows performance results of the NIM PFM and the NIM FS instrument. Most results were conducted when the two instruments were operated with laboratory electronics because there was only very limited time to calibrate the two instruments as whole units.

4.8.1. Proto Flight Model

Description of the Mass Spectrometer for the Jupiter Icy Moons Explorer Mission

Martina Föhn
University of Bern, Physics Institute
Sidlerstrasse 5
3012 Bern
martina.foehn@space.unibe.ch

André Galli
University of Bern, Physics Institute
Sidlerstrasse 5
3012 Bern
andre.galli@space.unibe.ch

Audrey Vorburger
University of Bern, Physics Institute
Sidlerstrasse 5
3012 Bern
audrey.vorburger@space.unibe.ch

Marek Tulej
University of Bern, Physics Institute
Sidlerstrasse 5
3012 Bern
marek.tulej@space.unibe.ch

Davide Lasi
University of Bern, Physics Institute
Sidlerstrasse 5
3012 Bern
davide.lasi@space.unibe.ch

Andreas Riedo
University of Bern, Physics Institute
Sidlerstrasse 5
3012 Bern
andreas.riedo@space.unibe.ch

Rico G. Fausch
University of Bern, Physics Institute
Sidlerstrasse 5
3012 Bern
rico.fausch@space.unibe.ch

Michael Althaus
University of Bern, Physics Institute
Sidlerstrasse 5
3012 Bern
michael.althaus@space.unibe.ch

Stefan Brüngger
University of Bern, Physics Institute
Sidlerstrasse 5
3012 Bern
stefan.bruengger@space.unibe.ch

Philipp Fahrer
University of Bern, Physics Institute
Sidlerstrasse 5
3012 Bern
philipp.fahrer@space.unibe.ch

Michael Gerber
University of Bern, Physics Institute
Sidlerstrasse 5
3012 Bern
michael.gerber@space.unibe.ch

Matthias Lüthi
University of Bern, Physics Institute
Sidlerstrasse 5
3012 Bern
luethi@space.unibe.ch

Hans Peter Munz
University of Bern, Physics Institute
Sidlerstrasse 5
3012 Bern
hanz-peter.munz@space.unibe.ch

Severin Oeschger
University of Bern, Physics Institute
Sidlerstrasse 5
3012 Bern
severin.oeschger@space.unibe.ch

Daniele Piazza
University of Bern, Physics Institute
Sidlerstrasse 5
3012 Bern
daniele.piazza@space.unibe.ch

Peter Wurz
University of Bern, Physics Institute
Sidlerstrasse 5
3012 Bern
peter.wurz@space.unibe.ch

Abstract—**The JUpiter ICy moons Explorer (JUICE) of the European Space Agency (ESA) will investigate Jupiter and its icy moons Europa, Ganymede and Callisto, with the aim to better understand the origin and evolution of our Solar System and the emergence of life. The Neutral gas and Ion Mass spectrometer (NIM) is one of six instruments of the Particle Environment Package (PEP) on board the JUICE spacecraft. PEP will measure neutral atoms and molecules, the ion population, and the electron population over an energy range covering from meV to MeV. The NIM instrument is designed to measure the chemical and isotope composition of the exospheres of three of Jupiter's satellites, the icy moons, both, during several flybys and during its final destination in Ganymede orbit. From measurements of the exosphere, we will derive the chemical composition of the surface, which will allow us a better understanding of the icy moons formation processes, interaction processes with the magnetospheric plasma and energetic particles of Jupiter's magnetospheric system.**

The NIM instrument is a compact time-of-flight mass spectrometer allowing measurements of thermal neutral molecules and ionospheric ions. To minimize the background radiation on the detector and protect electronics against the harsh radiation environment around Jupiter, elaborated radiation shielding was designed. NIM consists of two major subunits, namely, the ion-optical system and the electronics.

This study presents details on the technical design and the results obtained from the calibration campaigns of different subsystems of the flight instrument including a mass range of m/z 1 to 650, a mass resolution $m/\Delta m$ of at least 750 (FWHM), and an instantaneous dynamic range of almost 6 decades. These results are discussed in detail with respect to the scientific requirements. This performance in combination with its radiation tolerance allows for both a detailed analysis of the chemical composition of Jupiter's icy moons' exospheres and ionospheres, and to explore environments, where formation of life might be possible.

978-1-7281-7436-5/21/$31.00 ©2021 IEEE

TABLE OF CONTENTS

1. INTRODUCTION

The Neutral gas and Ion Mass spectrometer (NIM) is part of the Particle and Environment Package (PEP) on board the JUpiter ICy moons Explorer (JUICE). JUICE will investigate Jupiter, its radiation environment, and its icy moons Ganymede, Europa and Callisto as potential habitable worlds. The JUICE satellite will launch in June 2022 and will arrive in the Jupiter system in October 2029. It will start with an investigation of Jupiter's atmospheric structure and composition and its fast rotating magnetic field. During this time, JUICE will perform several flybys at Callisto and Ganymede followed up by two flybys at Europa. Europa has a young icy surface with a liquid water ocean beneath touching its silicate mantel. The main objective of the two flybys at Europa is to investigate Europa's non-ice components and its recently active areas, to determine the chemical composition of its exosphere, and its subsurface ocean. After the flybys at Europa, JUICE will use gravity assistance of Callisto to investigate Jupiter's atmosphere at high latitudes. During the flybys at Callisto, JUICE will take measurements of Callisto's internal structure, surface and exosphere. JUICE will then transfer to Ganymede, where it will take a global geological map of Ganymede's surface and investigate the local plasma environment in regards to the interaction of Ganymede's magnetic field with the magnetic field of Jupiter. The nominal mission will end in June 2033 by crashing the spacecraft on Ganymede [1].

PEP, as part of JUICE's scientific payload, consists of six instruments measuring electrons, ions and neutral particles in the energy range of 0.001 eV – 1 MeV to characterize Jupiter's and the moons' plasma environment [2]. NIM will be the first instrument to take in situ measurements of the chemical composition of the icy moons' exospheres. Their exospheres consist of particles released from their surface by ion bombardment, sublimation and photon interaction. With the in situ measurements, we will get a better understanding of the formation processes of the moons' exospheres and surfaces. In addition, we will get information about the surface compositions by the sputtered atoms and molecules.

In this contribution, we provide an overview covering different instrument components such as the ion optical system and the electronics, and present the results obtained on key performance studies such as ion storage capability, sensitivity, and mass resolution of the NIM ion-optical system. All the performance tests presented in this paper were conducted with the laboratory electronics, as the flight electronics was in production.

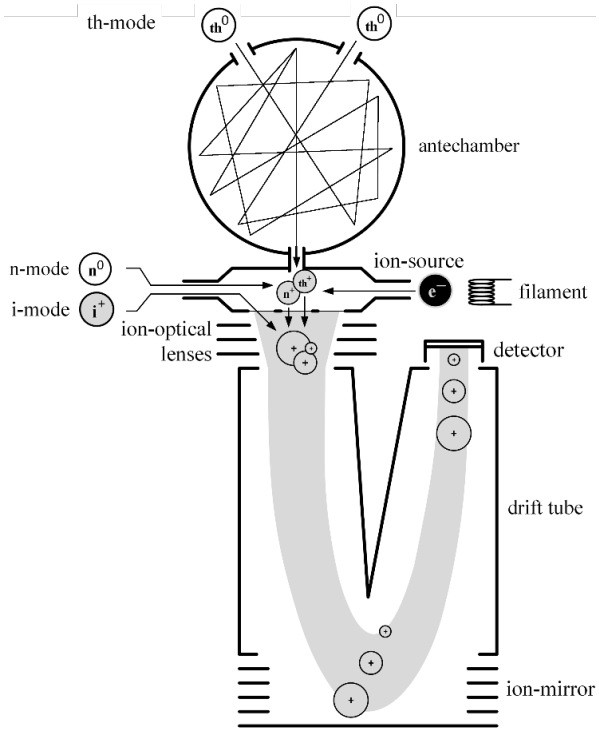

Figure 1. Schematics of the NIM ion-optical system.

Planetary Protection Concept of JUICE

The purpose of planetary protection is to prevent forward contamination of other celestial bodies with terrestrial life forms, and to ensure that future scientific investigations related to the origin of life are not compromised. In addition, it includes a policy for the protection of the Earth from extraterrestrial life carried by a spacecraft from interplanetary sample return missions. There exist five different planetary protection categories for space missions reflecting the level of interest and concern in regards to contamination [3].

The JUICE satellite will perform two flybys at Europa. These flybys are in the Planetary Protection category III because Europa contains a liquid water ocean with a young surface with active areas. JUICE had to demonstrate that the probability of a collision with Europa is below 10^{-4} or had to undergo active bioburden reduction. JUICE will be sterilized by the high radiation flux in the Jupiter system and has therefore not to take any further precautions regarding planetary protection [4].

Ganymede contains, like Europa, a liquid water ocean under a thick ice shell. In contrast to Europa, the liquid water ocean at Ganymede is trapped between two ice layers. The high pressure in the depth generates the lower ice layer [5]. Ganymede has a very old surface (100 million to 2 billion years) and did not show any activity in the recent past although it has some brighter regions where it shows rift valleys and ridges generated by intense surface stresses and

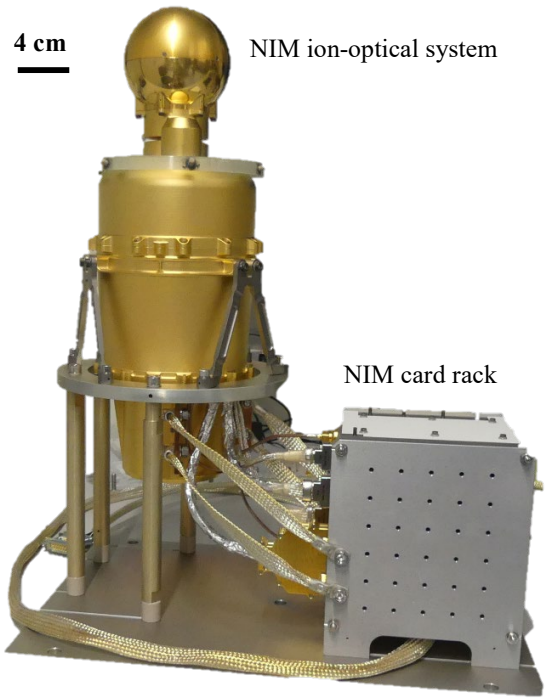

Figure 2. NIM ion-optical system with electronic box (card rack) attached.

subsequent cryovolcanism [6]. JUICE had to show that the likelihood for an organism to reach Ganymede's subsurface ocean is lower than 10^{-4}. The probability of landing in an active region on Ganymede's surface is about $2 \cdot 10^{-3}$. The probability of organisms to survive the cruise phase (10^{-1}), to survive the high radiation dose in Jupiter's orbit (10^{-1}) and the transport on to the surface (10^{-2}), the low probability of the burial mechanism (10^{-4}) reduces all together the total likelihood down to 10^{-11} of a biological contamination on Ganymede's surface. By assuming a typical bioburden of 10^6, which is a nominal value for a standard cleanroom environment, the requirements of 10^{-4} are met by a factor of five [4].

The current flight path of JUICE to Jupiter uses gravity assist of Earth, Mars and Venus. The flyby at Mars is in the Planetary Protection category III and the flyby at Venus is in category II. JUICE showed, that the probability of contamination of these two bodies is below 10^{-2} [4].

2. Design and Methods

NIM is a time-of-flight (TOF) mass spectrometer based on the design of our previous TOF instruments such as RTOF/ROSINA/Rosetta [7, 8], P-BACE/MEAP [9] and NGMS/Luna-Resurs [10, 11]. Compared to other mass spectrometer types, TOF mass spectrometers allow measuring the complete chemical fingerprint of a sample instantaneously instead of scanning over the mass range. This way, a much better spatial resolution during flybys can be obtained, compared to scanning mass spectrometer types such as quadrupole and magnetic sector instruments.

The mass resolution $R = m/\Delta m$ is calculated by $R = t_{tof}/2\Delta t$ where t_{tof} is the time-of-flight of an ion and Δt is the full width at half maximum (FWHM) of the recorded mass signal peak. The longer the drift path is, the longer the drift time t_{tof} will be, which typically results in a better mass resolution. Size limitations of the instrument limit the drift path length. Therefore, NIM uses in addition an ion mirror to almost double the drift path length. Furthermore, the mass resolution is improved by the energy focusing accomplished by the ion mirror [12]. The further possibility to increase the mass resolution would be to reduce Δt by improving the ion-optics for focusing of the ions on the detector.

The signal-to-noise ratio (SNR) is another key parameter in mass spectrometry and is defined as the signal peak height I_{sig} divided by the standard deviation of the noise level I_{noise}: $SNR = I_{sig}/std(I_{noise})$. We designed NIM to measure complex chemical compounds up to masses of 1000 u with a mass resolution up to $m/\Delta m$ 1000 and a SNR exceeding 6 decades [13], although based on present knowledge we do not expect masses higher than 100 u to be observed. The high mass resolution is required to distinguish between different mass peaks at high unit masses. Moreover, for a time-of-flight instrument the SNR is directly proportional to the mass resolution because improvements in the mass resolution are accomplished by improving time focusing and keeping all the ions at the mass line. In the laboratory, we are able to measure the residual gas in the vacuum chamber at a base pressure of a few 10^{-10} mbar. With a SNR of 6 decades, we are able to record partial pressure down to 10^{-16} mbar, which is the detection limit of such an instrument for an integration time of 5 seconds [10]. The highest exospheric pressure from the moons to be measured by NIM during the JUICE mission is in the range of 10^{-8} mbar [14]. NIM's sensitivity is sufficiently high to conduct sensitive chemical measurements at such a low pressure.

The NIM instrument underwent further miniaturization with respect to its predecessor instruments such as NGMS/Luna-Resurs: Whereas the NGMS instrument draws 23 W power in nominal operation [11], NIM will draw 18.5 W of power at maximum. The NIM ion-optical system weighs 3.13 kg where about 48 % of the mass is shielding material of the MCP detector to reduce noise induced by a high flux of energetic electrons accelerated by Jupiter's strong radiation environment. The harsh radiation environment also leads to a special design of the electronics and the detector. The detector has to be very small to minimize the amount of shielding material.

The NIM instrument is divided into two major parts: the ion-optical system and the control electronics (Figure 2). The ion-optical system consists of the actual ion source, the focusing optics, the ion mirror, and the detector (Figure 1). The control electronics consists of five electronic boards hosting low- and high-voltage power supplies, the filament- and motor-controller, the high voltage pulser and two field-programmable gate arrays (FPGAs). The FPGAs control the voltage outputs to the NIM ion-optical system,

they readout and preprocess the detector output signal, and communicate over a data processing unit (DPU) with the spacecraft (S/C).

NIM Ion Optical System

Particle Entrances—NIM allows measurements of neutral atoms and molecules and ionospheric ions. NIM has two entrances: a closed source entrance through an antechamber with a field-of-view (FoV) of 10/3 π sr to thermalize neutral particles, and an open source entrance with a FoV of 300° in azimuth and 10° in elevation angle for neutrals and ions (Figure 1). The antechamber thermalizes incoming neutrals by decelerating them within the interior of the sphere via multiple bounces with the chamber wall. This technique yields also to the particle density enhancement and subsequently an increase of the ion signal intensity while these atoms and molecules pass the ion source [15]. The antechamber's inner surface has to be chemically inert to inhibit chemical alterations of the gases to be measured. This measuring mode is called thermal mode (th-mode). The open source is defined by an entrance slit where neutral particles and ions directly enter the ionization region, without any interaction with the surface structure of the ion source. When measuring with the open source, a shutter closes the flight path between the antechamber and the ion source, to prevent particles collected by the antechamber from entering the ionization region. Incoming neutrals are ionized with an electron-emitting thermionic filament. This measuring mode is called neutral mode (n-mode). When measuring ions the mode is called ion mode (i-mode).

Filaments—NIM uses electron impact ionization with a typical electron energy of approximately 70 eV. Two redundant thermionic emitters provide the electrons in the NIM instrument. We found that BaO and Y_2O_3e filaments are most suitable for our application in NIM with preference to the latter ones [16]. The Y_2O_3e filaments have been designed in cooperation with *Kimball Physics, Wilton, USA*. Compared to the standard Y_2O_3 filaments produced by *Kimball Physics*, the Y_2O_3e filaments used for this application have an increased thickness of the Y_2O_3 coating for increasing their lifetime to 10,000 h operation time. In comparison, the BaO filaments under test have an expected lifetime of about 6,000 h [16]. The heating wires connecting the electron-emitting disc with the filament base of the Y_2O_3e filaments are longer than the wires of the standard Y_2O_3 filaments. Thus, the electron-emitting disc is better thermally decoupled from the filament base, which results in a reduced heat loss, and thus lower power consumption.

Because of the more delicate filament assembly design regarding the mechanical robustness, a few of the filament assemblies of the set of life-time test units were shock- and vibration-tested during the lifetime test for simulation of the transportation to space. The performance of these filaments was compared with the performance of not shocked or vibration tested filaments. Both sets of filaments showed similar performances in terms of power consumption required to reach the target emission and aging behavior. In addition, our life-time tests revealed that the higher temperature needed for Y_2O_3e to emit electrons compared to BaO may have compromised one of the electron beam guiding electrodes (repeller electrode) such that metallic whiskers grew between the repeller electrode and the filament causing a short circuit. Therefore, the material used for the repeller electrode was changed from stainless steel to

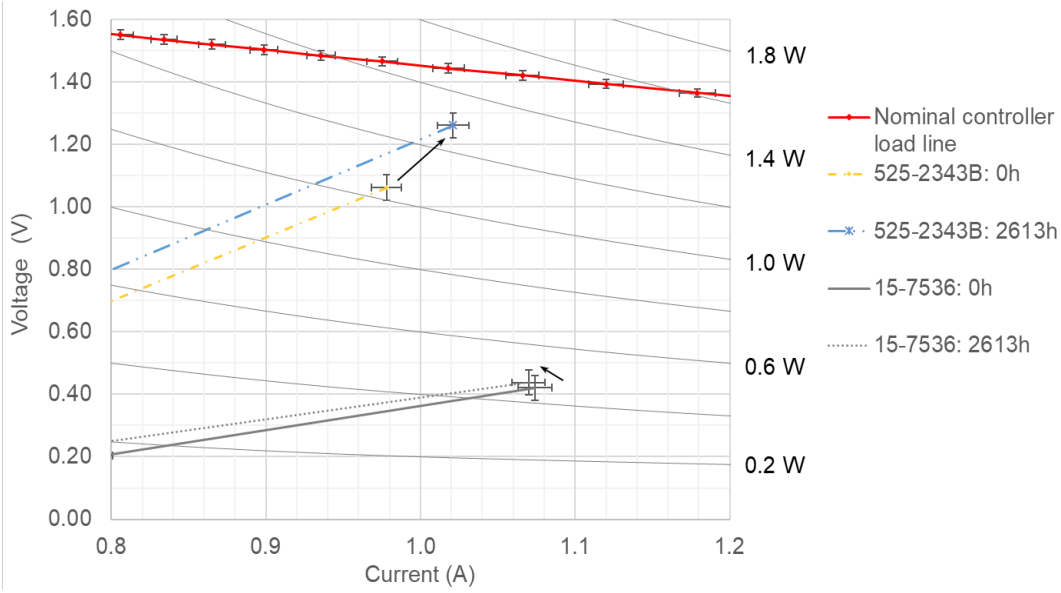

Figure 3. Electrical characteristics of a selected Y_2O_3e (525-2343B) and BaO (15-7536) filament and the Proto Flight filament controller board (Nominal controller load line). The curve for the Proto Flight controller board shows its maximal I-V capabilities at nominal supply voltage of 12.0 V. Hyperbolas in the background show the power levels [16]. Curves for the filaments show the theoretical and measured performance of one BaO and one Y_2O_3e filaments when virgin and after 2613 h of operation.

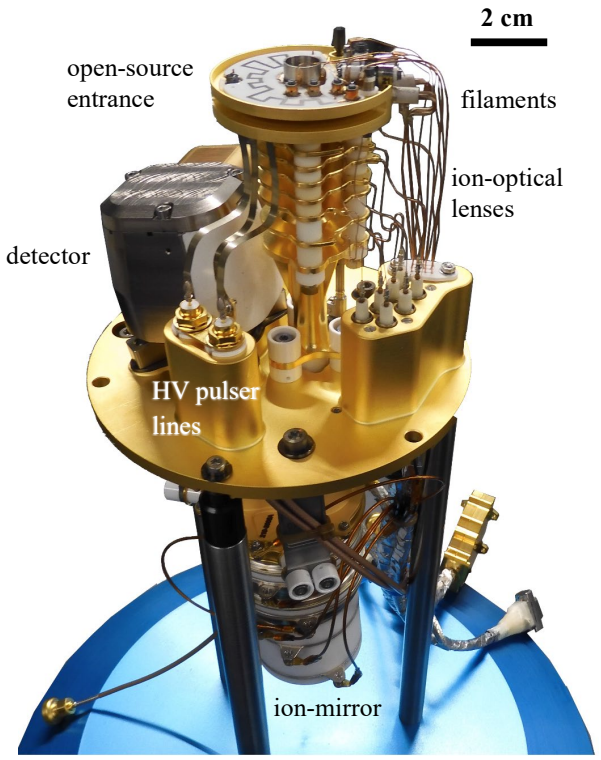

Figure 4. The NIM ion-optical system without the closed-source antechamber.

titanium for the NIM Proto Flight Model (PFM) as titanium is more temperature robust than stainless steel.

Figure 3 summarizes the electrical characteristics of a BaO, an Y_2O_3e filament and the PFM controller board at nominal operation voltage of 12 V DC. The two filaments were operated at a nominal emission current of 50 µA with commercial filament controller boards from *Spacetek Technology AG, Switzerland*. BaO (15-7536) draws less power than Y_2O_3e (525-2343B). The nominal operation time of NIM is about 2,000 h. The power for both filaments can always be provided for both types of filaments.

BaO filaments are known to suffer cathode poisoning when exposed to residual gases such as oxygen [17]. When BaO filaments are exposed to air, a carbonate layer is forming on top of the BaO surface. Therefore, the BaO cathodes have to be activated to get rid of this carbonate layer after every air exposure. The activation procedure is tedious and not favorable for a component used for space instrumentations although this procedure only had to be done once after the spacecraft reaches outer space. However, during calibration and testing in preparation for flight, this is a major complication. Y_2O_3(e) filaments are not affected by residual gas and no complicated conditioning procedure is required after air exposure. Therefore, they are better suited for such applications and the use in laboratory devices.

For the NIM sensor, we decided to use the Y_2O_3e instead of the BaO filaments. Because the Proto Flight filament controller board is able to provide power for the Y_2O_3e filaments, even when they have a higher power consumption than the BaO filaments. The longer lifetime and the simpler conditioning procedure of the Y_2O_3e filaments favor them over the BaO filaments.

Ion Optical System—Produced ions get extracted with a high voltage (HV) pulser creating a pulse with a repetition rate of 10 kHz. An ideal pulse would have a very short fall time of about a ns down from a static voltage bias of the order of volts to the negative extraction high voltage to give all extracted ions the same amount of energy. Ions leaving the ion source before the high voltage pulse is fully applied get less energy resulting in an energy spread and therefore induce a lower mass resolution [18]. Low mass ions have higher velocities at the same energy and leave the ion source faster than high mass ions. Therefore, they are more affected by an insufficiently fast fall time of the extraction pulse than high mass ions.

To allow storage of ions during the time between two extraction pulses, the electrodes in the ion source are kept on very stable potentials. Otherwise, only ions generated during application of the HV extraction pulse pass into the TOF section. Every ion produced but not stored during the time when no extraction pulse is applied, is lost. The ions that are lost onto the drift path produce additional electrical noise by the detector signal and decrease the sensitivity of the instrument [19]. Ion storage is essential for NIM to increase its capabilities while conducting measurements in an environment with pressure limits of 10^{-8} mbar down to 10^{-16} mbar. The ions extracted from the ion source are focused with 7-element ion-optical lenses and fly through the drift tube to the ion-mirror. The ion-mirror is used to increase the flight distance and for energy focusing of the ions.

During the vibration test in November 2019, the ion-source broke due to a bad brazing joint between the last electrode of the ion source and the drift tube, leading to a redesign of the ion-source [20]. In the new design, the electrodes of the ion-source are held together with tree screws with ceramic insulators between the electrodes (Figure 4). A similar design was already used in the NIM prototype.

Detector—The ions are detected with a high-speed Multi-Channel-Plate (MCP) detector. Each ion generates a short current pulse of about 0.5 ns pulse width, inducing a voltage signal of about 5-100 mV on the 50 Ω input of the front-end electronics. This short pulse width requires fast readout electronics with a sample frequency of 2 GHz. The MCP detector has an impedance-matched anode to minimize signal reflections at the cable interfaces [21].

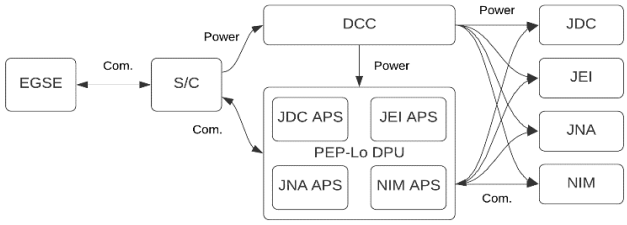

Figure 5. Schematics of the power and communication paths (Com.) between the Electrical Ground Support Equipment (EGSE) and the NIM instrument.

The NIM Electronics

Figure 5 shows a schematic drawing of the communication and power lines from the Electrical Ground Support Equipment (EGSE) to the NIM instrument. Commands from the EGSE are sent to the S/C. The S/C provides power to the DC-DC-Converter (DCC) that provides power for all four instruments indicated in Figure 5. For NIM, the DCC provides five different low voltages. The S/C provides 18.5 W for NIM [13] including 20 % margin. With a power conversion efficiency of the DCC of 72.5 %, the resulting net power consumption of the NIM instrument is 10.7 W. The communication of NIM with the S/C is via a DPU shared with the three other PEP-Lo instruments. The DPU contains hardware interface drivers and builds the interface for the application software (APS) of the different instruments. The APS handles the tele-commands from the spacecraft, prepares and sends the telemetry packages from the different instruments [22]. The DPU communicates over Low Voltage Differential Signaling (LVDS) with NIM. NIM has two FPGAs: a RTSX (Radiation-tolerant Antifuse-based FPGA) and a static random-access memory (SRAM) based Virtex-4.

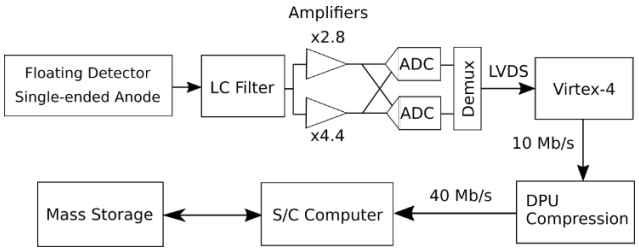

Figure 7. Detector signal path.

To start the NIM instrument, the APS commands the RTSX to load an image of the Virtex-4 from a magnetoresistive random-access memory (MRAM) to the Virtex-4. As soon as the Virtex-4 is started, the RTSX goes into bridge mode, i.e., commands from the DPU addressed to the Virtex-4 pass directly through. The Virtex-4 controls the different low- and high-voltage supplies (see Figure 6) and it is responsible for high-speed data processing by preparing the incoming detector signal. Due to the low on-chip memory capacity (BRAM) of this particular FPGA type, it is important to forward the measured data fast to the DPU for data compression and then further to the S/C mass memory.

Figure 7 shows the signal path of the detector signal. The analog raw signal from the detector is low-pass filtered (antialiasing) and fed into two different amplifiers. Depending on the signals expected amplitude, either the signal from the first or the second amplifier is fed into the two analog-to-digital converters (ADCs). Each ADC has a sampling rate of 1 GS/s resulting in a sampling rate of 2 GS/s when using both ADCs in interleaved mode. The sampled signal is transmitted to the Virtex-4, which generates the actual science data package. It adds information needed to

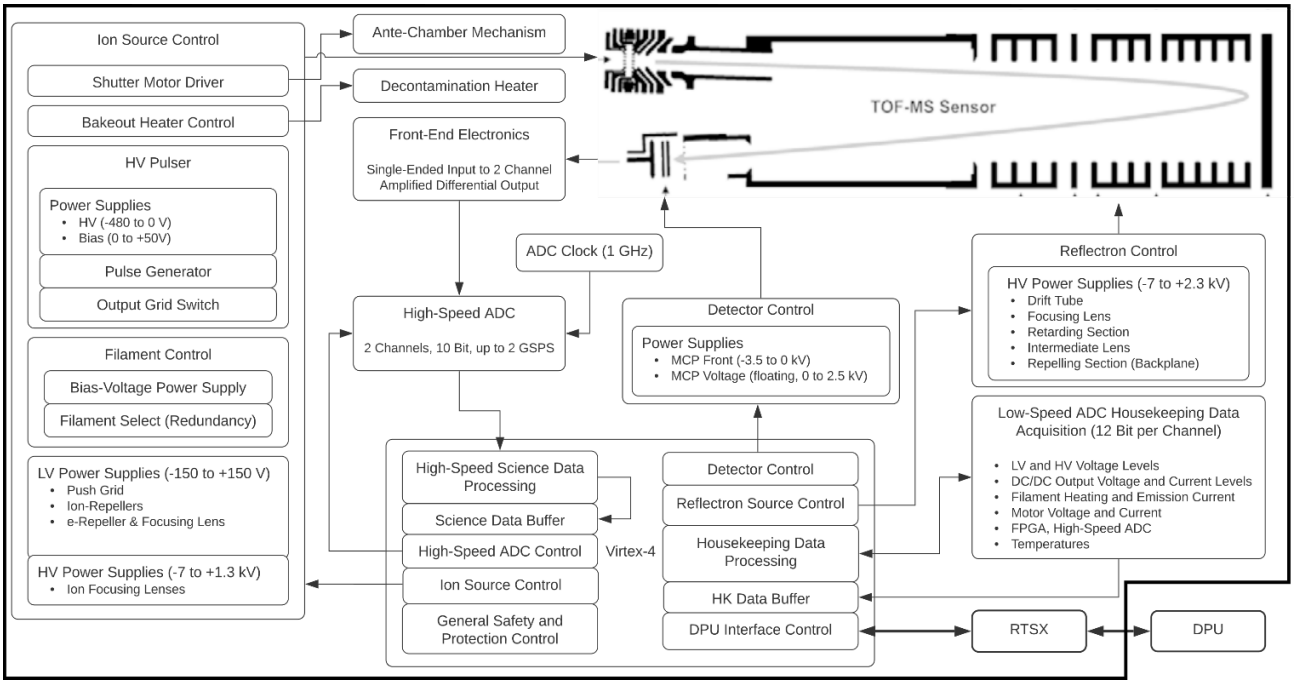

Figure 6. The NIM electronics control schematics.

evaluate the science data such as the emission current of the electron-emitting filament, the used voltage set, data acquisition time, etc., and forwards the data packages to the DPU.

Radiation Protection Concept

Jupiter has a harsh radiation environment mainly consisting of high energetic protons and electrons in the energy range of 0.01 – 50 MeV with a radiation flux of $10^6 – 10^7$ cm^{-2} sr^{-1} s^{-1} MeV^{-1} [23]. Protons are about two orders of magnitude less abundant than electrons and protons are easier to shield because their penetration range in matter is shorter than for electrons. Therefore, we focused the radiation shielding design on shielding against high energetic electrons. This can be done by using dense materials with a high proton number Z to slow down the electrons. These materials have the side effect that the fast electrons produce bremsstrahlung as secondary radiation when decelerated, which has also to be blocked. The production of bremsstrahlung increases with the proton number of the shielding material. For this purpose, we used a tungsten copper alloy as shielding material, which consists of Cu as a low Z material to slow down the electrons and W as high Z material to block the produced bremsstrahlung.

To prevent the NIM electronics from radiation damage, the electronic boards are in a special vault, the card rack, shared with the electronics of other PEP-Lo instruments. The card rack wall consists of 2 mm tungsten copper alloy, keeping the total ionization dose (TID) over the mission of the electronics below 100 kRad including a safety factor of 2 [20]. Components used in electronic circuits were selected by their sufficiently high radiation hardness. The shielding of cables are grounded to inhibit charging. For the FPGAs design we decided to use one radiation hard, one-time programmable (RTSX) and one radiation tolerant, reprogrammable (Virtex-4) FPGA. The radiation mitigation approach for the Virtex-4 follows the following concept: to correct bit flips induced by single event upsets (SEU) caused by the ionizing radiation, the RTSX frequently scrubs the Virtex-4 configuration, i.e. the RTSX overwrites the Virtex-4 configuration SRAM with the image stored in MRAM. In addition, triple-mode redundancy (TMR) and BRAM error correction codes (ECC) are implemented for the most critical functions executed by the Virtex-4, such as control loops for high-voltage cascades and filament current, safety limit checks, etc.

The most critical part in the ion-optical system is the MCP detector. High energetic electrons and ions increase the noise background, which leads to a lower sensitivity of the instrument. Without shielding, the count rate is about 10^5 counts/sec resulting in 10 counts per single waveform in Europa's radiation environment. To reduce the shielding volume of the detector, we used a flex printed circuit board (PCB) to fold the detector proximity electronics inside a small volume. Extensive simulations were done to get the optimal shielding design. The design was tested at the *High Intensity Proton Accelerator Facility, PSI Villigen, Switzerland* [24, 25, 26]. The detector shielding consists of an aluminum housing of 1 mm thickness covered by a 10 mm tungsten copper shielding. The outer shell of the NIM ion-optical system consists of 1 mm AlBeMet, a material consisting of aluminum and beryllium. In addition, a 6 mm tungsten copper shielding disc array is positioned behind the ion-mirror opposite the detector entrance to shield against radiation entering the detector directly. With this shielding concept, the noise level induced by radiation could be reduced by a factor of 100 [26].

As we verified the radiation shielding design of the detector, no further tests with the actual PFM detector are planned [24, 25, 26]. Radiation tests with the flight hardware would expose the flight hardware and detector to a siginifcant radiation dose before launch. Most likely, the sensor would have to remain a the radiation facility until the detector material activated during the test is no longer radioactive. This would be incompatible with the current schedule because the PFM sensor was delivered for integration onto the spacecraft in December 2020.

Measurement Conditions

All measurements were performed in a vacuum chamber with a chamber pressure of $1 \cdot 10^{-8}$ mbar or lower. The tests were done in the CASYMIR test facility located at the University of Bern [27]. CASYMIR is able to generate a neutral gas beam with velocities up to 5.5 km/s by heating the gas to a temperature of 600°C. The average beam velocity depends on the gas temperature and the mean molecular mass of the gas. To reach higher beam velocities, the amount of the carrier gas H_2 relative to the test gas has to be increased. CASYMIR has a gas inlet system to inject gases directly into the chamber with a leak valve to increase the chamber pressure with the test gas. For measurements where a neutral gas beam was used, the beam consisted of H_2 and Kr with a ratio of 20:1 unless otherwise mentioned. The chosen beam velocity was 2 km/s because that is the velocity of the S/C in Ganymede orbit, which will be 90% of the measuring time of the NIM instrument. All measurements were performed with the NIM PFM ion-optical system with the laboratory electronics attached.

3. RESULTS AND DISCUSSION

In this chapter, we discuss different performance tests of the NIM PFM ion-optical system. We also discuss the ion storage capability of the ion source subsequently followed by performance results of the ion optical system ($m/\Delta m$, SNR, mass range).

Ion Storage Capability

Ion storage during the time between two extraction pulses is essential to increase the sensitivity of the NIM instrument. Ion storage is facilitated by properly shaping the electron beam used for ionization [19]. We tested the ion storage capability for th-mode and n-mode of the ion-optical system with a neutral gas beam. The chamber pressure was

$(2 – 5) \cdot 10^{-9}$ mbar. The electron emission current I_{em} was varied in the range from 40 – 400 µA. When changing the electron emission current, the electric potential distribution in the ion source changes. Therefore, we optimized the low voltage electrodes in the ion source for each data point. Especially the backplane electrode opposite to the ion extraction grid changed significantly between 0 and –3.8 V depending on the voltage set and the electron emission current. In Figure 9, the corresponding electrode was set to -1.7 V. To focus the electron beam, this electrode had to be set to a more negative voltage the higher the electron emission current was applied. The electron beam holds the ions in the two spatial dimensions orthogonal to the electron propagation. In the dimension of the electron flight path, the ions are kept by the electric field generated by the low-voltage electrodes. These electrodes are in our source at around 130 ± 20 V depending on the electron emission current. They generate a strong positive field ring in the plane of the ion extraction grid and trap the ions in the direction of the electron flight path. Figure 9 shows the electric field with a sample voltage set of the ion source.

Figure 8 shows the measured data for the collected ion signal as a function of electron emission current. The data were fitted with a linear function for data points between 0 and 100 µA and with a quadratic function for emission currents higher than 100 µA. Kr was part of the neutral gas beam and H_2O was part of the residual gas inside the vacuum chamber. Up to 100 µA, the signal increases linearly with the emission current proportionally to the increase in electron current, and no ions are stored for I_{em} below 100 µA. Above 100 µA emission current, the signal intensity increases with a power law I_{em}^n with n between 2 and 3. Thus, the ion source shows an ion storage capability for all gases. When the emission current is increased from nominal 100 µA to 300 µA, we gain a factor of 3 in signal intensity directly from the current increase. Due to the ion storage capability, we gain an additional factor of 4 resulting in 12 times higher

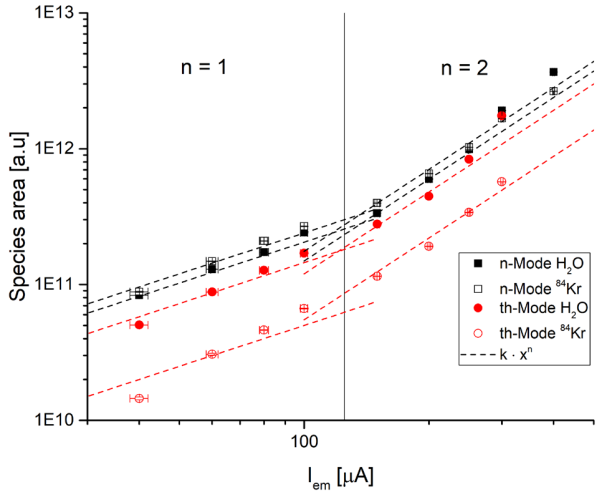

Figure 8. Ion storage capability of the NIM instrument for n-mode and th-mode. A neutral gas beam consisting of H_2 and Kr was used. H_2O was part of the residual gas.

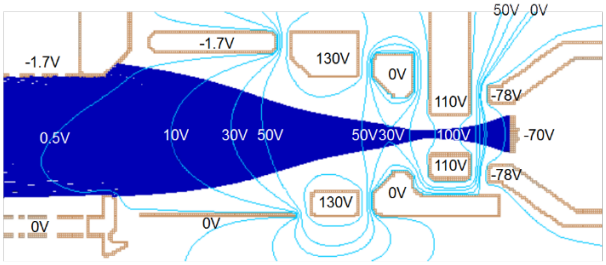

Figure 9. Ion source with sample voltage set applied the electrodes. In light blue are the potential lines and in dark blue simulated electron beam.

signal intensity when increasing the emission current by a factor of 3 as a proposed high sensitivity mode.

Ion storage is expected in the th-mode only, because the neutral atoms and molecules enter the ionization region perpendicular to the electron beam at thermal energies. The NIM instrument has a specially designed ion-source to store ions also in the n-mode. The generated ions in the n-mode have an initial velocity along the direction of the electron beam. The particular configuration of the ion repelling ring electrodes serves for the latter confinement of the ions produced inside this potential ring (electrodes with voltage +130 V in Figure 9). Atoms and molecules entering the ion-source with a velocity between 1 and 8 km/s and a mass between 1 and 100 u have a maximum kinetic energy of 33 eV and are easily trapped in this field configuration. For the Europa flyby where the S/C velocity is 4 km/s, masses up to 1000 u reach a kinetic energy of 80 eV and are therefore trapped in the potential field. The electric field also widens and defocuses the electron beam. Simulations with the software *SIMION from Scientific Instrument Services Inc. version 8.1.3* show, that the applied electric field focuses the electron beam (Figure 9) and makes ion storage possible also for ions entering the ion source in the direction of the electron flight path as it is observed in the n-mode.

Density enhancement behavior of the antechamber

Atoms and molecules enter the ionization region either directly through the open source entrance or they enter first the antechamber, where they get thermalized before they enter the ionization region. The total number density n_{tot} in the ionization region is the sum of particles entering the ionization region through the closed source entrance n_{cs} and particles entering the ionization region directly via the open source n_{os}. With the test facility, we are only able to direct the neutral gas beam through one of the two entrances at a time. Therefore, the total number density in the ionization region is equal to the contribution of the closed source. n_{cs} is then:

$$n_{cs} = n_a \sqrt{\frac{T_a}{T_s}} \frac{F(S)\, k\, \sin^2(\omega/2)\, \cos^2(\omega/2)}{1 - k \cos^2(\omega/2)} \frac{d_i^2}{d_i^2 + d_s^2} \qquad (1)$$

$$F(S) = e^{-S^2} + \pi^{1/2}\, S\, (1 + \mathrm{erf}(S))$$

$$S = v_{sc} \cos\chi \sqrt{\frac{m}{2k_B T_a}}$$

Where n_a is the number density of the neutral gas beam, T_a is the ambient gas temperature corresponding to the temperature of the neutral beam. T_s is the ion source temperature, k is the probability of a molecule being re-emitted after colliding with the surface. $k \approx 1$ for the gases we used for calibration. ω is the cone half-angle of the open source, d_i the opening diameter of the antechamber, d_s the diameter of the exit hole to the ion source. v_{sc} is the spacecraft velocity corresponding to velocity of neutral gas beam, χ the angle of the spacecraft with respect to the surface normal of the entrance aperture, m the mean molecular mass of the gas beam and k_B the Boltzmann-constant. With increasing spacecraft velocity v_{sc}, the number density in the ionization region has to increase when measuring with the closed entrance [28, 15].

To test this behavior, the neutral particle intensity was measured for different beam velocities. The beam velocity was varied by changing the mass ratio of H_2 to Kr in the neutral gas beam. This corresponds to a variation of the mean molecular mass of the beam and therefore to a variation in the beam velocity. The data in Figure 10 are pressure and flux corrected to take into account the decreasing signal intensity of Kr with increasing beam velocity due to the lower amount of Kr in the beam compared to H_2.

The measured data follow nicely the theoretical model for the two test gases. With H_2 and Kr we covered the main mass range of interest because Kr has a mass of 84 u. Earlier tests showed that the isotopic ratio of molecules measured with the antechamber are similar to the fragmentation pattern measured when molecules enter via the open source [28]. This indicates that no additional fragmentation happens in the antechamber due to collisions and chemical interactions of the molecules with the antechamber inner walls. Therefore, we successfully verified the proper functionality of the antechamber.

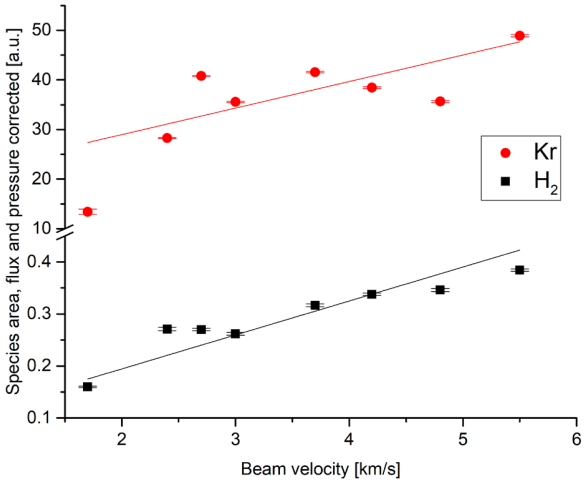

Figure 10. Signal intensity measured with the closed source antechamber in dependence of the velocity with H_2 and Kr as test gases.

Mass Range

NIM is supposed to measure masses up to 1000 u [4]. In the moons' exospheres, we only expect masses up to 100 u, unless something completely unexpected is present. However, with the ability to measure up to higher mass ranges, we will be able to measure also potential organic compounds with high masses up to 1000 u [29]. The calibration gas perfluoropheneanthrene (CAS nr. 306-91-2, chemical formula $C_{14}F_{24}$) was used to verify the performance of NIM to measure heavy species. Perfluoropheneanthrene breaks up into many fragments with different unit mass up to 624 u, the parent mass, when ionized with an electron beam, making it a common calibration substance for TOF mass spectrometers. The liquid test substance was heated to bring it into the gas phase. The gas was injected into the chamber with a leak valve set so that the chamber pressure increased to $6.6 \cdot 10^{-8}$ mbar. The filament emission current was set to 420 µA and the MCP voltage was set to 1.9 kV. Figure 11 shows the recorded mass spectrum, featuring mass peaks over the entire spectrum range. The mass with the lowest signal intensity tabulated by the manufacturer is mass 624 u, which is clearly visible in our mass spectrum. We even see a clear mass peak at 642 u, which is not tabulated by the manufacturer but results from a water adduct to the parent molecule.

Mass Resolution

According to the requirements stated in [20], NIM has to reach a mass resolution $m/\Delta m$ of 500 but to distinguish between different species of masses up to 1000 u, a mass resolution of 1000 is required. In addition, the previously built instrument at our institute, the NGMS instrument from

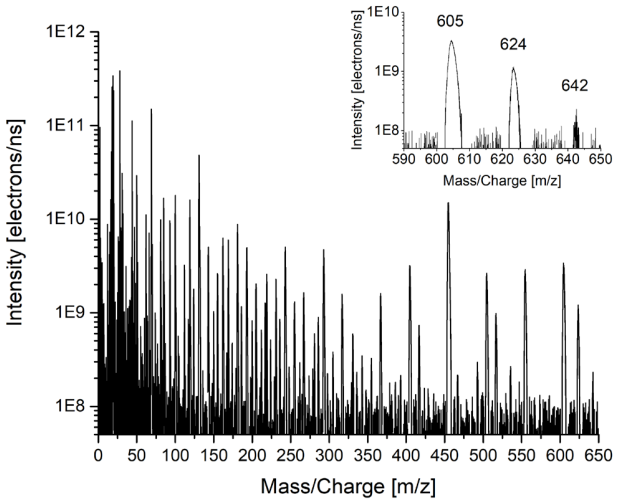

Figure 11. Mass spectrum recorded with NIM with FC5311 as calibration gas. Tabulated masses are up to 624 u. Highest mass recorded is 642 u. Chamber pressure was $6.6 \cdot 10^{-8}$ mbar. The filament emission current was 420 µA the MCP voltage was 1.9 kV.

the Luna-Resurs mission, reaches a mass resolution of 1000 [11]. Our aim for the NIM instrument is to achieve the same or a better performance than NGMS. Figure 12, left panel, shows a mass spectrum measured with the th-mode and Figure 12, right panel, shows a mass spectrum recorded with the n-mode. We used a neutral gas beam consisting of H_2 and Kr. The electron emission current for the th-mode was 60 µA and 100 µA for the n-mode. The mass spectra were recorded during the ion storage calibration campaign.

The peaks at *m/z* 85 and 87 are artifacts generated by the readout electronics. These peaks appear after mass peaks with a high signal intensity and start with a down slope before reaching their maximum. The ^{78}Kr isotope is barely above the noise level in the mass spectra due to the low electron emission current used for both measurements (see Figure 12). The Kr mass peaks appear slightly below their integer mass number due to the preliminary mass calibration. The peak shapes of the ^{78}Kr peaks are similar to the peak shape of the other Kr peaks. The small peak at m/z 78.66 in the th-mode spectrum could only be a triply charged species. In this case, also the single and double charged peaks of that species have to be visible because they are easier to detect, which is not the case. Therefore, we can conclude that this peak is a noise peak. The peak at m/z 79 is most likely noise.

The mass resolution for ^{84}Kr in the th-mode is *m/Δm* 757 (FWHM) and the mass resolution in the n-mode is *m/Δm* 534 (FWHM). The mass resolution in the n-mode is readily lower than the mass resolution measured in the th-mode because the incoming particles have a significant initial kinetic energy and they have to be deflected by 90° in the ion source to pass them into the drift tube. In the th-mode particles enter the ion-source straight and are therefore easier to accommodate and focus towards the detector system. Both modes fulfill the mission science requirements by having a mass resolution *m/Δm* higher than 500 but the mass resolution is smaller than the mass resolution we want to achieve. With the actual flight electronics, we expect to reach a higher mass resolution.

There is an additional aspect of the mass resolution in relation to the signal-to-noise ratio (SNR). In a TOF mass spectrometer, the mass resolution is established by focusing the ion packets in time and not by reducing the phase space of the ions like in other mass spectrometers (e.g. sector magnet instruments). Thus, for a higher mass resolution the peaks become higher and narrower which directly improves the SNR. Moreover, since the peaks become narrower, the contribution by noise becomes less since fewer time bins in the TOF spectrum are affected, which adds to the improvement in SNR. In summary, even if the high mass resolution is not needed for the spectral separation of species, every improvement in mass resolution improves the SNR in a TOF mass spectrometer.

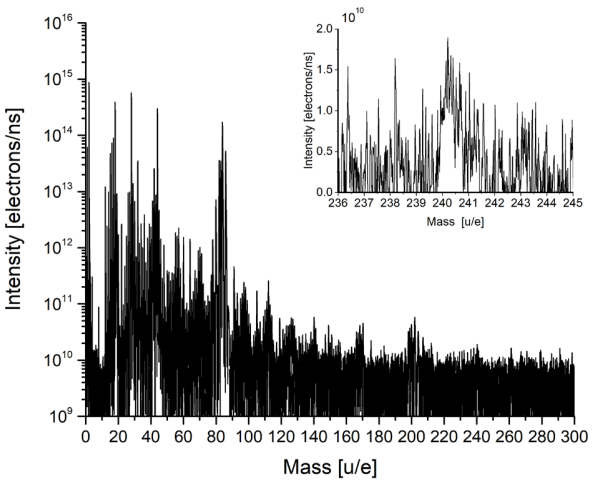

Figure 13. Mass spectrum recorded with NIM's th-mode showing a SNR of almost 6 decades.

Signal-to-Noise Ratio

The expected particle density of Europa's exosphere at a height up to 10'000 km above the moon's surface is in the range of 10 – 10^8 cm^{-3} [14], which corresponds to a pressure of 10^{-15} – 10^{-8} mbar. The closest distance the S/C will have to the moon's surface will be 400 km [30]. To conduct optimal measurements of Europa's exosphere, NIM has to achieve a SNR of about six decades. The tests were performed at a pressure of 10^{-9} mbar. The electron emission current was set

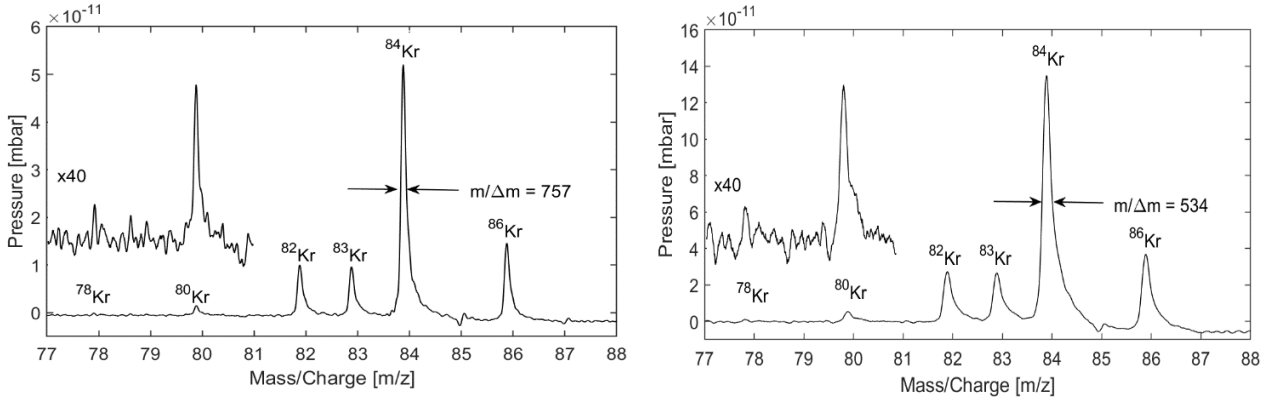

Figure 12. Two mass spectra recorded using NIM with a neutral gas beam consisting of H_2 and Kr with a ratio of 20:1. Left: Kr recorded in th-mode. The electron emission current was 60 µA. Right: Kr recorded in n-mode. The electron emission current was 100 µA.

to 400 µA in this study and we measured with a neutral gas beam. Figure 13 demonstrates the maximum SNR we were able to measure until now with the NIM ion-optical system. In the th-mode NIM reaches a SNR of almost 6 decades comparing the hydrogen peak and the peak at mass 240 u. This peak is a hydrocarbon peak originated from the residual gas compounds present in the vacuum chamber.

The SNR and the mass resolution depend on the proper focusing of the ions on the detector. The areas under the mass signal peaks are proportional to the number of detected ions of the corresponding mass peak. A better focusing of the ions on the detector leads to narrower and higher mass peaks because the area under the peaks stays the same. Therefore, a better focusing of the ions improves both the mass resolution and the SNR. The NIM ion-optical system has 19 focusing electrodes to be optimized and laboratory tests are still under investigation to improve the voltage set to reach higher performance.

4. SUMMARY

We introduced the NIM instrument electric structure and functionality including its connection to the spacecraft. We presented also the measurement results obtained with the NIM flight ion-optical system with laboratory electronics attached. We demonstrated a mass range of 642 u and a mass resolution of $m/\Delta m$ 750 (FWHM) for the th-mode and of $m/\Delta m$ 530 (FWHM) for the n-mode. NIM has a dynamic range of almost 6 decades and a good ion storage capacity.

NIM fulfills the requirements regarding mass resolution and dynamic range, although there the instrument will be further optimized during the cruise phase when optimizing the voltage sets applied to the electrodes of the ion optical system. The PFM was delivered for integration onto the JUICE spacecraft in December 2020. In early January 2021, the first tests of the whole instrument with flight electronics attached will start. These tests will be performed with the flight spare model.

ACKNOWLEDGMENTS

This project is supported by the Swiss Space Office through the ESA PRODEX program and by the Swiss National Science Foundation. The authors would like to thank also the many contributors at the University of Bern. Special thanks are to H.R. Elsener of EMPA for the invaluable collaboration. Moreover, we acknowledge the support of the PEP team, in particular: S. Karlsson (IRF), S. Jaskulek (JHU/APL), and S. Barabash (IRF).

REFERENCES

[1] O. Grasset, M. K. Dougherty, A. Coustenis, E. J. Bunce, C. Erd, D. Titov, M. Blanc, A. Coates, P. Drossart, L. N. Fletcher, H. Hussmann, R. Jaumann, N. Krupp, J.-P. Lebreton, O. Prieto-Ballesteros, P. Tortora, F. Tosi and T. Van Hoolst, "JUpiter ICy moons Explorer (JUICE): An ESA mission to orbit Ganymede and to characterise the Jupiter system," *Planetary and Space Science,* vol. 78, pp. 1-21, 2013.

[2] S. Barabash, S. Karlsson, M. Wieser, P. Brandt, J. Westlake, P. Wurz and M. Fränz, "Radiation mitigation in the Particle Environment Package (PEP) sensors for the JUICE mission," *European Planetary Science Congress,* vol. 10, 2015.

[3] COSPAR, "COSPAR Policy on Planetary Protection," 17 June 2020.

[4] H. Hussmann, P. Palumbo, R. Jaumann, M. Dougherty, Y. Langevin, G. Piccioni, S. Barabash, P. Wurz, P. Brandt, L. Gurvits, L. Bruzzone, J. Plaut, J.-E. Wahlund, B. Cecconi, P. Hartogh, R. Gladstone, L. Iess, D. J. Stevenson and Y. Kaspi, JUICE JUpiter ICy moons Explorer Exploring the emergence of habitable worlds around gas giants around gas giants, European Space Agency, 2014.

[5] O. Grasset, E. Bunce, A. Coustenis, M. K. Dougherty, C. Erd, H. Hussmann, R. Jaumann and O. Prieto-Ballesteros, "Review of Exchange Processes on Ganymede in View of Its Planetary Protection Categorization," *Astrobiology,* vol. 13, pp. 991-1004, 2013.

[6] G. Collins und T. V. Johnson, «Chapter 37 - Ganymede and Callisto,» in *Encyclopedia of the Solar System (Third Edition)*, Elsevier, 2014, pp. 813 - 829.

[7] H. Balsiger, K. Altewg, P. Bochsler, P. Eberhardt, J. Fischer, S. Graf, A. Jäckel, E. Kopp, U. Langer, M. Mildner, J. Müller, T. Riesen, M. Rubin, S. Scherer, P. Wurz, S. Wüthrich and E. Arjis, "Rosina – Rosetta Orbiter Spectrometer for Ion and Neutral Analysis," *Space Science Reviews,* vol. 128, pp. 745-801, 2007.

[8] S. Scherer, K. Altweg, H. Balsiger, J. Fischer, A. Jäckel, A. Korth, M. Mildner, D. Piazza, H. Reme und P. Wurz, «A novel principle for an ion mirror design in time-of-flight mass spectrometry,» *International Journal of Mass Spectrometry,* Bd. 251, pp. 73-81, 2006.

[9] D. Abplanalp, P. Wurz, L. Huber, I. Leya, E. Kopp, U. Rohner, M. Wieser, L. Kalla and S. Barabash, "A neutral gas mass spectrometer to measure the chemical composition of the stratosphere," *Advances in Space Research,* vol. 44, no. 7, pp. 870-878, 2009.

[10] P. Wurz, D. Abplanalp, M. Tulej and H. Lammer, "A neutral gas mass spectrometer for the investigation of lunar volatiles," *Planetary and Space Science,* vol. 74,

no. 1, pp. 264-269, 2012.

[11] R. G. Fausch, P. Wurz, M. Tulej, J. Jost, P. Gubler, M. Gruber, D. Lasi, C. Zimmermann and T. Gerber, "Flight electronics of GC-mass spectrometer for investigation of volatiles in the lunar regolith," *2018 IEEE Aerospace Conference,* pp. 1-13, 2018.

[12] B. A. Mamyrin, V. I. Karataev, D. V. Shmikk and V. A. Zagulin, "The mass-reflectron, a new nonmagnetic time-of-flight mass spectrometer with high resolution," *Zh. Eksp. Teor. Fiz.,* vol. 64, pp. 82-89, 1973.

[13] H. Andersson, P. Wurz, P. Brandt, S. Jaskulek and S. Barabash, "PEP EID- B (SE-01)," University of Bern, Bern, 2020.

[14] A. Vorburger and P. Wurz, "Europa's Ice-Related Atmosphere: The Sputter Contribution," *Icarus,* vol. 311, 2018.

[15] P. Wurz, A. Balogh, V. Coffey, B. K. Dichter, W. T. Kasprzak, A. J. Lazarus, W. Lennartsson and J. P. McFadden, "Calibration Techniques," ISSI Scientific Report Series, 2007.

[16] R. G. Fausch, "Mass Spectrometry for In Situ Planetary Research," University of Bern, Bern, 2020.

[17] H. Friedenstein, S. L. Martin and G. L. Munday, "The mechanism of the thermionic emission from oxide coated cathodes," *Reports on Progress in Physics,* vol. 11, no. 1, pp. 298--341, 1947.

[18] P. Wurz, *Lecture Notes Mass Spectrometry and Ion Optics,* Bern, 2017.

[19] D. Abplanalp, P. Wurz, L. Huber and I. Leya, "An optimised compact electron impact ion storage source for a time-of-flight mass spectrometer," *International Journal of Mass Spectrometry,* vol. 294, no. 1, pp. 33-39, 2010.

[20] D. Lasi, S. Meyer, D. Piazza, M. Lüthi, A. Nentwig, M. Gruber, S. Brüngger, M. Gerber, S. Braccini, M. Tulej, M. Föhn and P. Wurz, "Decisions and Trade-Offs in the Design of a Mass Spectrometer for Jupiter's Icy Moons," *2020 IEEE Aerospace Conference,* pp. 1-20, 2020.

[21] P. Wurz and L. Gubler, "Impedance-matching anode for fast timing signals," *Review of Scientific Instruments,* vol. 65, no. 4, pp. 871-876, 1994.

[22] M. Gruber, P. Gubler, M. Lüthi, P. Wurz and D. Lasi, "PEP-Lo NIM Instrument SW Design Document (ISDD)," 2017.

[23] H. D. Evans, E. J. Daly, P. Nieminen, G. Santin and C. Erd, "Jovian Radiation Belt Models, Uncertainties and Margins," *IEEE Transactions on Nuclear Science,* vol. 80, no. 4, pp. 2397-2403, 2013.

[24] H. Wojtek, L. Desorgher, K. Deiters, D. Reggiani, T. Rauber, M. Tulej, P. Wurz, M. Luethi, K. Wojczuk and P. Kalaczynski, "High Energy Electron Radiation Exposure Facility at PSI," *Journal of Applied Mathematics and Physics,* vol. 2, pp. 910-917, 2014.

[25] M. Tulej, S. Meyer, M. Lüthi, D. Lasi, A. Galli, D. Piazza, L. Desorgher, D. Reggiani, W. Hajdas, S. Karlsson, L. Kalla and P. Wurz, "Experimental investigation of the radiation shielding efficiency of a MCP detector in the radiation environment near Jupiter's moon Europa," *Nuclear Instruments and Methods in Physics Research Section B Beam Interactions with Materials and Atoms,* vol. 383, pp. 21-37, 2016.

[26] D. Lasi, M. Tulej, S. Meyer, M. Lüthi, A. Galli, D. Piazza, P. Wurz, D. Reggiani, H. Xiao, R. Marcinkowski, W. Hajdas, A. Cervelli, S. Karlsson, T. Knight, M. Grande and S. Barabash, "Shielding an MCP Detector for a Space-Borne Mass Spectrometer Against the Harsh Radiation Environment in Jupiter's Magnetosphere," *IEEE Transactions on Nuclear Science,* vol. 54, no. 1, pp. 605-613, 2017.

[27] S. Graf, K. Altweg, H. Balsiger, A. Jäckel, E. Kopp, U. Langer, W. Luithardt, C. B. Westermann and P. Wurz, "A cometary neutral gas simulator for gas dynamic sensor and mass spectrometer calibration : Space simulations in laboratory: Experiments, instrumentation, and modeling," *Journal of Geophysical Research,* vol. 109, 2004.

[28] S. Meyer, M. Tulej and P. Wurz, "Mass spectrometry of planetary exospheres at high relative velocity: direct comparison of open- and closed source measurements," *Geoscientific Instrumentation, Methods and Data Systems Discussions,* pp. 1-2, 08 2016.

[29] P. Wurz, D. Lasi, N. Thomas, D. Piazza, A. Galli, M. Jutzi, S. Barabash, M. Wieser, W. Magnes, H. Lammer, U. Auster, L. Gurvits and W. Hajdas, "An Impacting Descent Probe for Europa and the Other Galilean Moons of Jupiter," *Earth, Moon, and Planets,* 2017.

[30] S. Meyer, Development of a Neutral Gas- and Ion-Mass Spectrometer for Jupiter's Moons, Bern: University of Bern, 2017.

BIOGRAPHY

Martina Föhn *received an M. Sc. In physics from the University of Bern in 2017, with a thesis on the scattering properties of charge state conversion surfaces for space applications for the JUICE and the IMAP missions. She is now pursuing a Ph.D. in physics and is responsible for the calibration of NIM.*

André Galli *received a Ph.D. in Physics from the University of Bern in 2008. After a period as an engineer and technology consultant and his post-doctoral period at the Netherlands Institute for Space Research, he re-joined in 2012 the University of Bern as a scientist. His research topics cover a broad range from laboratory experiments in the context of icy surfaces in the solar system, data analysis for space missions (Mars Express, Venus Express, IBEX, Rosetta), to project science and management for upcoming space missions (JUICE and IMAP in particular).*

Audrey Vorburger *holds a B.S. and a M.Sc. in Electrical Engineering and Information Technology that she obtained from ETH Zurich in 2008. In 2013 she received her Ph.D. in Physics from the University of Bern. Having spent one and a half years as a post-doctoral researcher the American Museum of Natural History in NY, USA, she is now back at the University of Bern perusing her teaching certificate. She is a Co-I of SARA onboard Chandrayaan-1 and of PEP onboard JUICE.*

Marek Tulej *received a Ph.D. in Physical Chemistry from the University of Basel in 1999. After his post-doctoral period at Paul Scherrer Institute, he joined in 2008 the University of Bern as an instrument scientist for space missions, including Phobos-Grunt, Marco Polo-R, Luna-Resurs, and JUICE.*

Davide Lasi *received a B.Sc. and an M.Sc. in Chemistry from the University of Milano in 2004 and 2006, and an M.S. from MIT in 2018 (System Design and Management). He has been with the University of Bern since 2011, as project manager for the development of three space mass spectrometers, including NIM for JUICE. Since 2020, he is with the Thirty Meter Telescope (TMT).*

Andreas Riedo *received his Ph.D. in Physics in 2014 from the University of Bern. In 2016 he received a SNSF fellowship that allowed him to continue his research in Astrobiology at the Leiden University, The Netherlands. He extended his stay at the Leiden University with a MCSA fellowship for another two years before he moved in 2019 to the Free University Berlin after receiving the prestigious Einstein fellowship. In 2020 he moved to University of Bern and is currently appointed as researcher and project manager within the JUICE space mission.*

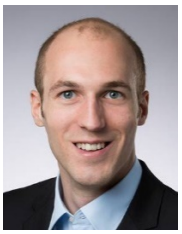

Rico Fausch *completed an apprenticeship as technical designer before he received a B.Sc. in Systems Engineering (micro technologies) from NTB University of Applied Science (Switzerland) in 2013 and a M.Sc. in Biomedical Engineering from University of Bern (Switzerland) in 2015. He has been with the Physics Institute of the University of Bern since 2016, where he received his Ph.D. in Physics in 2020 for the finalization of the NGMS/Luna-Resurs. As a post-doctoral researcher, he is involved in the design of several missions and space instrumentation including NIM/JUICE.*

Michael Althaus *received a HTL & B.Sc. in Electrical Engineering from Lucerne University of Applied Sciences and Arts with specialization in Information Technology in 1999. He worked as a research engineer at ESEC SA in Switzerland and at the Centre for Advanced Materials Joining, University of Waterloo, Canada. Before joining the University of Bern in 2018 for the NIM (JUICE) and the NGMS (Luna-Resurs) instruments, he worked as an R&D SW/HW engineer in the industry.*

Stefan Brüngger *received a B.Sc. in Mechanical Engineering from Bern University of Applied Sciences in 2007 and a M.Sc. in Systems Engineering Management from University College London in 2020. He joined the University of Bern in 2011 as mechanical development engineer. Since then he has worked on the design, development, integration and test of time of flight mass spectrometers and laboratory instrumentation, encompassing NIM for the ESA mission JUICE.*

Philipp Fahrer *received a B.Sc. in Electrical Engineering from Bern University of Applied Sciences in 2002. Before he joined the University of Bern in 2018, he worked as a hardware and FPGA design engineer in the industry.*

Michael Gerber *has been employed as a systems engineer at the University of Bern since 2014, where he works on ExoMars Cassis and JUICE PEP. He graduated in mechanical engineering in 2006 and moved to the University of Bern from RUAG Aviation where he was a systems engineer on fighter aircraft.*

Matthias Lüthi *holds an M.Sc. from ETH, Zürich (1996) and an EMBA in management of technology from EPF Lausanne (2009). He has more than 20 years of experience as a hardware design engineer and manager in high-tech industries in the US and Switzerland. He is the NIM electronics systems engineer.*

Hans Peter Munz *received a B.Sc. in Engineering from Bern University of Applied Sciences in 1994. He worked as Software Engineer for Swiss companies for more than 20 years. In 2018 he joined NIM team in this function.*

Severin Oeschger *received a B.Sc. in Microelectronics & Sensors from the Northwest University of Applied Sciences FHNW (Switzerland) in 2007. He is experienced in Electronics and Sensors as Electrical Engineer in research and development for more than 15 years. After working for a Swiss hearing aid brand, he joined the electronic group within the Space Research & Planetary Science Division in 2014. Where he worked as electrical engineer for the CHEOPS mission. He is currently working on the analogue hardware of the Neutral and Ion Mass Spectrometer (NIM) part of PEP on board ESA mission JUICE.*

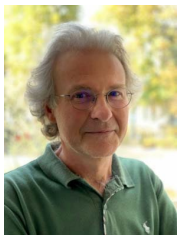

Daniele Piazza *has more than 20 years of experience in the design and development of space instruments. He has a Ph.D. in mechanical engineering from ETH Zurich and started his career in Formula 1. Since 2005 he leads the mechanical engineering group working on space instruments at the University of Bern.*

Peter Wurz *has a degree in electronic engineering (1985), an M.Sc. and a Ph.D. in Physics from Technical University of Vienna (1990). He has been a post-doctoral researcher at Argonne National Laboratory. At the University of Bern since 1992, he is a Professor of physics and since 2015 head of the Space Science and Planetology division. He has been Co-I and PI for many science instruments for space missions of ESA, NASA, ISRO, Roscosmos, and JAXA. He is PI of NIM and Co-PI of PEP onboard JUICE.*

4.8.2. Flight Spare

Ion Storage

Ion storage is very crucial for a time of flight mass spectrometer because every ion generated outside of the extraction pulse interval and not stored in the ionisation region is lost. Moreover, it can generate additional electrical noise on the detector signal line because these ions would arrive at an arbitrary time at the detector, with respect to the extraction pulse. In this test the ion storage capability of the ion source was analysed for thermal and neutral mode for hydrogen and krypton with velocities of 2 km/s and 4 km/s. The electron emission current was varied from 20 to 600 µA.

Ion storage of positive ions in x- and y- direction is supported by the negative space charge potential generated by the electron beam (see Chap. 2.4). Two ring electrodes, with a positive voltage applied, generate a positive potential ring to trap generated ions in y- and z- direction (Fig. 67). For emission currents from 20 to 600 µA according to Eq. (51) the negative potential in the centre of the electron beam is –0.1 to –3.0 V. Fig. 68, left panel shows the ion storage behaviour of the ion source of hydrogen and the right panel shows the ion storage behaviour of krypton. In case of no ion storage, the relationship between the electron emission current I_{em} and the signal intensity is linear because then only ions would be extracted that are generated during the time when the extraction pulse is applied on the extraction grid. In case of ion storage there is a about a quadratic relationship between I_{em} and the signal intensity.

When measuring with the thermal mode, the particles are slowed down in the antechamber until they have energies in the range of 26 meV ≙ 300 K and are therefore easy to trap in the potential field. When measuring with the neutral mode, particles enter the ionisation region directly. The kinetic energy of hydrogen for velocities between 2 – 4 km/s is 0.07 – 0.27 eV. Therefore, hydrogen can be trapped in the potential well generated by an electron beam with an emission current higher than 20 μA.

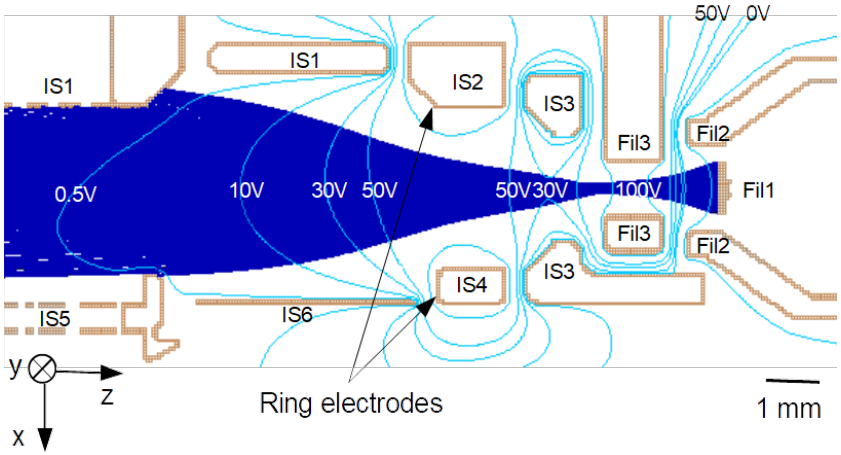

Figure 67: Ion storage source with sample voltage set applied to the electrodes. In light blue are the potential lines and in dark blue are the calculated trajectories of the electron beam.

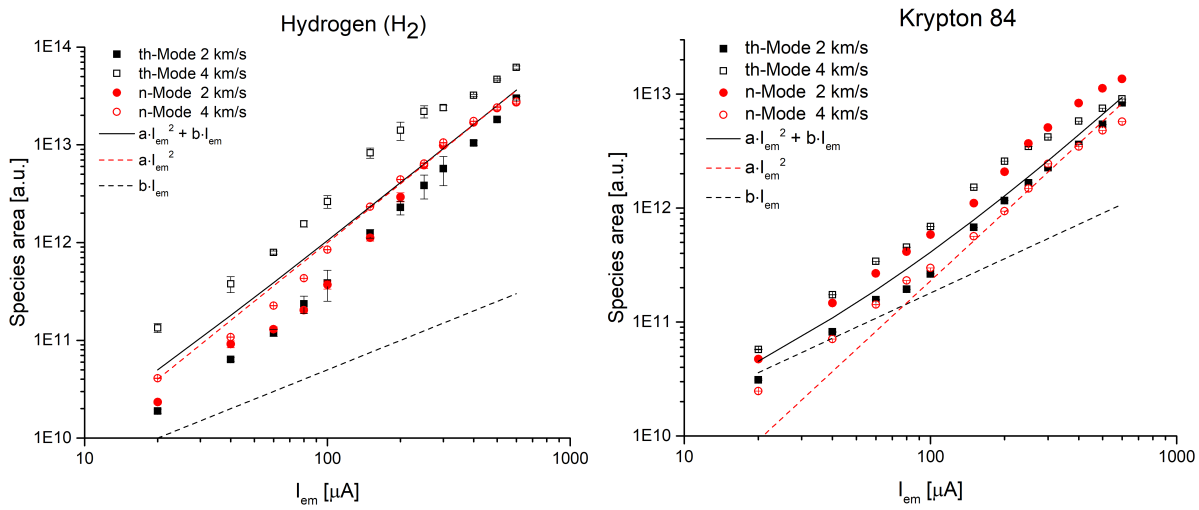

Figure 68: Ion storage measurements performed with the NIM flight spare ion-optical system operated with laboratory electronics for a neutral gas beam containing H_2 and ^{84}Kr for two different gas velocities.

The kinetic energy of ^{84}Kr for the same velocities is 2.8 – 11.2 eV. This energy exceeds the potential of the centre of the electron beam and the ions are therefore more difficult to trap with only the electron beam. The ions are kept in the middle of the ionisation region with the positive potential ring generated by the ring electrodes. According to Fig. 68 ion storage for ^{84}Kr starts to dominate at emission currents higher than 100 μA. In thermal mode, an increase in beam velocity leads to an increase in signal intensity due to the density enhancement effect (Chap. 2.5). Therefore a higher signal intensity is expected in thermal mode for 4 km/s compared to 2 km/s. Like in the PFM, the FS shows a nice ion storage capability. For krypton ion storage just starts at an emission current of 100 µA where hydrogen is stored already at lower emission currents due its lower kinetic energy at the same beam velocity.

Mass resolution and Signal-to-Noise Ratio

According to the requirements stated in [24] NIM has to achieve a mass resolution $m/\Delta m$ of 500 for neutral mode and of 1000 for thermal mode. NIM is designed to measure ions and neutral molecules with masses up to 1000 u. Therefore, a mass resolution m/Δm of 1000 is required to be able to distinguish between the adjacent masses at high mass units.

Fig. 69 shows two mass spectra recorded with the NIM FS ion-optical system operated with laboratory electronics. The electron emission current was 100 μA. The mass resolution m/Δm when measuring with the neutral gas mode is 708 and 830 when measuring with the thermal mode. With this mass resolution, NIM fulfils almost the requirements regarding the mass resolution for the two measuring modes.

The FS ion-optical system showed a better performance than with the PFM. The reason is that the FS ion-optical system was better optimised than the PFM. In addition, the voltages applied on some of the ion-optical lenses are extremely different between the two models (see Table 9 in App. A.3). The biggest difference is in the applied voltage of electrode IS 1 (Fig. 67). IS 1

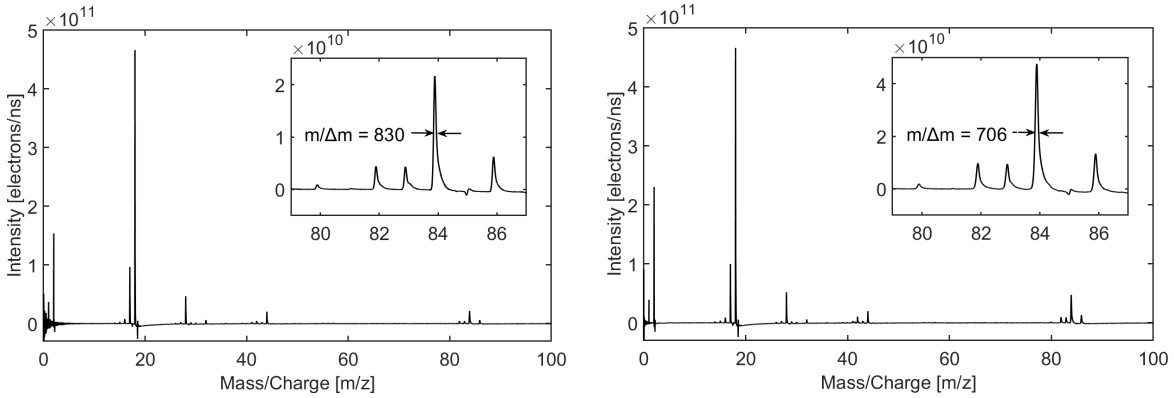

Figure 69: Mass spectra measured with the NIM flight spare ion-optical system with the laboratory electronics attached. Left: thermal gas mode. Right: neutral mode.

is the electrode opposite of the extraction grids (IS 5 and IS 6) and its functions are to guide the electron beam in the ionisation region and to establish a trapping field for the ions in the ionisation region together with the other ion-optical lenses. This is a very good example on which level the ion-optics has to be optimised to reach high performance with such a compact instrument as NIM. This shows also that even when the PFM and the FS ion-optical systems are the same from the mechanical point of view, small differences in the manufacturing process have an impact on the performance of the instrument depending where they are.
Fig. 70 shows another mass spectrum recorded with the FS instrument when operated with laboratory electronics. The highest SNR achieved was $6 \cdot 10^5$ and therefore almost 6 decades. The mass peaks m/z 355, 390 and 429 are some oil components with water adducts originating from the turbomolecular pumps of the test facility. m/z 415 is an artefact generated by the algorithm used for background subtraction. This peak is also wider than the other surrounding mass peaks. A SNR of 6 is important to conduct optimal measurements during the flybys at Jupiter's icy moons because the experted particle densities are in the range of 10 – 10^8 cm^{-3} [41, 40] corresponding to a partial pressure of 10^{-15} – 10^{-8} mbar. With a chamber pressure of $1.5 \cdot 10^{-9}$ mbar NIM has to achieve a SNR of 6 decades to measure particles at a pressure of 10^{-15} mbar.

In the following section a few performance results are discussed where the NIM ion-optical system was operated with the actual flight electronics. The instrument was at that time barely optimised.
Fig. 71, left panel shows a mass spectrum conducted with thermal mode and the right panel shows a spectrum recorded with the neutral mode. The electron emission current was 200 μA. The mass resolution at the current state is 490 m/Δm for neutral gas mode and 462 m/Δm for thermal mode. The mass resolution can be improved by further optimising the system as there was barely time to optimise the instrument as a whole unit. With an emission current of 300 μA the SNR is high enough to also show the ^{78}Kr isotope, which has a natural abundance of 0.36 % (Fig. 72).
A lot of potential to increase the SNR lies in the analysis and removal of the noise. One part

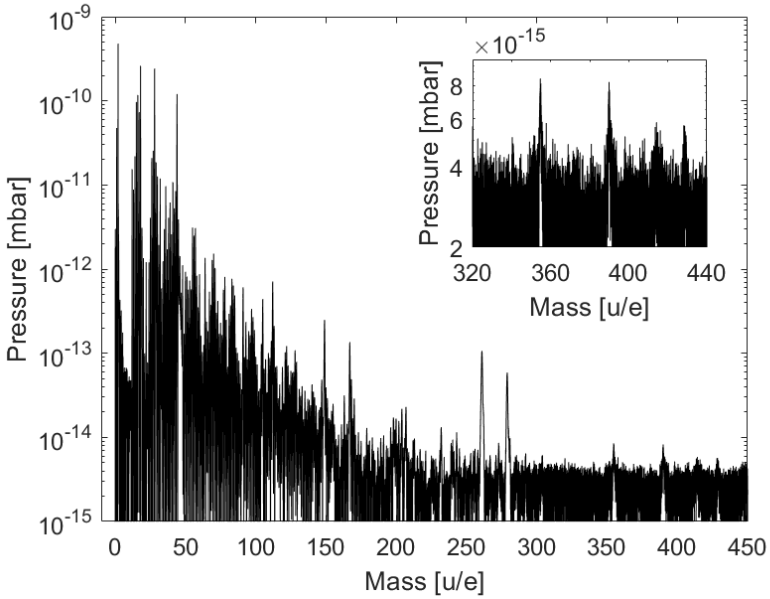

Figure 70: SNR plot for the NIM flight spare ion-optical system operated with laboratory electronics. The residual gas pressure was $1.5 \cdot 10^{-9}$ mbar.

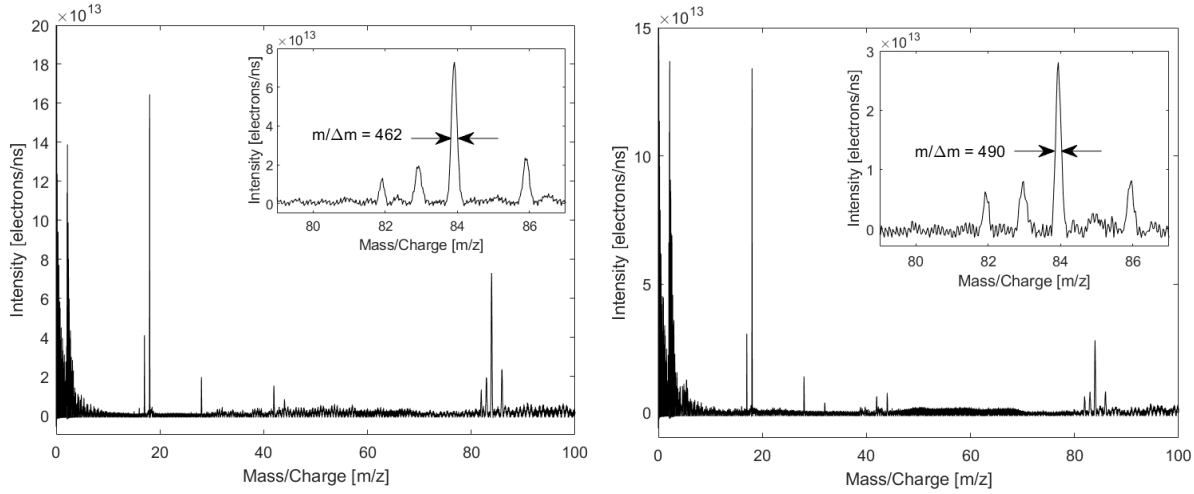

Figure 71: Mass spectra measured with the NIM flight spare instrument with the flight electronics attached. Filament emission current was 200 μA. Left: thermal gas mode. Right: neutral mode.

of the noise is moving depending on when the recording of the mass spectrum is started. In Fig. 71, left and right panel this noise appears between masses m/z 40 and 70. In Fig. 72 the noise part starts right after the interference by the extraction pulse and ends at m/z 30. At the moment it is unclear what induces that noise but with a proper filter this noise can be detected and significantly reduced during data processing without affecting the mass signal peaks.
Fig. 73 shows the evolution of the peak height of N_2 as a function of days during the thermal

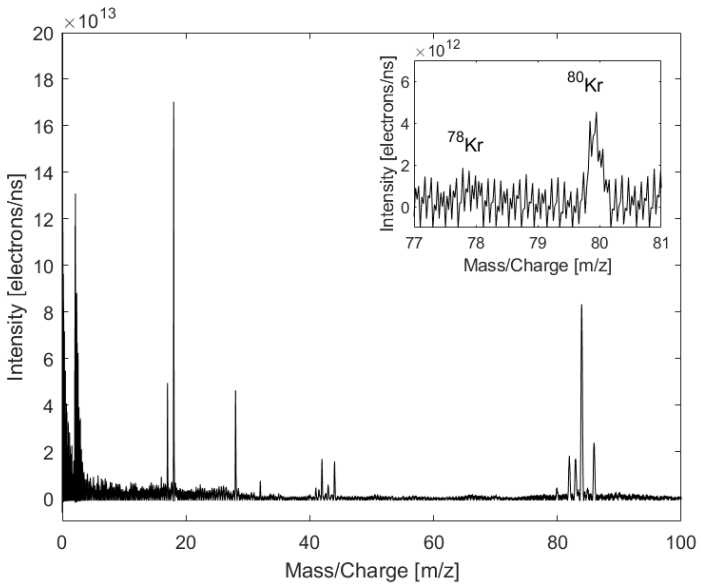

Figure 72: Mass spectrum measured with the flight spare instrument with the flight electronics attached with a filament emission current of 300 μA.

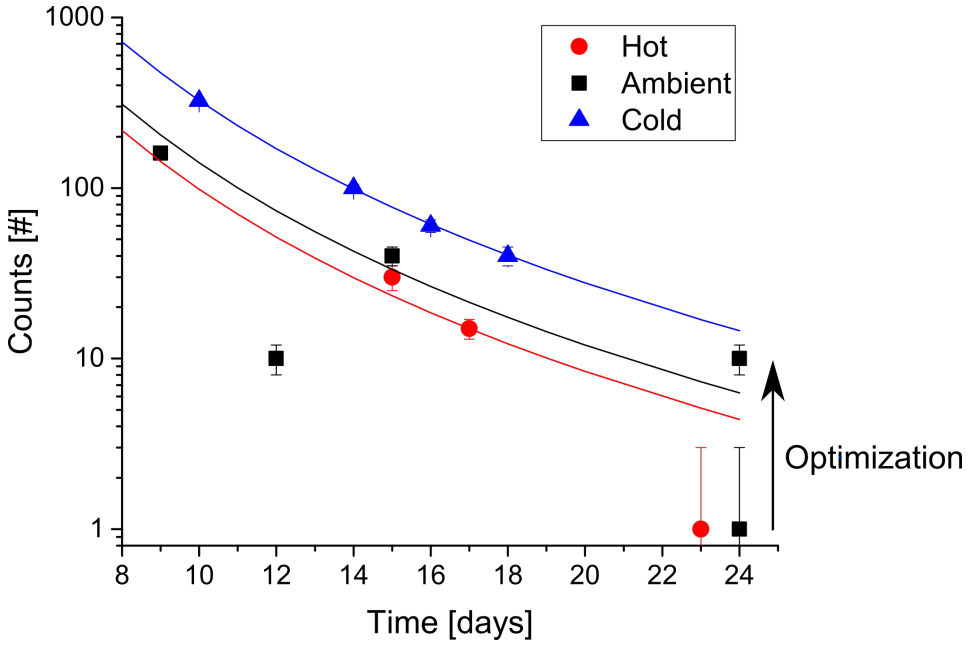

Figure 73: Peak height evolution of N_2 of the NIM FS instrument operated with flight electronics during the thermal vacuum tests.

vacuum test campaign. During the thermal vacuum test the instruments robustness and behaviour is tested when it is under thermal stress. The iteration of the different temperature plateaus is visible in the graphic by the sequence of the different measurement points between hot, cold and ambient cases. The measuring point at day 12 is an outlier. The data clearly

show a continues decrease of the signal height during operation although the used parameter set was the same for all measurements shown in the plot. The signal decline is a result of voltage drifts during the thermal cycling. When electric components are thermally cycled, thermal hysteresis effects on the electrical components can occur leading to voltage and current drifts. The readout electronics is also affected by these effects and therefore such drifts may not be noticed by the control system. Therefore, the system cannot readjust. To compensate these effects, the instrument has to be readjusted by optimising the voltages of the ion-optical lenses. The impact of the optimisation is very well visible when looking at the last data point at day 24 in the measuring series. The signal was barely visible in the noise and by a short manual optimisation of the system, a factor 10 in signal intensity was gained. With a complete optimisation recovery of the initial performance is expected. Although that is an extreme example how much can be gained by a short optimisation, it nevertheless shows the importance of having an autonomous optimisation system implemented in the flight software. The optimisation algorithm has yet to be implement. In the laboratory the optimisation can be done with the same software or manually. At the current state, the operation software is still not on a level allowing convenient manual optimisation because the flight software has higher priority to be ready before the start of the spacecraft. After the start there is only limited access to update the software on the spacecraft. The improvement of the usability of the software will be the next task in the implementation to finalise the flight software.

5. Summary and Outlook

At the beginning of a space mission, there stands always a main scientific question. In case of JUICE its to investigate Jupiter and its icy moons as a planetary system potentially harbouring life. To answer that question, the question is divided into much more concrete questions out of which specific requirements for instruments participating in the space mission result. For the specific case of the NIM instrument, these requirements are the needed mass resolution, the signal-to-noise ratio and the mass range NIM has to detect to determine the composition of the icy moons' exosphere with enough accuracy to set further constraints for exosphere modellers to understand the formation and evolution processes involved to form the icy moons.
The task of a scientist designing and building such an instrument is to identify the needed technical performance of the subsystems of the specific instrument based on the scientific requirements on the instrument performance mentioned above. Examples of such technical requirements are the range and stability of needed voltages to operate the instrument, switching times or gain. Other requirements arise from operations, e.g., the flyby trajectory and orientation of the spacecraft to the subject, which has to be investigated during the mission.
In the following, two examples are shown on which the iteration processes of improving the instrument is shown. On the example of the high-voltage pulse generator it is shown, how important it is to push the operating electronics to their limit to reach higher performance with the new instruments leading to better data and an improvement of our knowledge. The second example focuses on the flyby trajectory and the restrictions arising for the instrument design from the mission itself.

Two of the most important parameters of the high-voltage pulse generator used to extract the ions from NIM's ionisation region are the fall time and the bias voltage. The fall time has to be as short as possible to ensure that all ions get the same amount of energy. Otherwise, the mass resolution of especially low mass ions suffers (see Chap. 2.1). Typical fall times are in the range of a few ns and theory shows that this is a very critical parameter. Two different flight designs of the high voltage pulse generator were tested during the thesis using the prototype ion-optical system. The tests showed a clear preference to the one with the shorter fall time in agreement with the theory (see [27]). Another important parameter is the bias voltage, which is the voltage applied on the extraction grid when no high voltage pulse is applied. As shown in Chap. 4.8.2 and [17], the PFM and FS ion-optical systems have both a good ion storage capability when operated with laboratory electronics. To achieve that it is necessary to have a stable potential well in the ionisation region during the time when no extraction pulse is applied on the extraction grid. This requires that the voltages applied on the electrodes in the ionisation region do not fluctuate more than 100 mV. Laboratory tests showed that the most critical ones with respect to ion storage are the bias voltage applied on the extraction grid and the voltage applied on the grid opposite of the extraction grid. The flight pulse generator shows less good performance with regards to that parameter than the laboratory electronics (see Chap. 4.6). Due to other restrictions like the necessary radiation hardness of the electrical components limiting the number of options for certain components, this design was the best with the available resources.

Other requirements appear from the trajectory of the spacecraft. JUICE contains several different instruments. The orientation of the spacecraft depends on the instruments to enable them an optimal FoV on their target. For a spacecraft having solar panels for power generation, it is important for the solar panels to be oriented perpendicular to the Sun whenever possible to optimize power generation especially for missions with targets such far away from the Sun as the mission JUICE with target Jupiter, which introduces constraints on the spacecraft orientation. The second priority for the spacecraft orientation is that the camera has the best view of the observation target on the moons' surface.
For the NIM instrument in particular that meant to have a design with a big FoV to have a certain flexibility regarding the gas inflow direction into the instrument. NIM has an open-source and a closed-source entrance to measure neutral particles and ions directly and to thermalise neutral particles with the closed source antechamber to make advantage of the density enhancement behaviour to amplify the signal with that mode. Simulations of the trajectory of the spacecraft revealed that two entrance holes on the antechamber were necessary to be able to measure during the different flybys even though a second entrance hole leads to a lower performance of the closed-source antechamber (Chap. 2.5 and 2.6).

The NIM PFM was successfully delivered to the JUICE spacecraft in December 2020 and at the current state, the NIM FS model waits until the JUICE spacecraft started its journey to Jupiter in September 2022. Until then, the FS waits as it is the spare model for the case that something happens to the PFM on the spacecraft until launch. After the start of the spacecraft, the NIM FS has to be properly calibrated with the actual flight electronics. Most results presented in this thesis were conducted with laboratory electronics attached to the two ion-optical systems because there was only very little time to test the whole system. The NIM ion-optical system was first qualified as a separate unit and now there follows the calibration of the whole NIM instrument.
In addition, the flight software is still under development and has to be tested with the full system. The optimiser to optimised the voltage sets during the flight is still under development. As soon as it is available for tests, it has to be tested and the target function used to improve the voltage sets has to be adapted for NIM. First results of the FS ion-optical system operated with flight electronics revealed that there lies a lot of potential in the postprocessing of the data especially in regards to filtering. Therefore a proper filter has to be written to improve the SNR of the final spectra.
To have a proper calibration facility for the NIM instrument and future TOF instruments, the SATANS test facility (Supersonic cATion and ANion Source) is under development to generate neutral particle and ion beams with velocities from 1–15 km/s. The CASYMIR test facility is only able to generate neutral particle beams with velocities up to 4 km/s but the NIM instrument has to detect neutral particles and ions with velocities up to 8 km/s. Therefore, SATANS was developed to have a facility covering a higher velocity range for neutral particles and also for ions. Such a calibration facility in necessary to calibrate the FS instrument and to replicate the data recorded with the actual flight instrument on the satellite to understand the measured data. Therefore, a test setup is required able to reproduce the environment is space as close as possible. First tests performed with the NIM prototype on SATANS showed

promising results [33] but there is still a lot of potential in improving the performance and stability of SATANS. At the current state, SATANS is able to produce an ion beam with velocities between 1 – 15 km/s. As soon as the stability of the ion beam is improved, the system will be upgraded with a neutraliser to also produce a neutral particle beam in this energy range.

References

[1] D. Abplanalp. Development of a sensitive TOF-Mass Spectrometer for Space Research. Universität Bern, 2009.

[2] D. Abplanalp, P. Wurz, L. Huber, I. Leya, E. Kopp, U. Rohner, M. Wieser, L. Kalla, and S. Barabash. A neutral gas mass spectrometer to measure the chemical composition of the stratosphere. Advances in Space Research, 44(7):870–878, 2009. doi: 10.1016/j.asr.2009.06.016. URL http://dx.doi.org/10.1016/j.asr.2009.06.016.

[3] E. S. Agency. A history of astrometry - part i mapping the sky from ancient to pre-modern times. URL https://sci.esa.int/web/gaia/-/53196-the-oldest-sky-maps. Accessed: 2021-10-17.

[4] H. Anderson, P. Wurz, P. Brandt, S. Jaskulek, and S. Barabash. Pep eid-b (se-01).

[5] J. W. Arblaster. Selected electrical resistivity values for the platinum group of metals Part II: Rhodium and Iridium:. Johnson Matthey Technology Review, 60(1):4–11, 2016. doi: 10.1595/205651316X691618.

[6] R. Arevalo Jr, Z. Ni, and R. M. Danell. Mass spectrometry and planetary exploration: A brief review and future projection. Journal of Mass Spectrometry, 55(1):e4454, 2020. doi: https://doi.org/10.1002/jms.4454. URL https://analyticalsciencejournals.onlinelibrary.wiley.com/doi/abs/10.1002/jms.4454.

[7] H. Balsiger, K. Altwegg, P. Bochsler, P. Eberhardt, J. Fischer, S. Graf, A. Jäckel, E. Kopp, U. Langer, M. Mildner, J. Müller, T. Riesen, M. Rubin, S. Scherer, P. Wurz, S. Wüthrich, E. Arijs, S. Delanoye, J. De Keyser, E. Neefs, D. Nevejans, H. Rème, C. Aoustin, C. Mazelle, J. L. Médale, J. A. Sauvaud, J. J. Berthelier, J. L. Bertaux, L. Duvet, J. M. Illiano, S. A. Fuselier, A. G. Ghielmetti, T. Magoncelli, E. G. Shelley, A. Korth, K. Heerlein, H. Lauche, S. Livi, A. Loose, U. Mall, B. Wilken, F. Gliem, B. Fiethe, T. I. Gombosi, B. Block, G. R. Carignan, L. A. Fisk, J. H. Waite, D. T. Young, and H. Wollnik. Rosina - Rosetta orbiter spectrometer for ion and neutral analysis. Space Science Reviews, 128(1-4):745–801, 2007. ISSN 00386308. doi: 10.1007/s11214-006-8335-3.

[8] S. Barabash, P. Brandt, P. Wurz, and PEP Team. Particle Environment Package (PEP) for the ESA JUICE mission. In AAS/Division for Planetary Sciences Meeting Abstracts #48, volume 48 of AAS/Division for Planetary Sciences Meeting Abstracts, page 422.06, Oct. 2016.

[9] A. Boutonnet and G. Varga. JUICE- Jupiter Icy moons Explorer Consolidated Report on Mission Analysis (CReMA), esa document jui-esoc-moc-rp-001 edition, 04 2017.

[10] G. K. Burgess and R. G. Waltenberg. The emissivity of metals and oxides, II: Measurements with the micropyrometer. Physical Review, 4(6):546–547, 1914. doi: 10.1103/PhysRev.4.546.

[11] F. Cardarelli. Materials Handbook. Springer-Verlag London, 2008.

[12] G. Collins and T. C. Johnson. Chapter 37 - Ganymede and Callisto. Elsevier, 2014. URL

https://doi.org/10.1016/B978-0-12-415845-0.00037-2.

[13] P. D. Desai, T. K. Chu, H. M. James, and C. Y. Ho. Electrical resistivity of selected elements. Journal of Physical and Chemical Reference Data, 13(4):1069–1096, 1984. doi: 10.1063/1.555723. URL https://doi.org/10.1063/1.555723.

[14] ESA. Juice mission. URL http://www.esa.int/spaceinimages/Images/2017/07/Juice_mission. Accessed: 2017-10-07.

[15] R. G. Fausch. Mass Spectrometry for In Situ Planetary Research. Universität Bern, 2020.

[16] R. G. Fausch, P. Wurz, M. Tulej, J. Jost, P. Gubler, M. Gruber, D. Lasi, C. Zimmermann, and T. Gerber. Flight electronics of gc-mass spectrometer for investigation of volatiles in the lunar regolith. In 2018 IEEE Aerospace Conference, pages 1–13, 2018. doi: 10.1109/AERO.2018.8396788.

[17] M. Fohn, A. Galli, A. Vorburger, M. Tulej, D. Lasi, A. Riedo, R. G. Fausch, M. Althaus, S. Brungger, P. Fahrer, M. Gerber, M. Luthi, H. P. Munz, S. Oeschger, D. Piazza, and P. Wurz. Description of the Mass Spectrometer for the Jupiter Icy Moons Explorer Mission. IEEE Aerospace Conference Proceedings, 2021-March, 2021. ISSN 1095323X. doi: 10.1109/AERO50100.2021.9438344.

[18] P. V. GmbH. Quadrupole mass filter. URL https://www.pfeiffer-vacuum.com/en/know-how/mass-spectrometers-and-residual-gas-analysis/quadrupole-mass-spectrometers-qms/. Accessed: 2021-10-12.

[19] S. Graf, K. Altweg, H. Balsiger, A. Jäckel, E. Kopp, U. Langer, W. Luithardt, C. Westermann, and P. Wurz. A cometary neutral gas simulator for gas dynamic sensor and mass spectrometer calibration : Space simulations in laboratory: Experiments, instrumentation, and modeling. Journal of Geophysical Research, 109, 2004.

[20] C. R. G.Wells, H. Prest. Technical Note: Signal, Noise and Detection Limits in Mass Spectrometry. Agilent Technologies, 2011. doi: 5990-7651EN.

[21] A. E. Hedin, C. P. Avery, and C. D. Tschetter. An analysis of spin modulation effects on data obtained with a rocket-borne mass spectrometer. Journal of Geophysical Research, 69(21):4637–4648, nov 1964. doi: 10.1029/jz069i021p04637. URL https://doi.org/10.1029%2Fjz069i021p04637.

[22] C. Y. Ho, R. W. Powell, and P. E. Liley. Thermal conductivity of the elements.

[23] L. Hofer. Development of the gas chromatograph – mass spectrometer to investigate volatile species in the lunar soil for the Luna-Resurs mission. Universität Bern, 2015.

[24] H. Hussmann, P. Palumbo, R. Jaumann, M. Dougherty, Y. Langevin, G. Piccioni, S. Barabash, P. Wurz, P. van den Brandt, L. Gurvits, L. Bruzzone, J. Plaut, J. Wahlund, B. Cecconi, P. Hartogh, R. Gladstone, L. Iess, D. Stevenson, Y. Kaspi, O. Grasset, and L. Fletcher. JUICE JUpiter ICy moons Explorer: Exploring the emergence of habitable worlds around gas giants, volume ESA/SRE. ESA, 2014. Definition Study Report.

[25] B. Johnson. Power sources for space exploration. URL http://large.stanford.edu/

courses/2012/ph240/johnson1/. Accessed: 2021-10-12.

[26] D. Lasi, M. Tulej, S. Meyer, M. Lüthi, A. Galli, D. Piazza, P. Wurz, D. Reggiani, H. Xiao, R. Marcinkowski, W. Hajdas, A. Cervelli, S. Karlsson, T. Knight, M. Grande, and S. Barabash. Shielding an mcp detector for a space-borne mass spectrometer against the harsh radiation environment in jupiter's magnetosphere. IEEE Transactions on Nuclear Science, 64(1):605–613, 2017. doi: 10.1109/TNS.2016.2614040.

[27] D. Lasi, S. Meyer, D. Piazza, M. Lüthi, A. Nentwig, M. Gruber, S. Brüngger, M. Gerber, S. Braccini, M. Tulej, M. Föhn, and P. Wurz. Decisions and trade-offs in the design of a mass spectrometer for jupiter's icy moons. IEEE Aerospace Conference Proceedings, pages 1–20, 2020. doi: 10.1109/AERO47225.2020.9172784.

[28] E. Lassner and W.-D. Schubert. Tungsten. Springer US, 1999.

[29] W. R. McMahon and D. R. Wilder. Hight temperature spectal enissivity of yrrrium, smarium, gadolinium, erbuim and lutetium oxides. 1 1963. URL https://www.osti.gov/biblio/4704246.

[30] S. Meyer. Development of Fully Automated and Highly Precise Data Analysis for a Miniaturized Laser-Ablation Mass Spectrometer. Universität Bern, 2013.

[31] S. Meyer. Development of a Neutral Gas-and Ion-Mass Spectrometer for Jupiter's Moons. Universität Bern, 2017.

[32] S. Meyer, M. Tulej, and P. Wurz. Mass spectrometry of planetary exospheres at high relative velocity: direct comparison of open- and closed-source measurements. Geoscientific Instrumentation, Methods and Data Systems, 6(1):1–8, 2017. doi: 10.5194/gi-6-1-2017. URL https://gi.copernicus.org/articles/6/1/2017/.

[33] S. Meyer, M. Tulej, and P. Wurz. A low energy ion beam facility for mass spectrometer calibration: First results. Review of Scientific Instruments, 89(1):013305, 2018. doi: 10.1063/1.5006528. URL https://doi.org/10.1063/1.5006528.

[34] N. Milosevic, G. Vukovic, D. Z. Pavicic, and K. Maglic. Thermal properties of tantalum between 300 and 2300 k. International Journal of Thermophysics, 20:1129–1136, 1999.

[35] M. B. Neuland. In situ mass spectrometry for planetary exploration: Quantitative chemical composition measurements on planetary surfaces. Universität Bern, 2015.

[36] S. Scherer. Design of a high-performance Reflectron Time-of-Flight mass spectrometer for space applications. Universität Bern, 1999.

[37] S. Scherer, K. Altwegg, H. Balsiger, J. Fischer, A. Jäckel, A. Korth, M. Mildner, D. Piazza, H. Reme, and P. Wurz. A novel principle for an ion mirror design in time-of-flight mass spectrometry. International Journal of Mass Spectrometry, 251(1):73–81, 2006. ISSN 1387-3806. doi: https://doi.org/10.1016/j.ijms.2006.01.025. URL https://www.sciencedirect.com/science/article/pii/S1387380606000510.

[38] M. C. Sitja and A. E. Lopez. Pep nim field of view obstruction study.

[39] D. van Essen and W. C. Heerens. On the transmission probability for molecular gas flow

through a tube. Journal of Vacuum Science and Technology, 13(6):1183 – 1187, 1976.

[40] A. Vorburger and P. Wurz. Europa's ice-related atmosphere: The sputter contribution. Icarus, 311:135–145, 2018. ISSN 0019-1035. doi: https://doi.org/10.1016/j.icarus.2018.03.022. URL https://www.sciencedirect.com/science/article/pii/S0019103517305377.

[41] A. Vorburger, P. Wurz, H. Lammer, S. Barabash, and O. Mousis. Monte-Carlo simulation of Callisto's exosphere. Icarus, 262:14–29, 2015. ISSN 10902643. doi: 10.1016/j.icarus.2015.07.035.

[42] D. R. Williams. Jupiter. URL https://nssdc.gsfc.nasa.gov/planetary/planets/jupiterpage.html. Accessed: 2021-10-17.

[43] B. Wilthan, C. Cagran, and G. Pttlacher. Combined dsc and pulse-heating measurements of electrical resistivity and enthalpy of tungsten, niobium, and titanium. International Journal of Thermophysics, 26(4):1017–1029, 2005. doi: 10.1007/s10765-005-6682-z. URL https://doi.org/10.1007/s10765-005-6682-z.

[44] J. Wiza. Microchannel plate detectors. Nuclear Instruments and Methods, 162(1):587–601, 1979. ISSN 0029-554X. doi: https://doi.org/10.1016/0029-554X(79)90734-1. URL https://www.sciencedirect.com/science/article/pii/0029554X79907341.

[45] M. Wüest, D. S. Evans, and R. von Steiger. Calibration of Particle Instruments in Space Physics. 2007.

[46] P. Wurz. Lecture notes mass spectrometry and ion optics, 2017.

[47] P. Wurz, D. Abplanalp, M. Tulej, and H. Lammer. A neutral gas mass spectrometer for the investigation of lunar volatiles. Planetary and Space Science, 74(1):264–269, 2012. ISSN 0032-0633. doi: https://doi.org/10.1016/j.pss.2012.05.016. URL https://www.sciencedirect.com/science/article/pii/S0032063312001298. Scientific Preparations For Lunar Exploration.

A. Appendix

A.1. Papers

Decisions and Trade-Offs in the Design of a Mass Spectrometer for Jupiter's Icy Moons

Davide Lasi
University of Bern, Physics Institute
Sidlerstrasse 5
Bern, CH-3012 (Switzerland)
davide.lasi@space.unibe.ch

Stefan Meyer
University of Bern, Physics Institute
Sidlerstrasse 5
Bern, CH-3012 (Switzerland)
stefan.meyer@space.unibe.ch

Daniele Piazza
University of Bern, Physics Institute
Sidlerstrasse 5
Bern, CH-3012 (Switzerland)
daniele.piazza@space.unibe.ch

Mathias Lüthi
University of Bern, Physics Institute
Sidlerstrasse 5
Bern, CH-3012 (Switzerland)
luethi@space.unibe.ch

Andreas Nentwig
University of Bern, Physics Institute
Sidlerstrasse 5
Bern, CH-3012 (Switzerland)
andreas.nentwig@space.unibe.ch

Mario Gruber
University of Bern, Physics Institute
Sidlerstrasse 5
Bern, CH-3012 (Switzerland)
mario.gruber@space.unibe.ch

Stefan Brüngger
University of Bern, Physics Institute
Sidlerstrasse 5
Bern, CH-3012 (Switzerland)
stefan.bruengger@space.unibe.ch

Michael Gerber
University of Bern, Physics Institute
Sidlerstrasse 5
Bern, CH-3012 (Switzerland)
michael.gerber@space.unibe.ch

Saverio Braccini
University of Bern, LHEP
Sidlerstrasse 5,
Bern, CH-3012 (Switzerland)
saverio.braccini@lhep.unibe.ch

Marek Tulej
University of Bern, Physics Institute
Sidlerstrasse 5
Bern, CH-3012 (Switzerland)
marek.tulej@space.unibe.ch

Martina Föhn
University of Bern, Physics Institute
Sidlerstrasse 5
Bern, CH-3012 (Switzerland)
martina.foehn@space.unibe.ch

Peter Wurz
University of Bern, Physics Institute
Sidlerstrasse 5
Bern, CH-3012 (Switzerland)
peter.wurz@space.unibe.ch

Abstract—**This paper describes the Neutral gas and Ion Mass spectrometer (NIM) onboard ESA's JUpiter ICy moon Explorer (JUICE). Instead of detailing the nuts and bolts of the design, we recount it in terms of 'given', architectural, and design decisions. 'Given' decisions are relative to elements of the instrument defined at the outset of the project, which bound the solution space to be explored by the development team. These decisions comprise the definition of the instrument concept (time-of-flight), sample ionization, MCP detector, ion optics technology, radiation shielding, and allocation of electronics' functions. Architectural and design decisions regard other elements of the instrument defined during the preliminary and detailed design phases, after trade-offs accounting for both technical and programmatic factors. These decisions regard the instrument's ion source, mechanism, FPGA, emitters, PCB interconnect, detector, materials, circuitry of the emission controller and high-voltage pulser, and software. Lessons learned are discussed throughout, including decisions that, ex-post, should have been made differently. This recollection ends with the first mass spectrum acquired with the flight model.**

TABLE OF CONTENTS

978-1-7821-2734-7/20/$31.00 ©2020 IEEE

1. INTRODUCTION

This paper describes the Neutral gas and Ion Mass Spectrometer (NIM) of the Particle Environment Package (PEP) onboard ESA's JUpiter ICy moons Explorer (JUICE) [1]. In particular, this work interprets the development of the instrument in terms of decisions and trade-offs made to meet the ambitious science goals of the mission in the extreme environment of Jupiter (radiation), subject to tight resources (mass and power) and programmatic constraints.

The design of the instrument is recounted in terms of 'given', architectural, and design decisions. These include decisions about the instrument's sensor, electronics, software, and radiation shielding. This recollection ends with the first mass spectra acquired with the Proto-Flight Model (PFM).

We believe that this approach to recounting the development of the instrument in terms of decisions and trade-offs does a better service to the future generations of designers of space mass spectrometers than a mere description of the nuts and bolts of the final design. By telling not only the path that we followed but also the pattern of alternatives that we dropped, and why, we aim to provide a useful material that can inform the development of future similar instruments.

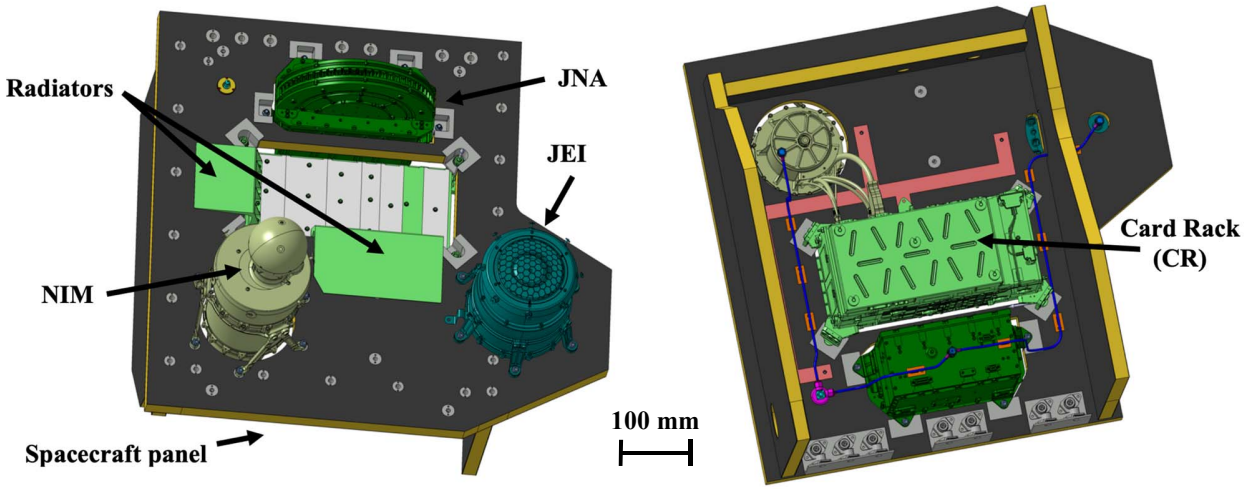

Figure 1 Overview of the Particle Environment Package (PEP) Nadir Unit (NU), including the Neutral gas and Ion Mass spectrometer (NIM), the Jovian Neutrals Analyzer (JNA) and the Jovian Electron and Ion analyzer (JEI) as of 2019.

2. Context

NIM is a Time-Of-Flight Mass Spectrometer (TOF MS) selected in 2013 for the ESA mission JUICE. The mission comprises multiple flybys of Jupiter's icy moons Europa, Callisto, and Ganymede and a final orbital phase around Ganymede. NIM is one of six instruments of PEP [2], which comprises four units. The PEP Nadir Unit (NU, Figure 1), where NIM is located, is accommodated on the nadir plane of the spacecraft (Figure 2).

The instrument is the 4th generation of TOF MS for application on a spacecraft developed by the University of Bern, after RTOF for ESA's Rosetta [3], P-BACE [4], and NGMS for Roscosmos' Luna-Resurs [5] [6]. The development of NIM benefited particularly from the latter, thanks to a partial overlap in time and team composition. Table 1 summarizes the key milestones of the project. The team comprised eight engineers (mechanics, electronics, FGPA, software), two modelers (structural, thermal), a senior scientist, about four technicians, a Ph.D. student, a project manager, and the PI.

The development of NIM presented several challenges. First, it took place in the context of a multi-instrument suite, for complex technical interfaces and programmatic dependencies of a 'team of teams.' Second, it had to address new issues related to the operation of a TOF MS in the Jupiter radiation environment (Figure 3), such as energetic electron detection efficiencies of Micro-Channel Plates. The Galileo dust detector [7], also a TOF instrument, had a different architecture, and the development of MASPEX [8], a TOF MS for NASA's Europa Clipper, was substantially concurrent with NIM's, and therefore faced similar challenges at about the same time. Finally, the instrument's design space was constrained by a number of risk-mitigation requirements from the JUICE project office put in place to mitigate risk of the first large-class mission and the first mission to Jupiter of the European Space Agency (ESA).

Table 1 Summary of key project dates.

Event	Year
Instrument proposal accepted (initiation)	2013
Requirements Review	2014
Preliminary Design Review (PDR)	2017
Critical Design Review (CDR)	2018
Proto-Flight Model delivery	2020
Launch	2022

3. Goals and Requirements

NIM is conceived to address the science goals of JUICE related to the understanding of the neutral exospheric and ionospheric composition and structure of Europa, Ganymede, and Callisto. Specifically, NIM will measure neutrals and ions in the exospheres of these icy moons during the early-mission's flybys (> 200–400 km altitude at closest approach)

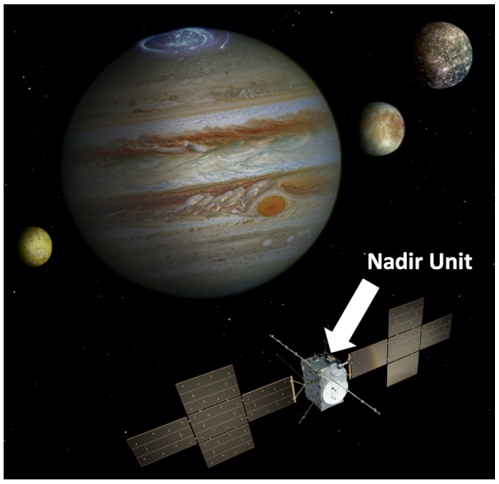

Figure 2 Location of the PEP Nadir Unit on the JUICE spacecraft (Credits: ESA and Airbus Defence and Space).

and the late-mission orbits around Ganymede (> 200–500 km altitude). The required spatial resolution is ~25–50 km.

The L3 instrument requirements are summarized in Table 2. They are derived from L1 science and L2 measurement requirements considering the spacecraft velocity (~4–7 km/s for flybys and ~2 km/s for Ganymede orbits) and the expected exospheric concentration from modeling ([9], [10], [11]).

These requirements defined the problem space to be addressed by the team. Although they may appear to be easily achievable for a state-of-the-art instrument, fulfilling them *within the allocated power and mass and in the Jovian radiation environment* (Figure 3) was the main challenge.

Table 2 Key instrument requirements.

Requirement	Value	Unit
Mass range	≥ 300	u
Mass resolution (M/ΔM, below 100u)	≥ 500	–
Measurement cadence	≥ 5*	s
Dynamic range (for 5s spectra)	≥ 10^5	–
Mass (instrument + shielding)	<3+3	kg
Power (before common DCC)	≤ 12	W
Data allocation (whole mission)	~2	GB

4. METHODS

We refer in this paper to three categories of decisions to recount the instrument development: 'given', architectural, and design decisions.

'Given' decisions denotes the choices about the system architecture or design made at the outset of the project or during the lengthy 'shaping phase' [12] preceding the formal initiation of the project. We defined this category of decision to distinguish what was an input to the development work (the 'given' decisions) and what its output (the architectural and design decisions). For NIM, some of the 'given' decisions resulted from incentives to use heritage and high-TRL solutions (legacy decisions), whereas other ones were made from reasonable evidence that they are the best or only solutions to meet the JUICE science goals, subject to the mission profile and technical and programmatic constraints. The qualifier 'given' highlights the fact that these decisions limited upfront the span of the solution space that the team could explore, and not much work was made by the team to explore alternative solutions. Moreover, it emphasizes their stability, in that they were never called into question later on (with one exception due to a late-test failure).

Architectural and design decisions indicate the choices made during preliminary (Phase B) and detailed (Phase C) design of the instrument after technical and programmatic trade-offs.

Architectural decisions regard the system's form and function, and ought to be made early on because it is hard to change them afterward [13]. Often, they are made under uncertainty, because there are not enough resources to gain sufficient information (e.g., through prototyping and testing).

Design decisions are relative to more specific details about the system or subsystems that often makes sense to address only after having taken other architectural decisions. These decisions are the outcome of in-depth engineering work by a mature project team, and they typically depend on the results of modeling, prototyping, and experiments. Some of these decisions can be postponed to grain more information, as long as they are not on the critical path.

In the course of a system's development that spans over several years, hundreds of decisions are made, and the task of summoning them may look daunting. We follow the 'magic number seven, plus or minus two' [14], to keep this list short and draw attention to the few decisions that mattered the most in the development of NIM.

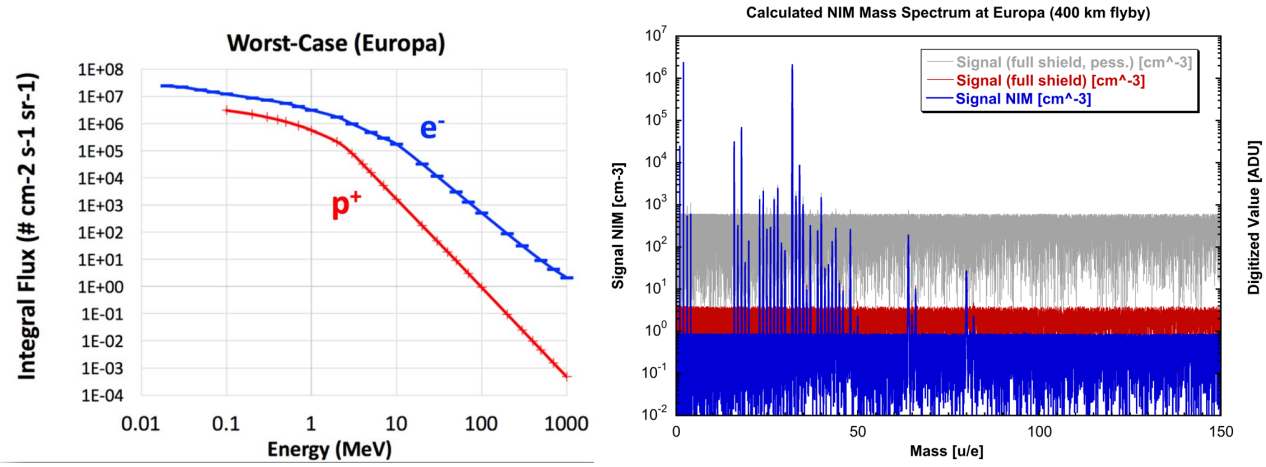

Figure 3 Left: radiation environment at Europa (sizing case for NIM). Right (reproduced from [22]): blue, calculated NIM calibrated mass spectrum at Europa for a flyby at an altitude of 400 km; gray, radiation background in absence of shielding; red, radiation background after shielding. Accumulation time: 5 s, repetition rate: 10 kHz.

Throughout the paper, we occasionally use the formalism of Object Process Methodology (OPM). Just knowing that 'ovals' represent processes and 'boxes' represents objects (instruments or operands of processes) is sufficient to understand the diagrams reported here. The appreciation of the finer details of these representations are left to the interested reader, to whom we suggest the recent ISO Standard ISO/PAS 19450:2015 as a handy reference and introduction to OPM.

5. 'GIVEN' DECISIONS

The following decisions about the instrument are considered to be 'given' because they had been already made by the time the project officially started in 2013, during the early study phase, or were made very soon after the project's initiation:

G1. The instrument be a reflectron TOF MS.

G2. The ionization of neutrals be via electron impact.

G3. The detector be a Micro-Channel Plate (MCP).

G4. The mass analyzer be based on the same ceramic ion optics construction successfully flown on previous missions and be unshielded from radiation.

G5. The instrument electronics be shielded from radiation by a common vault (Card Rack) shared with other PEP instruments, and the mass analyzer be exposed to radiation, except for the shielded detector.

G6. The instrument be interfaced to the spacecraft via primary Direct Current Converters (DCC) and a Data Processing Unit (DPU), provided by other PEP teams in Finland and Hungary and shared with other PEP instruments from Sweden and Germany.

G7. The control of the instrument and the processing of the data it generates (science and housekeeping) be via an application software model running on the common DPU, whereas the high-speed data processing and time-critical functions be performed by the NIM electronics using an FPGA.

These decisions, all architectural, limited the solution space that could answer the problem space set forth by the requirements in Table 2. They nailed down many key aspects of the architecture, as the Level 1 decomposition in Figure 4 and the functional architecture representation in Figure 5 show. Yet, making these decisions early on was necessary to start several lengthy design, procurement, manufacturing, and qualification tasks.

Decision About the Mass Analyzer (G1–G4)

The TOF MS architecture (G1) was selected for its superior capability of meeting the science requirements compared to alternatives, such as a quadrupole MS. Indeed, a TOF MS can

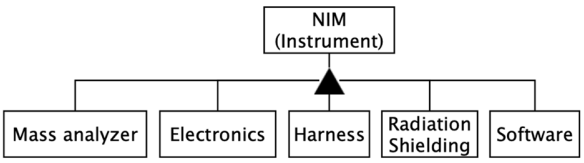

Figure 4 NIM Level 1 Decomposition.

achieve a dynamic range of ~2–3 decades on a single shot spectrum recorded in few μs that cover a broad mass range of >300 u. These spectra are then integrated into a histogram that is the ultimate science result (Figure 5). Working at a repetition rate of 10 kHz, a TOF MS can achieve a dynamic range of ~5–6 decades for integration time of the order of ~1–10 s. Thus it can offer quantitative analysis of samples with many and unevenly concentrated species, while providing a good spatial profiling along the trajectory of the spacecraft.

A quadrupole MS may would perform the same measurement by scanning the mass range and implementing gain switching to achieve the same or better sensitivity. But during the scanning, the sample concentration and composition may vary significantly (the exospheric column height has an exponential profile). Yet, a proper implementation of gain switching and the precise knowledge of the gain at every moment for a quantitative measurement is a major engineering challenge. These properties of a quadrupole MS make it less desirable than a TOF for a mission profile like JUICE's, because a TOF MS acquires spectra with the same gain across the whole m/z range at high repetition rate (kHz).

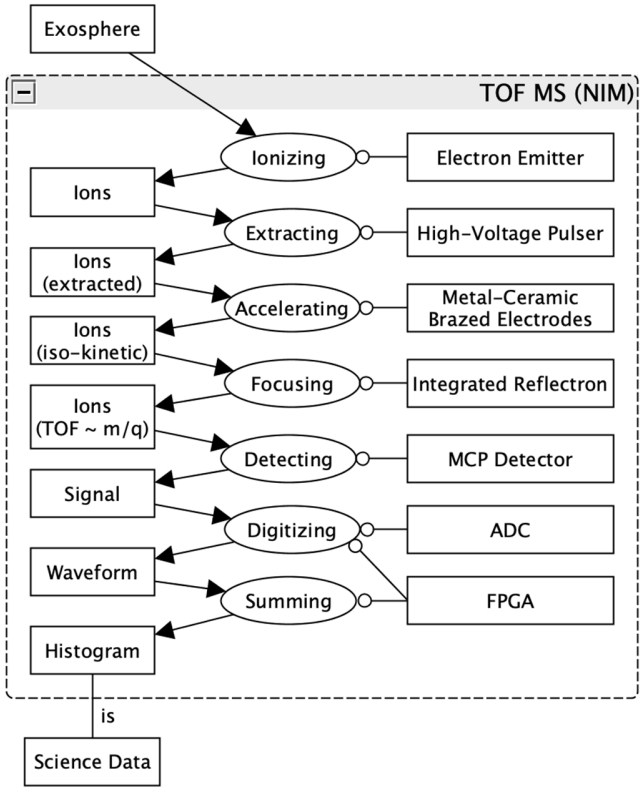

Figure 5 Architecture of NIM, as it was defined by the 'given' decisions at the outset of the project.

Having decided for a TOF architecture, an ion optics with a reflectron (an ion mirror), as opposed to a linear TOF design, was a natural choice considering the many advantages brought about by a reflectron (size reduction for the same flight path length and improved mass resolution). Solutions with a double mirror were briefly considered but soon dropped because incompatible with the allocated mass.

Electron impact was selected (G2) because it is well-established and easy to implement compared to other ionization mechanisms. It is also well-suited for the kind of atoms and molecules expected in the exospheres of Jupiter's icy moons: atomic species and simple inorganic molecules [11]. Besides, this ionization method is sufficiently versatile to accommodate for a capability to see the unexpected, such as more complex organic molecules that might be present in Europa's exosphere, or its purported water plumes.

An MCP detector (⌀ 10 mm) was baselined (G3) from the beginning. Alternatives, such as Channel Electron Multiplier (CEM), were excluded because of speed and size. An MCP can achieve ~500 ps pulse width, whereas a CEM typically generates 2–3 ns pulses. This difference translates in a factor ~2 in mass resolution (M/ΔM) in an instrument like NIM. Also, the reduced mass resolution impact negatively the signal to noise ratio (S/N), hence sensitivity, because in such a 'focusing instrument' M/ΔM ~ S/N. Moreover, a CEM is ~ 50% larger than an MCP for a significant mass penalty considering the need to enclose the detector in a ~10 mm Ta radiation shield. An MCP could provide maximum performance for less mass.

Metal-ceramic brazed elements and screen-printed electrodes (G4) were successfully qualified for previous missions (Rosetta, BepiColombo, Luna-Resurs). Moreover, the resulting 'monolithic' ion optics has several advantages compared to a 'discrete' metal-electrodes design. It is robust to mechanical and thermal loads, thus maintaining very precise electrodes positioning under stress, and it allows to build an 'integrated reflectron' as a seemingly continuous ion mirror [15] (Figure 6). Thanks to the narrow pitch of the spiral screen-printed electrodes, this design has a minimal field corrugation and optimizes the ratio between effective volume and size of the part. However, this technology has long procurement times for ceramic parts and requires complex manufacturing processes, such as brazing of ceramic and metallic electrodes that can withstand the launch loads. Moreover, the radiation hardness of the material used for printing the electrodes at the high total dose of JUICE was unknown (for details of radiation qualification with 18 MeV protons, up to 85 Mrad, see [16]).

Despite these complications, a two-decades-long experience with this technology led to commit early on to this heritage design (legacy decision). As discussed in Section 6 (decision D4), a failure during the PFM vibration test forced to revert this decision just a few months before PFM delivery, and revert to a discrete design to meet schedule. Ex-post, it is apparent that G4 could have been made differently for the ion source.

Figure 6 Integrated reflectors of previously built for Rosetta/RTOF and LUNA/NGMS (EMPA, Switzerland).

Decision About the Radiation Shielding (G5)

The need to shield the electronics and the detector differently emerged from the results of early simulation studies with GEANT4 [17]. On the one hand, maintaining the Total Ionization Dose (TID) of the electronics in the PEP Card Rack (Figure 1) below 50 krad required ~2 mm of Ta [18]. On the other hand, limiting the radiation-induced measurement (< ~10^5 events s^{-1} at the MCP at Europa, corresponding to ~10 counts s^{-1} in the spectrum factoring for the effective measurement time, Figure 3) required to enclose the ~10 cm^3 detector in a ~1kg 1–10–1mm Al-Ta-Al sandwich (details in [19], [20], [21], and [22]). These requirements made a clear case to minimize the volume of all elements to be shielded and to spot-shield the detector. Table 3 outlines the drivers and goals of this shielding strategy.

Table 3 Instrument radiation shielding strategy.

Design to (Driver)	Goal	Shielded element	Shielding element
End-of-life (Fluence, Si TID)	Survive <50 krad	Electronics	Vault (PEP)
Worst-case (Flux, $cm^{-2}\,s^{-1}$)	Measure <10^3 s^{-1}	Detector	Local (NIM)

Decisions About the Electronics (G6-G7)

Given the significant mass required to shield with ~2 mm Ta the electronics, there was a big incentive to accommodating as much electronics as possible inside 'common vaults' to minimize the surface area to be shielded. PEP implemented this strategy by accommodating two sensors' electronics inside a Card Rack (CR), together with common primary DCCs and a DPU (both cold-redundant), providing power,

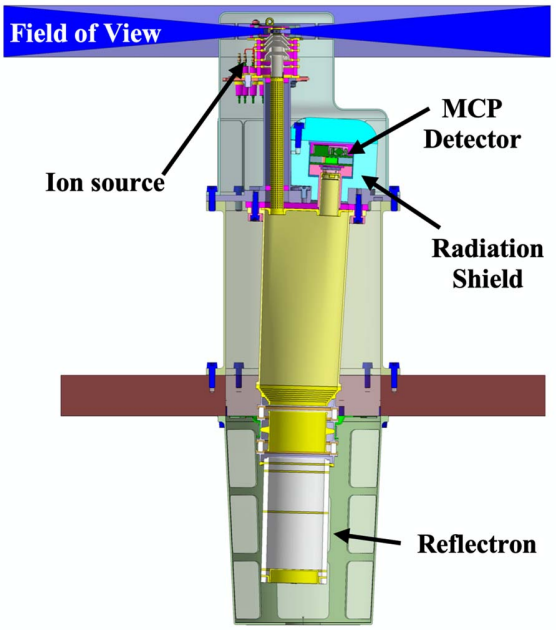

Figure 7 NIM mass analyzer's design as of early 2013. The blue areas show the field of view of the open ion source.

communication, and processing power to the four PEP-Lo sensors electrically interfaced to the spacecraft via the NU.

To minimize the amount of logic in NIM electronics and the associated board space, it was decided that the DPU process telecommands and telemetry, leaving the high-speed and time-critical control functions to the NIM electronics. This decision required the implementation of a 10 Mbps synchronous data interface between the DPU and NIM. It also required that the DPU be available to compress the raw data of NIM (and other PEP-Lo sensors) and transfer compressed data to the spacecraft's mass storage before the next measurement (measurement cadence: up to 1 s^{-1}).

The remaining functions to be provided by the NIM electronics that posed the most challenging requirements were the high-speed acquisition of the waveforms generated by the ADC (minimum 8 bits), their integration to produce histograms (without dead time), and the closed-loop control of the high-voltages of the ion optics. The selection of a 10 bit 2 GSPS ADC (ADC10D1000) as an optimal compromise between effective vertical resolution, power consumption, interfaces, and radiation hardness (100 krad) implied that:

- For a 2 GHz sampling rate, data are provided on four LVDS (Low Voltage Differential Signaling) lanes at 250MHz DDR (Double Data Rate, i.e., using both edges of the synchronous 250 MHz clock). Each of these data lanes is 10 bits wide, and data are spread over the lanes sample by sample so that the data processing unit requires data re-ordering.
- Given the parameters of the different operation modes, the maximum value accumulated in one bin of a histogram requires a 32-bit register.

The team concluded that no CPU-based solution was available in space-grade to meet these interface and memory requirements, together with the stringent timing requirement to provide closed-loop control of the high-voltages. Only FPGA and ASIC-based solutions were an option to fulfill the interfaces, memory, and timing requirements while being low power. Because the time and money to develop an ASIC were not available, an FPGA was baselined.

Early Design Concept

Figure 7 shows the design of the mass analyzer at this time, based on the outcome of these decisions and the first ion-optical simulations. The electronics began to take shape in the form of block diagrams and breadboards.

5. Architectural Decisions

The architectural decisions and trade-offs investigated in Phase B are listed in Table 4, ordered according to a well-known principle of mass spectrometry: 'follow the ions'.

A1. Ion Source

Ideally, NIM would use only an open-source (A1/Option 1), where the exospheric gas passes through a narrow slit and reaches the ionization region without touching any surface, thus allowing for the direct, uncompromised measurement of a pristine sample. However, this requires that the velocity vector of the inflow gas (i.e., of the spacecraft) be within the narrow Field of View (FoV) of such a slit, that is within ±5° about the nadir plane of the spacecraft. Very soon, however, this turned out to be incompatible with the evolution of the spacecraft attitude during flybys, which has to consider the attitude requirements of other instruments, too. This left two options: measure only in the very short time where the ram direction would be in this open source's FoV (~ 20 minutes around a flyby's closest approach) or implement a closed source in lieu of (A1/Option 2) or in addition (A1/Option 3) to the open-source.

Table 4 Key architectural decisions of NIM. The final decision is underlined.

Architectural Decision	Option 1	Option 2	Option 3
A1. Ion source	Open-	Closed-	<u>Both</u>
A2. Mechanism	Rotating (& 1 hole)	<u>Shutter (& 2 holes)</u>	–
A3. Emitter	Cold	<u>Hot</u>	–
A4. Detector	See Table 6		
A5. FPGA technology	Flash (RTG4)	Antifuse (RTAX)	<u>SRAM (Virtex-4)</u>
A6. PCB interconnect	External (backplane)	Internal (rigid)	<u>Internal (flex)</u>

A closed-source can be implemented with a so-called antechamber, a sphere placed on top of the instrument with one or more holes. This measurement concept is well-known and it has been successfully implemented in the past in space for Earth observation [23] and in interplanetary missions, including ONMS on Pioneer Venus [24] and NGIMS on MAVEN [25]. This solution allows measuring along the whole hyperbolic trajectory of a flyby because it provides a ~2π FoV about the axis of the hole(s) in the sphere. Besides, the sphere thermalizes exospheric neutrals and ions that are too energetic to be 'captured' by the open-source (i.e., > ~10 eV) thus extending the energy range of the instrument. Nonetheless, this sphere introduces the possibility of chemical modifications during the multiple impacts of the sample on its inner surfaces (e.g., fragmentation). This is undesirable as it may introduce artifacts in the mass spectra and complicate the reconstruction of the sample composition.

The preferred solution from a science perspective was to implement both an open and a closed source (A1/Option 3), the former used whenever the velocity vector is in its ±5° FoV, and the latter used in all other situations. This decision implied a substantial redesign of the mass analyzer, additional construction and operational complications, as well as a mechanism to switch between the two FoV (A2).

The changes to implement both sources, while feasible within the allocated mass and power, implied additional complexity in all domains: science (calibration of different modes), mechanics (implementation of mechanism), electronics (high-voltage design), FPGA and software (handling of multiple states and modes). Prioritizing science performance over technical and programmatic implications and risks, the team decided to implement both an open and closed source. This decision was not made based on a quantitative evaluation of the financial and schedule risk vs. science return but based on the perception that sufficient resources were available to accommodate this new scope, at the condition that the mechanism could be based on commercial motors modified and qualified in-house (see Section 6, D1).

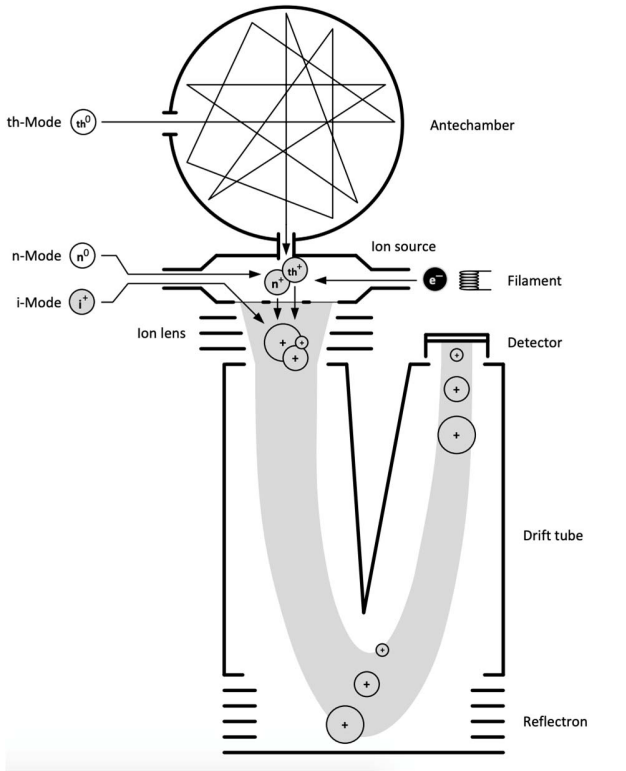

Figure 8 Sketch of NIM operational modes as results of taking decision A1/Option 3 (reproduced from [26]).

Figure 8 represents this decision and the instrument operational modes: 'thermal' (measurement of thermalized exospheric ions and neutral gas via the ante-chamber), and 'neutral' and 'ion' (measurement of exospheric/neutrals or ions via the open-source with/without electron emitters on). The viability of this architecture was simulated with SIMION and verified with the instrument prototype [26].

A2. Mechanism

The switching between the two FoV of the instrument (open and closed source as per A1) had to be realized within ~1s to avoid losing precious measurement time and spatial resolutions (spacecraft flyby velocity: ~4-7 km/s). Two designs were considered (A2): a rotating upper half of the sphere and a fixed sphere with a shutter (Figure 9).

The rotating sphere had a single hole at an angle of 30° from the axis of the mass analyzer (+Z) that, through rotation of the upper half of the sphere, could be oriented in the direction of the spacecraft's velocity vector. Moreover, by placing the sphere at a certain angle, the channel between the closed and open source could be blocked thus allowing to switch between the two FoV. The fixed sphere had two fixed holes at the same angle but towards the +Y and -Y axis, respectively, of the spacecraft's reference frame (to maintain the flexibility of flying the spacecraft in any of the two directions during a flyby).

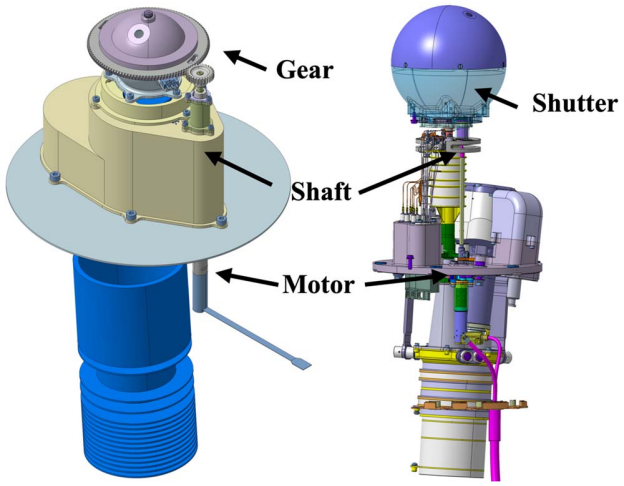

Figure 9 Left: rotating half-sphere design (A2/Option 1); right: fixed sphere with shutter design (A2/Option 2).

The switching between the open and the closed sphere was realized with a shutter closing and opening the small channel at the bottom of the sphere. The trade-off between the two was between performance and complexity: the rotating sphere ensured perfect alignment between the orientable hole and the spacecraft velocity vector, and a minimum ratio between the open and closed area, but it was more complex to implement. Initially, the rotating sphere was selected and a detailed design developed (Figure 9, left), but another requirement forced revert this decision and ultimately opt for the fixed sphere with shutter (Figure 9, right): cleanliness.

Indeed, it was realized that the rotating upper half of the chamber could not be effectively thermally coupled to the rest of the ion source and, therefore, it could not be decontaminated in flight, before each flyby, using the ceramic decontamination heater inside the ion-source. Accordingly, the upper half of the chamber would act as a cold-trap, potentially cumulating contamination during ground operations and in-flight in a critical location of the instrument (i.e., the sample introduction system). On the other hand, the fixed sphere could be heated efficiently, together with the rest of the ion source, at >80 °C, using the 5 W screen-printed ceramic heater in the ion source (details about heater's material and radiation qualification in [16]).

A3. Emitters

The ionization of neutrals via electron impact is typically performed using electors of ~70 eV generated by a cathode, for a current from ~0.1 to ~1 mA. Both 'hot' and 'cold' cathodes exist. The former consists of thermionic emitters, and the latter of a variety of technologies based on field-emission: Spindt cathodes (Sri International Inc., see [27] and [28]), Field Emitters Arrays (e.g., all-metal FEA from the Paul Scherrer Institute, Villigen, Switzerland, [29]) and carbon nanotubes [30]. Cold cathodes require as little as ~100 mW to operate, whereas hot cathodes require at least ~1 W; hence, there is a clear advantage in using cold cathodes on a power-constrained instrument like NIM.

Both hot and cold cathode emitters have spaceflight heritage. Hot cathodes were implemented in RTOF [3] on Rosetta, which included W(Re 3%) wires mounted on a spring-loaded socket. This design had the advantage of spreading emission along the length of the wire, thus allowing for higher emission current before hitting the limits imposed by space-charge effects. Cold cathodes were implemented on the Neutral Gas Experiment onboard the Vega spacecraft to the Halley comet in 1986 ([31] and [32]) and in the COPS ram ion source of Rosina [3] on Rosetta.

Despite the advantages of cold cathodes, the team ruled out this solution after consulting with experts in the field and realizing that there were no off-the-shelf solutions that could be implemented without a significant effort to demonstrate their suitability and reliability for the mission. In particular, at the required current level, there were unresolved reliability concerns of these technologies related to oxidation and adsorption on the emitter surface, which would be difficult to address. As far as carbon nanotubes were concerned, there were also emission current stability concerns. Finally, lack of evidence that these technologies could operate and survive in the harsh Jovian radiation environment made them TRL ~3.

Table 5 Trade-off between thermionic emitters.

Property	Y_2O_3 (baseline)	BaO (backup)
Lifetime (cycles)	*>10'000*	1'000
Power (W at 300 μA)	1.2	*0.85*
Emission at 1 W (μA)	> 50	*600*
Conditioning	*Simple*	Complicated
Heating current (A)	*0.9*	1.15
Venting to air	*No issue*	Cathode poisoning

Eventually, thermionic emitters based on enhanced-lifetime Y_2O_3 and BaO coated discs (Kimball Physics Inc., USA) were chosen as baseline and backup solution (Table 5), respectively. Notwithstanding the higher power consumption (~1.5 W after all losses are accounted for), thermionic emitters were very mature off-the-shelf components with space heritage (e.g., BaO was implemented in STROFIO for BepiColombo) and were expected to be robust to radiation effects. Thus, they carried a much lower risk. Moreover, long lifetime tests were necessary to prove that the filament could survive the ~10,000 h of operation for the entire mission, thus calling for a quick convergence on a technology to build and start these tests as early as possible. At the time of writing, seven filaments of each kind have been run at a nominal emission current of 300 μA for ~2,000 h of operation, including periodic on-off cycling every 8 h, showing nominal performance. Cold cathodes remain an attractive option for future missions, but a dedicated program is needed to increase their TRL beyond 3–4.

A4. Detector

As a key element for the performance of the instrument, the MCP detector was subject to plenty of attention in Phase B. There was an impelling need to finalize its baseline and build a flight-like detector to verify experimentally its capability to measure at Jupiter (with Europa instantaneous flux as sizing case). The four decisions to be made about the detector are summarized in Table 6.

Table 6 Detector decisions; the second option is generally preferable but harder to implement than the first one.

Decision	Option 1	Option 2
I. Anode	Single	Double
II. Floating	No	Yes
III. Signal read-out	Single ended	Double ended
IV. Anode	Disc	Spiral

I. Whether the detector should have a single or a double anode. The latter has the advantage of allowing for two signal lines with different gains to be implemented [33], for higher dynamic range, redundancy, but also increased complexity of implementation (more signals to be routed through the shielding, extra space required in the electronics).

II. Whether the detector should be floating or not. The former gives the advantage of more degrees of freedom in the ion-optics design and detector operation because the final potential of the ions is not constrained by the ~2 kV of the front-plate of the MCP detector assembly, but it requires to implement ~nF capacitors on the signal path next to the anode. Such capacitors have poor high-frequency performance and are voluminous, thus working against the goal of minimizing the detector's size to minimize the shielding mass.

III. Whether a single (50 Ω) or double (100 Ω) ended signal read-out should be implemented. The latter gives the advantage of more signal (due to the lack of the termination resistors to ground), more freedom of selecting the anode impedance due to the presence of a transformer, and a better common-mode noise susceptibility if well-balanced. However, this has the disadvantage of requiring more custom (most standard parts with good high-frequency performance are tuned for 50 Ω). Moreover, feeding the detector signal directly to the ADC input (which is also differential) did not seem feasible with sufficient performance. This also required the implementation front-end gain stage, which meant a conversion to single-ended somewhere along the signal path or a differential gain stage, such as a balun, which did not exist with sufficient bandwidth (from ~DC to ~1 GHz).

IV. Whether a disc or spiral anode should be implemented. The former provides larger signals, but not a perfect impedance matching, whereas the latter provides a better matching, but a somewhat lower signal due to the impedance termination at one side of the spiral.

Different anodes designs were conceived (Figure 10) and the expected pulse width was calculated for different types of PCBs with ε_r ranging from 2.9 to 10.2 using PCB Toolkit (v6.64, Saturn PCB Design, Inc.).

Figure 10 Different type of MCP detector anodes: circle, broad spiral, narrow spiral, and double spirals (last two). In all cases, outer anode ⌀ = 8 mm, red circle gives the active MCP area.

The resulting pulse width was ~170–270 ps and 480–780 ps for anodes with 2 and 7 spiral turns, respectively, with the lower values of the range for ε_r = 2.9 and the higher values for ε_r = 10.2. Note that pulse widths below 500 ps are well-matched with the 2 GSPS acquisition rate of the ADC. A selection of these designs was realized and tested in a prototype detector setup.

We decided to implement a single anode design (Decision I) because the double anode design required a more complex solution for the data acquisition using more power, and more PCB space than were available for this design. Alternative electronic designs, using newly available parts that had not space heritage yet, would have met the power and PCB space requirements, but presented a significant development risk and thus were rejected.

Given the test results, a single-spiral anode with 4 turns and 0.9 mm width was selected (Decision IV, similar to the second design in Figure 10) as an optimal compromise between pulse width (290–470 ps) and impedance matching.

While we managed to overcome most of the problems of a double-ended detector and build a working laboratory prototype, the performance was not good enough to justify the effort to implement this design in flight-quality, also considering that significant uncertainty remained about its feasibility. So single-ended was selected (Decision III).

The results of ion optics simulations made a strong case for selecting a floating detector (Decision II), despite the disadvantages due to the bulky high-voltage capacitors. To minimize the volume of the detector, a compact design based on a folded rigid-flex PCB was devised. The resulting detector has a volume of only 8 cm^3 (Figure 11). This design, enclosed in a 1–10–1 mm Al–Ta–Al radiation shield weighing 1.1 kg, was verified by simulation and experiments with 11–345 MeV (details in [19], [20], [21], and [22]).

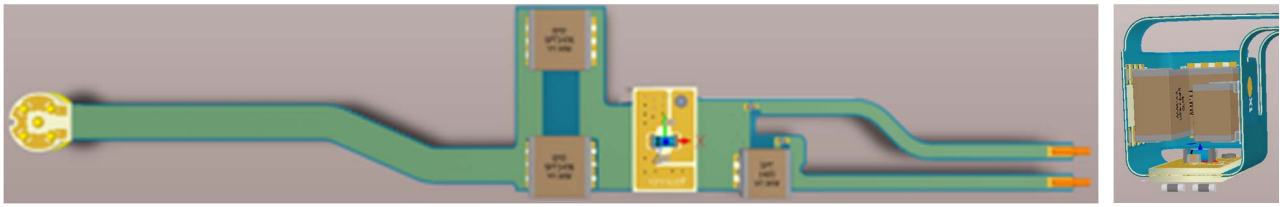

Figure 11 Left, flat rigid-flex PCB (120 x 35 mm); right, folded detector (20 x 23 x 23 mm).

A5. FGPA

The most critical architectural decision about the electronics design was the selection of the FPGA, because of the impact on the electronics design, mass and power, and programmatic aspects. Indeed, a different choice of FGPA leads to different auxiliary components needed for its implementation (programming), workflows (depending on whether or not it is reprogrammable), power consumption (a very scarce resource!) and ultimately impact on cost and schedule. At the time of making this decision, in early 2017 (PDR), a new component was being launched on the market, Microsemi's RTG4: a radiation-hardened by design and low-power FPGA. This component would have perfectly fit the requirements of NIM and was indeed chosen as the initial baseline (Figure 12, top). However, this brand new FPGA was considered by ESA to be not enough mature for JUICE; therefore, the team had to devise alternative solutions using components that were already available and deemed acceptable for flight.

Two alternatives were identified, based on reprogrammable (Xilinx's Virtex-4) and non-reprogrammable (Microsemi's RTAX-4000) chips. The latter required a multi-chip architecture requiring as many as four FPGAs because of the limited memory resources of the RTAX-4000. Specifically, 192 kB of BRAM is needed to store a complete histogram compared to 67.5 kB available in one chip. Solutions to use external fast SRAM were prohibitively expensive in terms of power consumption (~2–3W) because the address and data ports of the external chip has to be running during the whole acquisition time, whereas for internal memory only the ports of one BRAM per data lane are active at any given time.

A design based on the reprogrammable Virtex-4 would be identical to the RTG4 baseline design except for the MRAM needed to hold the FPGA configuration image and a small FPGA or microcontroller needed to load the FPGA's SRAM based configuration memory at power-up. In principle, even a simpler solution to configure the FPGA using an external PROM (using the so-called master-serial mode) exists, but the only identified space-grade parts to do so (XQR17V16 from Xilinx and 3DPO64M08VS2299 from 3D PLUS) were rated only at 50 krad TID, thus not meeting the ≥100 krad requirement for the electronics in the PEP electronics' vault (CR designed for 50 krad, leading to 100 krad with a margin of 2). Table 7 summarized the key findings of the detailed trade-off study that led to selecting Virtex-4 as baseline (A5/Option 3).

Although this solution provided the benefit of the flexibility of a reprogrammable FPGA, which can be updated even after launch, it introduced significant design complexity. First, Virtex-4 does not have any native Triple Module Redundant (TMR) flip-flops. Therefore, three standard flip-flops had to be combined, which could be done to some extent by the synthesis tool, but also at the level of the functional blocks. This also posed a risk, because an improper implementation of TMR could result in a logic yet more susceptible to SEUs. Moreover, a TMR design created from standard flip-flops is vulnerable, in that the necessary interconnects between the flip-flops are controlled by an SEU-susceptible configuration memory. Therefore, it was mandatory to implement a scrubbing mechanism that periodically refreshes the FPGA configuration (from a calculation of expected error rate, scrubbing rate should be once every 1–5 minutes). Finally, TMR at minimum triples (or more, depending on the actual design) the required logic resources, and a higher level of utilization may lead to a yet higher power consumption.

All in all, the choice of the FPGA design of NIM is far from the ideal technical solution that could have been implemented with state-of-the-art technology, but it was considered the best solution within the constraints of the project.

The final design baseline includes a Microsemi's RTSX72 non-reprogrammable FPGA plus an MRAM to configure and scrub the Virtex-4. The system also has the flexibility of configuring the Virtex-4 via the common DPU, which takes much longer but is a convenient fallback solution.

A6. PCB interconnect

The size of the electronics vault was estimated based on the PCB area of previous similar instruments built by the team, resulting in the allocation of two 125 x 130 x 58 mm frames. Early design concepts of the electronics spanned across several boards, including a mixed-signal board, as follows:

i. *Controller PCB*, a half-frame board accommodating FPGA, ADC, the detector front-end, and the mechanism motor controller.

ii. *Pulser PCB*, a half-frame board hosting the high voltage pulser circuit.

iii. *Low-voltages PCB*, a half-frame board accommodating the low-voltages power supply for the ion source's electrodes and the controller of the electron emitters.

iv. *High-voltages PCB*, a half-frame board including all high-voltage power supplies for the electrode of the ion source, the reflectron, and the detector.

v. *Programmer PCB*, a small satellite board attached to the controller holding the components necessary to program the Virtex-4.

Boards ii, iii, and iv had to be connected to board i, where the instrument control logic relies. How these PCBs would be connected was critical because it had widespread effects on the design of the NIM electronics, of the NU CR in general, and ultimately on the mass of the instrument.

Table 7 Decision matrix for the selection of the FPGA; + means better, - means worse.

Criterion	RT4G150		RTAX4000SL		XQR4VFX60 (Virtex-4)	
Power cons.	++	2.88 W	-	4.05 W	-	3.96 W
Extra mass	++	0 g	- -	+470 g	- +	~45 g (with MRAM) 0g (with PROM)
Design process	++	Flexible	- -	One shot	+ -	Flexible (with MRAM) Less flexible (with PROM)
Radiation hard	+	By design	+	By design	-	By screening
TMR	+	FF & SET filters	+	FF	- -	To be implemented
Configuration	+	Flash memory	++	Anti-fuse	- -	SRAM (need scrubbing)
Flight heritage	-	None	++	Extensive	+	Some
Assembly process on PCB	-	None approved (CG1657)	++	Well known (CQ352)	+	Project qualification (CN1144)
Cost estimate	+	~$250,000	- -	~$1,100,000	++	~$100,000
Availability	-	New component	+	Available immediately	+	Available immediately
Risks	Results of EV / QML-V qualification tests. Potential PCB assembly issues.		Difficult design process. High cost.		Development efforts to implement TMR and scrubbing.	
Non-compliances	None.		Exceed mass and power allocation, do not meet all science requirements.		Exceed mass and power allocation.	

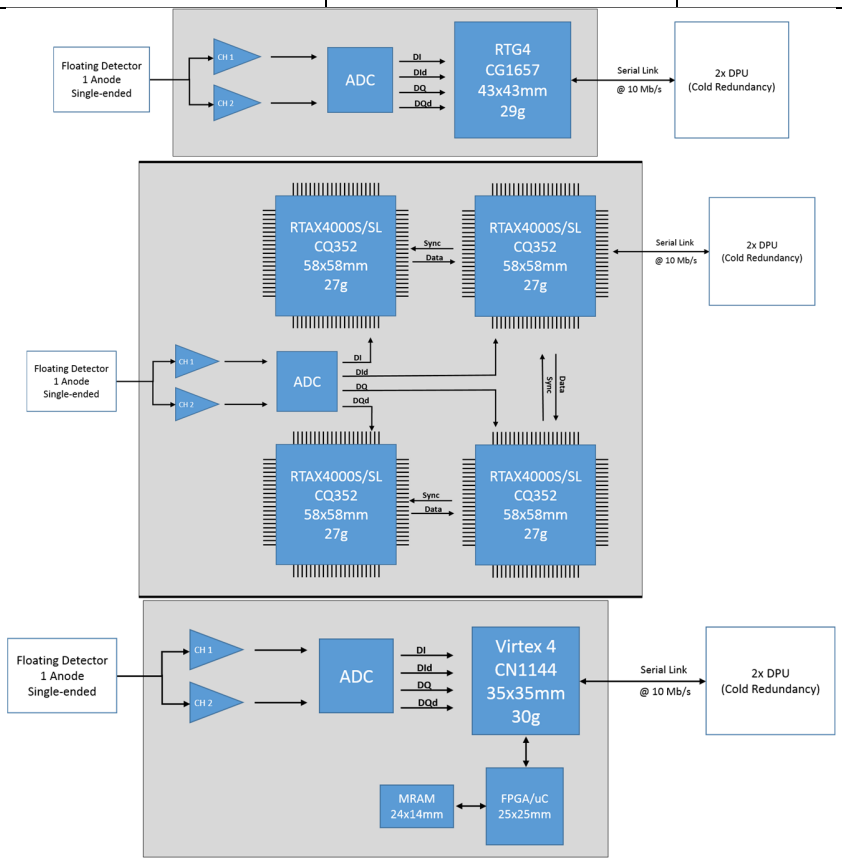

Figure 12 The different designs of the front-end and high-speed data acquisition via FPGA considered for NIM in Phase B (2016) based on RTG4 (top), RTAX4000 (middle), and Virtex-4 (bottom). A nearly identical diagram can be drawn for the bottom solution with a 16x17 mm PROM instead of an FPGA or a microcontroller together with MRAM.

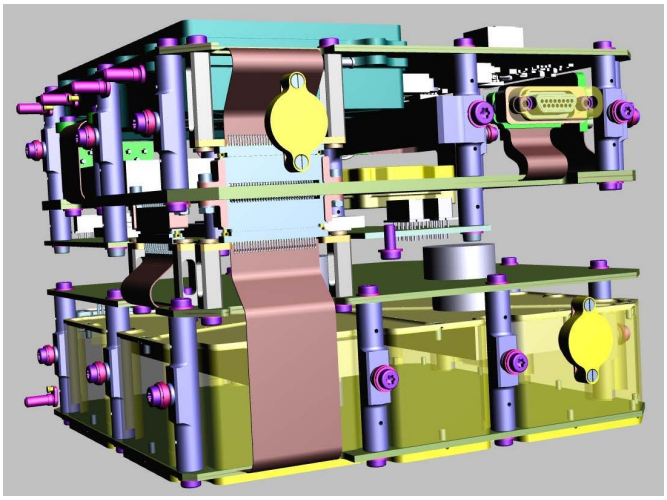

Figure 13 Rendering of the interconnection among boards by means of rigid-flex PCBs (A6 / Option 3).

The trade-off for the PCB interconnect was the following:

- An interconnect external backplane (A6/Option 1) was preferable for the electronics design, as it maximized the board area available for the placement of components. However, it created a dependency with the mechanical design due to the time needed to finalize the definition of the connectors. Moreover, closing the opening in the 2 mm Ta-thick electronics vault, the CR, to avoid creeping-in radiation is all but a trivial task, hence increasing the complication and risks associated with the CR mechanical design.

- An interconnect with internal rigid connectors (A6/Option 2) was preferable for manufacturability, as it allows to rely on standard rigid PCBs. However, rigid connectors require plenty of board area that cannot be used for placing components, thus increasing the risk that the allocated board space be insufficient. Because of the heavy mass penalty associated with an increase in the dimension of the CR (either with an extra frame or with larger frames) this solution had a high-risk of forcing later to descope functionality to fit in the defined frame size, or to exceed the mass allocation.

- An interconnect with internal flex connectors (A6/Option 3) would overcome the limitations of the other two solutions, and completely decouple the problem of the internal connection of electronics with the mechanical design of the CR frames, but at the cost of the high complexity and risk of manufacturing many-layers rigid-flex PCBs.

Eventually, Option 3 was baselined (Figure 13) on grounds of its apparent benefits, and somewhat not fully aware of the manufacturing risk that this solution was embedding. Indeed, the controller PCB ended up being an 18-layer design, whose manufacturing was considered to be of the highest risk by the supplier. Mitigating this risk required a layout rework (~1 month of schedule delay) and the acceptance of the possibility that the manufacturing of the board might fail. Although everything resolved for the best in the end, ex-post it would have been appropriate to consider the PCB manufacturing risks in more depth during the performance of this decision's trade-off.

6. Design Decisions

There is always some degree of ambiguity about what is to be considered an architectural or a design decision. An instrument like NIM is the outcome of hundreds of decisions, and there is a fuzzy boundary between a handful architectural decisions that ought to be taken early on and cannot be postponed (barring the perdition of working in a vast solution space), and the rest of design decisions that can be defined as part of 'normal work', as we idiomatically said of the application of engineering skills to solve a well-defined challenge.

While it is easy to call a very local choice that has no impact on the rest of the system a design decision (e.g., choosing a particular electronic component for a memory, or a specific conductive coating of a non-metallic parts) there are several decisions at the 'mesoscale' whereby drawing a line is not trivial. While criteria exist to qualify a decision as architectural [13], the boundary between architectural and design decisions remains fuzzy and somewhat dependent on the particular perspective that one takes on a system. For limitation of space, we focus hereafter on a selection of design decisions. In the end, we provide an overview of the design that synthesizes other decisions that we cannot discuss here.

D1. Motor Magnet

To operate the shutter mechanism, a modified commercial motor was baselined. Two alternatives were considered: brushless DC servomotors series 0824 (⌀ 8 mm x length 24.1 mm, mass: 5.2 g, NdFeB magnet) and 1628 (⌀ 16 mm x length 28 mm, mass: 30 g, SmCo magnet) by Faulhaber Minimotor SA, Switzerland. The former was better because of the smaller size and lower mass, whereas the latter was better because of the higher radiation hardness of SmCo compared to NdFeB [34]. While a ⌀ 8 mm motor with SmCo magnet was feasible, a standard magnet of that size was not available and a new dimensioning of the coil was required, for a lengthy and expensive custom design.

Table 8 A selection of design decisions about NIM.

Design Decision	Option 1	Option 2
D1. Motor magnet	SmCo	NdFeB
D2. Emission controller	DC	AC
D3. High voltage pulser	1 switch	2 switches
D4. Ion source electrodes	Nb+Ti/Mo	MoCu
D5. Automated optimizer	Yes	No

To make a decision, radiation tests were performed to verify the degradation of the two magnets at the dose level of the mission. Both commercial motor's NdFeB and SmCo magnets were irradiated with 18 MeV p^+, at the same cyclotron facility described in [16], up to a target dose of 15 Mrad (mission dose behind ~2 mm Al x margin of 4), with a 50 nA beam current for 45'. The magnets were mounted on a rotating mechanism allowing to uniformly expose it to the beam inside the irradiation chamber in vacuum. An additional irradiation with the static magnet and a Pt-1000 temperature sensor bonded on its surface was performed to exclude thermal effects. The magnetization was measured before and after irradiation with a Gauss-meter and a custom adapter ensure reproducibility of the probe positioning.

The irradiation on the rotating magnets causes a loss of magnetization of ~16% for NdFeB and ~2% for SmCo (the latter considered to be within the measurement error). The temperature of both (static) magnets during irradiation never exceeded 80 °C, thus excluding that losses of magnetization could be due to exceeding the Curie temperature at bulk level (~300 °C for NdFeB and ~700 °C for SmCo). However, this could not exclude damages due to local thermal effects.

To understand the nature of the observed damages, ~5 months after irradiation, when the magnets were not radioactive anymore, samples of the irradiated magnets were sent to the motor provider for characterization and re-magnetization. The NdFeB sample showed magnetic moment losses not exceeding 10%, which could be explained in terms of annealing effects, or differences in the measurement setup (manual measurement at the irradiation facility with handheld magnetometer compared to a better measurement with Helmholtz coil). After re-magnetization, the NdFeB magnets recovered the original magnetic moment entirely. The SmCo sample was within ±1% the magnetic moment before irradiation, indicating that it did not experience any radiation damage or that annealing occurred. These results demonstrated that the radiation did not induce significant irreversible structural changes in the magnets, and probably only caused local demagnetization, due to exceeding the Curie temperature, that could be fully recovered with a re-magnetization. These thermal effects could be considered an artifact of the accelerated dose rate of ground tests compared to space, thus granting that the performed test be indicative of a worst-case scenario that will hardly be approached in reality. In any case, even considering the worst-case loss of the magnetic moment of the NdFeB sample (~16%), the residual magnetic moment was yet higher than that of a SmCo (weaker) magnet of the same size (~30% lower than for a same-size NdFeB magnet). Therefore, the off-the-shelf NdFeB commercial motor was baselined, with minor modifications performed in house to make it suitable for flight (Parylene coating of the magnet, use of dry MoS_2 lubricant, and replacement of plastic parts).

D2. Emission controller

Two different types of emission controllers were considered, using DC or AC to power the thermionic emitters, both of which had a heritage of implementation in space-grade (TRL 8). An engineering model of the AC filament controller (heritage design from [6]) showed an efficiency ~10% higher for the same type of ~1 W thermionic filament than a previous DC controller after considering all DC/DC converters efficiency. Therefore, an AC controller was selected and implemented (Figure 14), despite the disadvantage of having a ~30 kHz frequency that could be an EMC concern, and the less reliable housekeeping value of heating and emission current.

D3. High-Voltage Pulser

The performance of a TOF MS is highly sensitive to the shape of the high-voltage pulse applied to extract the ions in the acceleration region of the ion source. Ideally, a perfect rectangular pulse with a height of ~500–800 V and a duration of a few hundred ns is required. In practice, the performance of switches (MOSFETs) available in space-grade, derating requirements, and high-frequency effects (e.g., Gibbs phenomenon at sharp pulse edges) only allow to approximate this ideal behavior. For NIM, the 100 krad radiation hardness requirement limited the choice of high-voltage MOSFETs to a handful of candidates: Fuji's 2SK4189 and 2SK4190, and International Rectifier's IRHNJ67434 and IRHNJ67C30. The latter was baselined because of the better voltage rating and lower capacitance compared to the other components.

Yet, the desire of a ~500–800V pulse height led to a trade-off between two designs: using one or two MOSFETs in cascade (Figure 15). The former is limited by the 80% derating requirement to 480V but faster, ~5–6 ns fall time, whereas the latter allows to cover the full range of voltage after

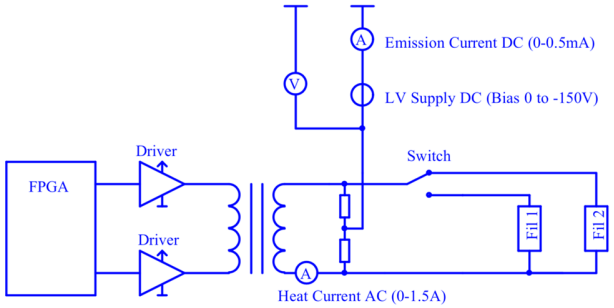

Figure 14 Simplified schematics of the AC filament controller, showing the two cold-redundant filaments.

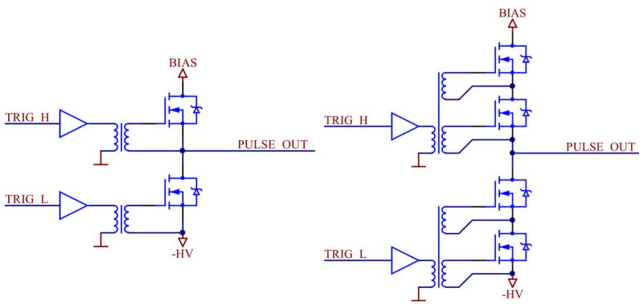

Figure 15 Simplified schematics of the 'fast' (left) and the 'slow' (right) pulser.

derating but is slower (+2–3 ns). Measurements with engineering models and the instrument's prototype (Figure 16) showed that the two-switches ('slow') design led to low mass resolution for low masses (<100 u) and a loss of sensitivity for pulse heights > ~400 V, thus failing to deliver the main utility of this design. This led to opt for the one-switch ('fast') design despite the pulse amplitude limitations due to derating. The dependence of the mass resolution on mass, proportional to √m, indicates that the pulser switching speed is a limiting factor of the instrument's performance.

D4. Ion Source Electrodes

Ion sources previously developed by the same team were manufactured as two-pieces electrodes with Ti_6Al_4V (NGMS/Luna-Resurs) or Mo (RTOF/Rosetta) conical electrodes welded to Nb rings, which were brazed on ceramic insulator (Al_2O_3 97.6%). The manufacturing of one-piece electrodes made of Nb was hard, and the Nb surface finish was insufficient for ion-optical applications. On the other hand, Ti_6Al_4V and Mo could not be directly brazed to the ceramic insulators because of the CTE mismatch. Therefore, Nb rings or Ti_6Al_4V plus copper rings had to be used in connection with the ceramic insulator, for a complicated (yet proven) manufacturing process.

During the design of NIM, we identified a new material that could allow for a single-piece electrode design, easy to manufacture, and with the same CTE of alumina: Mo85Cu15, a sintered alloy. By using this material the number of parts and joining processes could be reduced. The trade-off was choosing between a high-TRL and low-TRL solution in consideration of the reduced manufacturing complication.

Extensive characterizations of the new material and processes were performed, including mechanical tests [35]. Based on this positive evidence, the new material was baselined for all ion source electrodes except the last one, maintained in Ti_6Al_4V because it was connected to a drift tube made with the same material (Figure 17).

Nevertheless, the ion source failed unexpectedly during the PFM sensor vibration test in November 2019, with a clear cut

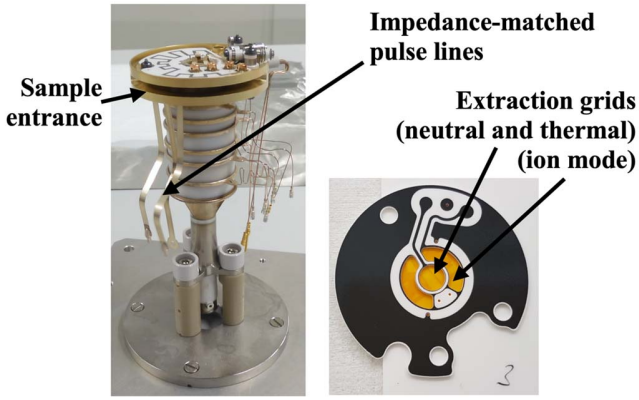

Figure 17 Ion source stack (left) and metallized ceramic extraction electrode (right).

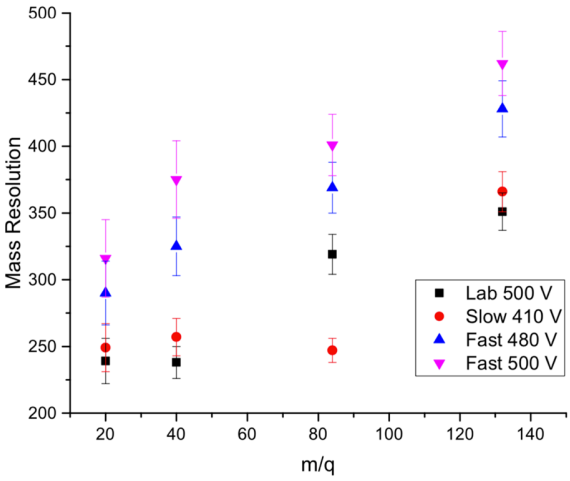

Figure 16 Variation of the mass resolution for the two pulser designs at different pulse heights.

breaking point at the joining between the last electrode and the drift tube (i.e., the only electrode made in the 'old' material Ti_6Al_4V). Ex-post, the most likely cause for this failure was traced to the plating process applied before brazing. All electrodes were plated with TiAlN followed by W and Cr + Au. This process proved to be suitable for the new Mo85Cu15 material, but for reasons that are yet to be understood did not provide a proper surface finish for the old Ti_6Al_4V material, which should have been instead Ni plated, as in the past. This process change lowered the TRL of the part, compromising the structural properties not of the new material, but of the old material treated with a new process.

As the ion source was not mechanically tested at subsystem-level, but only at system-level, the issue was discovered very late in the project, just four months before the deadline to deliver the PFM sensor for integration in the PEP NU. Because the lead time to procure new monolithic ion sources was ~6 months, the monolithic design was abandoned in favor of a new design based on discrete metal-electrodes (Figure 18) that could be built in-house. From an ion optics point of view, the discrete design is already proven as it the same as the instrument prototype [26]. From the mechanical point of view, this is very simple, and an early finite-elements

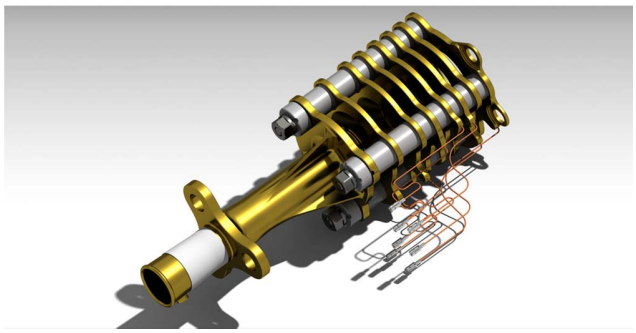

Figure 18 The redesigned ion source using discrete metal electrodes made of gold-plated aluminum (7075), standard ceramic insulators (Al_2O_3 and ATZ) with titanium bolts spot welded to the first titanium lens, and titanium nuts.

model indicated that the first modes could be expected above 300 Hz, thus meeting the requirements. This new ion source is in manufacturing at the time of writing and will be available for integration in the PFM in February 2020.

The lessons learned are two. On the positive side, the Mo85Cu15 remains a possible solution for the realization of robust monolithic ceramic-metal brazed ion sources with a simpler manufacturing process, as the structural failure could not be attributed to the new material, but rather to an incorrect process applied to an electrode made with the old material. On the negative side, it shows, ex-post, that the adoption of a complicated monolithic ceramic-metal brazed ion source (the 'given' decision G4) may have been an unnecessary complication from the beginning for this instrument. Ex-ante, building the 4th instrument in a row using a heritage technology that worked seamlessly for the previous two decades appeared as a natural choice, even if a simpler discrete design might as well have met the requirements. With today's awareness of the risks, a thorough trade-off study, qualification program, and change control will have to be performed for metal-ceramic brazed elements in future instruments.

D5. Automated Optimizer

An automated particle-swarm optimizer turned out to be very effective to find optimal settings of the ion optics of TOF mass spectrometers [36]. This algorithm allows for a broad exploration of the parameter space of an ion optical system in search of an optimal set that maximizes a score function (e.g., amplitude, peak width, or a combination thereof). During this exploration, it can happen that the settings of the ion optics be far away from nominal-operation ones. In this case, the electrons emitted by the filament (~100s μA) may end up on any electrodes of the ion optics and charge it, if such an electrode has not the capability to sink current. When an electrode charges up, the functionality of the optimizer is impaired, because the relationship between the applied potential and the effective potential of that electrode in the next step(s) of the optimization becomes arbitrary. Either the instrument can detect charging, stop the optimizer and power supplies, and wait for discharging before continuing the optimization, or the power supplies of the ion optics shall be designed with the capability to sink the emission current.

On an instrument like NIM, highly constrained in terms of power and board space, there is an incentive to design simple circuitry, such as one-quadrant power supplies. Under nominal settings of the ion optics, the current flowing through the electrodes is substantially null; therefore, a one-quadrant power supply suffices. RTOF [3] on Rosetta, for instance, was designed this way. Unfortunately, this design is incompatible with a particle-swarm optimizer for the reasons related to charging described above. However, implementing a two- or four-quadrants power supply (depending on polarity requirements) approximately doubles the development effort and complexity of the circuitry, thus requiring more board space.

Experience with previous instruments showed improvements in mass resolution and S/N up to factor ~2 by using an automated particle-swarm optimizer instead of a manual optimization of the ion optics. Moreover, manual optimization would be complicated to handle for NIM, because of the long signal travel time between Earth and Jupiter.

The eventual decision for NIM was to implement power supplies with a capability to both source and sink currents to support the optimizer. The emission current during optimization, however, is limited to <150 μA, instead of the nominal ~300 μA, to facilitate the design of converters that could both support optimization and have a very low standby power during nominal operation of the ion optics.

Overview of the Final Design

The final design of the sensor (with the new discrete ion source) and of the electronics are shown in Figure 19 and Figure 20. These representations summarize the outcome of all the decisions discussed here, plus a few more that could not be discussed here for limitations of space.

For example, the structural supporting structure in Figure 19 is different from Figure 7's, which was conceived for the original concept of the NU including an AlBeMet baseplate to which the sensors were bolted onto. This baseplate was

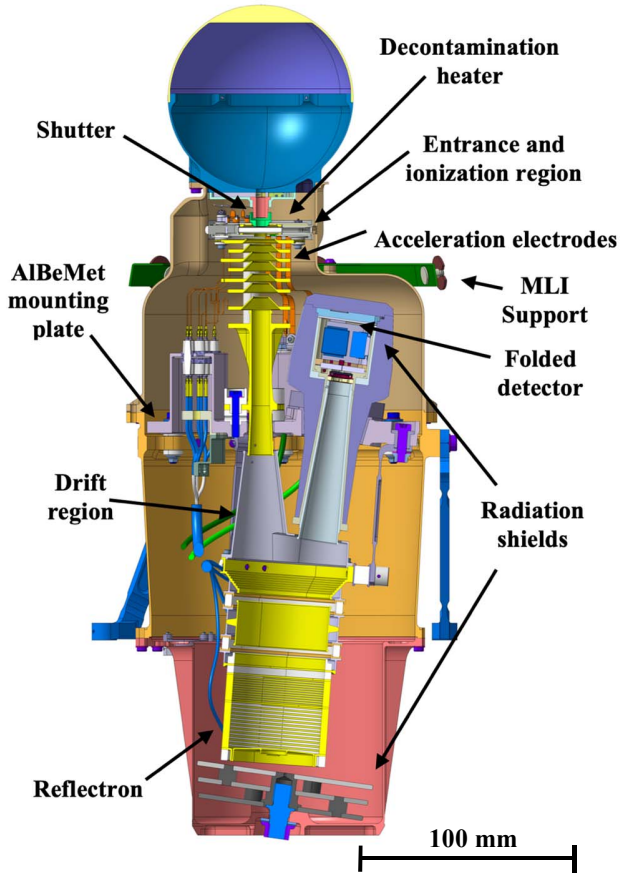

Figure 19 Section of the NIM sensor's flight design.

later replaced by a carbon fiber panel for higher handling safety, requiring a structural redesign of the sensor with an internal AlBeMet mounting plate supported by isostatic feet to compensate for the structural stress due to panel deformation. Above this AlBeMet plate, the only allowed materials are metal and ceramic to maximize cleanliness.

The final implementation of the shielding deviates from that tested in [22] in that the heavy-Z material of the graded shield has been changed from Ta to W85Cu15 for better manufacturability. In addition, the 6 mm Ta disc at the bottom has been split in three 2 mm discs, distance by 4 mm, to take advantage of the increase geometrical deviation of the electrons away from narrow open channel toward the MCP, as suggested by limited experimental results (unpublished) during the detector radiation testing campaign [22].

It is worth noting that the thermal control of the NIM sensor is entirely passive. The unit does not need any survival or operational heater. The whole sensor head is enclosed by Multi-Layer Insulation (MLI) up to the MLI support shown in Figure 19. The part of the sensor above the panel faces the space environment, whereas the part below the panel faces a –50 °C spacecraft cavity. The 5 W heater in the ion source is only operated several hours before a measurement to clean the ion source and the antechamber at > 80 °C.

7. RESULTS

The first mass spectrum measured with the PFM is shown in Figure 21. It has been acquired with the instrument in the configuration of Figure 22. The voltages were optimized by hand starting from the simulation results of the thermal mode.

The measured mass resolution of ^{84}Kr for the residual gas measurement is 305 ± 15 and the S/N 608. Additional measurements were performed with a 2.7 km/s neutral gas beam consisting of hydrogen and krypton in CASYMIR [37]. The mass resolution of ^{84}Kr in thermal mode was 404 ± 25 and the S/N 235. The mass resolution of ^{84}Kr in neutral mode was 417 ± 27 and the S/N 1,456. At the current state, the instrument performance is the same as the prototype [26]. When the sensor will be integrated with the flight electronics, supposed to be better than laboratory electronics, using short cables, mass resolution and S/N are expected to improve.

The replacement of the monolithic ion source with the discrete ion source (see Section 6, Decision D4) is not expected to have a significant effect on performance. Indeed, the prototype, ion-optically identical to the PFM, was realized with a discrete ion source and had the same performance as the PFM with the monolithic ion source. Nevertheless, the calibration of the sensor will have to be repeated.

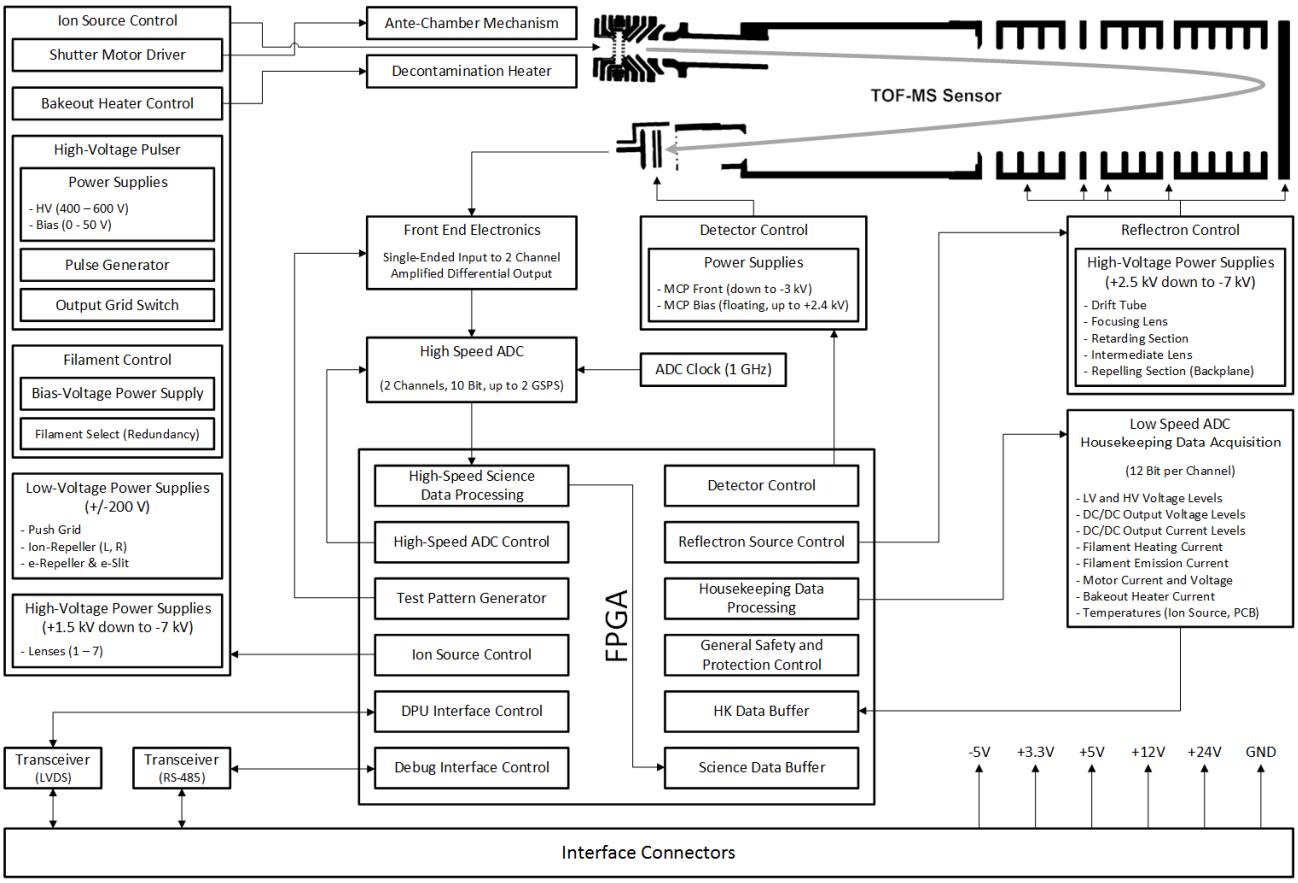

Figure 20 Block diagram of NIM's flight electronics.

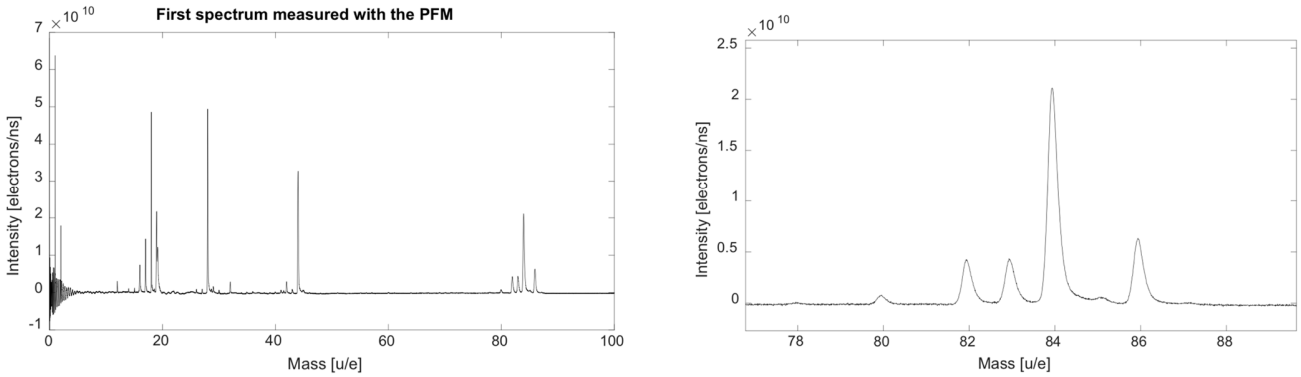

Figure 21 First spectrum measured with the PFM in residual gas mode; full spectrum to the left and zoom-in on Kr isotopes to the right (residual gas pressure $1.5 \cdot 10^{-9}$ mbar, increased by leaking krypton gas into the chamber until reaching $4 \cdot 10^{-9}$ mbar). The spectrum is the result of the integration of 1 million waveforms. A background file recorded with emission current off is subtracted to compensate for the noise induced by the high voltage pulser.

CONCLUSIONS

In this paper, we retraced our path through the key decisions and trade-offs made in the design of a Time-of-Flight Mass Spectrometer for Jupiter's icy moons: the NIM instrument onboard ESA's JUICE mission. We described decisions defined at the outset of the project *(*which we called *'given' decisions*) that bound the solution space explored by the development team, as well as the *architectural* and *design decisions*, and their trade-offs, made in Phase B and C of the project. Throughout, we highlighted technical and programmatic factors affecting these decisions. Moreover, we discussed how a late-test failure during the flight-model vibration test exposed one 'given' decisions that, ex-post and perhaps even ex-ante, should have been done differently.

This account both connects the dots of previously published work and presents new results, including the first mass spectra acquired with the instrument. While this is necessarily a partial description of the instrument's design, history, and results, it does offer a perspective that no deep dive into the many thousand pages of project documentation could offer.

Figure 22 NIM sensor Proto-Flight Model before the start of qualification and calibration in mid-2019.

All in all, we believe that this paper offers a useful collection of ideas, concepts, lessons learned, and insights that can inform the decisions about the architecture and design of future similar instruments.

It is worth saying that all decisions that we made looked the 'right ones' ex-ante, while we strived to achieve the best outcomes 'thinking inside the box' given to us. Therefore, future teams developing similar instruments under different constraints, incentives, and risk appetites could as well opt for entirely different choices.

We trust that describing not only the design solutions that we implemented but also the alternatives that we traded off and dropped can encourage a broad exploration of the design space of future time-of-flight mass spectrometers. If this will lead to yet better instruments and science, the intent of this paper will have been met.

ACKNOWLEDGEMENTS

We acknowledge the contribution of the many people at the University of Bern whose experience and skills were essential for the success of this project. We also wish to thank H.R. Elsener of EMPA for the invaluable collaboration since Rosetta. Moreover, we acknowledge the contribution of the PEP team, which positively influenced aspects of the design of NIM; in particular: S. Karlsson (IRF), S. Jaskulek (JHU-APL), and S. Barabash (IRF). The thorough work of the reviewers is highly appreciated, as it was of significant help and guidance to improve this manuscript.

This project has been funded by the Swiss Space Office, via the ESA PRODEX Office, and the Swiss National Science Foundation.

REFERENCES

[1] Grasset, O., Dougherty, M. K., Coustenis, A., Bunce, E. J., Erd, C., Titov, D., ... & Hussmann, H. (2013). JUpiter ICy moons Explorer (JUICE): An ESA mission to orbit Ganymede and to characterize the Jupiter system. Planetary and Space Science, 78, 1-21.

[2] Barabash, S., Karlsson, S., Wieser, M., Brandt, P., Westlake, J., Mitchell, D., ... & Fränz, M. (2015, October). Radiation mitigation in the Particle Environment Package (PEP) sensors for the JUICE mission. In European Planetary Science Congress (Vol. 10).

[3] Balsiger, H., Altwegg, K., Bochsler, P., Eberhardt, P., Fischer, J., Graf, S., ... & Müller, J. (2007). Rosina–Rosetta orbiter spectrometer for ion and neutral analysis. Space Science Reviews, 128(1-4), 745-801.

[4] Abplanalp, D., Wurz, P., Huber, L., Leya, I., Kopp, E., Rohner, U., ... & Barabash, S. (2009). A neutral gas mass spectrometer to measure the chemical composition of the stratosphere. Advances in space research, 44(7), 870-878.

[5] Hofer, L., Wurz, P., Buch, A., Cabane, M., Coll, P., Coscia, D., ... & Tulej, M. (2015). Prototype of the gas chromatograph–mass spectrometer to investigate volatile species in the lunar soil for the Luna-Resurs mission. Planetary and space science, 111, 126-133.

[6] Fausch, R. G., Wurz, P., Tulej, M., Jost, J., Gubler, P., Gruber, M., ... & Gerber, T. (2018, March). Flight electronics of GC-mass spectrometer for investigation of volatiles in the lunar regolith. In 2018 IEEE Aerospace Conference (pp. 1-13). IEEE.

[7] Griin, E. (1992). F echtig, H., Hanner, MS, Kissel, J., Lindblad, B. A., Linkert, D., Linkert, G., Morfill, GE and Zook, HA, The Galileo Dust Detector. Space Sci. Rec, 60, 317-340.

[8] Brockwell, T. G., Meech, K. J., Pickens, K., Waite, J. H., Miller, G., Roberts, J., ... & Wilson, P. (2016, March). The mass spectrometer for planetary exploration (MASPEX). In 2016 IEEE Aerospace Conference (pp. 1-17). IEEE.

[9] Vorburger, A., Pfleger, M., Lindkvist, J., Holmström, M., Lammer, H., Lichtenegger, H. I., ... & Wurz, P. (2019). 3D□modeling of Callisto's Surface Sputtered Exosphere Environment. Journal of Geophysical Research: Space Physics.

[10] Vorburger, A., & Wurz, P. (2018). Europa's ice-related atmosphere: The sputter contribution. Icarus, 311, 135-145.

[11] Plainaki, C., Cassidy, T. A., Shematovich, V. I., Milillo, A., Wurz, P., Vorburger, A., ... & Brandt, P. C. (2018). Towards a global unified model of Europa's tenuous atmosphere. Space science reviews, 214(1), 40.

[12] Miller, R., & Lessard, D. R. (2001). The strategic management of large engineering projects: Shaping institutions, risks, and governance. MIT press.

[13] Crawley, E., Cameron, B., & Selva, D. (2015). System architecture: strategy and product development for complex systems. Prentice Hall Press.

[14] Miller, G. A. (1956). The magical number seven, plus or minus two: Some limits on our capacity for processing information. Psychological review, 63(2), 81.

[15] Scherer, S., Altwegg, K., Balsiger, H., Fischer, J., Jäckel, A., Korth, A., ... & Wurz, P. (2006). A novel principle for an ion mirror design in time-of-flight mass spectrometry. International Journal of Mass Spectrometry, 251(1), 73-81.

[16] Lasi, D., Tulej, M., Neuland, M. B., Wurz, P., Carzaniga, T. S., Nesteruk, K. P., ... & Elsener, H. R. (2017, July). Testing the radiation hardness of thick-film resistors for a time-of-flight mass spectrometer at jupiter with 18 MeV protons. In 2017 IEEE Radiation Effects Data Workshop (REDW) (pp. 1-9). IEEE..

[17] Agostinelli, S., Allison, J., Amako, K. A., Apostolakis, J., Araujo, H., Arce, P., ... & Behner, F. (2003). GEANT4—a simulation toolkit. Nuclear instruments and methods in physics research section A: Accelerators, Spectrometers, Detectors and Associated Equipment, 506(3), 250-303.

[18] Karlsson, S. (2016, June). PEP radiation modelling report (PA-06.01). Rep. JUI- IRF-PEP-RP-002 v1.0.

[19] Desorgher, L. (2010, March). Radiation simulation study for the PEP-NU on the LAPLACE mission. SpaceIT GmbH, Bern, Switzerland, Rep. JGO- PEP-TN-0901 v1.0.

[20] Tulej, M., Meyer, S., Lüthi, M., Lasi, D., Galli, A., Desorgher, L., ... & Wurz, P. (2015). Detection efficiency of microchannel plates for e^- and π^- in the momentum range from 17.5 to 345 MeV/c. Review of scientific instruments, 86(8), 083310.

[21] Tulej, M., Meyer, S., Lüthi, M., Lasi, D., Galli, A., Piazza, D., ... & Kalla, L. (2016). Experimental investigation of the radiation shielding efficiency of a MCP detector in the radiation environment near Jupiter's moon Europa. Nuclear Instruments and Methods in Physics Research Section B: Beam Interactions with Materials and Atoms, 383, 21-37.

[22] Lasi, D., Tulej, M., Meyer, S., Lüthi, M., Galli, A., Piazza, D., ... & Hajdas, W. (2016). Shielding an MCP detector for a space-borne mass spectrometer against the harsh radiation environment in Jupiter's magnetosphere. IEEE transactions on nuclear science, 64(1), 605-613.

[23] Spencer, N. W., & Carignan, G. R. (1988). In situ measurements of thermospheric composition, temperature and winds by mass spectrometry. Adv. Space Res. Vol. 8, No. 5–6, pp (5)107–(5)117.

[24] Niemann, H. B., Booth, J. R., Cooley, J. E., Hartle, R. E., Kasprzak, W. T., Spencer, N. W., ... & Carignan, G. R. (1980). Pioneer Venus orbiter neutral gas mass spectrometer experiment. IEEE Transactions on Geoscience and Remote Sensing, (1), 60-65.

[25] Mahaffy, P. R., Benna, M., King, T., Harpold, D. N., Arvey, R., Barciniak, M., ... & Johnson, C. S. (2015). The neutral gas and ion mass spectrometer on the Mars atmosphere and volatile evolution mission. Space Science Reviews, 195(1-4), 49-73.

[26] Meyer, S., Tulej, M., & Wurz, P. (2017). Mass spectrometry of planetary exospheres at high relative velocity: direct comparison of open-and closed source measurements. Geoscientific instrumentation, methods and data systems, 6(1), 1-8.
[27] Curtis, C. C., & Hsieh, K. C. (1986). Spacecraft mass spectrometer ion source employing field emission cathodes. Review of Scientific Instr., 57(5), 989-990.
[28] Spindt, C. A. (1968). A thin-film field-emission cathode. Journal of Applied Physics, 39(7), 3504-3505.
[29] Tsujino, S., Beaud, P., Kirk, E., Vogel, T., Sehr, H., Gobrecht, J., & Wrulich, A. (2008). Ultrafast electron emission from metallic nanotip arrays induced by near infrared femtosecond laser pulses. Applied Physics Letters, 92(19), 193501.
[30] Zhang, H., Li, D., Wurz, P., Cheng, Y., Wang, Y., Wang, C., ... & Fausch, R. G. (2019). Residual Gas Adsorption and Desorption in the Field Emission of Titanium-Coated Carbon Nanotubes. Materials, 12(18), 2937.
[31] Curtis, C. C., Fan, C. Y., Hsieh, K. C., Hunten, D. M., Ip, W. H., Keppler, E., ... & Erö, J. (1988). Comet P/Halley neutral gas density profile along the Vega-1 trajectory measured by the Neutral Gas Experiment. In Exploration of Halley's Comet (pp. 360-362). Springer, Berlin, Heidelberg.
[32] Anguero, V. M., & Adamo, R. C. (1998, November). Space applications of spindt cathode field emission arrays. In 6th Spacecraft Charging Technology (pp. 347-352).
[33] Managadze, G. G., Wurz, P., Sagdeev, R. Z., Chumikov, A. E., Tuley, M., Yakovleva, M., ... & Bondarenko, A. L. (2010). Study of the main geochemical characteristics of Phobos' regolith using laser time-of-flight mass spectrometry. Solar System Research, 44(5), 376-384.
[34] Mesa, J. L., Fernández, A. B., Hernando, C., McHenry, M. E., Aroca, C., Alvarez, M. T., & Diaz-Michelena, M. (2014, July). Effects of gamma-ray radiation on magnetic properties of NdFeB and SmCo permanent magnets for space applications. In 2014 IEEE Radiation Effects Data Workshop (REDW) (pp. 1-4). IEEE.
[35] Elsener, H.R., Rheingans, B., Jeurgens, L.P.H., Burgdorf, T., Brüngger, S., Piazza, D., & Wurz, P (2019, May). Brazed metal-ceramic components for space applications. In Proceedings of the 12th International Conference on Brazing, High Temperature Brazing and Diffusion Bonding. DVS-Berichte 353, 207-214. Aachen, Germany.
[36] Bieler, A., Altwegg, K., Hofer, L., Jäckel, A., Riedo, A., Sémon, T., ... & Wurz, P. (2011). Optimization of mass spectrometers using the adaptive particle swarm algorithm. Journal of mass spectrometry, 46(11), 1143-1151.
[37] Graf, S., Altwegg, K., Balsiger, H., Jäckel, A., Kopp, E., Langer, U., ... & Wurz, P. (2004). A cometary neutral gas simulator for gas dynamic sensor and mass spectrometer calibration. Journal of Geophysical Research: Planets, 109(E7).

BIOGRAPHY

Davide Lasi *received a B.Sc. and an M.Sc. in Chemistry from the University of Milano in 2004 and 2006, and an M.S. from MIT in 2018 (System Design and Management). He has been with the University of Bern since 2011, as project manager for the development of three space mass spectrometers, including NIM for JUICE.*

Stefan Meyer *received a Ph.D. in Physics from the University of Bern in 2017, leading the development of NIM ion optics design. Since 2018, he works as Hearing Research Physicist at Bern University Hospital. Prior, he worked as a hardware engineer at RUAG Electronics. He received a B.A. in Electronics Engineering from University of Applied Sciences HTA Biel, Switzerland in 2003.*

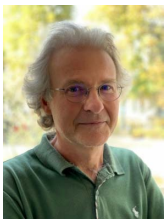

Daniele Piazza *has more than 20 years of experience in the design and development of space instruments. He has a Ph.D. in mechanical engineering from ETH Zurich and started his career in Formula 1. Since 2005 he leads the mechanical engineering group working on space instruments at the University of Bern.*

Matthias Lüthi *holds an M.Sc. from ETH, Zürich (1996) and an EMBA in management of technology from HEC Lausanne (2009). He has more than 20 years of experience as a hardware design engineer and manager in high-tech industries in the US and Switzerland. He is the NIM electronics systems engineer.*

Andreas Nentwig *received a B.Sc. and M.Sc. in Engineering from Bern University of Applied Sciences, specializing in electrical energy technologies and environment. After working for a Swiss company as Project Manager and Engineer for RF & Microwaves systems, he has been analog hardware engineer for NIM.*

Mario Gruber *received a B.Sc. in Computer Science from Bern University of Applied Sciences in 2008. At the University of Bern, he has been responsible for flight and ground software of LASMA and NGMS for Luna and NIM for JUICE mass spectrometers, and he has contributed to the success of CaSSIS on ExoMars' Trace Gas Orbiter.*

Stefan Brüngger *received a B.Sc. in Mechanical Engineering from Bern University of Applied Sciences in 2007. Since 2017, he is pursuing an M.Sc. in Systems Engineering Management at UCL (London). At the University of Bern, he worked as a mechanical design engineer for NIM on JUICE.*

Michael Gerber *has been employed as a systems engineer at the University of Bern since 2014, where he works on ExoMars Cassis and JUICE PEP. He graduated in mechanical engineering in 2006 and moved to the University of Bern from RUAG Aviation where he was a systems engineer on fighter aircraft.*

Saverio Braccini *is a Professor of physics at the Laboratory for High Energy Physics of the University of Bern. He proposed the realization of an innovative medical cyclotron for radioisotope production and multi-disciplinary research at Bern University Hospital. He contributed to developing new accelerators, detectors, and experiments of CERN's LEP and LHC.*

Marek Tulej *received a Ph.D. in Physical Chemistry from the University of Basel in 1999. After his post-doctoral period at Paul Scherrer Institute, he joined in 2008 the University of Bern as an instrument scientist for space missions, including Phobos-Grunt, Marco Polo-R, Luna-Resurs, and JUICE.*

Martina Föhn *received an M. Sc. in physics from the University of Bern in 2017, with a thesis on the scattering properties of charge state conversion surfaces for space applications for the JUICE and the IMAP missions. She is now pursuing a Ph.D. in physics and is responsible for the calibration of NIM.*

Peter Wurz *has a degree in electronic engineering (1985), an M.Sc. and a Ph.D. in Physics from Technical University of Vienna (1990). He has been a post-doctoral researcher at Argonne National Laboratory. At the University of Bern since 1992, he is a Professor of physics and since 2015 head of the Space Science and Planetology division. He has been Co-I and PI for many science instruments for space missions of ESA, NASA, ISRO, Roscosmos, and JAXA. He is PI of NIM and Co-PI of PEP onboard JUICE.*

Journal of Applied Physics ARTICLE scitation.org/journal/jap

Cadmium telluride as a potential conversion surface

Cite as: J. Appl. Phys. **129**, 045303 (2021); doi: 10.1063/5.0033701
Submitted: 18 October 2020 · Accepted: 12 January 2021 ·
Published Online: 29 January 2021

Jonathan Gasser,[1,a)] Martina Föhn,[1] André Galli,[1] Elisa Artegiani,[2] Alessandro Romeo,[2] and Peter Wurz[1]

AFFILIATIONS

[1]Physics Institute, Space Research and Planetary Sciences, University of Bern, Sidlerstrasse 5, 3012 Bern, Switzerland
[2]Department of Computer Science, Laboratory for Photovoltaics and Solid State Physics, University of Verona, Strada le Grazie 15, 37134 Verona, Italy

[a)]**Author to whom correspondence should be addressed:** jonathan.gasser@space.unibe.ch

ABSTRACT

In instruments for low energetic neutral atom imaging of space plasmas, a charge state conversion surface (CS) is used to convert neutral atoms into ions for detection. We investigated a cadmium telluride (CdTe) coated sample as a novel material candidate regarding its suitability to be used as a CS. We measured the efficiency of converting H and O atoms into negative ions by surface scattering, as well as their angular scattering distribution, for energies from 195 eV to 1 keV at 8° incidence angle. Also, the energy distribution of scattered particles was recorded for incident O_2^+ ions, which confirms that molecules are mainly scattered as single atoms. The mean energy loss per atom was about 45%. The negative ion yield from scattering off CdTe was up to 13% for O and about 2% for H, which is comparable to other CS coatings in use. CdTe shows a nearly circular angular scattering cone of width comparable to established CS materials. We conclude that CdTe is a viable CS coating material for ENA instruments in space applications.

I. INTRODUCTION

Spaceborne instruments for energetic neutral atoms (ENAs) continue to be a highly relevant tool for interplanetary and interstellar space plasma research. Reviews on scientific techniques and instrumentation for imaging of space plasmas can be found in Gruntman,[13] Williams *et al.*,[38] and Wurz.[40] Several past and present space missions have been equipped with an ENA instrument at low energies, such as IMAGE,[22] Mars and Venus Express,[3,4] Chandrayaan-1,[2,6,16] and BepiColombo.[24] The well-known IBEX mission[9,20] has brought light on, among others, the global heliospheric structure by observing the plasma of the heliospheric interface via ENAs from Earth's orbit. While IBEX is expected to run until at least 2025, its successor mission the Interstellar Mapping and Acceleration Probe (IMAP) is currently under development,[21] with a low-energetic ENA camera being among the scientific instruments. Most recently, the upcoming JUICE mission (Jupiter Icy Moons Explorer)[10] by ESA also includes two ENA instruments for low- and high-energy ENAs in its particle environment package.[5]

All the low-energetic neutrals instruments for space research rely on an efficient method of ionization for the ENAs to electrically analyze the ENAs.[40] To date, in the low-energy range, the most widely used method and so far the only space-proven is via surface conversion: Neutral particles strike a highly polished charge-state conversion surface (CS) at a grazing angle of incidence and thereby pick up an electron while being scattered. An overview of negative ion sources and their application to accelerator physics and plasma research is given in Faircloth and Lawrie.[7]

The underlying physical theory of particle charge conversion upon surface scattering at a grazing incidence angle is still not understood in full detail. Quite a few theoretical models exist for special types of surfaces such as metals or alkali halides.[19,39] Negative ionization happens via resonant electron transfer from the crystal lattice to the incident atom's electron affinity level. Thus, a low work function in the surface material enhances electron transfer to the atom. However, diamond and other insulator surfaces with high work function showed comparably high negative ionization efficiency,[42] which are probably promoted by surface states.

The efficiency of converting neutral atoms into ions and the scattering properties strongly depend on the CS material. A high yield of negative ions and a narrow angular scattering cone both directly alter the instrument efficiency by improving the throughput of downstream ion-optical elements within the instrument. In space ENA imaging instruments, the CS should at least yield about 1% negative ions for the ENA species of interest (predominantly H and O). Even though this seems a low value, the 1% ion yield is required for an acceptable signal to background level, which is a key criterion especially in low-energy ENA instrumentation.[40] Compared, e.g., to electron impact ionization, with efficiencies of about 10^{-4}, this is still respectable for a passive ionization method. Moreover, this ionization method does not require electrical power, which is a big advantage for space instrumentation. In addition, CS materials for space applications should be chemically stable and mechanically robust on long time scales, without possibly hazardous components, show no degeneration or surface charging effects, and should be readily available at affordable cost. Various materials have been considered and investigated over the past decades (cf., Wurz *et al.*[41] and references therein).

Among the highest negative ion yields have been reported for aluminum oxide[26] (Al_2O_3) and diamond-like carbon[1,23,30,36] (DLC), conversion surfaces, which both have been successfully applied in several space missions, e.g., in BepiColombo[24] and IBEX.[9] Nevertheless, there is interest in finding potential CS materials offering improved conversion efficiencies, less angular scattering, and less energy scattering to achieve even better performance in future space instrumentation.

Cadmium telluride (CdTe) was chosen as a candidate surface material based on the high atomic mass of its two components, Cd and Te, compared to the atoms of interest in space plasma research. In the binary collision model, ion-surface scattering happens via a single ideal collision of the incident atom (mass m_1, kinetic energy E_i) with a surface atom (mass m_2) in the crystalline lattice at rest. The incident atom is scattered by the angle θ from its initial trajectory, thereby some portion (p_2', E_2') of the energy-momentum is transferred to the lattice atom. The relative amount of the incident atom's kinetic energy lost in the collision, $\delta E_i/E_i$, would then depend on the mass ratio according to

$$\frac{\delta E_i}{E_i} = \frac{E_2'}{E_i} = \frac{m_1}{m_2}\sin^2(\theta)\left(1 + \frac{1}{4}\left(1 - \frac{m_1}{m_2}\right)^2 \sin^2(\theta)\right) + \mathcal{O}(\theta^6) \quad (1)$$

for small deflection angles θ. If applicable, this suggests that the energy transfer from the incident atom to the surface should be reduced for mass ratios m_2/m_1 much larger than one, as opposed to carbon or oxygen atoms in CS coating materials such as DLC or Al_2O_3 ($m_C/m_O \simeq 0.75$, $m_O/m_{Ne} \simeq 0.8$). For CdTe, the most abundant isotopes are ^{110}Cd, ^{111}Cd, ^{112}Cd, ^{114}Cd, ^{126}Te, ^{128}Te, and ^{130}Te, which yields mass ratios of $m_{Cd}/m_O \geq 6.8$ and $m_{Te}/m_O \geq 7.8$.

Moreover, CdTe is a II–IV semiconductor material. It has a crystalline sphalerite structure ($F\bar{4}3m$), a lattice constant of 6.48 Å, and a direct band gap of 1.56 eV. Its work function is about $\Phi = 5.7$ eV and the melting point is above 1300 K, and it is nearly insoluble in water. CdTe is widely used as an absorber material in thin film solar cells.[11,12] Alloyed with Hg or Zn, it makes an efficient infrared (IR), x-ray, or gamma ray detector material.[18,27,33,34] Furthermore, CdTe is used for IR optical windows and lenses. It, therefore, fulfils the aforementioned criteria to be considered a suitable CS material for space applications. Other similar semiconductor materials with the same crystal structure have a larger bandgap and reveal other disadvantages (e.g., ZnTe is flammable, CdSe is toxic and a suspected carcinogen, GaAs oxidizes over time, and ZnSe may react with acids to form toxic H_2Se). Despite its heavy metal component, the possible harmfulness of CdTe is very moderate and is further evaluated due to its wide application in photovoltaic research and production.

II. SETUP AND METHODS

A. ILENA test facility

The measurements were done in the Imager for Low Energetic Neutral Atoms (ILENA) test facility[35] at University of Bern. The ILENA setup consists of an electron impact ion source, a 90° sector magnet for ion species selection, a beam guiding system, a rotatable sample holder, and a movable two-dimensional imaging multichannel plate (MCP) detector with an angular field-of-view of 21° × 21° as seen from the sample center. A schematic overview of ILENA is shown in Fig. 1. The experimental setup is contained in a vacuum chamber equipped with a turbo molecular pump and an ion getter pump, which establish a base pressure in the low to mid-10^{-8} mbar range.

In the ion source, positive test gas ions are produced and extracted by a post-acceleration voltage of 100 V–3 kV. The ion beam is then focused and guided into the sector magnet, where the ion species of interest is selected by applying the appropriate magnetic field normal to the ion beam. The ion beam passes through a 1 mm diameter pinhole before it strikes the CS sample under an adjustable grazing incidence angle. In the scattering

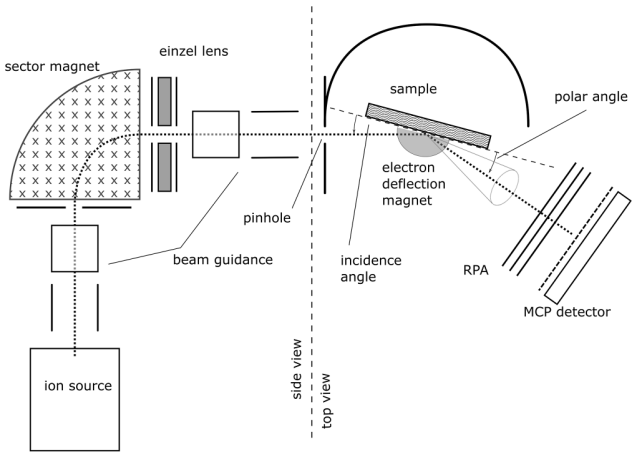

FIG. 1. ILENA measurement setup.

interaction with the CS, a memory loss of the initial charge state of the atom happens,[7,28,37,42] i.e., atoms of different charge state (H^+, H^0, H^-) experience the same scattering and negative ion yield. The interaction can, therefore, be regarded as acting between a neutral atom and the CS. This was also experimentally confirmed in Jans *et al.*[15]

A weak vertical magnetic field is used at the CS to direct released secondary electrons back onto the CS. After charge-exchange interaction with the sample, the particles are scattered toward the MCP detector. A retarding potential analyzer (RPA) prevents positive ions from reaching the detection subsystem; low-energy electrons are rejected likewise by a slight negative potential grid in front of the detector. Therefore, only neutral atoms and negative ions are detected.

The MCP detector itself consists of five consecutive MCPs mounted in front of a quadrilateral resistive anode. A subsequent analog position computing unit determines the location of each detected particle. The entire detector unit, including the RPA, is shielded electrostatically. It can be rotated about the polar axis at the sample holder center from $\theta = 0°$ to 90°. The entire MCP detector may optionally be floated on a high negative potential to reject negatively charged ions.

B. Sample preparation and characterization

The CS sample under test consists of a highly polished Si wafer coated with cadmium telluride (CdTe) of about 35 nm thickness, according to parameters during the fabrication process. Two identical trapezoidal Si wafer facets of about $18 \times 28\,mm^2$ and 1 mm thickness were prepared for coating. Initial surface roughness was about 0.1 nm rms. The CdTe layer was deposited at the Laboratory for Photovoltaics and Solid State Physics, University of Verona, Italy. CdTe was deposited by thermal evaporation in vacuum with a deposition rate of 0.29 nm/s at a pressure of 10^{-5} mbar. CdTe lumps are put in a graphite crucible and brought to a temperature of around 700 °C, the deposition rate, and the thickness is controlled by a quartz thickness monitor. The process duration was 2 min. The substrate temperature reached 90 °C during the coating process. According to Heisler *et al.*,[14] these conditions might result in a slight Te excess of a few percent compared to the nominal stoichiometric ratio (Cd:Te = 1:1), which is not considered relevant for this application. The surface of one CdTe-coated sample was investigated for its roughness using atomic force microscopy (AFM) at the Department of Chemistry and Biochemistry, University of Bern. We measured the surface roughness from AFM scans at three different locations on the sample: one near the center, another one near the lower left rim, and a third near the upper right rim. The AFM operates at ambient conditions with a FlexAFM scan head and a Tap190AI-G cantilever. Each location was scanned twice, with an imaging resolution of 256×256 pixels per $5\,\mu m$ and $1\,\mu m$, respectively.

Figure 2 shows an AFM image of the CdTe surface. It reveals a granular surface structure with about 25 nm grain size. On large scales, the coated surface is homogeneous with only very few small defects. The measured surface roughness was averaged over the total area of three spots, which all showed very similar results for

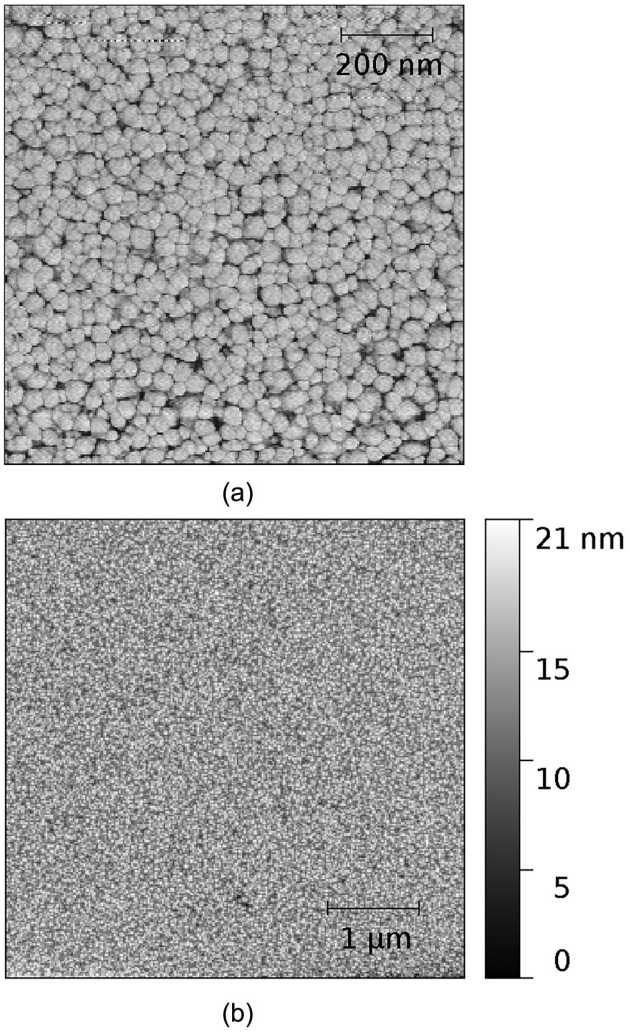

FIG. 2. AFM image of the CdTe surface. (a) Phase image that clearly shows the granular structure. The image area is $1\,\mu m^2$. (b) Grayscale-coded height profile. The image area is $5\,\mu m^2$.

all scanned spots at either imaging resolution. This yields a surface roughness $\mathcal{R}$ of

$$\mathcal{R} = 2.8 \pm 0.05\,nm_{rms}$$

with maximal height differences of about 20 nm peak-to-valley. This is significantly rougher than previous tested samples of different materials, by a factor of 2–3[1,23] to more than a factor of 10.[26,36] Furthermore, we obtained the coating thickness by measuring the height difference at the edge of the coated area, because a margin of about 2 mm remained uncoated. At several places along the coating edge, the surface height was compared

for two points separated about 600 μm across the coating edge. The CdTe coating thickness was measured to be 38.0 $\pm$ 4.0 nm using interferometry.

C. Measurement procedure

After the sample installation, the vacuum chamber was baked out during 48 h at a temperature of $T = 80\,^{\circ}$C. Before starting a measurement, test gas was inserted into the ion source, which increases the pressure in the vacuum chamber, and held in dynamical equilibrium at a pressure of $(4.0 \pm 0.1) \times 10^{-7}$ mbar. The typical base pressure before gas insertion was $(2.5 \pm 0.5) \times 10^{-8}$ mbar.

An ion beam was produced and ion-optical throughput was optimized using the focusing and deflection plates. For each test gas, a series of five consecutive measurements was performed, alternating between floating and the grounded detector subsystem to keep track of long-term system stability (cf., Fig. 3 in Neuland *et al.*[23]). When high-voltage floating the detector, it only accepts neutrals ($N_h = N_0$), while on ground potential, negative ions and neutrals $N_z = N_- + N_0$ are detected. In each single measurement, at least 10^6 counts were collected to guarantee sufficient statistics.

The negative ionization yield η is then computed[8] from the numbers $\tilde{N}_{(0,-)}$ of neutral atoms and negative ions scattered off the CS,

$$\eta = \frac{\tilde{N}_-}{\tilde{N}_0 + \tilde{N}_-} = 1 - \frac{1}{1 + \alpha \frac{N_-}{N_0}} = 1 - \frac{1}{1 + \alpha \left(\frac{N_z - N_h}{N_h}\right)}, \qquad (2)$$

where the parameter $\alpha = \kappa_0/\kappa_- < 1$ is the ratio of the detection efficiencies of neutrals and negative ions and $N_{(z,h)}$ are the number of counts detected, respectively, with zero and high negative retarding potential. α depends on particle species and energy.[25,32] The values used here lie within the range $0.5 < \alpha < 1$.

In this setup, a possible measured background emerges from recoil sputtered particles off the CS, especially secondary H and O from a persisting thin water layer adsorbed on the surface of the sample in the present pressure range. We use the noble gases He and Ne, with atomic masses comparable to those of H and O, respectively, as a proxy for the sputtering background, and subtract these values from the measured data. Since noble gases do not form stable negative ions, the total measured negative ion yield is considered to be due to sputtering.

For acceleration voltages below 500 V, the efficiency of forming atomic positive hydrogen and oxygen ions in the ion source was too low to achieve reasonably good statistics. Instead, positive molecular ions (H_2^+, O_2^+) were selected and accelerated to twice the nominal energy. This is justified since the vast majority of molecules break up into single atoms during interaction with the CS at the given energies,[15,17,42] so that the measured negative ion yield is essentially the same as for atomic H or O.

We assign an estimated energy uncertainty of $\pm$10% to these data points to take into account that the kinetic energy of the molecule may be unevenly partitioned among the separate atoms in the molecule dissociation upon surface scattering from the CS. The respective time-of-flight spectra can be found in Jans *et al.*[15] Additionally, the angular distribution of scattered atoms is recorded using the 2D-imaging MCP detector. The full-width at half-maximum (FWHM) in azimuthal (tangentially to the surface) and polar (normal to the surface) direction is measured for all species at various incident energies by reading out the extend of the 50% contour line in the angular distributions.

In a third part, we investigated the effective energy distribution of the scattered ion beam by the retarding potential analysis. For this purpose, the countrate was monitored at constant incident energy E_i while varying the retarding potential in steps of 100 V from 1.3 E_i/q down to 0 V. At high RPA voltage, only the scattered neutral atoms can reach the detector. When lowering the RPA voltage, an increasing amount of negative ions whose energy exceeds the retarding potential will be detected. To close the measurement sequence, data at the highest retarding potential were taken again, and the data were corrected for a slow linear time trend. The energy distribution of scattered negative ions was then computed as the counts difference between adjacent RPA values and is normalized by the constant number of detected neutrals. The energy distribution of scattered neutrals cannot be directly monitored by this method. However, we assume the particle energy distribution does not depend on the charge state, so that the obtained distribution is considered representative for the total set of scattered oxygen ions and atoms.

III. RESULTS AND DISCUSSION

A. Negative ionization yield

The negative ionization yield of H and O atoms upon scattering at a CdTe conversion surface was measured for energies from 195 eV to 1000 eV per atom at an incidence angle of 8°. The results are shown in Fig. 3. Background values measured with He and Ne, respectively, at the same energies are subtracted from the H and O data to account for recoil sputtering of surface atoms. For helium, the measured negative ion yield was 1.7% at 195 eV, increasing to 2.9% at 1000 eV. For neon, the measured negative ion yield was 3.1% at 250 eV and 4.3%–4.6% for energies from 390 eV to 1000 eV. The value at 195 eV could not be measured for Ne due to ion source instability at this low energy. Instead, the same value as for 250 eV was subtracted from oxygen at 195 eV as sputtering background.

We find a negative hydrogen ionization yield of 2%–3% for incident energies between 195 eV and 1000 eV, showing only a slight increase over the energy range within the uncertainties. For oxygen, the negative ionization yield is about 8.6% at 195 eV and increases to about 12.8% at 1000 eV.

The results found here for a CdTe-coated CS are comparable to those found previously for other coatings: Allenbach *et al.*[1] found very similar negative ionization yield for B-doped DLC. Neuland *et al.*[23] likewise report $\eta \simeq 2\%$ for H on metallized DLC, and $\eta = 10\%$–12% for O. Various DLC-coated CS candidates for IBEX were tested by Wahlström *et al.*[36] and slightly higher negative ion yields were found, 11–20% for O, and 2–4% for H. Scheer[30] did a similar investigation using various H-terminated DLC samples that showed comparable results. Negative ion yields for Al_2O_3 were in the same range[26] as in this work for oxygen ($\eta_O = 9\%$ to 13%), but considerably higher for hydrogen ($\eta_H = 3.5\%$ up to 4.6%).

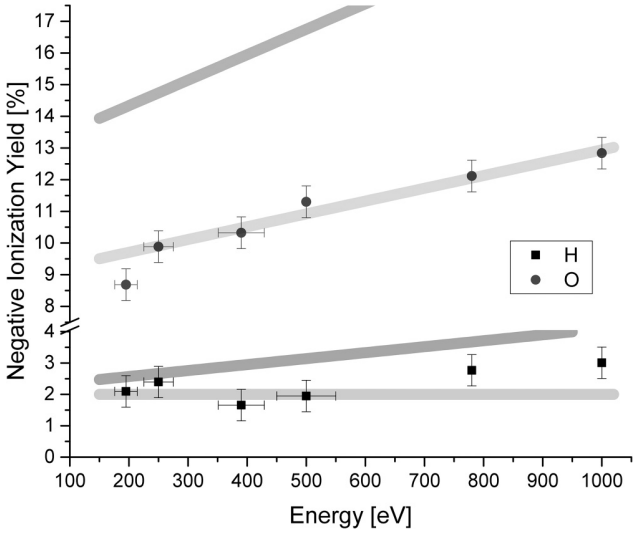

FIG. 3. Negative ionization yield of H and O atoms upon scattering at a CdTe conversion surface under 8° incidence angle for different incident energies per atom. Points with indicated energy uncertainty were done using primary molecular ions with twice the energy. Underlying grayscale bars represent the trends found in previous measurements with DLC samples. Dark gray: results from Scheer *et al.*[30] and Wahlström *et al.*;[36] light gray: results from Neuland *et al.*[23] and Allenbach *et al.*[1]

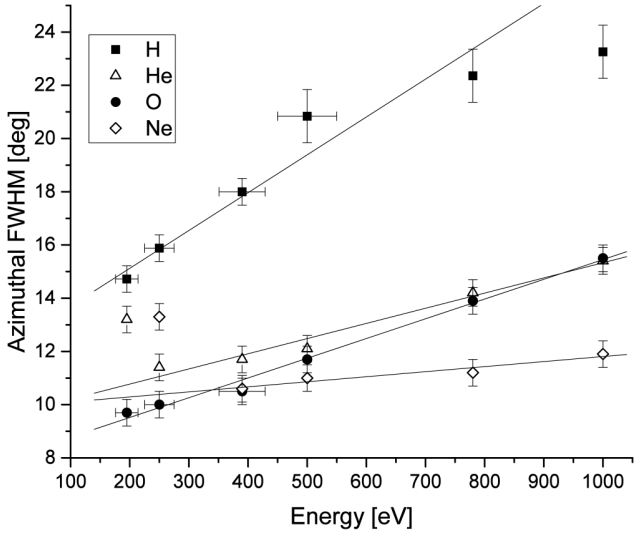

FIG. 4. Azimuthal FWHM of scattered atoms off the CdTe surface at different incident energies at 8° incidence angle. Linear fit lines are shown to guide the eye.

B. Angular scattering distribution

The angular scattering FWHM of H, He, O, and Ne was measured in azimuthal and polar directions for energies from 195 eV to 1000 eV per atom upon scattering on a CdTe-coated CS at an incidence angle of 8°. The results are displayed in Figs. 4 and 5. Hydrogen shows the broadest scattering distribution of more than 14° azimuthal and 16° polar FWHM, while the other species show angular FWHM of 10°–15° in both directions. Values above 20° were on or beyond the detector edge and were obtained using a Gaussian fit in the azimuth direction and a log-normal in the polar direction using a least-squares fit. We estimate a 10% uncertainty in the incident energy per atom for measurements done using molecular primary ions, as explained in Sec. II C.

The angular scattering width increases with particle energy in both angular directions, except for He and Ne at the lowest measured energy. This trend is in accordance with our expectations from previous results with DLC-[1,23,36] and Al_2O_3-coated CS samples.[26,29] While the azimuthal scattering width is usually broader than the polar width by typically about 30%, we see here that for the CdTe-coated CS the azimuthal and polar widths differ by less than 10% for all particle species and energies. The azimuthal widths found here are within the range of angular scattering reported for other coatings. The polar widths are slightly higher compared to the results in Allenbach *et al.*,[1] Neuland *et al.*,[23] Riedo *et al.*,[26] and Wahlström *et al.*[36]

For the application in ENA instruments, a narrow angular scattering cone is strongly favored, as it directly improves the possible instrument throughput of the downstream ion optics. The tested CS sample showed a tolerable but rather high surface roughness in comparison with previous candidates. Moreover, it showed a particular granular structure under the AFM scan rather than a homogeneously smooth surface. While Wahlström *et al.*[36] see no

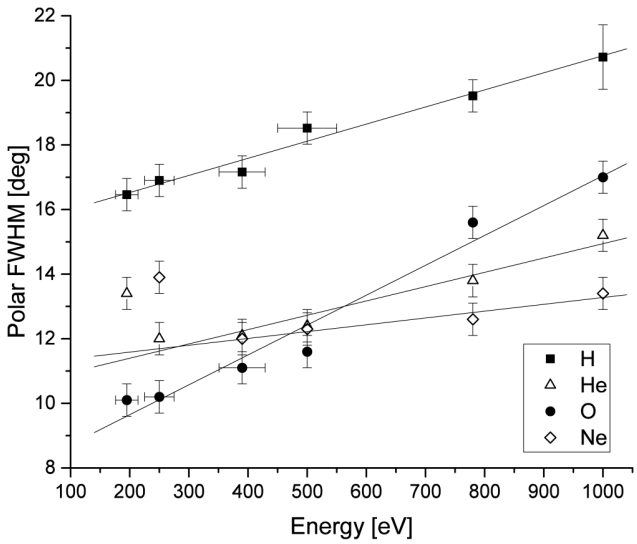

FIG. 5. Polar FWHM of scattered atoms off the CdTe surface at different incident energies at 8° incidence angle. Linear fit lines are shown to guide the eye.

influence of surface roughness on angular scattering, Riedo *et al.*[26] relate broader angular scattering to changes in the surface structure at few Å smooth surfaces, even if the surface roughness increased only insignificantly. This effect will be even larger at rougher surfaces, and angular scattering is expected to be reduced by a smoother coating. This, in turn, depends on the coating process and the underlying Si wafer roughness.

C. Energy distribution

The energy distribution of the scattered particles was investigated using the retarding potential method. A primary O_2^+ ion beam of $E_i = 1000$ eV/q (500 eV per atom) was directed onto the CdTe-coated sample. The fraction of negative ions was then monitored while varying the RPA potential from 1300 V down to 0 V. In Fig. 6, the differential of scattered oxygen ions, normalized to the number of scattered neutral particles, is plotted against the retarding potential.

We observe all negative ions scattered off the CdTe CS at energies below 600 eV. Above ion energies of 500 eV/q, the data are in accordance with zero scattered particles. Small fluctuations are due to statistical variability in the experiment. The RPA measurement shows that all incident molecular ions break up into atoms in the scattering interaction. This agrees with the results found in Wurz *et al.*[42] and Jans *et al.*,[15] where a time-of-flight analysis was used. Otherwise, we should see some fraction of scattered ions still carrying an energy of 500–1000 eV with only some fraction of their energy lost in the scattering process.

The data point around 50 eV is likely dominated by a low-energy component, which originates from ions sputtered off the CS rather than direct scattered O^- ions. This Sigmund–Thompson sputtering background[31] drops off as $\propto E^{-2}$, as indicated in Fig. 6.

The mean energy of scattered O^- ions is about $\langle E \rangle = 273 \pm 30$ eV. This corresponds to a mean energy loss of about $\langle dE/E_i \rangle = 45\%$ for O atoms from primary molecules in the scattering process, which is well in agreement with the energy loss at the IBEX-Lo CS (cf., Fig. 18 in Fuselier *et al.*[9]), where the reported values are $(45 \pm 15)\%$ for O^- ions at about 500 eV.

A similar energy distribution was obtained using primary H_2^+ ions with an energy of 1500 eV, however with a much smaller fraction of scattered negative ions (up to 1%/100 V) and thus much larger relative uncertainties.

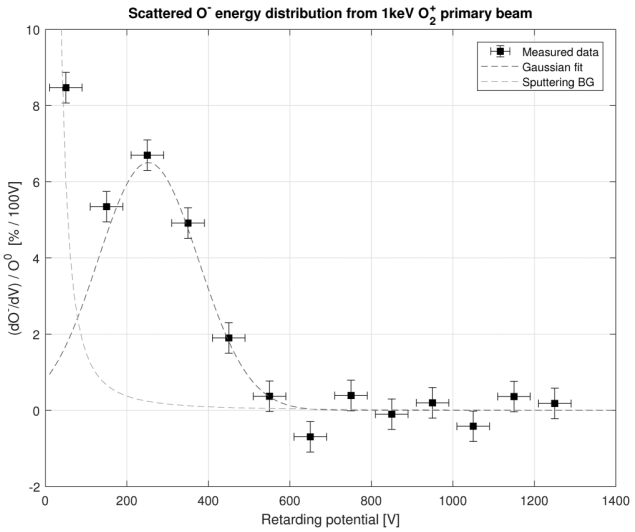

FIG. 6. Energy distribution of scattered O^- ions off the CdTe CS as percentage of total scattered neutral oxygen. The primary O_2^+ ions were accelerated to 1000 eV and were scattered under 8° incidence angle. The low-energetic sputtering background and a Gaussian fit to the scattered O^- energy distribution are indicated.

IV. CONCLUSION

A CdTe-coated Si wafer sample was investigated in the ILENA test facility[35] at University of Bern for its suitability as potential conversion surface in future ENA detection instruments in space research. One key characteristic of a CS is the smoothness on atomic scales. The surface roughness of the CdTe sample under test was investigated by AFM microscopy and was found to be $\mathcal{R} = 2.8$ nm rms, which is near the upper limit for suitable CS as seen from the measurements of angular scatter. Moreover, the granular structure is of concern for the angular and energy scatter. Improvements in the smoothness and homogeneity of the coating are possible in the fabrication process. By chemical (nitro phosphoric or bromine methanol etching) or physical (plasma) etching, it is possible to further reduce the surface roughness. Alternatively, epitaxially grown coating might lead to smoother surfaces.

The scattering properties of the CdTe CS, i.e., the negative ionization yield and the angular scattering width, were measured in the ILENA test facility for various energies at 8° incidence angle. Moreover, the energy distribution of scattered O was recorded. This shows that incident molecular ions are effectively split upon scattering and are scattered as individual atoms. The mean energy loss of about 45% turns out to be higher than previously expected. Our hypothesis that a CS material consisting of heavier atoms compared to C or O could significantly reduce the scattering energy loss could not be confirmed with the present CdTe coating. However, the results are comparable to other CS surfaces in use.

Over all, scattering results for CdTe are comparable to other established CS materials for space applications. Scattered negative ionization yields should exceed at least the 1% threshold for H to get further consideration as a CS.[42] This threshold requirement is readily fulfilled with CdTe. Given that an even smoother coating with CdTe is feasible, it should be possible to reduce angular scattering. In conclusion, we find that CdTe is indeed a possible alternative CS coating material for use in future ENA instruments.

ACKNOWLEDGMENTS

We warmly thank Dr. Vitali Grozovski at DCB, University of Bern, for his great support with AFM microscopy. This work was supported by the Swiss National Science Foundation.

DATA AVAILABILITY

The data that support the findings of this study are available from the corresponding author upon reasonable request.

REFERENCES

[1]M. Allenbach, M. Neuland, A. Riedo, and P. Wurz, Appl. Surf. Sci. **427**, 427 (2017).
[2]S. Barabash, A. Bhardwaj, M. Wieser, R. Sridharan, T. Kurian, S. Varier, E. Vijayakumar, V. Abhirami, K. Raghavendra, S. Mohankumar, M. Dhanya, S. Thampi, K. Asamura, H. Andersson, Y. Futaana, M. Holmström, R. Lundin, J. Svensson, S. Karlsson, and P. Wurz, Curr. Sci. **96**, 526 (2009); available at http://repository.ias.ac.in/64228/
[3]S. Barabash, R. Lundin, H. Andersson, K. Brinkfeldt, A. Grigoriev, H. Gunell, M. Holmström, M. Yamauchi, K. Asamura, P. Bochsler, P. Wurz, R. Cerulli-Irelli, A. Mura, A. Milillo, M. Maggi, S. Orsini, A. Coates, D. Linder, D. Kataria, and J. Thocaven, Space Sci. Rev. **126**, 113 (2006).
[4]S. Barabash, J.-A. Sauvaud, H. Gunell, H. Andersson, A. Grigoriev, K. Brinkfeldt, M. Holmström, R. Lundin, M. Yamauchi, K. Asamura, W. Baumjohann, T. Zhang, A. Coates, D. Linder, D. Kataria, C. Curtis, K. Hsieh, B. Sandel, A. Fedorov, and P. Bochsler, Planet. Space Sci. **55**, 1772 (2007).
[5]S. Barabash, P. Wurz, P. Brandt, M. Wieser, M. Holmström, Y. Futaana, G. Stenberg Wieser, H. Nilsson, A. Eriksson, M. Tulej, A. Vorburger, N. Thomas, C. Paranicas, D. Mitchell, G. Ho, B. Mauk, D. Haggerty, J. Westlake, M. Fränz, and D. Grodent, Proc. Eur. Planet. Sci. Congr. **8**, EPSC2013 (2013); available at https://meetingorganizer.copernicus.org/EPSC2013/EPSC2013-709.pdf
[6]A. Bhardwaj, S. Barabash, Y. Futaana, Y. Kazama, K. Asamura, D. McCann, R. Sridharan, M. Holmström, P. Wurz, and R. Lundin, J. Earth Syst. Sci. **114**, 749 (2005).
[7]D. Faircloth and S. Lawrie, New J. Phys. **20**, 025007 (2018).
[8]M. Föhn, "Application of surface physics for instruments in space science," master thesis (University of Bern, 2017).
[9]S. Fuselier, P. Bochsler, D. Chornay, G. Clark, G. Crew, G. Dunn, T. Friedmann, H. Funsten, A. Ghielmetti, J. Googins, M. Granoff, J. Hamilton, J. Hanley, D. Heirtzler, E. Hertzberg, D. Isaac, B. King, U. Knauss, and S. Zaffke, Space Sci. Rev. **146**, 117 (2009).
[10]Y. Futaana, S. Barabash, X.-D. Wang, M. Wieser, G. S. Wieser, P. Wurz, N. Krupp, and P. Brandt, Planet. Space Sci. **108**, 41 (2015).
[11]M. Gloeckler, I. Sankin, and Z. Zhao, IEEE J. Photovoltaics **3**, 1389 (2013).
[12]M. Green, E. Dunlop, J. Hohl-Ebinger, M. Yoshita, N. Kopidakis, and X. Hao, Prog. Photovoltaics Res. Appl. **28**, 629 (2020).
[13]M. Gruntman, Rev. Sci. Instrum. **68**, 3617 (1997).
[14]C. Heisler, M. Brückner, F. Lind, C. Kraft, U. Reislöhner, C. Ronning, and W. Wesch, J. Appl. Phys. **113**, 224504 (2013).
[15]S. Jans, P. Wurz, R. Schletti, K. Brüning, K. Sekar, W. Heiland, J. Quinn, and R. Leuchtner, Nucl. Instrum. Methods Phys. Res. Sect. B **173**, 503 (2001).
[16]Y. Kazama, S. Barabash, M. Wieser, K. Asamura, and P. Wurz, AIP Conf. Proc. **1144**, 109 (2009).
[17]A. Kleyn, J. Phys. Condens. Matter **4**, 8375 (1992).
[18]W. Lei, J. Antoszewski, and L. Faraone, Appl. Phys. Rev. **2**, 041303 (2015).
[19]J. Los and J. Geerlings, Phys. Rep. **190**, 133 (1990).
[20]D. McComas, F. Allegrini, P. Bochsler, M. Bzowski, M. Collier, H. Fahr, H. Fichtner, P. Frisch, H. Funsten, S. Fuselier, G. Gloeckler, M. Gruntman, V. Izmodenov, P. Knappenberger, M. Lee, S. Livi, D. Mitchell, E. Moebius, T. Moore, S. Pope, D. Reisenfeld, E. Roelof, J. Scherrer, N. Schwadron, R. Tyler, M. Wieser, P. Wurz, and G. Zank, Space Sci. Rev. **146**, 11 (2009).
[21]D. McComas, E. Christian, N. Schwadron, N. Fox, J. Westlake, F. Allegrini, D. Baker, D. Biesecker, M. Bzowski, G. Clark, C. Cohen, I. Cohen, M. Dayeh, R. Decker, G. de Nolfo, M. Desai, R. Ebert, H. Elliott, H. Fahr, and E. Zirnstein, Space Sci. Rev. **214**, 116 (2018).
[22]T. Moore, D. Chornay, M. Collier, F. Herrero, J. Johnson, M. Johnson, J. Keller, J. Laudadio, J. Lobell, K. Ogilvie, P. Rozmarynowski, S. Fuselier, A. Ghielmetti, E. Hertzberg, D. Hamilton, R. Lundgren, P. Wilson, P. Walpole, T. Stephen, B. Peko, B. van Zyl, P. Wurz, J. Quinn, and G. Wilson, Space Sci. Rev. **91**, 155 (2000).
[23]M. Neuland, A. Riedo, J. Scheer, and P. Wurz, Appl. Surf. Sci. **313**, 293 (2014).
[24]S. Orsini, S. Livi, K. Torkar, S. Barabash, A. Milillo, P. Wurz, A. Di Lellis, and E. Kallio; the SERENA team, Planet. Space Sci. **58**, 166 (2008).
[25]B. Peko and T. Stephen, Nucl. Instrum. Methods Phys. Res. Sect. B **171**, 597 (2000).
[26]A. Riedo, M. Ruosch, M. Frenz, J. Scheer, and P. Wurz, Appl. Surf. Sci. **258**, 7292 (2012).
[27]U. Roy, G. Camarda, Y. Cui, R. Gul, A. Hossain, G. Yang, J. Zázvorka, V. Dedic, J. Franc, and R. James, Sci. Rep. **9**, 1620 (2019).
[28]J. Scheer, W. Brüning, T. Fröhlich, P. Wurz, and W. Heiland, Nucl. Instrum. Methods Phys. Res. Sect. B **157**, 208 (1999).
[29]J. Scheer, P. Wahlström, and P. Wurz, Nucl. Instrum. Methods Phys. Res. B **267**, 2571 (2009).
[30]J. Scheer, M. Wieser, P. Wurz, P. Bochsler, E. Hertzberg, S. Fuselier, F. Koeck, R. Nemanich, and M. Schleberger, Adv. Space Res. **38**, 664 (2006).
[31]P. Sigmund, Phys. Rev. **184**, 383 (1969).
[32]T. M. Stephen and B. L. Peko, Rev. Sci. Instrum. **71**, 1355 (2000).
[33]T. Takahashi and S. Watanabe, Nucl. Sci. IEEE Trans. **48**, 950 (2001).
[34]S. Velicu, G. Badano, Y. Selamet, C. Grein, J. Faurie, D. Rafol, and R. Ashokan, J. Electron. Mater. **30**, 711 (2001).
[35]P. Wahlström, J. Scheer, A. Riedo, P. Wurz, and M. Wieser, J. Spacecr. Rockets **50**, 402 (2013).
[36]P. Wahlström, J. Scheer, P. Wurz, E. Hertzberg, and S. Fuselier, J. Appl. Phys. **104**, 034503 (2008).
[37]M. Wieser, P. Wurz, K. Brüning, and W. Heiland, Nucl. Instrum. Methods Phys. Res. Sect. B **192**, 370 (2002).
[38]D. Williams, E. Roelof, and D. Mitchell, Rev. Geophys. **30**, 183, (1992).
[39]H. Winter, Phys. Rep. Rev. Sect. Phys. Lett. **367**, 387 (2002).
[40]P. Wurz, *The Outer Heliosphere: Beyond the Planets* (Copernicus Gesellschaft e.V., Katlenburg-Lindau, 2000), p. 251.
[41]P. Wurz, J. Scheer, and M. Wieser, J. Surf. Sci. Nanotechnol. **4**, 394 (2006).
[42]P. Wurz, R. Schletti, and M. Aellig, Surf. Sci. **373**, 56 (1997).

A.2. Data sheets

PHOTONIS USA
P.O. Box 1159
Sturbridge, MA 01566
United States of America

T +1 800 648 1800 (US & Can)
T +1 508 347 4000 (Intl calls)
F +1 508 347 3849
E sales@usa.photonis.com
www.photonis.com

Chevron MCP and Detector Initial Start-up and Electrical Test Procedure

NOTES: Read the entire start-up procedure before applying any voltages.
Refer to Diagram 1 - Typical Wiring Diagrams - for each detection mode.
The suggested bias voltage for a Resistive Anode Encoder (RAE) is 300 volts.

CAUTION:
Do not exceed 1000V per Microchannel Plate (MCP) for 40:1 aspect ratio MCPS. 1200V/MCP for 60:1 aspect ratio MCPS.
When installing flange mounted detectors gradually tighten the bolts in a star pattern (DO NOT exceed 20 foot-pounds per bolt). Failure to do so could cause the fiberoptic to crack.

RECOMMENDATIONS:
For optimal lifetime, operate the detector at the minimum voltage necessary to obtain a useable signal.
Do not operate the phosphor screen at a higher than recommended potential.

PROCEDURE
Make all connections to the assembly.
Check all electrical connections for possible shorted or open circuits.
Pump down to $2x10^{-6}$ torr and hold for at least 15 hours.

VOLTAGE APPLICATION

Electron/Negative Ion/UV Photon Detection: (for a metal anode or Resistive Anode Encoder, skip to next section)

Phosphor Screen
Ground the input of the assembly (V_i). Apply voltage to the phosphor screen (V_a) in +250V, 1 minute increments. Stop at +1.0 kV.
Apply voltage to the output of the assembly (V_o) in +100V, 2 minute increments. Stop at +1.0 kV.
Increase the voltage to Va in +100V, 5 minute increments to +3.0 kV. Wait 5 minutes.
Increase the voltage to Va in +100V, 10 minute increments to +4.0 kV. Wait 5 minutes.
Simultaneously increase the voltage to V_a and V_o in +100V, 10 minute increments to +4.5 kV at V_a and +1.5 kV at V_o.
For screens requiring a 5.0 kV potential - Increase the voltage to V_a in +100V, 10 minute increments to +5.5 kV. Wait 10 minutes.
For screens requiring a 5.0 kV potential - Increase the voltage to V_a in +50V, 10 minute increments to +6.5 kV. Wait 10 minutes.
Simultaneously increase the voltage to V_a and V_o in +50V, 10 minute increments to +2.0 kV at V_o.
When through using the detector, turn off the voltage to V_a. When the voltage drops below +2.0 kV, turn off the voltage to V_o.

Metal Anode/Resistive Anode Encoder
Ground the input of the assembly (V_i). Apply the specified anode bias to V_a.
Increase the voltage to both V_a and V_o in +100V, 2 minute increments by +1.0 kV at V_a and to +1.0 kV at V_o. Wait 5 minutes.
Increase the voltage at V_o and V_a in +100V, 5 minute increments to +1.5 kV at V_o. Wait 10 minutes.
Increase the voltage at V_o and V_a in +50V, 5 minute increments to +2.0 kV at V_o.
When through using the detector, turn off the voltages to V_o and V_a.

Positive Ion/UV Photon Detection (for a metal anode or Resistive Anode Encoder, skip to next section).

Phosphor Screen
Ground the output of the assembly (V_o). Apply voltage to the phosphor sheen (V_a) in +250V, 1 minute increments. Stop at +1.0 kV.
Apply voltage to the input of the assembly (V_i) in -100V, 2 minute increments. Stop at -1.0 kV.
Increase the voltage to V_a in +100V, 5 minute increments to +2.0 kV. Wait 5 minutes.
Increase the voltage to V_a in +100V, 10 minute increments to +3.0 kV. Wait 5 minutes.
Adjust the voltage to V_i in -100V, 10 minute increments to -1.5 kV.
For screens requiring a 5.0 kV potential - Increase the voltage to V_a in +100V, 10 minute increments to +4.0 kV. Wait 10 minutes.
For screens requiring a 5.0 kV potential - Increase the voltage to V_a in +50V, 10 minute increments to +5.0 kV. Wait 10 minutes.
Adjust the voltage to V_i in -50V, 10 minute increments to -2.0 kV.
When through using the detector, turn off the voltages to the V_i and V_a.

Metal Anode/Resistive Anode Encoder
Ground the output of the assembly (V_o). Apply the specified anode bias to V_a.
Apply voltage to V_i in -100V, 2 minute increments. Stop at -1.0 kV. Wait 2 minutes.
Adjust the voltage at V_i in -100V, 5 minute increments to -1.5 kV. Wait 5 minutes.
Adjust the voltage at V_i in -50V, 10 minute increments to -2.0 kV.
When through using the detector, turn off the voltages to V_i and V_a.

TYPICAL WIRING DIAGRAMS

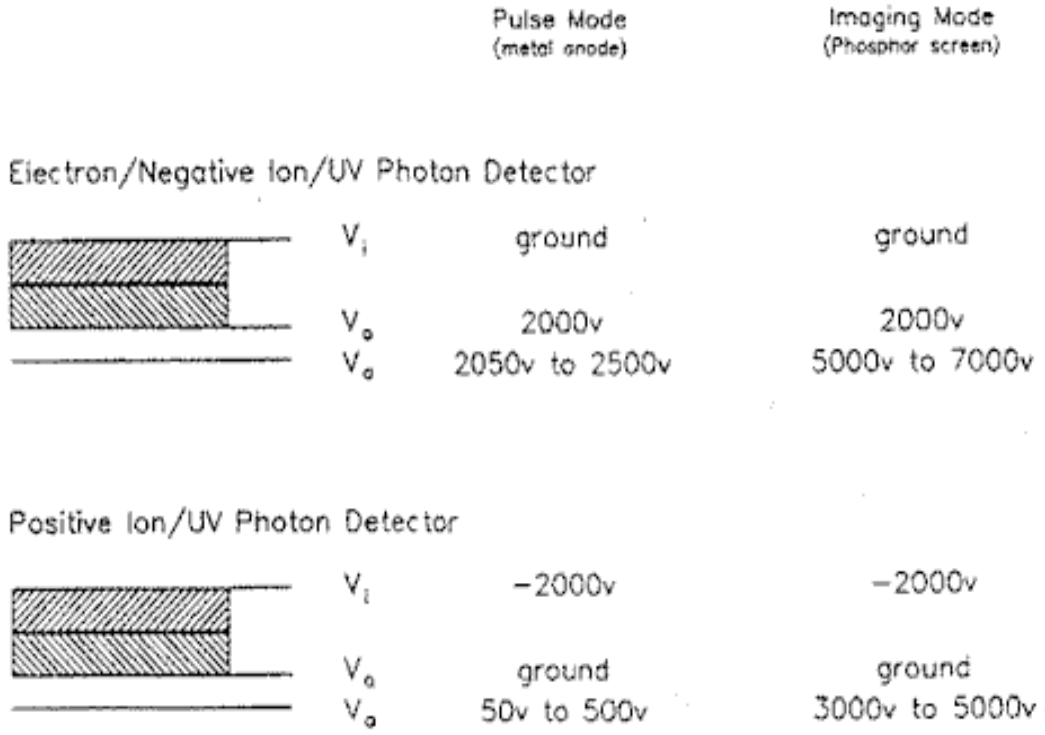

A.3. Voltage Table

# electrode	name	PFM		FS	
		th-Mode [V]	n-Mode [V]	th-Mode [V]	n-Mode [V]
IS 1	push grid	-0.2	-1	-1.1	-1.25
IS 2	ion-repeller l	150	122.5	125	122.5
IS 3	entrence	0	0	0	0
IS 4	ion-repeller r	150	142	143	148
IS 5/6	Pulser Bias	0	0	0.2	0.3
IS 5/6	Pulser HV	-480	-480	-480	-480
IS 7	lens 1	-300	182	-1300	-1500
IS 8	lens 2	-1800	-2221	-3400	-3250
IS 9	lens 3	-1500	-1150	-1250	-1750
IS 10	lens 4	-3200	-1121	-2125	-2500
IS 11	lens 5	-1600	-3565	-2800	-2500
IS 12	lens 6	-2400	-1197	-1750	-1850
IS 13	lens 7	-3000	-1573	-5000	-5000
R 2	focusing	-6450	-5477	-6600	-6700
R 4	retarding 1	-400	146	0	150
R 8	intermediate	-1200	-1091	-1035	-1025
R 15	backplane	20	-20	175	200
UMCP		1850	1900	1900	1950
MCP Front/ D4	D/ Front	-2500	-2600	-2500	-2500
FIL 1	filament (bias)	-70	-70	-70	-70
FIL 2	e-repeller	-72	-70	-70	-70
FIL 3	e-slit	110	104	95	100

Table 9: Voltage sets for NIM PFM and FS instruments.

Acknowledgement

First of all I thank Prof. Peter Wurz for the great opportunity to work during the last four years in his team. This thesis gave me insight in a lot of different fields ranging from mechanical to electrical engineering into project management. The work was diverse and educational in a lot of different aspects.

I would like to thank the members of the PEP NIM team on Fig. 74 and also those who did not make it to the picture.

Special thanks go to Stefan Meyer who introduced me to the NIM instrument and for his support at the beginning of my PhD. André Galli as an office mate and also for the very amusing and educational discussions especially during the time writing this thesis.

Harald Mischler, Georg Bodmer, Adrian Etter and Joël Gonseth for their technical support in the laboratory. Daniele Piazza, Michael Gerber and Stefan Brüngger from the construction office. Matthias Lüthi, Severin Oegschger, Andreas Nentwig, Michael Althaus, Philipp Fahrer and Hans Peter Munz from the electronics workshop.

My family, the members of the Wabschli-WG, Dinierclub and the Friday beer for their support and distraction during the non-office hours.

Figure 74: PEP NIM team with a few outliers missing ;).

Erklärung

gemäss Art. 18 PromR Phil.-nat. 2019

Name/Vorname: Föhn Martina

Matrikelnummer: 11-105-145

Studiengang: Physics

Bachelor ☐ Master ☐ Dissertation ☑

Titel der Arbeit: NIM: The Neutral Gas and Ion Mass Spectrometer to Explore the Galilean Ice Worlds

LeiterIn der Arbeit: Prof. Peter Wurz

Ich erkläre hiermit, dass ich diese Arbeit selbständig verfasst und keine anderen als die angegebenen Quel-len benutzt habe. Alle Stellen, die wörtlich oder sinn-gemäss aus Quellen entnommen wurden, habe ich als solche gekennzeichnet. Mir ist bekannt, dass andern-falls der Senat gemäss Artikel 36 Absatz 1 Buchstabe r des Gesetzes über die Universität vom 5. September 1996 und Artikel 69 des Universitätssta-tuts vom 7. Juni 2011 zum Entzug des Doktortitels be-rechtigt ist.
Für die Zwecke der Begutachtung und der Überprüfung der Einhaltung der Selbständigkeitserklärung bzw. der Reglemente betreffend Plagiate erteile ich der Univer-sität Bern das Recht, die dazu erforderlichen Perso-nendaten zu bearbeiten und Nutzungshandlungen vor-zunehmen, insbesondere die Doktorarbeit zu vervielfäl-tigen und dauerhaft in einer Datenbank zu speichern sowie diese zur Überprüfung von Arbeiten Dritter zu verwenden oder hierzu zur Verfügung zu stellen.

Ort/Datum

Unterschrift

Curriculum Vitae

Name:	Martina Föhn
Date of Birth:	4. February 1993
Place of Birth:	Schwyz

Education

01.2018 – 12.2021	PhD in Physics, Physics Institute, Space Research and Planetary Sciences Division, University of Bern, Switzerland Thesis: *NIM: The Neutral Gas and Ion Mass Spectrometer to Explore the Galilean Ice Worlds*
01.2016 – 11.2017	MSc in Physics, Physics Institute, Space Research and Planetary Sciences Division, University of Bern, Switzerland Thesis: *Application of Surface Physics for Instruments in Space Science*
09.2011 – 01.2016	BSc. in Physics, Institute of Applied Physics, University of Bern, Switzerland Thesis: *Optical stimulation of the earthworm's nerve cord*
08.2007 – 07.2011	Gymnasium at Theresianum Ingenbohl with specialisation in Biology and Chemistry

Professional Experience

2012 – present	Private tutor in Mathematics and Physics
2016 – present	Teaching Assistant at the Physics Institute, University of Bern, Switzerland.